THÈSE

En vue de l'obtention du

DOCTORAT DE L'UNIVERSITÉ DE TOULOUSE

Délivré par : *l'Université Toulouse 3 Paul Sabatier (UT3 Paul Sabatier)*

Présentée et soutenue le *03/07/2015* **par :**

TIANGANG YIN

Modélisation 3D du transfert radiatif pour simuler les images et données de spectroradiomètres et Lidars satellites et aéroportés de couverts végétaux et urbains.

3D radiative transfer model for simulating satellite and airborne imaging spectroscopy and LiDAR data of vegetation and urban canopies.

JURY

STÉPHANE JACQUEMOUD	Professeur d'université	Université Paris Diderot
GRÉGOIRE VINCENT	Chargé de Recherche	IRD-AMAP-CIRAD
XAVIER BRIOTTET	Directeur de recherche	ONERA
FRÉDÉRIC BARET	Directeur de recherche	INRA-EMMAH-CAPTE
JOSIANE COSTERASTE	Ingénieur	CNES
JEAN-BAPTISTE FERET	Chargé de Recherche	IRSTEA (UMR-TETIS)
JACQUELINE ROSETTE	Research Officer	Swansea University

École doctorale et spécialité :
SDU2E : Océan, Atmosphère et Surfaces Continentales
Unité de Recherche :
Centre d'Etudes Spatiales de la BIOsphère (UMR 5126)
Directeur de Thèse :
Jean-Philippe Gastellu Etchegorry
Rapporteurs :
Stéphane Jacquemoud, *Grégoire Vincent*

Dédié à ma mère et ma femme

Dedicated to my mother and my wife

献给我的母亲和妻子

Acknowledgements

The years of pursuing a PhD is a fruitful and memorable period, which I would cherish in my whole life time. It is my great pleasure and honor to take this opportunity to say thank you to many people who helped me during this journey.

Foremost, I would like to express my deepest gratitude to my thesis supervisor, Professor Jean-Philippe Gastellu-Etchegorry, for his continuous guidance, inspirations, supports and encouragements throughout the period. Without the robust foundation of his great effort during the past 20 years in making DART a mature model, this dissertation would not have been possible. He is respectable as both a researcher and a friend. I especially appreciate his attitude and enthusiasm for pursuing truth and excellence in research, which will be the objectives of my future career as a researcher.

I would like to thank the DART team: Nicolas Lauret, Thomas Cajgfinger, Tristan Gregoire, Jordan Guilleux and Lucas Landier, for continuously improving DART code, functionalities (SQL databases, etc.) and modeling components (atmosphere, water, etc.), particularly during the past 6 months which I spent writing papers. I will miss our systematic weekly work meetings. Special thanks to Nicolas for his excellent management of DART computer science, scientific collaboration, especially for LIDAR, and patience in helping me to implement new DART functionalities. He deserves a perfect dissertation next year.

I would like to say thank you to all the previous DART team members, including Eloi Grau, Maïlys Lopes, Francois Gonard, Ruzena Janoutova, as well as Zbyněk Malenovský and Jean-Baptiste Féret who shared their expertise in spectrometry applied to vegetation, which inspired my research. I appreciated also working with all past and present master and PhD students in DART team, including Josselin Aval, Laurine Marmisse, Sahar Benhmida, Lucas Moresve, Fabien Leclerc, etc. I wish them all bright professional and personal lives.

Many thanks to Jeremy Rubio, Bruce Cook, Douglas Morton and Guoqing Sun from Goddard Space Flight Center. During my stay at NASA, I appreciated their hospitality and guidance on present and future LIDAR systems. Many thanks to Fabian Schneider from Remote Sensing Laboratories (University of Zurich) for his fruitful collaboration, which incited me to improve DART 3D projection.

I would like to say thank you to the reviewers of my thesis, Professor Stéphane Jacquemoud and Dr. Grégoire Vincent, for their detailed and valuable remarks and corrections, which definitely make this dissertation a better one.

Thanks to all colleagues in CESBIO, for their friendly smiles and daily hellos. I thank also the

security staffs for their night hellos. Working far into the night is now forbidden by the administration.

A special thank to my previous group leader, Emmanuel Christophe, who initially recommended me to come to work in CESBIO. Another thank you to Jordi Inglada, who recommended me to join the DART team. Without their recommendations, I would never have got the chance to start this thesis.

Thanks to my family and friends in China, Singapore and France, for all their supports.

Last but never the least, the most sincere appreciations to my mother and my wife, who gave me the best supports to pursue my dream with their patiences, trusts and love.

List of publications

Articles

1. **T. Yin**, J. P. Gastellu-Etchegorry, N. Lauret, E. Grau, J. Rubio, "A new approach of direction discretization and oversampling for 3D anisotropic radiative transfer modeling", Remote Sensing of Environment, pp. 135, 213-223., 2013.

2. J. P. Gastellu-Etchegorry, **T. Yin**, N. Lauret, T. Cajgfinger, T. Gregoire, E. Grau, J. B. Feret, M. Lopes, J. Guilleux, G. Dedieu, Z. Malenovský, B. D. Cook, D. Morton, J. Rubio, S. Durrieu, G. Cazanave, E. Martin, T. Ristorcelli, "Discrete anisotropic radiative transfer (DART 5) for modelling airborne and satellite spectroradiometer and LIDAR acquisitions of natural and urban landscapes", Remote Sensing 7 (2), 1667–1701., 2015.

3. **T. Yin**, N. Lauret, J. Gastellu-Etchegorry, "Simulating images of passive sensors with finite field of view by coupling 3-D radiative transfer model and sensor perspective projection", Remote Sensing of Environment (In Press), 2015.

4. J. P. Gastellu-Etchegorry, **T. Yin**, N. Lauret, et al. "Simulation of satellite, airborne and terrestrial LiDAR with DART (I): waveform simulation with quasi-Monte Carlo ray tracing", Remote Sensing of Environment, (Under review) 2015.

5. **T. Yin**, N. Lauret, J. P. Gastellu-Etchegorry, et al. "Simulation of satellite, airborne and terrestrial LiDAR with DART (II): ALS and TLS multi-pulse acquisitions, photon counting, and solar noise", Remote Sensing of Environment, (Under review) 2015.

6. **T. Yin**, J. B. Feret, J. P. Gastellu-Etchegorry, N. Lauret, et al. "In-flight fusion for simulated data of airborne imaging spectrometer and waveform LiDAR multi-sensor system through DART model", Remote Sensing of Environment, (Ready to submit) 2015.

Conferences

1. **T. Yin**, J. Rubio, J. P. Gastellu-Etchegorry, E. Grau, N. Lauret, " Direction discretization for radiative transfer modeling: An introduction to the new direction model of dart", In Geoscience

and Remote Sensing Symposium (IGARSS), 2012 IEEE International (pp. 5069-5072). IEEE. , Munich, Germany, 2012 (Oral)

2. J. P. Gastellu-Etchegorry, N. Lauret, F. Leclerc, P. Roche, E. Grau, **T. Yin**, J. Rubio, G. Dedieu, "Assessment of the potential of a high spatial resolution geostationary system", In Geoscience and Remote Sensing Symposium (IGARSS), 2012 IEEE International (pp. 233-236). IEEE. , Munich, Germany, 2012 (Oral)

3. **T. Yin**, J. Inglada, J. Osman, "Time series image fusion: Application and improvement of STARFM for land cover map and production", In Geoscience and Remote Sensing Symposium (IGARSS), 2012 IEEE International (pp. 378-381). IEEE. , Munich, Germany, 2012 (Oral)

4. J. Inglada, J. Osman, **T. Yin**, "Fusion of Sentinel-2 and Proba-V/Sentinel-3 Images for Multi-Temporal Land-Cover Map", 32nd EARSeL Symposium 2012: Advances in Geosciences, Mykonos Island, Greece, 2012 (Oral)

5. **T. Yin**, J. P. Gastellu-Etchegorry, E. Grau, N. Lauret and J. Rubio, "Simulating satellite waveform Lidar with DART model", In Geoscience and Remote Sensing Symposium (IGARSS), 2013 IEEE International (pp. 3029 - 3032). IEEE. , Melbourne, VIC, Australia, 2013 (Oral)

6. J. P. Gastellu-Etchegorry, **T. Yin**, E. Grau, N. Lauret, J. Rubio, "Lidar radiative transfer modeling in the Atmosphere", In Geoscience and Remote Sensing Symposium (IGARSS), 2013 IEEE International (pp. 4554 - 4557). IEEE. , Melbourne, VIC, Australia, 2013 (Oral)

7. F. D. Schneider, **T. Yin**, J. P. Gastellu-Etchegorry, F. Morsdorf, M.E. Schaepman, "At-Sensor Radiance Simulation for Airborne Imaging Spectroscopy", Workshop on Hyperspectral Image and Signal Processing: Evolution in Remote Sensing (WHISPERS), 2014 IEEE. , Lausanne, Switzerland, 2014, (In Press) (Oral)

8. D. C. Morton, J. Rubio, J. P. Gastellu-Etchegorry, B. D. Cook, M. O. Hunter, **T. Yin**, J. R. Nagol, M. M. Keller, "Modeling Diurnal and Seasonal 3D Light Profiles in Amazon Forests", American Geophysical Union, Fall Meeting 2013, abstract No. B42C-02, 2013

9. E. Grau, S. Durrieu, R. Fournier, J. P. Gastellu-Etchegorry, **T. Yin**, N. Lauret, M. Bouvier, "Comparing voxelisation methods of 3D terrestrial laser scanning with Radiative Transfer simulation to assess vegetation density", ForestSAT2014, Riva del Garda (TN), Italy, 2014 (Oral)

Abstract

Radiation propagation and interaction within Earth landscapes and atmosphere are decisive factors for data acquired by Earth observation devices. These data depend on instrumental (spectral band, spatial resolution, field of view (FOV), etc.) and experimental (landscape and atmosphere architecture and optical properties, etc.). The rapid developments in remote sensing techniques requires appropriate tools for validating their working principles and improving the operational use of remote sensing data. Radiative Transfer Model (RTM) is a celebrated tool to simulate remote sensing measurements for various applications, including validation of existing systems, inversion for implicit parameters retrieval, preparation of future systems, etc. Discrete Anisotropic Radiative Transfer (DART) model is recognized by the scientific community as one of the most complete and efficient RTMs.

This dissertation presents my contributions to DART. Traditional RTMs simulate products, as landscape Bidirectional reflectance/temperature distribution function (BRDF/BTDF) or single-pulse waveform of LIght Detection and Ranging (LIDAR) device, which in many cases do not correspond to actual data. My general objective was to design and implement new modeling into DART for improving its potential to simulate actual remote sensing data (e.g. camera, pushbroom imager, LIDAR, etc.), for any realistic sensor and platform configurations. This new modeling makes it possible to compare simulated and actual data in a pixel-wise or pulse-wise manner, which greatly expands and improves DART practicability and efficiency.

My contributions concern 4 domains in DART. Each one constitutes a chapter of this dissertation.

1. Discretization of the directions over the 4π space.

   DART uses discrete ordinate and exact kernel methods to simulate radiation propagation in an Earth/atmosphere scene. A novel approach for the 4π space discretization and oversampling is implemented in DART. Traditional methods do not define, or inaccurately, the solid angle centroids and geometric shapes. These defects result in non-conservative energy or imprecise modeling if the total number of directions is small. The new approach provides discretized directions with well-defined shape, and uniform or cosine-weighted distribution of solid angles, which improves simulation results.

2. Simulating images of passive sensors with finite FOV.

   Existing RTMs can be categorized as pixel-level and image-level models. Pixel-level models use abstract description of a simulated scene (e.g. total leaf area index, overall fraction of shadows,

etc.), and calculate a quantity such as BRDF and BTDF for the whole scene. Image-level models generate radiance, reflectance or temperature images of the scene, through orthographic projection of rays that exit the scene onto an image plane. Pixel-level and image-level models neglect the multi-directional acquisition in the sensor finite FOV, which is not realistic for pixel-wise comparisons with large-scale remote sensing data. Here, a sensor-level model called converging tracking and perspective projection (CTPP) is implemented for simulating images of cameras and cross-track sensors, by coupling DART with classical perspective projection and parallel-perspective projection, respectively.

3. Simulating LIDAR data.

   Many RTMs have LIDAR waveform simulation implemented, but their results are inaccurate (e.g. abstract scene description, or account of first-order scattering only) or take very large computation time. For example, pure Monte-Carlo (MC) models have the trade-off between processing speed and precision. DART employs a novel quasi-MC method, which provides accurate results with fast processing speed, for any instrumental configuration (platform altitude, LIDAR orientation, footprint size, etc...). Multi-pulse data are generated for simulating satellite, airborne and terrestrial laser data, with realistic configurations (LIDAR position, platform trajectory, scan angle range, etc.). They can be converted into industrial LIDAR data format for being processed by dedicated LIDAR data processing softwares. A post-processing approach is also developed to convert LIDAR waveform into photon counting LIDAR data, through modeling single photon detector acquisition.

4. In-flight Fusion of LIDAR and imaging spectrometer data.

   The combined simulation of multi-pulse LIDAR and passive cross-track imaging spectrometers, including hyperspectral sensors, is integrated into DART. This method is specially designed for data of imaging spectrometer and LIDAR multi-sensor system, in which all sensors share the same acquisition geometry. It corresponds to a two sources (sun and laser LIDAR) and one sensor (LIDAR telescope) system. Basically, the approach starts with the simulation of a LIDAR multi-pulse acquisition and the sun-induced radiance image of a passive sensor. Then, the LIDAR FOV projected regions in the ground image plane are segmented from the passive sensor image, which is also projected on the ground image plane. Two applications are presented: estimation of solar noise in LIDAR signal (especially in photon-counting LIDAR) in Section 4.2, and in-flight fusion of LIDAR and imaging spectrometer data in Section 5.

In addition to these modeling improvements, DART can now import actual acquisition configurations (i.e., platform trajectory and view angles per pixel / LIDAR pulse) for simulating actual LIDAR and imaging spectrometer data. It further facilitates the comparison of actual and simulated data. Multi-thread parallelization in also comprehensively introduced, which greatly accelerates DART simulations.

Résumé

La propagation du rayonnement et son interaction dans les paysages terrestres et l'atmosphère sont des facteurs décisifs pour les données acquises par les instruments d'observation de la Terre. Ces données dépendent des configurations instrumentales (bande spectrale, résolution spatiale, champ de vision (FOV), etc.) et expérimentales (architecture et propriétés optiques du paysage et de l'atmosphère, etc.). L'évolution rapide des techniques de télédétection nécessite des outils appropriés pour valider leurs principes de travail et améliorer l'utilisation opérationnelle des données de télédétection. Les modèles de transfert radiatif (RTM) sont l'outil de référence pour simuler les mesures de télédétection pour diverses applications : validation des systèmes existants, inversion des mesures en termes de paramètres implicites, préparation de futurs systèmes, etc. Le modèle DART (Discrete Anisotropic Radiative Transfer) est reconnu par la communauté scientifique que le RTM le plus complet et efficace.

Cette thèse présente mes contributions à DART. La majorité des RTMs simulent des produits, comme les fonctions de distribution de la réflectance (BRDF) et température (BTDF) ou bien la forme d'onde LIDAR d'impulsion unique, ce qui dans de nombreux cas ne correspond pas aux données réelles. Mon objectif général a été de concevoir, implanter et mettre en œuvre une nouvelle modélisation dans DART pour améliorer sa capacité à simuler les données de télédétection (e.g., caméra, pushbroom spectroradiomètre, LIDAR, etc.), pour toute configuration réaliste de capteur et de plates-forme. Cette nouvelle modélisation permet de comparer les données réelles et simulées par pixel ou par impulsion LIDAR, ce qui élargit considérablement le potentiel de DART, et améliore donc son efficacité.

Mes contributions concernent quatre domaines dans DART. Chacun constitue un chapitre de cette thèse.

1. La discrétisation les directions de l'espace 4π.

   DART utilise les méthodes des ordonnées discrètes et du noyau exact pour simuler la propagation du rayonnement dans les paysages terrestres et l'atmosphère dans l'espace 4π. Une nouvelle approche pour discrétiser et sur-échantillonner cet espace a été conçue et implantée dans DART. Les méthodes classiques ne définissent pas, ou mal, le centroïde et la forme des angles solides, ce qui implique une non conservation de l'énergie et une modélisation imprécise si le nombre total de directions est petit. La nouvelle approche fournit des directions discrétisées avec une forme bien définie, de distribution uniforme ou pondérée par le cosinus de l'angle zénithal, ce qui améliore les résultats de simulation.

2. Simuler des images de spectroradiomètre avec FOV fini.

   Les RTMs peuvent être classés comme des modèles "pixel" et "image". Les modèles "pixel" calculent une quantité unique (e.g., BRDF, BTDF) pour l'ensemble de la scène simulée, à partir d'une description abstraite de cette scène (e.g., indice foliaire total, fraction globale d'ombres, etc.). Les modèles "image" produisent une distribution spatiale de luminance, réflectance ou température de la scène. Les images sont générées par projection orthographique des rayons qui sortent de la scène sur un plan image. Ces 2 types de modèles négligent le fait que l'acquisition est multi-directionnelle, car le FOV d'un capteur ne peut en général être supposé nul. Cette simplification peut entrainer de fortes erreurs lors de comparaisons pixel par pixel entre mesures réelles et simulées. Le modèle CTPP a été conçu et implémenté pour résoudre ce problème. Il est basé sur le suivi de rayons convergeants et la projection perspective. Il permet de simuler des images de caméras, pushbroom, etc.

3. Simuler des données LIDAR.

   Beaucoup de RTMs intègrent la possibilité de simuler des formes d'onde LIDAR, mais en général de manière imprécise (e.g., représentation de la scène, prise en compte de la seule diffusion d'ordre 1, etc.) ou avec de très grands temps de calcul. Ainsi, les modèles Monte-Carlo classiques doivent faire le compromis entre la vitesse de traitement et la précision. DART emploie une méthode "quasi-Monte Carlo" qui permet d'obtenir des résultats précis avec des vitesses de traitement rapides, pour toute configuration instrumentale (altitude de la plateforme, attitude du LIDAR, taille de l'empreinte, etc.). Les données multi-impulsions sont générés pour simuler les LIDARs satellites, avions et terrestres, avec des configurations réalistes (position du LIDAR, trajectoire de la plateforme, plage de l'angle de vue, etc.). Elles peuvent être converties au format de données LIDAR "industrielles" pour être traitées par des logiciels dédiés de traitement de données LIDAR. Une approche de post-traitement est également développée pour convertir les simulations de formes d'onde LIDAR en données LIDAR de comptage de photons, via la modélisation de l'acquisition par des détecteurs à comptage de photons.

4. Fusion de données LIDAR et d'image de spectroradiomètre.

   La simulation combinée de LIDAR multi-impulsions et d'image de spectro-radiomètre, y compris les capteurs hyperspectraux, est intégrée dans DART. Il s'agit d'une configuration à deux sources (soleil, laser LIDAR) et un système de capteur (télescope du LIDAR). L'approche débute par la simulation 'une acquisition multi-impulsions LIDAR et de l'image d'un spectro-radiomètre. Ensuite, les régions LIDAR FOV localisées dans le plan image du sol sont segmentées au sein de l'image du spectro-radiomètre, qui est également projetée sur le plan image du sol. Deux applications sont présentées : estimation du bruit solaire dans le signal de LIDAR (surtout en comptage de photons LIDAR), et fusion de données LIDAR et d'images de spectro-radiomètre.

En plus de ces améliorations de modélisation, DART peut désormais importer des configurations

d'acquisition réelles (trajectoire de la plateforme, angle de vue par pixel du spectro-radiomètre et par impulsion LIDAR) pour simuler des données LIDAR et images réalistes de spectro-radiomètre. La comparaison précise de données réelles et simulées est ainsi possible. De plus, parallélisation multi-thread a été implémentée, ce qui accélère grandement les simulations DART.

Contents

General introduction

Satellite and airborne sensors are increasingly used by scientists and policy makers for studying and managing the Earth's environment, including forests, agriculture crops, and urban areas. Generally speaking, remote sensing (RS) observations make it possible to study land surfaces (e.g. digital elevation model, soil moisture, etc.), as well as biophysical (e.g., leaf area index, leaf angle distribution, etc.) and biochemical (e.g., chlorophyll content, etc.) properties of vegetation, at different time and space resolutions, over different areas. For this objective, RS data acquired with given instrumental (spectral resolution, view direction, sensor field-of-view, etc.) and experimental (surface and atmosphere conditions, sun direction, etc.) configurations are commonly translated into qualitative and quantitative parameters that characterize the Earth's surfaces.

Among RS techniques, Imaging Spectroscopy (IS) and Light Detection and Ranging (LiDAR) are celebrated tools for mapping the Earth landscapes from the ultraviolet to the thermal infrared (TIR) spectral domain (0.32μm - 15μm). Their retrieved data from passive and active acquisitions are essentially complementary to each other, which help estimating both constitution and structure of the Earth's surfaces.

IS is a passive RS technique which measures upwelling spectral radiance value per pixel, combining both emitted and reflected components of the Earth's landscape and the atmosphere. The received radiance flux per pixel can be transformed into reflectance (ratio of reflected and incident radiation), usually in the visible (VIS) and the short-wave infrared (SWIR) spectral domains, and into brightness temperature, usually in the TIR domain. In the spectral domain from VIS to SWIR, RS signals are mostly due to the reflection of solar radiation from the atmosphere and Earth surfaces. When acquired under appropriate conditions, the recorded reflected radiometric signals from an imaging spectrometer provide information about the biophysical and biochemical properties of the Earth's ecosystems (Asner, 1998; Ustin et al., 2004). At sensor level, satellite imaging spectrometers acquire top of atmosphere (TOA) radiance, and airborne sensors acquire radiance with partial atmosphere ranging from ground up to their altitudes. Most imaging spectrometers mounted on satellites and aircrafts are usually cross-track imagers (e.g. linear pushbroom camera, whiskbroom scanner), while those mounted on UAVs are usually frame cameras. They acquire data through their finite field of views (FOVs) with appropriate sensor models. They generate images using different geometry configurations: classical perspective projection (Sonka et al., 2008) for cameras, and parallel-perspective projection (Chai and Shum, 2000; Gupta and Hartley, 1997) for cross-track imagers.

LiDAR is an active RS technique which generates laser beam (i.e., pulse) as a radiation source and measure the amplitudes and the travel time (time of flight) between the pulse emission and returns to calculate the ranges (distance) to each of the objects encountered by the pulse. LiDAR devices are increasingly used in RS and terrestrial systems for many applications: topography (Hladik et al., 2013b), vegetation architecture and dimensions (Montesano et al., 2015; Popescu et al., 2011; Yang et al., 2013), urban mapping (Yan et al., 2015), bathymetry (Quadros et al., 2008), atmosphere constituents (Zhang et al., 2011), etc. The return amplitude of each LiDAR pulse can also be converted into the apparent reflectance of the target. The combination of range measurements with knowledge of platform location and attitude provides a three-dimensional (3-D) representation of the observed landscape. Therefore, through measurements of multiple pulses, data from multiple LiDAR pulses can be used to infer 3-D structure of vast landscapes (Lefsky et al., 2002). LiDAR waveform is the temporal discretization of the ranged backscattered signal. In addition, a waveform records continuous returned signal when pulse penetrates through atmosphere and vegetation, which informs the constituents and distributions of mediums. RS LiDARs are usually categorized according to the size of the region covered by their illumination pulses, which is inferred by platform altitude and beam divergence. Those onboard satellites have large footprint, like the 64m diameter footprint of the Geoscience Laser Altimeter System (GLAS) of the Ice, Cloud and land Elevation Satellite (ICESat) (Zwally et al., 2002). Those onboard aircrafts (airborne laser scan (ALS)), have usually small footprint, like the less than 1m footprint diameter of the LiDAR system on the Carnegie Airborne Observatory (CAO) for altitudes less than 2km (Asner et al., 2012, 2007). In addition, ground based LiDAR devices, also called terrestrial laser scan (TLS), is increasingly used. For example, for vegetation studies, it is used for tree structure retrieval through the calculation of the location of the observed scattering elements (Rosell et al., 2009). Points from TLS acquisitions can lead to precise 3D tree representations that can be used further by computer graphics software for visualization and by models (Côté et al., 2011, 2009) to simulate remotely sensed data. Model simulations with this 3D vegetation representation (Schneider et al., 2014a) has proved to be more accurate than with abstract vegetation representation with turbid medium (Ross, 1981).

Models (i.e., reflectance model) that simulate the reflection of solar radiations from Earth surfaces and the atmosphere are essential tools for understanding and using RS signals in the VIS, NIR and SWIR spectral domains. There exists different categories of reflectance models. They are derived from a number of sources including radiative transfer (RT) theory (Chandrasekhar, 1969), planetary astronomy (Hapke et al., 1993) and many other areas of physical science and engineering. The diversity of influences and methods developed and tested for a whole range of other applications may be regarded as an advantage. Indeed, it explains an ability of adaptation. There is often a great deal of crossovers from one model category to another, and several approaches are often combined in a single model. Some major model categories are introduced below.

Empirical models are generally the simplest type of reflectance model. They do not describe the biophysical parameters and processes that shape the bidirectional reflectance factor (BRF), but they provide a mathematical description of observed patterns in BRF datasets. They attempt to describe the

reflectance of the Earth surfaces under various viewing and illumination conditions by fitting some functions (usually polynomials) to the observed reflectance data. This approach has two major advantages: 1) No assumption is necessarily made regarding the studied landscape (i.e., Earth scene); 2) The chosen function can be arbitrarily complex in order to describe the surface reflectance to a desired degree of accuracy. In practice, the functions that are selected are simple enough for analytical inversion of RS data. More complex functions may fit a wide variety of reflectance data, but are also more likely to fit to an inaccurate result than a lower order polynomial under certain circumstances. Empirical models can rely on simplified physical principles of geometrical optical (GO) models and RT theory. For example, linear kernel driven (LiK) models (Liu et al., 2010; Roujean et al., 1992; Wanner et al., 1995) calculate BRF as the sum of an isotropic term and anisotropic functions (kernels) that characterize volume and surface scattering. MODIS, POLDER, MSG/SEVIRI, AVHRR, VEGETATION land surface BRF/albedo products are mainly generated using LiK models to invert the BRF parameters of multi-angular bidirectional reflectance in clear skies (You et al., 2014). Another example is the Rahman-Pinty-Verstraete (RPV) model (Rahman et al., 1993), and its latter inversion accelerating versions: the Modified RPV (MRPV) (Martonchik, 1997) and EMRPV (Engelsen et al., 1996) models. These models are widely used for their analytical nature and use of only a few input parameters. The major disadvantage of empirical models is the limited linkage between their input parameters and the physical scattering behavior of Earth surfaces, as well as the RT theories. As a result, empirical reflectance models tend to be very useful for correction / normalization of directional effects in multi-angular reflectance data, but of little use for the derivation of biophysical parameters from reflectance data.

Increasing demand for more universal satellite data products for landscape characteristics has spurred advances in theoretical understanding and modeling of IS and LiDAR signals of 3-D landscapes for various experimental and instrumental configurations (radiometric accuracy, spatial/spectral/temporal resolutions, etc.). IS signals correspond essentially to the BRF and brightness temperature function (BTF). Instrumental configuration is given by sensor technical specifications, including: FOV, full width at half maximum (FWHM), spectral sampling, and viewing geometry. Experimental configuration corresponds to:

- The date of acquisition, which defines the angles of sun direction.
- Landscape geometrical configuration and optical properties.
- Atmospheric geometry and optical properties (gas and aerosol density profiles, scattering phase functions and single scattering albedo).

Physical models are formulated by considering the fundamental physical principles of radiation interaction within the atmosphere and Earth landscapes according to experimental and instrumental configurations. They all approximate the description of the propagation medium (i.e., the simulated scene). For example, a real vegetation canopy is a structurally complex arrangement of objects (e.g., leaves, stems, buds, gaps between leaves etc.), which can all be considered as scattering elements in the

context of radiation interception. In addition, the 3-D spatial distribution of all canopy elements, with their own optical properties, must be considered. However, this realistic 3D description is likely to be extremely computationally expensive. Furthermore, the atmosphere and ground with topography must be considered. Most models use approximations of radiation laws. Some models such as Monte Carlo ray tracing (MCRT) and Radiosity have been developed to simulate photon transport exactly, but their computation times are usually tremendous.

Physical models work with landscapes that are simulated as homogeneous or heterogeneous scenes. Most common homogeneous models, also called turbid models, represent vegetation as a superposition of horizontally homogeneous layers that are filled with turbid medium. Turbid medium (Ross, 1981) is the most common technique that is used to simplify the description of vegetation in order to model its scattering, and consequently its reflectance. It is a medium such that there is a length scale in which the locations of absorbing and scattering elements (leaves) in the medium (canopy) are amenable to be described using the concept of statistical density distribution of infinitely small planar elements (Smolander et al., 2006). The very first physical models used this turbid representation to model general trends such as the evolution of crop BRF/BTF in relation to phenological LAI changes. The two major drawbacks of turbid models are that scatterers are assumed to be homogeneously distributed and that the size of the scatterers within the canopy is not considered. However, canopy reflectance strongly depends on effects (e.g., shadows) due to the heterogeneous distribution of scatterers. Moreover, the sizes and orientations of scatterers control specific features of canopy reflectance such as the hot spot effect (Kuusk, 1991) with its sharp peak in reflectance observed in and around the backscatter (opposition) direction. Usually, improvement of physical models requires advancement in representation of landscapes, as their 3-D complexity (i.e., topography, tree and building distribution, etc.) greatly affects optical observations. Classically, representation of heterogeneous landscapes is based on i) discretization of the spatial variable into a 3-D set of spatial nodes called voxels (Kimes and Kirchner, 1982; Myneni et al., 1991) that contain turbid medium, and/or ii) representation of each individual landscape element with facets as geometrical primitives.

Geometric optical (GO) models simulate the BRF of objects on the Earth surface as a function of their physical dimensions and structures, using the laws of geometric optics. For instance, they represent a forest stand as a combination of approximated geometrical shapes of tree crowns with corresponding shadows and background forest floor material (Peddle et al., 2003). All these parameters are defined with surface optical properties that integrate implicitly the volume light scattering. Modeling is based on the computation of scene fractions of sunlit canopy, sunlit background, and shadows, which is a potential source of modeling inaccuracy. Therefore, GO models perform better in simulations of "open" landscapes (e.g., sparse forest stands). Li and Stralher (Li and Strahler, 1992) developed one of the first GO models. The more recent 4-scale model (Chen and Leblanc, 1997) simulates tree crowns as discrete geometrical objects: cone and cylinder for conifers, and spheroid for deciduous trees. Individual leaves in deciduous canopies and shoots in conifer canopies, defined with a given angular distribution, are populating branches with a single inclination angle. This model uses a geometrical multiple scattering

scheme with view factors (Chen and Leblanc, 2001). The 5-Scale model (Leblanc and Chen, 2000) is an extension of the 4-Scale model that includes the LIBERTY model (Dawson et al., 1998), which simulates needle-leaf optical properties.

Radiative transfer models (RTM), also called physical RTMs, use physically described mechanisms to simulate the propagation of radiation through Earth systems, and consequently RS acquisitions. They rely on RT equation, which relates the change in radiation along a ray path to local absorption, scattering and thermal emission. Since these models work with realistic representations of Earth landscapes, they can be robust and accurate. Generally speaking, simulation of bottom of atmosphere (BOA) and TOA BRF and BTF involves RT of four components:

1. Soil (e.g., Hapke model (Hapke, 1981))
2. Foliar element (e.g., PROSPECT model (Feret et al., 2008; Jacquemoud and Baret, 1990))
3. Canopy (e.g., SAIL model (Verhoef, 1984))
4. Atmosphere (e.g., MODTRAN (Berk et al., 1987) or 6S (Vermote et al., 1997) models). Some models, such as DART (Gastellu-Etchegorry et al., 1996; Grau and Gastellu-Etchegorry, 2013), directly simulate the Earth-atmosphere interactions using inputs from soil and leaf RTMs.

Multiple scattering and consequently energy conservation are usually the major sources of inaccuracies of these models, because, conversely to 1st order scattering, it has no simple analytical form.

Major solutions of RTMs are based on either of the following four mathematical methods: i) N-flux, ii) Radiosity, iii) Successive Orders of Scattering, and iv) Monte Carlo. In case of N-flux method, the radiation is propagated along N discrete ordinates (directions), which correspond to N RT equations. For example, the SAIL model (Verhoef, 1984) uses four differential equations corresponding to four directional fluxes within a horizontally homogeneous landscape: one sun flux, two isotropic upward and downward fluxes and one flux along a sensor viewing direction. However, a more detailed consideration of the RT anisotropy can require a much larger number of fluxes (e.g., more than 100) (Yin et al., 2013b). Contrary to the N-flux method that computes the volumetric radiation balance in the 3-D space, the Radiosity method (Borel et al., 1991) is based on the radiation balance equation of a finite number M of discrete scatterers, which requires computation of the view factors between all M elements. It is, therefore, based on inversion of a $M \times M$ matrix, which is time consuming if M is too large, e.g. in case of complex landscape elements such as trees. The Successive Orders of Scattering (SOS) method is one of the oldest and conceptually simplest solutions of the multiple scattering. It uses an iterative calculation of successive orders of scattering, where total radiance vector is expressed as a sum of contributions from photons scattered a number of times ranging from 0 to a pre-defined maximum number. For example, the SOSVRT model (Duan et al., 2010) simulates polarized RT in vertically inhomogeneous plane-parallel media. The Monte Carlo (MC) method involves simulation of the chain of scattering events incurred by a photon in its path from the source to the receiver or to its absorber. An advantage of this technique is explicit computation of only single scattering properties (Disney et al., 2000). However, it requires

long computational time, which is a strong technical limiting constraint. Indeed, every object within a scene must be represented accurately in three dimensions along with associated radiometric properties and this information must be stored in memory. In addition, many rays must be fired per image pixel in order to achieve a convergent solution that represents the scattering behavior of the scene to within some accuracy threshold. Thus, a numerical integration (i.e., Monte Carlo integration) must be carried out. Clearly, the more detailed the scene, the more calculations are required for each photon. Well-known examples of MC models are Drat (Lewis, 1999), FLIGHT (North, 1996) Raytran (Govaerts and Verstraete, 1998), and DELiS (Ristorcelli, 2013; Ristorcelli et al., 2014).

In short, RTMs that can consider the Earth and atmosphere complexity are, therefore, ideal tools for linking remotely sensed data to the surface parameters. Comparison of actual and simulated remotely sensed data is difficult if simulated data are not realistic in terms of both geometry and radiometry. Many works have been devoted for improving RTMs and accurate simulations of the 3-D Earth's surfaces constructed by explicit physical features and elements with associated optical properties. Comparing with other models, 3-D model can provide more accurate results in straight-forward modeling of RS products because of its comprehensive parameterization and detailed accounts of ray propagation and interactions in 3-D space. However, due to the the complexity of 3-D models, the processing speed is usually slower, which is the most obvious disadvantage. The inversion of 3-D model is more complete since many parameters are considered in the model. There are several inversion approaches for 3-D models. By fixing all parameters except a limited number of interesting ones, some analytical inversion approaches of other models can be directly applied to the products of 3-D models. For some case when a simple analytical inversion does not exist or can not reach the required accuracy level, look-up tables are uaually applied which can be quite accurate but require a large ammount of computational time.

Intercomparison among RTMs is gradually developed with the increasing requirement of modeling accuracy. The RAMI (Radiative Transfer Model Intercomparison) experiment of the Joint Research Center of European Commission is a typical example (Pinty et al., 2001b, 2004; Widlowski et al., 2011a,b, 2007). This experiment has been continuously improved during the past 15 years. It provides reference reflectance values of simple and complex 3-D Earth scenes. One of the main challenges faced by RAMI is the lack of absolute reference standards from actual measurements. Any comparison of RTMs with actual data is quite complicated due to numerous factors, such as errors of geometric construction of 3-D scenes, incomplete object parameterization and sensor noise associated to the measurements. The RAMI defined references are based on the convergent results throughout years of experiments using several "credible" RT models (Widlowski et al., 2008). Another challenge of the intercomparison experiment is the limitation of comparable results provided by RTMs. Most comparisons were only done for the scene BRF, albedo (terminology following (Schaepman-Strub et al., 2006)), and to a lesser extent, LiDAR waveform of a single pulse.

The Discrete Anisotropic Radiative Transfer (DART) model is one of the most comprehensive physically based 3-D models that simulates the Earth-atmosphere radiation interaction from visible to thermal infrared wavelengths (Gastellu-Etchegorry et al., 1996, 2012, 2004a). It uses discrete ordinate and exact

kernel methods to simulate radiation propagation in an Earth/atmosphere scene. It has been developed since 1992. It models optical signals at the entrance of imaging radiometers and laser scanners on-board satellites and airplanes, as well as the 3-D radiative budget, of urban and natural landscapes for any experimental configuration and instrumental specification. It is recognized as one of the "credible" RTMs and provides references in RAMI experiments. It is freely distributed for research and teaching activities.

The content of the 5 chapters of this dissertation is introduced below. It mostly corresponds to 6 publications in rank A journals (3 published, 2 submitted, and 1 to be submitted soon). The main objective of this dissertation is to improve DART model for simulating RS signals with realistic accounts of the sensor configuration and acquisition geometry. I introduced new modeling approaches that link the DART simulations with IS and LiDAR measurements for better validation of the current RS devices, and more comprehensive preparation for future systems. A major objective was to simulate IS and LiDAR data which can be pixel-wisely and pulse-wisely compared with actual data. Chapter 1 introduces DART general modeling theory. For more detailed information, Gastellu-Etchegorry et al. (1996) is the best reference. In addition, chapter 1 summarizes the most recent DART developments (V5) which are separately presented in the following chapters. Chapters 2 to 5 present the four modeling developments that I designed and implemented during my PhD. They focus on different but implicitly connected topics in DART:

- Chapter 2: Direction discretization and oversampling.

  In DART, the angular distribution of directions that are used to track radiation can impact a lot the simulation of RS signals. I designed and implemented a new method, iterative uniform squared discretization (IUSD), for discretizing the 4π space of discrete directions along which rays and photons propagate in DART. It combines the advantages of both traditional DOM and FVM, with well defined shape and exact center for the description of each discretized direction. It uses "squared" angular sectors with an analytical expression that allows one to construct the direction with flexible input parameters. With this approach, scattering calculation can combine both numerical quadrature and analytical integration. The 0^{th} and 1^{st} moments of traditional direction discretization method are exactly verified. A regional direction oversampling approach is also implemented for the case of very anisotropic scattering (e.g. hot spot). Different cases are investigated: optimal shape of angular sectors on the 4π sphere, oversampling of planes and angular zones, and use of directions that are not centered on their associated sectors Ω_n for more accurate RT modeling. Results show that the IUSD method is more accurate than the S_n DOM, the $N_\theta \times N_\phi$ FVM and the FT_n FVM methods in the case of multiple scattering within turbid medium simulation.

- Chapter 3: Simulation of passive sensor images through finite sensor field on view (FOV).

  The FOV of RS sensors (e.g. imaging spectrometers) is not zero. Hence, pixels of the same acquired image are observed under various sensor viewing directions. One important constraint

for comparing RTM with sensor data is the neglect of sensor geometric configuration in RTMs. Indeed, mapping 3-D objects onto a 2-D image plane (IP) (a mesh grid with pre-defined size), uses a specific projection method, which impacts the radiance value acquired by a passive sensor as 2 ways: the geometrical distortion by the projection (e.g. object near to the sensor appears larger on the image), and the directional variation of reflectance according to different view angles within its FOV. In machine vision, classical perspective projection (Sonka et al., 2008) is applied for cameras, and parallel-perspective projection (Chai and Shum, 2000; Gupta and Hartley, 1997; Zhu et al., 2004) is applied for cross-track imagers. They are both crucial for obtaining exact radiance values and their spatial distribution in the IPs. I introduced a modeling approach that links DART to 3-D perspective projection to simulate actual sensor acquisitions: the so-called convergent tracking and perspective projection (CTPP). With this implementation, the original simulation results of DART are assessed for various research domains, including: 1. Passive sensor imaging; 2. Video captured by unmanned aerial vehicle (UAV); 3. Local hot spot (HS) effect in a RS image; 4. Pixel-wise comparison between simulated orthorectified perspective-projection images; and 5. Radiance variation among images acquired by airborne and spaceborne systems with different sensor altitudes. This modeling approach allowed me to improve the results of Schneider et al. (2014a) for pixel-wise comparison of at-sensor radiance image between DART simulation and APEX (Appendix II).

- Chapter 4: Simulation of LiDAR data. It contains two sections.

  - Section 4.1: Simulation of the waveform of a single LiDAR pulse. Waveform LiDAR (wLiDAR) measures time of flight of returned signals, transforms signals into analog electrical counts in volts, and records them as continuous temporal bins (Shan and Toth, 2008). A LiDAR waveform can reflect both distance from the LiDAR position to a scattering element through a sharp peak in the waveform, and the distribution of a continuous medium (e.g. air, water, turbid vegetation...) through waveform amplitude variation as a laser pulse penetrates the medium. A general-purpose simulation tool of wLiDAR can help to evaluate the influences of instrumental and experimental configurations on remotely acquired waveforms, and to develop inversion algorithms for specific system. This section presents a new quasi-MCRT model that was designed and implemented into DART to simulate wLiDAR. Basically, it relies on two new methods for accelerating the selection of scattering directions, and tracking photons in the direct mode. It provides accurate results with fast processing speed, for any instrumental configuration (platform altitude, LiDAR orientation, footprint size, etc.). An atmosphere model is also implemented and validated with analytical evaluation, which does not exist in most RTMs.
  - Section 4.2: Simulation of LiDAR data for multiple pulses. Waveform acquisition associated to the emission of multiple pulses along different directions leads to 3-D point cloud that informs on the optical properties and locations of the scattering elements which give rise

to the measured signals (Wagner, et al., 2006). Among wLiDAR devices, airborne laser scan (ALS) uses small-footprint LiDAR for acquisition over a swath that is defined by the platform and sensor configuration (Mallet and Bretar, 2009). The decomposed points from ALS pulses can be classified into Earth surface types (ground, vegetation canopy, etc.) (Zhang et al., 2003). Similarly, TLS is increasingly used for tree structure retrieval through the calculation of the location of the observed scattering elements (Rosell et al., 2009). This section presents an extension of the single pulse LiDAR model of DART to simulate multi-pulse satellite, airborne and terrestrial LiDAR acquisition. An important practical advantage is that output data can be converted into an industrial LiDAR format, the sorted pulse data (SPD) (Bunting et al., 2013b), and hence processed into point cloud by the associated open-source data processing software, the SPDlib (Bunting et al., 2013a). DART was also extended for simulating photon counting LiDAR (pcLiDAR) (Montesano et al., 2015). Furthermore, solar noise in LiDAR signal is simulated. DART LiDAR modeling is illustrated with the simulation of a few systems, including the wLiDAR system of the CAO, the ILRIS terrestrial LiDAR system of Optech Inc (www.optech.com), the Multiple Altimeter Beam Experimental LiDAR (MABEL, McGill et al. (2013)) of NASA's Goddard Space Flight Center, as well as the Advanced Topographic Laser Altimeter System (ATLAS, Anthony et al. (2010)) which will be onboard the upcoming 2nd generation of NASA Ice, Cloud, and Land Elevation Satellite (ICESat-2, Abdalati et al. (2010)).

- Chapter 5: In-flight Fusion of IS and LiDAR multi-sensor system.

  RS devices with different specifications, such as active and passive sensors, can provide complementary information about the Earth's surfaces. IS and LiDAR data are complementary to each other, which helps estimating both constitution and structure of the Earth's ecosystem. In order to facilitate data registration and fusion, the preferred solution is often to install all RS sensors of interest on board the same platform. Then, data fusion can be achieved during the acquisition with a so-called in-flight fusion method (Asner et al., 2007). It can be achieved also after acquisition with a post processing method. Several Imaging Spectrometer and LiDAR Multi-sensor Systems (ISLMS) have been employed in airborne RS, including Carnegie Airborne Observatory (CAO, Asner et al. (2012, 2007)), National Ecological Observatory's Airborne Observation Platform (NEON AOP, Kampe et al. (2010)), and NASA Goddard's LiDAR, Hyperspectral and Thermal Airborne Imager (G-LIHT, Cook et al. (2013)). Chapter 5 presents a new approach which I designed and recently implemented in DART to simulate in-flight fusion of ISLMS data. This approach combines the passive sensor image simulation presented in Chapter 3 and multi-pulse LiDAR data simulation in Chapter 4. It corresponds to a two sources (sun and laser LiDAR) and one sensor (LiDAR telescope) system. Examples of in-flight fusion are demonstrated for both urban and vegetation landscapes.

Most mentioned developments are implicitly connected. For example: the virtual direction and vir-

tual flux concepts introduced in Chapter 2 are the prerequisites of the automatic steering virtual direction (ASVD) and flux in Chapter 3. Similarly, the ASVD and its virtual flux introduced in Chapter 3 are the prerequisites of Ray Carlo approach in Chapter 4. In addition, the fusion algorithms presented in Chapter 5 combine multi-view sensor image simulation (Chapter 3) and multi-pulse simulation (Chapter 4), which is used for simulating LiDAR solar noise estimation. These connections are further elaborated in the abstract of each chapter, and the final conclusion of this dissertation.

I want to stress that all the presented developments rely on a very strong collaborations with other members of the DART team, both in computer science and physical modeling. For example, I collaborated a lot with Nicolas Lauret for designing and improving LiDAR modeling. he fact that DART is a patented code with licenses distributed by Paul Sabatier University, but managed by the DART team, and also the fact that all improvements are integrated in the DART version that is available to licensees, is very demanding for the team in three major domains:

- Design and implementation of new modeling and functionalities. These developments are usually done in the frame of projects or collaborations with licensees, with the objective to improve DART science, whatever the requests of licensees. For example, collaboration with NASA GSFC was very fruitful for developing LiDAR modeling, in the frame of the preparation of DESDynl mission. Generally speaking, the introduction / improvement of new functionalities is decided during our weekly meetings. Then, it is designed and implemented by the scientists who is the most concerned. Any new implementation is realized under the supervision of Nicolas Lauret who acts as the responsible of DART computer science.

- Help to DART licensees. Usually, licensees can ask for help and/or clarification of DART functionalities. Jean-Philippe Gastellu-Etchegorry manages relationships with all licensees, including the DART web site. He answers to questions of licensees and gives them some help. Sometimes, especially if there is a need to correct or improve DART functionalities and if fits with the scientific/technological domain of one of us, a member of the team takes in charge the task. For example, SQL databases are managed by Thomas Cajgfenger, Tristan Gregoire and Jordan Guilleux. Any new implementation is done under the control of Nicolas Lauret.

- Computer science work for maintaining DART as an operational model. It implies many tasks for maintaining and up-dating operating systems, C++ libraries, Java, Python, SQL libraries, and also for managing the non regression tests, the cross-compilation, the distribution of DART versions, etc. This is mostly done by Tristan Gregoire under the supervision of Nicolas Lauret. The tasks to perform cannot always be known in advance. For example, late 2014, we realized that Java SWT code that is used for DART graphic user interface (GUI) is no more compatible with most recent Linux versions. It implies to rewrite the whole DART GUI, which requires about 18 months of development. By the way, the GUI will be much improved. This GUI development is being done by Jordan Guilleux, in collaboration with Nicolas Lauret.

Introduction générale

Les capteurs embarqués sur satellite et aéroporté sont de plus en plus utilisés par les scientifiques et par les décideurs politiques pour étudier et gérer notre environnement : forêts, zones agricoles, espace urbain, etc. Il s'agit de capteurs passifs et actifs qui opèrent avec des caractéristiques instrumentales très diverses (domaines spectraux, champ de vue, résolutions spatiale, temporelle, spectrale et radiométrique, etc.), différentes configurations (direction et heure d'observation, d'observation, etc.) et qui mesurent différentes quantités (énergie, temps, phase, fréquence,...). Par suite, la télédétection constitue un outil unique pour étudier notre planète à différentes échelles de temps et d'espace. Ainsi, elle renseigne sur les propriétés biophysiques de la végétation comme la biomasse foliaire, et l'humidité des sols. Pour cela, les mesures de télédétection acquises pour une configuration instrumentale donnée (résolution spatiale, direction de visée, etc.) et une configuration expérimentale donnée (état de surface, condition atmosphérique, direction solaire, etc.) sont plus ou moins directement traduites en paramètres quantitatifs et qualitatifs des surfaces terrestres.

Les spectroradiomètres imageurs et les LiDARs sont les techniques de télédétection mises en avant pour cartographier les paysages terrestres et leurs propriétés biophysiques à partir de mesures dans les domaines spectraux du visible à l'infrarouge thermique. Les radiomètres imageurs mesurent les flux (luminances) sous forme de vecteurs bidimensionnels (2D). Ces luminances peuvent être transformées en réflectance (BRF) de surface (rapport des flux réfléchi et incident) si elles sont acquises dans les bandes du visible et proche infrarouge, et en température de brillance de surface (BTF) si elles sont acquises dans l'infrarouge thermique. Les satellites imageurs spectroscopiques mesurent des luminances au sommet de l'atmosphère (TOA). Ces luminance résultent de mécanismes de diffusion et d'absorption du rayonnement solaire au sein des paysages terrestres et de l'atmosphère. Les mesures des capteurs aéroportés sont plus ou moins affectées par l'atmosphère selon leur altitude. Les capteurs LIDAR ont un mode d' acquisition très différent des radiomètres. Ce sont des capteurs actifs qui utilisent un faisceau laser comme source de photons. Ils mesurent le temps de trajet des photons qu'ils émettent entre leur émission et leur réception, sachant que ces photons ont été diffusés par l'atmosphère ou par un élément de la surface terrestre observée. Cette mesure renseigne sur la distance entre le LiDAR et le diffuseur. La combinaison de ces mesures de distance avec la connaissance de la position et attitude de la plateforme permet d'obtenir une représentation tridimensionnelle (3D) du paysage observé.

La demande croissante de produits de surface dérivés de mesures satellites a induit de grandes avancées concernant la compréhension et la modélisation des mesures des spectroradiomètres et des

LiDARs acquises pour les paysages terrestres 3D, pour différentes configurations expérimentales et instrumentales (précision radiométrique, résolutions spatiale, spectrale et temporelle, etc.). La configuration instrumentale est définie par des quantités caractéristiques du capteur comme le champ de vue (FOV), la largeur à mi-hauteur (FWHM), l'échantillonnage spectral, et la géométrie d'observation. La configuration est souvent définie par la date d'acquisition (direction solaire), l'architecture et les propriétés optiques des éléments du paysage observé et les conditions atmosphériques (profils de densités des gaz et aérosols, fonctions de diffusion, albédo de diffusion simple).

Les modèles qui représentent les mesures de télédétection sont essentiels pour comprendre et interpréter ces mesures, mais aussi pour concevoir les futures missions satellites chargées d'observer la Terre et son atmosphère. Il existe de nombreux types de modèles. Ils reposent sur des approches plus ou moins complexes qui font appel à différents domaines des mathématiques et de l'ingénierie. Cette diversité d'influences et de méthodes développées et testées sur un vaste champ d'applications peut être vue comme un avantage, car elle indique une certaine capacité d'adaptation. Les modèles sont souvent classés en différentes catégories. Il y a en général beaucoup de recouvrement entre les approches utilisées, et différentes approches sont souvent combinées en un seul modèle. Les principales approches utilisées pour représenter la réflectance des surfaces terrestres sont résumées ci-dessous.

Les modèles empiriques sont en général les modèles les plus simples pour représenter le facteur de réflectance bidirectionnel (BRF). En effet, ils ne s'appuient pas sur les paramètres biophysiques caractéristiques des paysages observés. Ils tentent simplement de décrire la réflectance des surfaces terrestres pour des conditions variables d'illumination et de visée en ajustant au BRF observé des fonctions qui sont souvent de simples polynômes. Cette approche a deux avantages majeurs. 1) Aucune hypothèse sur le type de scène terrestre considéré n'est nécessaire. 2) La fonction choisie peut être arbitrairement complexe afin de décrire le comportement de la réflectance de surface avec un degré de précision désiré. En pratique, les fonctions qui sont sélectionnées sont suffisamment simples pour une inversion analytique des données de télédétection. Des fonctions plus complexes peuvent ajuster un jeu plus varié de mesures de réflectance, mais sont aussi plus enclins à ajuster un "mauvais" résultat qu'un polynôme de degré inférieur. Les modèles empiriques peuvent utiliser des approches très simplifiées dérivées de l'optique géométrique (GO) et de la théorie de transfert radiatif (TR). Ainsi, les modèles linéaires à noyau calculent la réflectance directionnelle comme la somme de fonctions isotrope et anisotrope (noyaux) qui caractérisent la diffusion de volume et de surface. Par exemple, les produits de surface (albedo, etc.) MODIS, POLDER, MSG/SEVIRI, AVHRR, VEGETATION sont en général obtenus par inversion des mesures satellites avec de tels modèles. Le modèle appelé "Pinty-Verstraete" (RPV), et sa version ultérieure adaptée à l'inversion MRVP (Modified RPV), est un autre exemple. Ces modèles sont très répandus, du fait de leur forme analytique et de leur faible nombre de paramètres d'entrée.

Le désavantage majeur des modèles empiriques est qu'ils ne lient pas leurs paramètres d'entrée au comportement diffusif des surfaces terrestres. Par suite, ces modèles tendent à être très utiles pour la correction et normalisation des effets directionnels dans les jeux de données multi-angulaires, mais peu efficaces, voire inutiles, pour dériver des paramètres de surface des mesures de réflectance.

Les modèles physiques peuvent relier leurs paramètres d'entrée au comportement diffusif des surfaces terrestres. Ils sont formulés en considérant les principes physiques fondamentaux de l'interaction du rayonnement avec l'atmosphère et les surfaces terrestres. Tous ces modèles font des hypothèses simplificatrices sur le milieu de propagation (i.e., scène simulée). Ainsi, un couvert végétal est un ensemble d'éléments (feuilles, aiguilles, branches, etc.) qui peuvent tous jouer le rôle de diffuseurs. De plus, l'arrangement spatial (i.e., architecture) de ces éléments doit aussi être pris en compte, mais une prise en compte réaliste peut être très coûteuse en termes de temps calcul. De plus, l'atmosphère et le relief doivent aussi être pris en compte. La plupart des modèles utilisent des approximations des lois qui régissent le rayonnement. Les modèles basés sur le suivi de rayon avec l'approche Monte Carlo (MCRT) ont été conçus pour simuler de manière exacte la propagation de photons et donc du rayonnement.

Les modèles physiques opèrent avec des paysages qui sont simulés comme des scènes homogènes ou hétérogènes. Dans une scène dite homogène, la végétation est représentée comme la superposition couches homogènes horizontales qui sont remplies par un milieu turbide. La plupart des modèles qui opèrent sur des scènes homogènes sont souvent appelés "modèles turbides". Le milieu turbide (Ross, 1981) est le mode de représentation le plus simple pour décrire la végétation dans le but de modéliser sa diffusion, et par suite sa réflectance. C'est un milieu tel qu'il existe une dimension spatiale en deçà de laquelle la position des éléments foliaires absorbants et diffusants du couvert végétal peut être décrite comme une distribution statistique d'éléments plans infiniment petits (Smolander, 2006). Les premiers modèles physiques utilisaient cette approche pour simuler les tendances générales, comme l'évolution des réflectances et températures de brillance des cultures en lien avec l'évolution du LAI. Les modèles turbides ont deux limitations majeures : les diffuseurs sont supposés être distribués de manière homogène et la taille des diffuseurs n'est pas prise en compte, alors que la réflectance de la végétation dépend beaucoup des effets (ombre,...) dus à l'hétérogénéité de la distribution des diffuseurs. L'orientation des diffuseurs est uniquement prise en compte de manière statistique. La représentation turbide des milieux ne permet pas une prise en compte réaliste de l'architecture des couvets. Il en résulte une simulation souvent très inexacte de phénomènes comme le hot spot (phénomène d'opposition) qui donne souvent lieu à un pic de réflectance selon la direction dite de rétrodiffusion. La représentation des paysages avec prise en compte de leur hétérogénéité repose sur i) la discrétisation de l'espace en une distribution spatiale 3D de nœuds appelés voxels (Kimes, 1982 ; Myneni, 1991) qui contiennent de la matière turbide, et/ou ii) la représentation de chaque élément de paysage par des primitives géométriques, ici appelées facettes. D'une manière générale, l'amélioration des modèles physiques requiert l'amélioration de la modélisation de l'architecture des paysages, car leur complexité 3D (i.e., relief, distribution d'arbres et de maisons, etc.) affecte beaucoup les mesures de télédétection.

Les modèles basés sur l'optique géométrique (GO: Geometric optical models) simulent la réflectance des surfaces terrestres comme une fonction de leurs dimensions physiques et de leur architecture. Ainsi, ils peuvent traiter une parcelle forestière comme une distribution spatiale de formes géométriques associées aux couronnes des arbres, au-dessus d'un plan horizontal, avec des parties éclairées et non éclairées (Peddle, 2003). Chaque partie est caractérisée par des propriétés optiques prédéfinies qui intègrent de

manière implicite les diffusions de volume qui surviennent dans les couronnes d'arbres. Cette approche simplificatrice est une source potentielle d'importante imprécision. Par suite, les modèles géométriques sont plus adaptés aux couverts ouverts (e.g., parcelle forestière peu dense). Li and Stralher (1992) ont développé un des premiers modèles géométriques. Le modèle "4-scale" (Chen, 1997) simule les couronnes d'arbre comme des éléments géométriques discrets : cône et cylindre pour les conifères, et des ellipsoïdes pour les décidus. Les feuilles dans les couverts de décidus, et les pousses dans les couverts de conifères, définies par des distributions angulaires données, sont distribuées sur les branches. Ce modèle utilise une approche géométrique basée sur les facteurs de vue, pour simuler les diffusions multiples (Chen, 2001). Le modèle "5-Scale" (Leblanc, 2000) est une extension du modèle "4-Scale". Il inclue le modèle foliaire LIBERTY (Dawson, 1998) pour simuler les propriétés optiques de feuilles et aiguilles.

Les modèles de transfert radiative (MTR) simulent la propagation du rayonnement dans les paysages terrestres et l'atmosphère à partir d'une approche basée sur la modélisation physique des mécanismes de diffusion mis en jeu. Ils s'appuient sur l'équation du transfert radiatif. Cette équation exprime en tout point le changement du champ de rayonnement (luminance) le long d'une direction du fait des phénomènes locaux d'absorption, de diffusion et d'émission thermique. Ces modèles peuvent être robustes et précis, car ils peuvent travailler avec des représentations réalistes des paysages terrestres.

En général, la simulation de la réflectance et de la température de brillance à toute altitude, du bas au haut de l'atmosphère, s'appuie sur 4 composantes :

1. Sol (e.g., modèle d'Hapke (Hapke, 1981)).
2. Elément foliaire (e.g., modèle PROSPECT (Jacquemoud, ; Feret, 2008)).
3. Couvert (e.g., modèle SAIL model (Verhoef,).
4. Atmosphère (e.g., modèles MODTRAN (,) et 6S (Vermote, 1997). Des modèles comme DART (Gastellu-Etchegorry et al., 1996) simulaent la propagation du rayonnement dans le système "terre - atmosphere".

Les diffusions multiples, et par suite la conservation de l'énergie, constituent la principale source d'imprécision de ces modèles, car contrairement aux diffusions d'ordre 1, elles ne peuvent être représentées par une expression analytique simple.

Les solutions des modèles de transfert radiatifs (TR) s'appuient en général sur une des approches mathématiques suivantes : i) La méthode des N-flux ii) La méthode de radiosité iii) La méthode des ordres successifs de diffusion (Successive Orders of Scattering : SOS) et iv) La méthode Monte-Carlo. Dans la méthode N-flux, le rayonnement se propage le long de N directions discrètes, qui correspondent aux équations du modèle de transfert radiatif. Par exemple, le modèle SAIL (Verhoef, 1984) utilise quatre équations différentielles correspondantes aux quatre flux directionnels dans un paysage horizontalement homogène : une équation gère la propagation du flux solaire, deux équations gèrent la propagation des 2 flux isotropes montants et descendants et une équation gère la propagation du rayonneent

selon la direction d'observation du capteur. En fait, une modélisation relativement précise, dans le cas de milieux réels, c'est à dire en présence de flux diffus non isotropes, peut nécessiter un beaucoup plus grand nombre d'équations différentielles et de flux associés (ex : plus de 100) (Yin et al., 2013b). La méthode de radiosité (Borel et al., 1991) repose sur un principe différent. Elle s'appuie sur des équations qui expriment l'équilibre radiatif d'un nombre fini M de diffuseurs et absorbants, à l'aide de facteurs de vue entre tous ces M éléments. Sa solution repose sur l'inversion de matrices qui nécessitent un temps de calcul conséquent si M est trop grand, comme dans le cas de paysages contenant des éléments complexes, comme les arbres. La méthode des ordres successifs de diffusion est une des plus anciennes méthodes, et conceptuellement une des solutions les plus simples, pour représenter les diffusions multiples. Elle utilise un calcul itératif de la diffusion. Ainsi, le modèle SOSVRT (Duan et al., 2010) simule le TR polarisé dans des milieux plans, hétérogènes selon la verticale. La méthode de Monte-Carlo (MC) implique la simulation d'une chaine d'évènements (diffusion, absorption) d'un photon à partir d'un point source qui pour des raisons techniques n'est en général pas la source de rayonnement du système étudié, mais le détecteur. L'avantage majeur de cette technique est que toute diffusion multiple est traitée comme une suite de diffusions d'ordre 1. Elle ne s'appuie donc pas, à l'inverse des autres modèles, sur des approximations de la modélisation des diffusions multiples (Disney et al., 2000). Sa contrainte majeure est le temps de calcul. En effet, de nombreux rayons doivent être envoyés pour chaque pixel de l'image à simuler afin d'obtenir une solution convergente qui représente le comportement de la diffusion des rayons à l'intérieur de la scène avec une précision donnée. Ainsi, une intégrale sur les photons mesurés doit être effectuée, ce qui implique que plus la scène est détaillée, et plus le nombre de calculs à effectuer pour chaque photon est grand. Des exemples connus de modèles sont Drat (Lewis, 1999), FLIGHT (North, 1996) et Raytran (Govaerts, 1998).

En résumé, les modèles de transfert radiatifs peuvent opérer sur des représentations réalistes des surfaces terrestres la Terre et de l'atmosphère, ce qui fait d'eux des outils idéaux pour relier les mesures de télédétection aux paramètres de surface. Le modèle de transfert radiatif DART (Discrete Anisotropic Radiative Transfer) est un des modèles 3D les plus complets pour simuler le transfert radiatif dans le système "Terre - Atmosphère", dans le domaine spectral du visible à l'infrarouge thermique. Ce modèle est développé depuis 1992. Il a pour objectif de simuler le signal optique des spectro-radiomètres imageurs et des LiDARs multi-impulsions embarqués à bord des satellites et des avions, ainsi que le bilan radiatif 3D, pour tout paysage naturel et urbain, et pour toutes les configurations expérimentales et instrumentales. Il est distribué par l'Université Paul Sabatier sous forme de licences gratuites pour les activités de recherche et d'enseignements.

Les 5 chapitres de ce mémoire présentent les travaux réalisés durant cette thèse. Ils correspondent à 6 papiers dans des journaux de rang A : 3 papiers publiés, 2 papiers soumis et 1 papier prêt à être soumis. Mon objectif majeur a été d'améliorer le modèle DART dans le but de simuler les mesures des LiDARs et radiomètres imageurs avec plus de précision, c'est-à-dire en prenant en compte leurs caractéristiques instrumentales et leur géométrie d'acquisition. Le modèle DART est ainsi devenu beaucoup mieux adapté à la validation des systèmes d'observation actuels et à la préparation des misions spatiales futures.

Le premier chapitre introduit les généralités sur la modélisation dans DART. Pour des informations plus détaillées sur la modélisation théorique développée, la meilleure référence est Gastellu-Etchegorry et al. (1996). De plus, il résume la plupart des développements récents dans DART, qui sont présenté dans les chapitres 2 à 5. Il s'agit de développements différents, mais très interdépendants.

- Chapitre 2: Discrétisation et sur-échantillonnage des directions. La distribution angulaire des directions utilisées pour le suivi de rayons peut beaucoup impacter la simulation des mesures de télédétection. J'ai conçu et implémenté une nouvelle méthode appelée "iterative uniform squared discretization: IUSD" qui discrétise l'espace 4π en un nombre fini de directions discrètes le long desquelles le rayonnement se propage dans DART. Cette méthode combine les avantages des méthodes classiques DOM et FVM : forme angulaire bien définie et un point central exact pour chaque direction. Elle utilise des secteurs angulaire carrés. L'emploi d'une expression analytique pour décrire ce secteurs permet l'ajout de directions quelconques (e.g., direction d'observation d'un satellite) et le sur-échantillonnage de régions angulaires. Un intérêt majeur de l'approche est que le transfert radiatif peut ensuite être calculé avec une approche qui combine des intégrations numériques et des intégrations analytiques, ce qui accélère beaucoup les calculs. Les moments 0^{th} et 1^{st} de la discrétisation classique sont exactement définis. Le sur-échantillonnage de régions de la sphère est bien adapté au cas de la diffusion anisotrope (e.g. hot spot). Plusieurs cas sont étudiés : forme optimale des secteurs angulaires sur la sphère 4π, sur-échantillonnage de plans et régions de la sphère, et emploi de directions non centrées sur leurs secteurs angulaires Ω_n pour améliorer la modélisation du transfert radiatif. Les résultats montrent la supériorité de la méthode IUSD par rapportaux méthodes DOM et FVM.

- Chapitre 3 : Simulation de capteurs passifs imageurs avec champ de vue (FOV) fini. Le FOV des capteurs de télédétection n'est pas nul, comme cela est en général considéré dans les modèles de télédétection. Par suite, les pixels d'une même image sont observés selon des directions de visée différentes. Négliger cette variation des directions de visée est source d'incohérence entre les mesures simulées et mesurées. En effet, la création d'images d'objets 3D sur un plan 2D implique une projection spécifique qui conditionne les luminances mesurées : distorsion géométrique (e.g. un objet proche du capteur apparaît plus grand dans l'image), et variation angulaire de la luminance selon la direction de visée à l'intérieur du FOV. En synthèse d'image, la projection "perspective" (Sonka et al., 2008) est utilisée pour les caméras, et la projection "parallèle-perspective" (Chai and Shum, 2000; Gupta and Hartley, 1997; Zhu et al., 2004) est utilisée pour les capteurs qui observent dans un plan qui coupe la direction de la plateforme. La prise en compte de ces projections est essentielle pour obtenir des simulations précises. Par suite, j'ai introduit dans DART une modélisation qui tient compte de la projection perspective 3D: la méthode "convergent tracking and perspective projection : CTPP". Ainsi, le domaine d'application de DART a été largement étendu. Cette approche a été utilisée pour améliorer les résultats obtenus par Schneider et al. (2014a) lors de la comparaison pixel à pixel de simulations DART et du capteur hyperspectral

APEX (Appeendix II) dans le cas d'une forêt alpine.

- Chapitre 4. LiDAR. Ce chapitre comprend 2 sections.

  - Section 4.1: Simulation de forme d'onde due à une impulsion LiDAR. Un LiDAR forme d'onde (wLiDAR) mesure le temps de retour de l'impulsion qu'il a émise. Le signal électyrique associé est enregistré en tant que suite de points de mesure (bin) (Shan and Toth, 2008). Une forme d'onde LiDAR indique à la fois la distance entre le LiDAR et le milieu observé et la distribution de la matière à l'intérieur de ce milieu. Le fait de disposer de modèles d'acquisition LiDAR est essentiel pour bien comprendre et exploiter les mesures LiDARs. Cette section présente la modélisation quasi Monte Carlo originale qui a été introduite dans DART pour simuler les mesures LiDARs. Cette modélisation s'appuie sur deux méthodes originales conçues pour accélérer le choix des directions de diffusion et pour effectuer le suivi des photons en mode direct. Elle opère pour toute configuration (altitude de la plateforme, direction de visée, dimension du footprint, etc.). La modélisation au sein de l'atmosphère est introduite, ce qui est très original par rapport aux autres modèles LiDARs de la communauté scientifique.
  - Section 4.2: Simulation de mesure LiDAR multi-impulsions. L'acquisition de formes d'onde associées à l'émission de multiples impulsions selon différentes directions génère un nuage 3-D de points qui renseignent sur les propriétés optiques et la position des diffuseurs qui sont à l'origine des signaux mesurés (Wagner, et al., 2006). Les wLiDARs embarqués sur avion (airborne laser scan : ALS) opèrent avec un petit footprint dans une zone définie par la plateforme et la configuration du LiDAR (Mallet and Bretar, 2009). Les points du nuage 3-D peuvent être classés en tant qu'élément d'occupation du sol (sol, couvert végétal, etc.) (Zhang et al., 2003). De même les TLSs sont de plus en plus utilisés pour mesurer l'architecture des arbres (Rosell et al., 2009). Cette section présente une extension de la modélisation LiDAR mono-impulsion de DART au cas de la confguration LiAR multi-impulsions satellite, aéroportée et terrain. Un point technique important est que les produits de simulation peuvent être exportés dans un format standard : sorted pulse data (SPD) (Bunting et al., 2013b). Par suite, les produits DART peuvent être traités avec SPDlib (Bunting et al., 2013a), c'est-à-dire un logiciel de traitement LiDAR dédié. J'ai aussi étendu la modélisation DART au cas des LiDARs dits à comptage de photons (pcLiDAR) (Montesano et al., 2015). De plus, j'ai introduit la modélisation du bruit solaire. La modélisation LiDAR est illustrée avec la simulation de plusieurs systèmes : Carnegie Airborne Observatory (CAO : Asner et al. (2012, 2007)), ILRIS terrestrial LiDAR system de Optech Inc (www.optech.com), et le Multiple Altimeter Beam Experimental LiDAR (MABEL, McGill et al. (2013)) de la NASA. Le cas de l'Advanced Topographic Laser Altimeter System (ATLAS : Anthony et al. (2010)) qui sera prochainement embarqué sur le satellite "Ice, Cloud, and Land Elevation Satellite" (ICESat-2, Abdalati et al. (2010)) est aussi considéré.

- Chaptre 5: Fusion en vol de mesures de radiomètre et LiDAR. Des capteurs avec différentes caractéristiques t /ou qui opèrent selon différentes configurations fournissent des informations complémentaires sur les surfaces terrestres observées. Ceci est typiquement le cas des mesures des LiDARs et radiomètres. Pour faciliter la superposition géométrique de ces types d'information, une solution classique consiste à embarquer les différents capteurs considérés sur la même plateforme. Cette approche permet de fusionner les données acquises directement en vol (Asner et al., 2007), ou bien après. Plusieurs systèmes opèrent ainsi : CAO, NEON AOP (National Ecological Observatory's Airborne Observation Platform : Kampe et al. (2010)), et G-LIHT (Goddard's LiDAR, Hyperspectral and Thermal Airborne Imager : Cook et al. (2013)). J'ai conçu une méthode originale de fusion des données de LiDAR et de radiomètre. L'approche repose sur la simulation de capteur à FOV non nul introduite au chapitre 3 et la modélisation LiDAR multi-impulsion introduite au chapitre 4. Il s'agit d'une configuration à deux sources (soleil, LiDAR) et un capteur (LiDAR). Cette fusion est illustrée ave le cas de couverts urbains et végétaux.

Les développements présentés ci-dessus ont été réalisés en étroite collaboration avec les membres de l'équipe DART, à la fois pour la partie informatique et pour la modélisation physique. Ainsi, j'ai beaucoup collaboré avec Nicolas Lauret pour la conception et l'amélioration de la modélisation LiDAR. D'autre part, le fait que DART soit distribué sous la forme de licences (par l'Université Paul Sabatier) à des utilisateurs qui travaillent dans des domaines et centres de recherche très divers a de fortes implications sur les méthodes de travail au sein de l'équipe DART, comme indiqué ci-dessous.

- Conception et implémentation de nouvelle modélisation et de nouvelles fonctionnalités.

  Ces développements sont souvent effectués dans le cadre de projets ou collaborations avec des détenteurs de licences, avec l'objectif de développer la physique de DART. Par exemple, la collaboration avec NASA GSFC a contribué au développement de la modélisation du LiDAR, dans le cadre de la préparation de la mission DESDynl mission. En général, l'introduction / amélioration de nouvelles fonctionnalités est décidée lors de réunions hebdomadaires, et est réalisée par les personnes de l'équipe les plus concernées, sous la supervision de Nicolas Lauret qui assure le rôle de responsable de l'informatique de DART.

- Aide pour les détenteurs de licences DART.

  Vu le nombre de licenciés DART, des demandes d'aide et de clarification sont régulièrement transmises à l'équipe. Jean-Philippe Gastellu-Etchegorry gère les relations avec tous les détenteurs de licence, y compris le site internet de DART. Certaines demandes se traduisent par le besoin de corriger ou d'améliorer une fonctionnalité de DART. Ce travail est alors réalisé par le membre de léquipe le plus concerné par la demande scientifique/technologique. Par exemple, Thomas Cajgfinger et Tristan Grégoire gèrent les demandes concernant les bases de données SQL, Jordan Guilleux et Nicolas Lauret gèrent les demandes concernant l'interface graphique, etc. Durant ma thèse, j'ai géré les questions concernant la modélisation du TR atmosphérique et du LiDAR, ainsi

que la simulation de caméra et pushbroom. Toute nouvelle implémentation est effectuée sous le contrôle de Nicolas Lauret.

- Travail informatique pour maintenir DART opérationnel.

  Le maintien de DART en tant qu'outil opérationnel implique beaucoup de travail, au vu de l'importance du code (400 000 lignes de code) et des outils informatiques mis en jeu. Ainsi, il est nécessaire de maintenir et mettre à jour les systèmes d'exploitation, les librairies C++, Java, Python, les librairies SQL. Il est aussi nécessaire de maintenir et mettre à jour les systèmes qui gèrent les tests de non régression, la compilation croisée, la distribution des versions de DART, etc. Ceci est majoritairement fait par Tristan Gregoire et Nicolas Lauret. Les tâches à effectuer ne sont pas toujours prévisibles. Par exemple, fin 2014, il est apparu que le code Java SWT qui est utilisé dans l'interface graphique de DART (GUI) est de moins en moins compatible avec l'évolution des systèmes Linux. Ceci implique de réécrire entièrement l'interface graphique de DART, c'est-à-dire près de 18 mois de développement. Ce développement est effectué par Jordan Guilleux. Il débouchera sur une interface très améliorée de DART. Tout le travail informatique est fait sous la supervision de Nicolas Lauret.

Chapter 1

Introduction to DART Version 5

Radiative transfer models capable of simulating the Earth and atmosphere complexity are, therefore, ideal tools for linking remotely sensed data to the surface parameters. The Discrete Anisotropic Radiative Transfer (DART) model is one of the most comprehensive physically based 3D models simulating the Earth-atmosphere radiation interaction from visible to thermal infrared wavelengths.

In this chapter, the physical bases of DART and its latest functionality for simulating imaging spectroscopy of natural and urban landscapes with atmosphere, including the perspective projection of airborne acquisitions and LIDAR waveform and photon counting signals, are generally introduced in Section 1.1 with the article "Discrete anisotropic radiative transfer (DART 5) for modeling airborne and satellite spectro-radiometer and LIDAR acquisitions of natural and urban landscapes". This article can be considered as the summary of my dissertation. I am the second author of this article. Jean-Philippe Gastellu-Etchegorry plays the leading role in this article for organizing materials, writing background, developing theory, and analyzing simulations in this article. I contribute to DART 5 developments, implementations, in different scientific domains presented in the paper. They include passive sensor image simulation model, single-pulse and multi-pulse LIDAR model, imaging spectroscopy and LIDAR fusion model, and Atmosphere-Earth coupling model. For the other authors' contributions, please refer to the **Author Contributions** section of the article.

The major points that are covered in this article are detailed in Chapters 2 to 5, with one or two papers per chapter. The direction discretization (Section 2 of the paper in Chapter 1) is detailed in Chapter 2. The multi-view sensor image simulation (Section 5 of the paper in Chapter 1) is detailed in Chapter 3. The LIDAR simulation (Section 4 of the paper in Chapter 1) is detailed in Chapter 4. The in-flight fusion simulation (Section 6 of the paper in Chapter 1) is detailed in Chapter 5.

1.1 Article: Discrete anisotropic radiative transfer (DART 5) for modeling airborne and satellite spectroradiometer and LIDAR acquisitions of natural and urban landscapes

Remote Sens. **2015**, *7*, 1667-1701; doi:10.3390/rs70201667

OPEN ACCESS

remote sensing

ISSN 2072-4292

www.mdpi.com/journal/remotesensing

Article

Discrete Anisotropic Radiative Transfer (DART 5) for Modeling Airborne and Satellite Spectroradiometer and LIDAR Acquisitions of Natural and Urban Landscapes

Jean-Philippe Gastellu-Etchegorry [1,*], Tiangang Yin [1], Nicolas Lauret [1], Thomas Cajgfinger [1], Tristan Gregoire [1], Eloi Grau [1], Jean-Baptiste Feret [1], Maïlys Lopes [1], Jordan Guilleux [1], Gérard Dedieu [1], Zbyněk Malenovský [2,3], Bruce Douglas Cook [4], Douglas Morton [4], Jeremy Rubio [4], Sylvie Durrieu [5], Gregory Cazanave [6], Emmanuel Martin [6] and Thomas Ristorcelli [6]

1 Centre d'Etudes Spatiales de la BIOsphère (CESBIO) - UPS, CNES, CNRS, IRD, Université de Toulouse, 31401 Toulouse cedex 9, France ;
E-Mails : tiangang.yin.85@gmail.com (T.Y.); nicolas.lauret@cesbio.cnes.fr (N.L.); cajgfingert@cesbio.cnes.fr (T.C.); gregoiret@cesbio.cnes.fr (T.G.); eloi.grau@gmail.com (E.G.); jb.feret@gmail.com (J.-B.F.); mailys.lopes@gmail.com (M.L.); guilleuxj@cesbio.cnes.fr (J.G.); gerard.dedieu@cesbio.cnes.fr (G.D.)

2 Institute for Conservation Biology, School of Biological Sciences, University of Wollongong, Wollongong 2522, Australia; E-Mail: zbynek.malenovsky@gmail.com

3 School of Land and Food, University of Tasmania, Hobart 7001, Australia

4 NASA's Goddard Space Flight Center, Greenbelt, MD 20771, USA;
E-Mails: bruce.cook@nasa.gov (B.D.C.); douglas.morton@nasa.gov (D.M.); rubio.jeremy@gmail.com (J.R.)

5 TETIS - Irstea, Cirad, AgroParisTech/ENGREF, 34196 Montpellier Cedex 05, France;
E-Mail: sylvie.durrieu@teledetection.fr

6 Magellium, 31520 Ramonville-Saint-Agne, France;
E-Mails: gregory.cazanave@magellium.fr (G.C.); emmanuel.martin@magellium.fr (E.M.); thomas.ristorcelli@magellium.fr (T.R.)

***** Author to whom correspondence should be addressed;
E-Mail: jean-philippe.gastellu-etchegorry@cesbio.cnes.fr; Tel.: +33-561-55-6130.

Academic Editors: Heiko Balzter and Prasad S. Thenkabail

Received: 16 November 2014 / Accepted: 23 January 2015 / Published: 5 February 2015

Abstract: Satellite and airborne optical sensors are increasingly used by scientists, and

policy makers, and managers for studying and managing forests, agriculture crops, and urban areas. Their data acquired with given instrumental specifications (spectral resolution, viewing direction, sensor field-of-view, *etc.*) and for a specific experimental configuration (surface and atmosphere conditions, sun direction, *etc.*) are commonly translated into qualitative and quantitative Earth surface parameters. However, atmosphere properties and Earth surface 3D architecture often confound their interpretation. Radiative transfer models capable of simulating the Earth and atmosphere complexity are, therefore, ideal tools for linking remotely sensed data to the surface parameters. Still, many existing models are oversimplifying the Earth-atmosphere system interactions and their parameterization of sensor specifications is often neglected or poorly considered. The Discrete Anisotropic Radiative Transfer (DART) model is one of the most comprehensive physically based 3D models simulating the Earth-atmosphere radiation interaction from visible to thermal infrared wavelengths. It has been developed since 1992. It models optical signals at the entrance of imaging radiometers and laser scanners on board of satellites and airplanes, as well as the 3D radiative budget, of urban and natural landscapes for any experimental configuration and instrumental specification. It is freely distributed for research and teaching activities. This paper presents DART physical bases and its latest functionality for simulating imaging spectroscopy of natural and urban landscapes with atmosphere, including the perspective projection of airborne acquisitions and LIght Detection And Ranging (LIDAR) waveform and photon counting signals.

Keywords: radiative transfer; DART 5 model; imaging spectroscopy; spectroradiometer; LIDAR; camera projection

1. Background

Remote sensing (RS) observations facilitate global studies of the land surface and biophysical properties of vegetation (e.g., leaf biomass, soil moisture). In this study, we are addressing Imaging Spectroscopy (IS) and LIght Detection and Ranging (LIDAR) RS techniques that are mapping the Earth landscapes from the visible to the thermal infrared spectral domains (between 0.3 μm and 50 μm). Imaging spectroradiometers measure fluxes (radiance) as two-dimensional (2D) arrays (images). Radiance fluxes can be transformed into landscape reflectance ρ (ratio of reflected and incident radiation) of visible (VIS) and near infrared (NIR) wavelengths, and into landscape brightness temperature T_B in the case of thermal infrared (TIR) acquisitions. Satellite IS sensors acquire Top Of Atmosphere (TOA) data, a combination of scattering and absorption from the Earth surface and atmosphere, whereas airborne RS observations are typically considered as Bottom Of Atmosphere (BOA) if acquired right above the Earth surface. LIDAR sensors use a laser beam as a photon source and measure the travel time between the laser pulse emission and its reflected return to calculate the range (distance) to the objects encountered by the emitted pulse. The combination of range measurements with knowledge of platform location and attitude provides a three-dimensional (3D) representation of the observed landscape.

Empirical relationships, such as the correlation of RS and field-measured data (e.g., Leaf Area Index—LAI), were one of the first methods used for RS data interpretation. A typical example is the estimation of LAI from the Normalized Difference Vegetation Index, defined as $\mathrm{NDVI} = \frac{\rho_{\mathrm{PRI}} - \rho_{\mathrm{red}}}{\rho_{\mathrm{PRI}} + \rho_{\mathrm{red}}}$ [1]. Although simple, fast and straightforward, these methods are site and sensor specific, and thus insufficiently robust and universally inapplicable. Increasing demand for more universal satellite data products for landscape characteristics has spurred advances in theoretical understanding and modeling of IS and LIDAR signals of 3D landscapes for various experimental and instrumental configurations (radiometric accuracy, spatial/spectral/temporal resolutions, *etc.*). IS signals correspond essentially to the bi-directional reflectance factor (BRF) and brightness temperature function (BTF). Instrumental configuration is given by sensor technical specifications, including: field-of-view (FOV), full-width-at-half-maximum (FWHM), spectral sampling, and viewing geometry. Experimental configuration corresponds to:

(1) The date of acquisition (sun angular position),

(2) Landscape geometrical configuration and optical properties

(3) Atmospheric parameters (gas and aerosol density profiles, scattering phase functions and single scattering albedo).

It must be noted that improvement of recent RT models requires, in general, advancement in representation of landscapes, as their 3D complexity (*i.e.*, topography, distribution of trees and buildings, *etc.*) greatly affects optical observations. Three most frequent types of BRF simulating models, ordered according to their increasing complexity, are: semi-empirical, geometrical optical and radiative transfer models.

1.1. Semi-Empirical Models

These models are widely used for their analytical nature and use of only a few input parameters. They do not attempt to describe the biophysical parameters and processes that shape BRF, but they provide a mathematical description of observed patterns in BRF datasets. They rely on simplified physical principles of geometrical optical (GO) models and RT theory. For example, linear kernel driven (LiK) models [2–4] calculate BRF as the sum of an isotropic term and anisotropic functions (kernels) that characterize volume and surface scattering. For example, MODIS, POLDER, MSG/SEVIRI, AVHRR, VEGETATION land surface BRF/albedo products are mainly generated using LiK models to invert the BRF parameters of multi-angular bidirectional reflectance in clear skies [5]. Another example is the Rahman-Pinty-Verstraete (RPV) model [6], and its latter inversion accelerating versions: the Modified RPV (MRPV) [7] and EMRPV [8] models. These models are widely used for their analytical nature and use of only few input parameters.

1.2. Geometric Optical Reflectance Models

Geometric optical (GO) models simulate the BRF of objects on the Earth surface as a function of their physical dimensions and structure. For instance, they consider forest stands as a combination of approximated geometrical shapes of tree crowns with corresponding shadows and background forest floor material [9], each of them with predefined surface optical properties that integrate implicitly the

volume light scattering. Modeling is based on the computation of scene fractions of sunlit canopy, sunlit background, and shadows, which is a potential source of modeling inaccuracy. Therefore, GO models perform better in simulations of "open" landscapes (e.g., sparse forest stands). Li and Stralher [10] developed one of the first GO models. More recent 4-scale model [11] simulates tree crowns as discrete geometrical objects: cone and cylinder for conifers, and spheroid for deciduous trees. Individual leaves in deciduous canopies and shoots in conifer canopies, defined with a given angular distribution, populate branches with a single inclination angle. This model uses a geometrical multiple scattering scheme with view factors [12]. The 5-Scale model [13] is an extension of 4-Scale that includes the LIBERTY model [14], which simulates needle-leaf optical properties.

1.3. Radiative Transfer Models

Radiative transfer (RT) models, also called physical RT models, simulate the propagation of radiation through Earth systems and the RS acquisitions using physically described mechanisms. They rely on an RT equation, which relates the change in radiation along a ray path due to local absorption, scattering and thermal emission. Since these models work with realistic representations of Earth landscapes, they can be robust and accurate. Generally speaking, simulation of BOA and TOA BRF and BTF involves RT of four components:

(1) Soil (e.g., Hapke model [15])
(2) Foliar element (e.g., PROSPECT model [16])
(3) Canopy (e.g., SAIL model [17])
(4) Atmosphere (e.g., MODTRAN [18] or 6S [19] models).

Some models, such as the Discrete Anisotropic Radiative Transfer (DART) model [20], directly simulate the Earth-atmosphere interactions using inputs from soil and leaf RT models. Multiple scattering and consequently energy conservation is the usual major source of inaccuracies of these models, because, conversely to first order scattering, it has no simple analytical form.

The solutions of RT models are based on the following four mathematical methods: (i) N-flux, (ii) radiosity, (iii) Successive Orders of Scattering, and (iv) Monte Carlo. In case of N-flux method, the radiation is propagated along N number of discrete ordinates (directions), which correspond to N RT equations. For example, the SAIL model [17] uses four differential equations corresponding to four directional fluxes within a horizontally homogeneous landscape: one sun flux, two isotropic upward and downward fluxes and one flux along a sensor viewing direction. However, a more detailed consideration of the RT anisotropy can require a much larger number of fluxes (e.g., more than 100) [21]. Contrary to the N-flux method that computes the volumetric radiation balance in the 3D space, the radiosity method [22] is based on the radiation balance equation of a finite number N of discrete scatterers, which requires computation of the view factors between all N elements. It is, therefore, based on inversion of a NxN matrix, which is time consuming if N is too large, e.g., in case of complex landscape elements such as trees. The Successive Orders of Scattering (SOS) method is one of the oldest and conceptually simplest solutions of the multiple scattering. It uses an iterative calculation of successive orders of scattering, where the total radiance vector is expressed as a sum of contributions from photons scattered a number of times ranging from 0 to a pre-defined maximum number. An example is the SOSVRT model [23] that simulates

polarized RT in vertically inhomogeneous plane-parallel media. The Monte Carlo (MC) method involves simulation of the chain of scattering events incurred by a photon in its path from the source to the receiver or to its absorber. An advantage of this technique is explicit computation of only single scattering properties [24]. On the other hand, it requires long computational time, which is a strong technical limiting constraint. Well-known examples of MC models are Drat [25], FLIGHT [26] or Raytran [27].

Finally, RT models work with landscapes that are simulated as homogeneous or heterogeneous scenes. Homogeneous scenes are represented as a superposition of horizontally homogeneous layers of turbid medium (*i.e.*, random distribution of infinitely small planar elements). The very first RT models used this approach to model general trends such as the evolution of crop BRF/BTF in relation to phenological LAI changes. The approach of homogeneous turbid layers is, however, insufficient for description of complex landscape architectures. The heterogeneous landscapes are being simulated in two following ways (or their combination): (i) discretization of the spatial variable into a 3D set of spatial nodes called voxels [28,29] that contain turbid medium, and/or (ii) representation of each individual landscape element with triangular facets as geometrical primitives.

The objective of this paper is to present the latest advances in DART (DART 5 version) modeling of airborne and satellite IS as well as LIDAR data of architecturally complex natural and urban landscapes. After introducing the physical theory, we present recent development in DART modeling of IS and LIDAR acquisitions. Finally, an ability to simulate airborne image acquisitions with the projective perspective and also a fusion of modeled IS with LIDAR data are demonstrated as new model functionalities.

2. DART Theoretical Background and Functions

DART is a three-dimensional (3D) model computing radiation propagation through the entire Earth-atmosphere system in the entire optical domain from visible to thermal infrared parts of the electromagnetic spectrum (EMS) [30,31]. As shown in Figure 1, it simulates 3D radiative budget and reflected radiation of urban and natural landscapes as acquired by imaging radiometers and LIDAR scanners aboard of space and airborne platforms. The DART model, developed in the CESBIO Laboratory since 1992, can work with any 3D experimental landscape configuration (atmosphere, terrain geomorphology, forest stands, agricultural crops, angular solar illumination of any day, Earth-atmosphere curvature, *etc.*) and instrument specifications (spatial and spectral resolutions, sensor viewing directions, platform altitude, *etc.*). DART forward simulations of vegetation reflectance were successfully verified by real measurements [32] and also cross-compared against a number of independently designed 3D reflectance models (e.g., FLIGHT [26], Sprint [33], Raytran [27]) in the context of the RAdiation transfer Model Intercomparison (RAMI) experiment [34–38]. To date, DART has been successfully employed in various scientific applications, including development of inversion techniques for airborne and satellite reflectance images [39,40], design of satellite sensors (e.g., NASA DESDynl, CNES Pleiades, CNES LIDAR mission project [41]), impact studies of canopy structure on satellite image texture [42] and reflectance [32], modeling of 3D distribution of photosynthesis and primary production rates in vegetation canopies [43], investigation of influence of Norway spruce forest structure and woody elements on canopy reflectance [44], design of a new chlorophyll estimating vegetation index for a conifer forest canopy [45], and studies of tropical forest texture [46–48], among others.

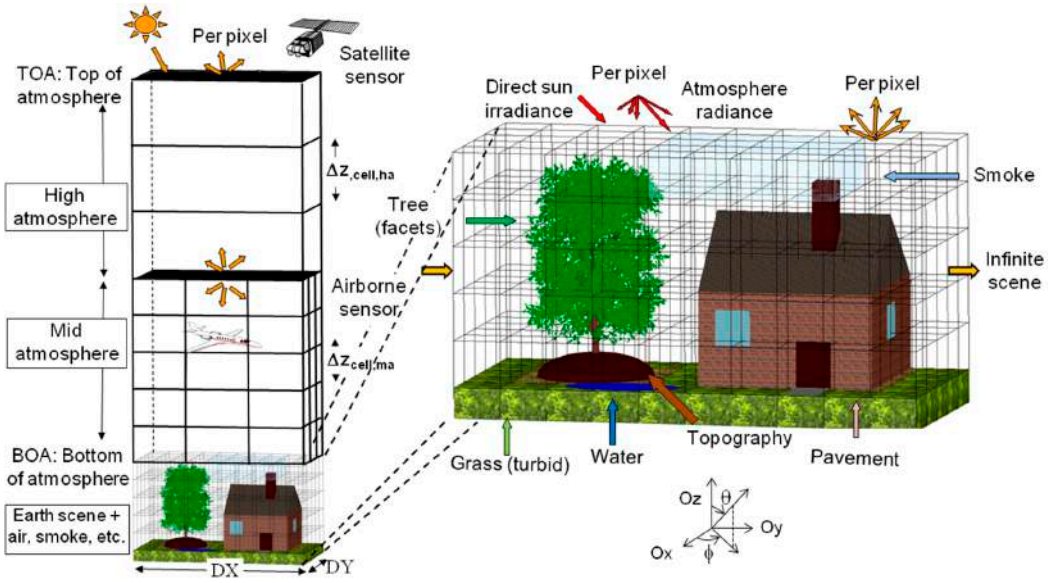

Figure 1. DART cell matrix of the Earth/Atmosphere system. The atmosphere has three vertical levels: upper (*i.e.*, just layers), mid (*i.e.*, cells of any size) and lower atmosphere (*i.e.*, same cell size as the land surface). Land surface elements are simulated as the juxtaposition of facets and turbid cells.

DART creates and manages 3D landscapes independently from the RT modeling (e.g., visible and thermal infrared IS, LIDAR, radiative budget). This multi-sensor functionality allows users to simulate several sensors with the sample landscape. Major scene elements are: trees, grass and crop canopies, urban features, and water bodies. A DART simulated tree is made of a trunk, optionally with branches created with solid facets, and crown foliage simulated as a set of turbid cells, with specific vertical and horizontal distributions of leaf volume density. Its crown shape is predefined as ellipsoidal, conical, trapezoidal, or others. Trees of several species with different geometric and optical properties can be exactly or randomly located within the simulated scene of any user-defined size. Grass and crops are simulated as turbid media that can be located anywhere in space. Urban objects (houses, roads, *etc.*) contain solid walls and a roof built from facets. Finally, water bodies (rivers, lakes, *etc.*) are simulated as facets of appropriate optical properties. Specific 3D transformations and optical properties can be assigned to each landscape object. Additionally, DART can use external libraries (Figure 2) to import, and to some extent edit (e.g., translation, homothetic and rotation transformations) landscape elements, digital elevation models (DEM) and digital surface models (DSM) produced by other software or measured in field. Importantly, the imported and DART-created landscape objects can be combined to simulate Earth scenes of varying complexity. The optical properties of each landscape element and the geometry and optical properties of the atmosphere are specified and stored in SQL databases.

Figure 2. Examples of natural and artificial 3D objects imported by DART, simulated using triangular facets: (**a**) wheat plant, (**b**) corn plant, (**c**) rice canopy, (**d**) sunflower plant, (**e**) cherry tree and (**f**) airplane.

DART landscapes, hereafter called "scenes", are constructed with a dual approach as an array of 3D cells (voxels) where each scene element, with any geometry, is created as a set of cells that contains turbid media and/or facets (triangles and parallelograms). Turbid medium is a statistical representation of a matter, such as fluids (air, soot, water, *etc.*) and vegetation foliage or small-sized woody elements. A fluid turbid medium is a volume of homogeneously distributed particles that are defined by their density (particles/m^3), cross section (m^2/particle), single scattering albedo, and scattering phase function. Turbid vegetation medium is a volume of leaf elements that are simulated as infinitely small flat surfaces that are defined by their orientation, *i.e.*, Leaf Angle Distribution (LAD; sr^{-1}), volume density (m^2/m^3), and optical properties of Lambertian and/or specular nature. Finally, a facet is a surface element that is defined by its orientation in space, area and optical properties (Lambertian, Hapke, RPV and other reflectance functions with a specular component, and also isotropic and direct transmittance). It is used to build virtual houses, plant leaves, tree trunks or branches. Vegetation canopies can, therefore, be simulated as assemblies of turbid medium voxels or geometrical primitives built from facets or combination of both.

Atmospheric cells were introduced into DART in order to simulate attenuation effects for satellite at-sensor radiance and also to model the influence of atmosphere on the radiative budget of Earth surfaces. The atmosphere can be treated as an interface above the simulated Earth scene or as a light-propagating medium above and within the simulated Earth scene, with cell sizes inversely proportional with the particle density. These cells are characterized by their gas and aerosols contents and spectral properties (*i.e.*, phase functions, vertical profiles, extinction coefficients, spherical albedo, *etc.*). These quantities can be predefined manually or taken from an atmospheric database. DART contains a database that stores the properties of major atmospheric gases and aerosol parameters for wavelengths between 0.3 μm and 50 μm [18]. In addition, external databases can be imported, for instance from the AErosol RObotic NETwork (AERONET) or the European Centre for Medium-Range Weather Forecasts (ECMWF). Atmospheric RT modeling includes the Earth-atmosphere radiative coupling (*i.e.*, radiation that is emitted and/or scattered by the Earth can be backscattered by the atmosphere towards the Earth). It can be simulated for any spectral band within the optical domain from the ultraviolet up to the thermal infrared part of electromagnetic spectrum. The Earth-atmosphere coupling was successfully cross-compared [49,50] with simulations of the MODTRAN atmosphere RT model [18].

A basic DART simulation procedure is carried out with four processing modules: (i) Direction, (ii) Phase, (iii) Maket, and (iv) Dart (Figure 3). The Direction module computes discrete directions of

light propagation with radiation being propagated along N discrete directions Ω_n with an angular sector width $\Delta\Omega_n$ (sr). Any number of N discrete directions (Ω_n, $\Delta\Omega_n$) can be specified with any Ω_n angular distribution and for any $\Delta\Omega_n$ solid angle range, as for example for oversampling angular regions with an anisotropic radiative behavior such as the hop spot configuration [51]. The discrete directions are calculated automatically or adapted to any user specified configuration. They include a set of U directions that sample the 4π space ($\sum_{u=1}^{U} \Delta\Omega_u = 4\pi$) and V directions ($\Omega_v$, $\Delta\Omega_v$) that are called fictive directions because fluxes along these directions do not contribute to fluxes along any other direction where N = U + V. Importantly, in addition to these discrete directions, DART can also track radiation along any direction in the 4π space, for example for simulating airborne acquisitions and LIDAR signals. These so-called flexible directions are not pre-defined. Their number depends on the number of emitting and scattering elements towards the sensor. Depending on the scene dimensions, the number of flexible directions can exceed 10^6.

Optical properties for all non-flexible discrete directions are pre-computed with the Phase module. It computes the scattering phase functions of all scene and atmosphere elements depending on their geometry and optical properties. For example, the phase functions of vegetation depend on the actual leaf reflectance and transmittance and the plant specific LAD.

The Maket module builds the spatial arrangement of landscape elements within a simulated scene. Scene features are created and/or imported as 3D objects with specified optical properties. Importantly, scene cell dimensions (Δx, Δy, Δz) define the output spatial sampling, and cell dimensions in DART can be varied within the same scene in order to optimize the final resolution.

Finally, the Dart module computes radiation propagation and interactions for any experimental and instrumental configuration using one of the two computational approaches: (i) Ray tracking and (ii) Ray-Carlo. Ray tracking simulates radiative budget and images of optical airborne and satellite radiometers. For that, it tracks iteratively radiation fluxes W(r, Ω_n) along N discrete directions (Ω_n), and one flexible flux, at any location r [20,21]. These fluxes are defined by three components: their total intensity, the radiation unrelated to leaf biochemistry and the polarization degree associated to first order scattering. The values of these components depend on thermal emission and/or scattering, which in turn depend on local temperature and optical properties of intercepted surfaces or volumetric scattering elements. A scattering event at iteration *i* gives rise to N fluxes, and the event is repeated in latter iterations. The fraction of W(r, Ω_i) that is scattered along a given Ω_j direction is defined by the local scattering phase function $P(\Omega_i \rightarrow \Omega_j)$, with Ω_i being a non-fictive discrete direction, or a set of discrete directions, and Ω_j being a direction that can be discrete, fictive and flexible.

The second modeling approach simulates terrestrial, airborne, and satellite LIDAR signals from waveforms and photon counting RS instruments. It combines two methods that are described in the LIDAR section. Using Monte Carlo and ray tracking techniques [52–54], the Ray-Carlo method tracks radiometric quantities corresponding to photons with specific weights, which are for simplicity reasons called just photons. During a scattering event, the so-called Box method determines the discrete direction of photon scattering using the same scattering functions as the Ray tracking approach. Simultaneously a photon with a very small weight is tracked to the LIDAR sensor. Ray tracking can additionally simulate solar noise that is present in a LIDAR signal.

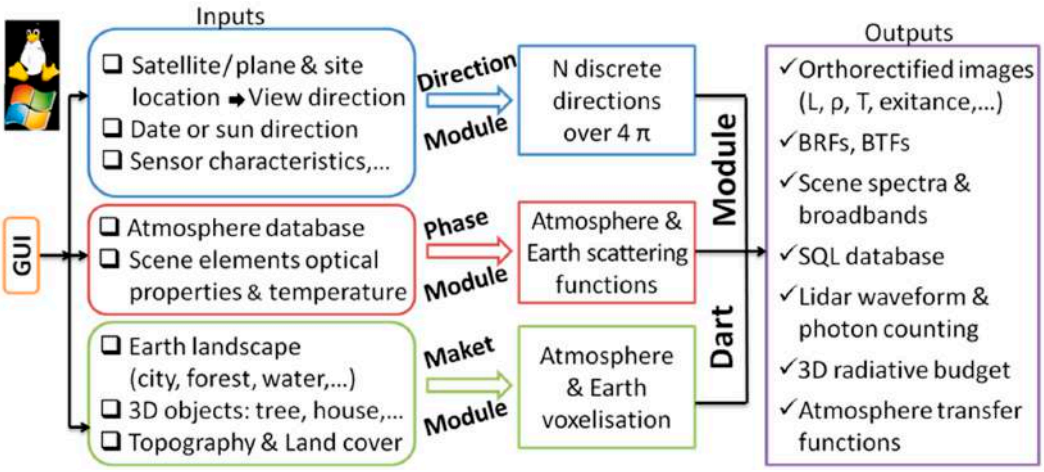

Figure 3. *Scheme illustrating DART model architecture:* four processing modules (Direction, Phase, Maket, Dart) and input data (landscape, sensor, atmosphere) are controlled through a GUI or pre-programmed scripts. The Sequence module can launch multiple DART simulations simultaneously on multiple processor cores producing effectively several RT products.

Apart from the four basic modules, the following supportive tools are integrated in DART distribution to facilitate quick and easy simulations and subsequent analysis of simulated results:

- Calculation of foliar reflectance and transmittance properties with the PROSPECT leaf RT model [16], using leaf biochemical properties (*i.e.*, total chlorophyll content, carotenoid content, equivalent water thickness and leaf mass per area) and leaf mesophyll structural parameter.
- Computation of scene spectra and broadband image data (reflectance, temperature brightness, and radiance), using a sensor specific spectral response function for either a single DART simulation with N spectral bands, or for a sequence of N single spectral band simulations.
- Importation of raster land cover maps for creating 3D landscapes that contain land cover units, possibly with 3D turbid media as vegetation or fluid (air pollution, low altitude cloud cover, *etc.*).
- Importation or creation of Digital Elevation Models (DEM). DEMs can be created as a raster re-sampled to the DART spatial resolution or imported either from external raster image file or as a triangulated irregular network (TIN) object.
- Automatic initiation of a sequence of Q simulations with the Sequence module. Any parameter (LAI, spectral band, date, *etc.*) A_1, …, A_M can take N_1, …, N_M values, respectively, with any variable grouping ($Q \leq \prod_{i=1}^{M} N_i$). Outcomes are stored in a Look-Up Table (LUT) database for further display and analysis. It is worth noting that a single ray tracking simulation with N bands is much faster than the corresponding N mono-band simulations (e.g., 50 times faster if $N > 10^3$).
- The simulated 3D radiative budget can be extracted and displayed over any modeled 3D object and also as images of vertical and horizontal layers of a given 3D scene.
- The transformation from facets to turbid medium objects converts 3D plant objects (trees) composed of many facets ($> 10^6$) into a turbid vegetation medium that keeps the original 3D foliage density and LAD distribution. This method remediates constraints limiting RT simulations

with many vegetation objects (e.g., forest) that lead to too large computational times and computer memory requirements.

- The creation of 3D objects by using volumes with pre-defined shapes that can be filled with various 3D objects (triangles, discs, *etc.*). This functionality allows a quick test of simple hypotheses, as for instance the influence of vegetation leaf shape and size in turbid media simulations.
- The transformation of LIDAR multi-pulse outputs into industrial Sorted Pulse Data (SPD) format [55]. Implementation of the SPDlib software allows users to create, display, and analyze their own LIDAR point clouds [56].
- Display tools for visualization and quick analysis of spectral images and LIDAR waveform and photon counting outputs, *etc.*

While the basic DART modules are programmed in C++ language (~400,000 lines of code), most external tools are written in Python language. In addition, a Graphic User Interface (GUI), programmed in Java language, allows users to manage model inputs (RT approach, scene geometry, view direction, *etc.*), to specify required output products (BRF, radiative budget, *etc.*), display results, and run the external scripts. A strong feature of DART is acceleration of RT modeling using multithreaded computation, allowing use of a specified number of processor cores simultaneously, which results in a near linear scaling of the processing time.

3. Ray Tracking Approach for Modeling Spectroradiometer Acquisitions

Ray tracking in heterogeneous 3D landscapes [20] and atmosphere [50] is based on exact kernel and discrete ordinate methods with an iterative and convergent approach. Radiation intercepted by scene elements at iteration i is scattered during the following iteration $i + 1$. The iterative process stops when the relative difference in scene exitance between two consecutive iterations is less than a specified threshold. In addition, any ray is discontinued if its angular power ($W \cdot sr^{-1}$) is smaller than the scene mean angular power that is scattered at first iteration, multiplied by a user specified coefficient.

The ray tracking approach has three simulation modes: reflectance (R), temperature (T), and combined (R + T). The R mode allows simulating the shortwave optical domain using the sun as the primary source of radiation and the atmosphere as the secondary source. Landscape and atmosphere thermal emissions are neglected. The opposite is true in the (T) mode, where the solar radiation is neglected. Finally, all radiation sources are combined in (R + T) mode, which is particularly useful for simulating RS signals in the spectral domain of 3–4 µm. Dependence of thermal emission on temperature and wavelength is modeled with Planck's law, while the Boltzmann's law can be used when simulating radiation budget over the whole electromagnetic spectrum.

The finite DART simulation can be conducted over three landscape arrangements: an infinite repetitive landscape with repetitive topography, an infinite repetitive landscape with continuous topography, and a spatially isolated scene, each of them managing exiting rays differently. A ray {A - A_1} that exits the flat infinite repetitive scene at point A_1 re-enters the scene through the symmetric point B_1 along the same direction (Figure 4). The path ray {A - A_1 - B_1 - A_2 - B_2 - …- C} is, therefore, equivalent to the path {A - C'}. In a similar fashion, a ray {A - A_1} that exits the infinite repetitive scene with continuous topography at point A_1 re-enters the scene under the same direction through the point B_1, which is vertically shifted by the distance equal to the ground altitude offset between the exit and re-entry

sides of the scene. In case of an isolated scene, a ray that exits the scene is dismissed; *i.e.*, it does not re-enter the scene.

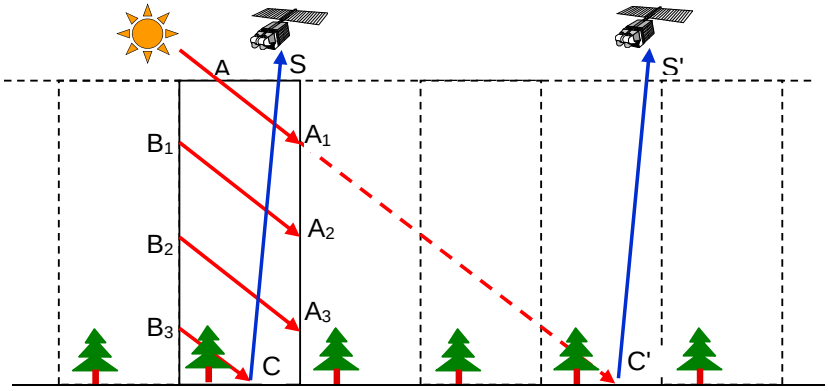

Figure 4. Simulation of a flat infinite repetitive landscape.

The Earth-atmosphere RT is simulated in five consecutive stages (Figure 5) [50]:

- Stage 1 is tracking the sun radiation and the atmosphere thermal emission through the atmosphere. It calculates radiance transfer functions per cell and per discrete direction from the mid/high atmosphere interlayer to the sensor, TOA and BOA levels. This stage gives the downward BOA radiance $L_{BOA}(\Omega^{\downarrow})$, upward TOA radiance $L_{TOA}(\Omega^{\uparrow})$ and also upward $L_{sensor}(\Omega^{\uparrow})$ and downward $L_{sensor}(\Omega^{\downarrow})$ radiance at sensor altitude.
- Stage 2 is tracking within the landscape the downward BOA radiance $L_{BOA}(\Omega^{\downarrow})$, originating from the stage 1, and the landscape thermal emission. This stage provides the landscape radiation budget, albedo, and upward BOA radiance $L_{BOA}(\Omega^{\uparrow})$, before the Earth-atmosphere radiative coupling.
- Stage 3 is tracking the BOA upward radiance $L_{BOA}(\Omega^{\uparrow})$, obtained during stage 2, through the atmosphere back to the landscape. Radiance transfer functions of stage 3 provide the downward BOA radiance $L_{BOA}(\Omega^{\downarrow})$, which is extrapolated in order to consider the multiple successive Earth-atmosphere interactions.
- Stage 4 is tracking downward BOA radiance $L_{BOA}(\Omega^{\downarrow})$, resulting from stage 3, within the landscape. It uses a single iteration with an extrapolation for considering all scattering orders within the Earth scene. This stage results in landscape radiation budget and upward BOA radiance $L_{BOA}(\Omega^{\uparrow})$.
- Stage 5 applies the stage 3 radiance transfer functions to the upward BOA radiance of stage 4. The resulting radiance is added to the atmosphere radiance, which is calculated within the first stage, to produce the radiance at sensor ($L_{sensor}(\Omega^{\uparrow})$) and TOA ($L_{TOA}(\Omega^{\uparrow})$) levels.

The entire RT procedure results in the following two types of products:

(1) Images at three altitude levels: BOA, TOA and anywhere between BOA and TOA. They can be camera and/or scanner images with projective and/or orthographic projection, as well as ortho-projected images that allow superimposing the landscape map and images simulated for various viewing directions.

(2) 3D radiative budget: distribution of radiation that is intercepted, absorbed, scattered and thermally emitted. It is useful for studying the energy budget and functioning of natural and urban surfaces.

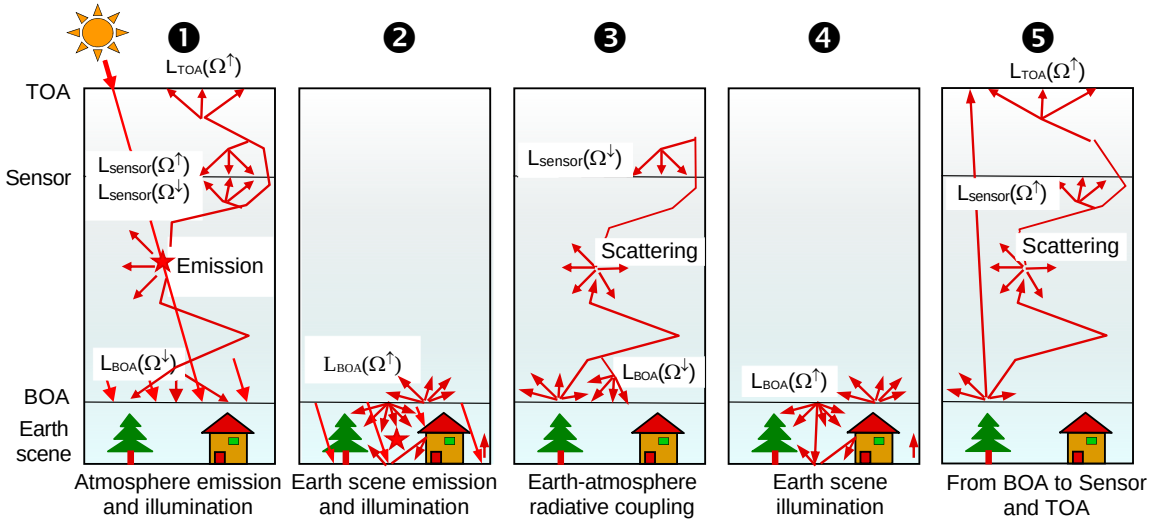

Figure 5. Five stages of the DART algorithm that models RT of the Earth-atmosphere system.

Finally, scattering and emission of a DART cell corresponds to surface and volume interactions. It is modeled using a sub-division of each cell into D^3 sub-cells, resulting in six D^2 cell sub-faces. This approach improves greatly the spatial sampling, resulting in shorter computational time, and requires less computer memory than using cells with a dimension divided by D, which is very beneficial for simulating scenes with dense turbid cells and large scene elements.

3.1. Surface Interactions with Facets

A ray of light incident on a facet (Figure 6a) interacts with its front side but not with its rear side. Thus, depending on the type of object, any surface can be simulated using only top facets or using top and bottom facets with opposite normal vectors, and optionally with different optical properties. Any facet is characterized by a direct transmittance T_{dir} along its normal direction Ω_n, a Lambertian transmittance T_{diff}, and a reflectance R with $T_{diff} + R \leq 1$. R can be isotropic (Lambertian) or anisotropic. Direct transmittance along Ω_s is equal to $[T_{dir}]^{1/|\Omega_s.\Omega_n|}$. For an incident irradiance E along Ω_n, scattered exitance is equal to $E \cdot (1 - T_{dir}) \cdot R$ and transmitted diffuse exitance is equal to $E \cdot (1 - T_{dir}) \cdot T_{diff}$ .Surface reflectance anisotropy can be described by parametric functions (e.g., Hapke [15], RPV [6]), with a specular component, defined by a surface refraction index, an angular width and a multiplicative factor.

The point M_{int} that represents light interception by a facet is modeled as a centroid of all interceptions on that facet. It is calculated per DART constructed sub-cell, among the D^3 sub-cells, which is improving spatial sampling, particularly if facets have large dimensions compared to cell dimensions. Storing the intercepted radiation for every direction is computationally expensive, especially for large landscapes with many cells. Thus, a simplifying mechanism storing intercepted radiation per ray incident angular sector $\Omega_{sect,k}$, where $\Omega_{sect,k}$ is a set of neighboring discrete directions that sample the 4π space of directions ($\Sigma_k \cdot \Omega_{sect,k} = 4\pi$), was adopted [57,58]. Scattering at an iteration *i* is then computed from energy

locally intercepted within incident angular sectors $\Omega_{sect,k}$ at iteration $i - 1$. Although, one can define as many angular sectors as discrete directions, ten sectors are sufficient to obtain very accurate results, with relative errors smaller than 10^{-3} [30]. Facets belonging to the same cell can intercept rays scattered and emitted by other facets. Rays exiting the cell through the same cell sub-face are grouped per discrete direction (Figure 6b), reducing the number of rays to track and consequently decreasing total computational time.

Facet thermal emission is simulated according to Planck's or Boltzmann's law, using the corresponding facet temperature and optical properties [59].

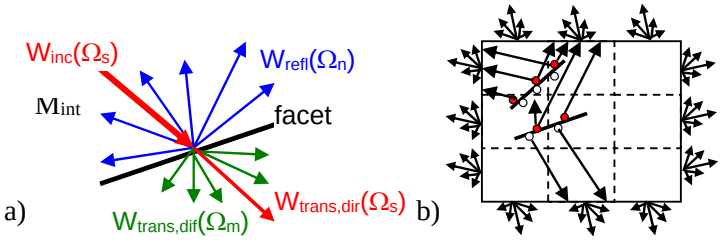

Figure 6. Facet scattering. (**a**) Single facet with an incident flux $W_{inc}(\Omega_s)$. It produces reflection $W_{refl}(\Omega_n)$ and direct $W_{trans,dir}(\Omega_s)$ and diffuse $W_{trans,dif}(\Omega_m)$ transmission. (**b**) Interaction of two facets in cell with 27 sub-cells (only nine are illustrated in 2D figure). Each facet has a single scattering point per sub-cell, with an intercepted radiation per incident angular sector.

3.2. Volume Interactions within Turbid Vegetation and Fluid Cells

When a ray crosses a turbid cell, two interception points M_{int} are computed along its path within the cell (Figure 7a). The first point is computed for upward scattering and the second one for downward scattering. As several rays cross each cell, possibly through the same sub-face, two simplifying steps are adopted. First, M_{int} is calculated per incident cell sub-face *s*, through which the rays entered the cell, in order to improve spatial sampling, particularly in presence of scenes with large cells. Second, similarly to facet interactions, the intercepted radiation is calculated per incident angular sector $\Omega_{sect,k}$. The first order scattering is computed at each iteration using the intercepted radiation that corresponds to the incident ray that entered the cell through one or several sub-faces. Thus, intercepted vector sources $W_{int}(s, \Omega_{sect,k})$ are stored per sub-face *s* and per incident angular sector $\Omega_{sect,k}$. Then, we have: $W_{int}(s, \Omega_{sect,k}) = \Sigma\Omega_s \cdot W_{int}(s, \Omega_s)$, with $\Omega_s \subset \Omega_{sect,k}$. The first order scattering of the direct solar flux can be computed exactly, because the sun direction is considered as a sector. Within cell multiple scattering (Figure 7b) is analytically modeled [20]. Similarly to the case of facets, rays exiting the same cell sub-face in the same direction are grouped together in order to reduce computational time (Figure 7c).

Cell thermal emission is simulated with Planck's or Boltzmann's law and a temperature-independent factor that depends on the cell optical properties and directional extinction coefficient. In order to reduce the RT computation time, this factor is pre-computed as a volume integral in a specified spatial sampling, per cell sub-face, discrete direction and type of turbid medium [59].

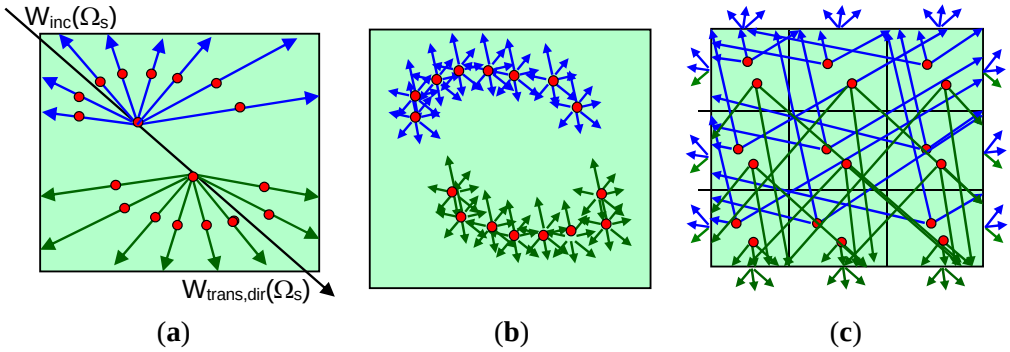

Figure 7. Turbid cell volume scattering: (**a**) two 1st order interception points per incident ray with associated first order scattered rays, and their second order interception points (red), (**b**) analytically computed within-cell second order scattering, and (**c**) first order interception points, which are grouped per incident angular sector and per cell sub-face crossed by the incident rays. Rays exiting the cell are grouped per exiting cell sub-face and per discrete direction.

The spatial resolution of DART images is equal to the cell size ($\Delta x, \Delta y$) divided by a user-defined factor η that sets a spatial oversampling. It is applied during the image creation procedure when upward fluxes are stored into an image array with ($\Delta x/\eta$, $\Delta y/\eta$) pixel sizes. These images can be re-sampled to the pixel-size of any RS sensor by a DART module or by any digital image processing software. Their radiometric accuracy is usually better than if being simulated with a cell size equal to the sensor pixel size. Figure 8 shows DART nadir and oblique images of the citrus orchard site simulated within the RAMI IV experiment [38]. The tree crowns were simulated as a juxtaposition of turbid cells that were transformed into turbid medium from original facet based trees. Cell size of 20 cm was small enough to keep a very good description of 3D tree crown architecture. Its combination with $\eta = 2$, allows observation of shadows casted by tree trunks and branches. The simulation with facet-based trees gave very similar reflectance values, however they needed longer computation times [58]. DART can also simulate images of urban scenes. As an example, an example of St. Sernin Basilica (Toulouse, France), with urban elements and trees modeled as combination of facets and turbid medium, is shown in Section 5.

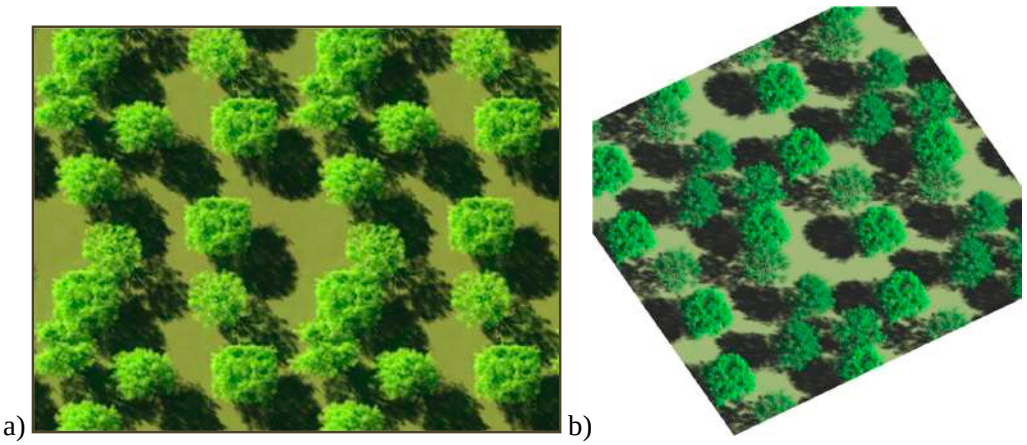

Figure 8. DART simulated RGB composite of satellite image in natural colors for a virtual tree formation displayed in: (**a**) nadir, and (**b**) oblique view.

The possibility to simulate time series of images acquired by a geostationary satellite was recently introduced into DART in the frame of a Centre National d'Etudes Spatiales (CNES, France) project preparing a future high spatial resolution geostationary satellite. The aim was to design a tool that calculates the time interval, for any date and for any region on the Earth, during which the useful radiance $L_{u,TOA}$ that originates from the Earth surface is reliable, while considering the expected sensor relative accuracy (~3%), sensor signal-to-noise ratio, atmosphere, local topography, *etc.* $L_{u,TOA}$ is the difference between TOA radiance and radiance L_{atm} due to the atmosphere only. Four typical African landscapes (grass savannah, tree savannah, tropical forest, desert), with varying parameters such as spatial resolution, signal-to-noise ratio and elevation were considered. Simulations used local atmosphere conditions from the AERONET network and ECMWF database. Three specific DART features were used: (i) RT modeling through a spherical atmosphere, (ii) automatic computation of satellite view direction for each Earth coordinates, and (iii) automatic calculation of sun direction for any date, satellite and scene coordinates, *etc.* Figure 9 illustrates the capacity of DART to simulate geostationary satellite radiance images above Africa at Latitude 0° N, Longitude 17° E and altitude of 36,000 km. In this example, the Earth surface was simulated as Lambertian, with a bare ground reflectance "brown to dark gravelly loam" obtained from the USDA Soil Conservation spectra library. At 443 nm, L_{atm} variability is large, especially for regions at sunset and sunrise. This demonstrates that the accuracy of $L_{u,TOA}$ depends on the location, season and atmosphere conditions, with sunrise and sunset being the worst conditions. A typical task during the preparation stage of a future satellite mission is to assess the optimal spatial resolution for studying a given type of landscape. This problem was investigated with the assumption that radiance spatial variability, as represented by radiance standard deviation, is the textural information of interest. Figure 10 shows the hourly variation of the standard deviation of $L_{u,toa}$ at 665 nm for the desert sandy landscape (barchans dune), with spatial resolution ranging from 1 m up to 100 m, for 21 June 2012. As expected, the spatial variability of $L_{u,TOA}$ decreases as image spatial resolution coarsens, which allows selection of the optimal spatial resolution.

a)

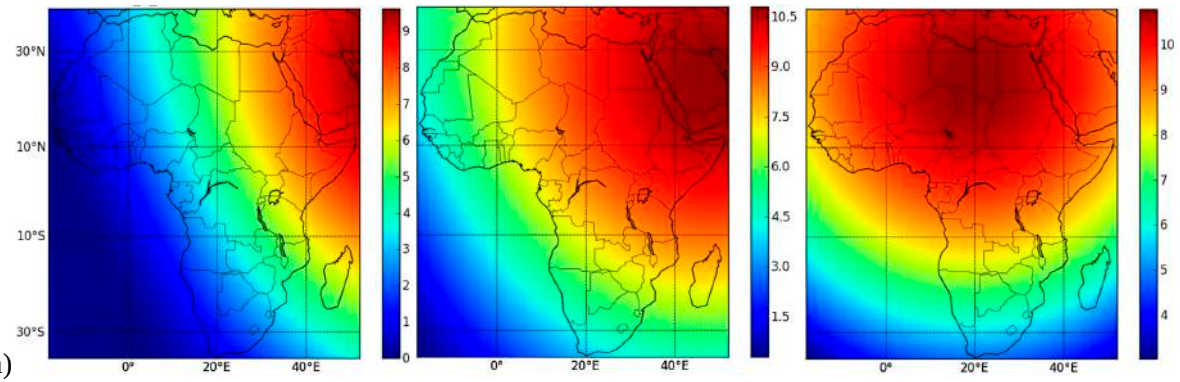

Figure 9. *Cont.*

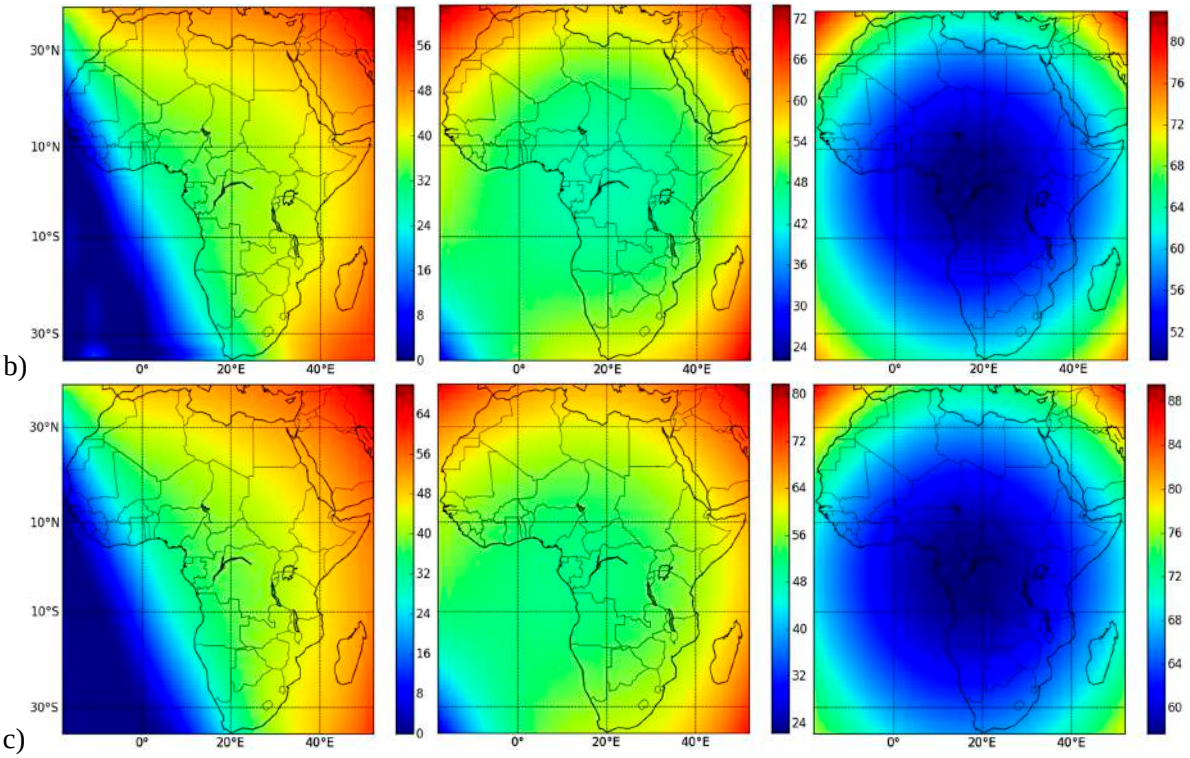

Figure 9. DART simulated BOA (**a**), atmosphere (**b**) and TOA (**c**) radiance (W/m^2/sr/µm) at 443 nm, for 6 h 44 m (**left**), 8 h 44 m (**middle**) and 10 h 44 m (**right**) UTC as measured by a geostationary satellite at Latitude 0° N, Longitude 17° E and 36,000 km altitude on 21 June 2012.

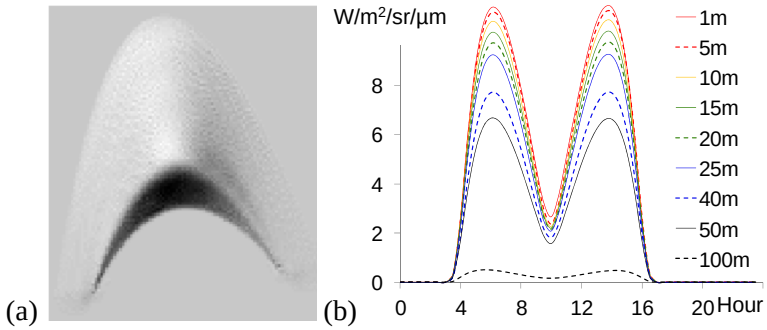

Figure 10. Spatial variability of the useful radiance $L_{u,TOA}$ of a sandy desert dune (25.5º N, 30.4º E, altitude of 78 m), acquired by a future geostationary satellite (0º N, 17º E, altitude of 36,000 km) at 665 nm on 21 June 2012. (**a**) DART simulated radiance image of a barchan dune at solar noon. (**b**) Hourly standard deviation of $L_{u,TOA}$ for spatial resolution from 1 m up to 100 m. Sand reflectance was obtained from the ASTER spectral library.

4. Modeling LIDAR Signal with Ray-Carlo and Box Methods

New features related to LIDAR simulations, such as the simulation of airborne LIDAR full-waveform products of single and multiple pulses, as well as LIDAR photon counting and terrestrial LIDAR observations, were recently introduced in DART [53,54]. Figure 11 shows the typical geometry configuration of an airborne laser scanner (ALS). The sensor is defined by a circular footprint with a radius $R_{footprint}$ defined by the LIDAR illumination solid angle $\Delta\Omega_{footprint}(\alpha_{footprint})$, the ALS altitude H_{LIDAR} and the footprint area $S_{footprint} = \pi \cdot R^2_{footprint}$. In case of an oblique central illumination direction with a zenith angle θ_L, the 1st order illuminated surface has an elliptical shape with a major axis $\frac{R_{footprint}}{\cos^2 \theta_L}$, a minor axis $\frac{R_{footprint}}{\cos \theta_L}$, and an area $S_{illumin} = \frac{S_{footprint}}{\cos^3 \theta_L}$. Photons launched within $\Delta\Omega_{footprint}$ can have any angular distribution (e.g., Gaussian) and pulse characteristics. A photon scattered in the atmosphere at (x,y,z) can illuminate $S_{illumin}$ within the solid angle $\Delta\Omega$ (x,y,z). The LIDAR field of view (FOV) is defined either directly as S_{FOV} or by the angle α_{FOV}. The viewed surface covers the area $S_{view} = \frac{S_{FOV}}{\cos^3 \theta_L}$. In Figure 11, the ground surface is assumed to be horizontal. However, in presence of terrain topography, the ground altitude is the minimum altitude of provided topography. A photon, which is scattered in atmosphere or landscape at the (x,y,z) position, can irradiate the LIDAR sensor in directions within the solid angle $\Delta\omega$ (x,y,z), defined by the sensor aperture area A_{LIDAR}.

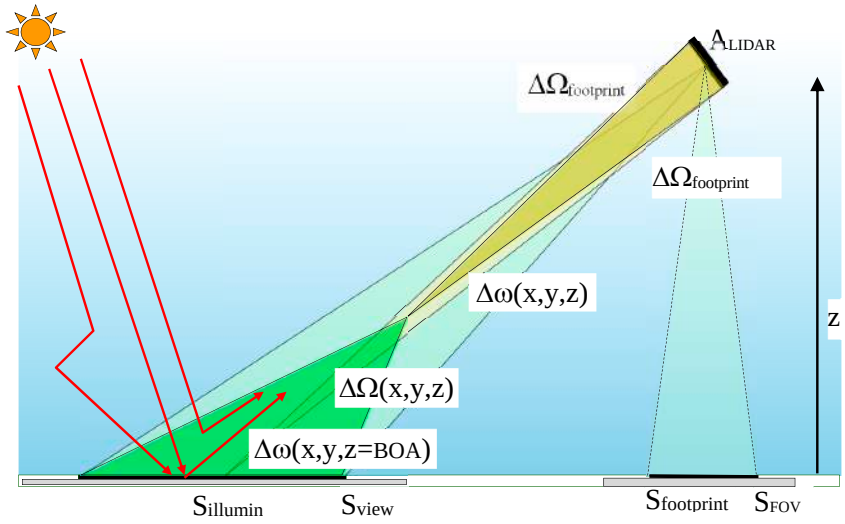

Figure 11. The LIDAR geometry configuration, with horizontal ground surface.

The Monte Carlo (MC) photon tracing method is frequently used for simulating LIDAR signals [60,61]. It simulates multiple scattering of each photon as a succession of exactly simulated single scattering events, and produces very accurate results. MC can determine if and where photon interception takes place and if an intercepted photon is absorbed or scattered. However, a tiny FOV of LIDAR $\Delta\Omega_{FOV}$ with an even tinier solid angle $\Delta\omega$ (x,y,z), within which the sensor is viewed by scattering events both imply that the probability for a photon to enter the sensor is extremely small. This case, therefore, requires a launch of a tremendous number of photons, which is usually computationally unmanageable. Introduction of anisotropic phase functions into scene elements further increases this number.

Consequently, most of the LIDAR simulating RT models use a reverse approach, *i.e.*, they are tracing photons from the sensor instead of from their source [61]. DART, however, uses a different approach for forward simulations of LIDAR signal. Each photon launched from the LIDAR transmission source is tracked within the Earth-atmosphere scene until it is absorbed, measured by sensor or rejected out of the scene. Two modeling methods were devised in order to reduce the computational time constraint: the Ray-Carlo and the Box methods.

4.1. Ray-Carlo: Photon Tracing Method

Any DART volume and/or surface element is characterized by its scattering phase function $P(\Omega_n \rightarrow \Omega_m)$. For each photon intercepted by a scene element at (x,y,z) location, the classical MC random pulling uses the element's single scattering albedo to determine if the photon is scattered, and subsequently what is the discrete direction Ω_m, $\Delta\Omega_m$) of the scattered photon. For each scattering event, a particle, called photon for simplicity reasons, is sent to a randomly selected discrete direction (Ω_m, $\Delta\Omega_m$) with a weight proportional to the solid angle $\Delta\Omega_m$ and the phase function $P(\Omega_n \rightarrow \Omega_m)$, and another particle is sent directly towards the LIDAR sensor along the direction ω (x,y,z) with a weight proportional to the solid angle Δω (x,y,z) and the phase function $P(\Omega_n \rightarrow \omega$ (x,y,z)). The photon along the direction (Ω_m, $\Delta\Omega_m$) will contribute to multiple scattering events, conversely to the photon that is sent to the sensor. The latter one has an energy that is negligible compared to the photon scattered along (Ω_m, $\Delta\Omega_m$), mostly because Δω (x,y,z) << $\Delta\Omega_m$. The photon along Δω (x,y,z) is tracked towards the sensor with an energy (weight) that may decrease, or even become null, as being attenuated by existing landscape and/or atmosphere elements. The energy and the travelled distance are recorded when the photon reaches the sensor. The accumulation of these photons builds up the waveform output, which is used to produce the photon-counting signal via a statistical approach. In practice, scattering of photons sent to the LIDAR is neglected in our modeling approach, because their energy is negligibly small.

Figure 12 illustrates graphically the DART Ray-Carlo method. A photon of weight w_{in}, propagated along the direction Ω_{in}, is intercepted in position (x_1,y_1,z_1). If the MC random pulling provides a positive scattering decision, the photon (weight $w_{DART,1}$) is scattered along the DART discrete direction (Ω_{n1}, $\Delta\Omega_{n1}$) and the position (x_1,y_1,z_1) is verified if the direction towards LIDAR (ω_1) is within $\Delta\Omega_{FOV}$. In case of positive answer, the photon (weight $w_{LIDAR,1}$) is sent towards the LIDAR sensor along the direction ω_1 within the solid angle Δω (x_1,y_1,z_1). The following two equations must be satisfied during this process:

$$w_{in} = w_{LIDAR,1} + w_{DART,1} \quad (1)$$

And

$$\frac{w_{LIDAR,1}}{w_{DART,1}} = \frac{\int_{\Delta\omega(x_1,y_1,z_1)} P(\Omega_{in} \rightarrow \Omega)\, d\Omega}{\int_{\Delta\Omega_{n1}} P(\Omega_{in} \rightarrow \Omega)\, d\Omega} \quad (2)$$

For any scattering order i, the direction {ω_i, Δω (x_i,y_i,z_i)} is calculated and the condition within $\Delta\Omega_{FOV}$ is checked. It must be noted that ω_i is a flexible direction, independent of the discrete directions. Millions of flexible directions can be simulated, each per a scattering event. For this reason, the phase functions $P(\Omega_n \rightarrow \omega)$ of flexible directions cannot be pre-computed as in the case of discrete directions. Thus, $P(\Omega_n \rightarrow \omega_i)$ is assumed to be equal to $P(\Omega_n \rightarrow \Omega_{mi})$, where ω_i lies within the solid angle $\Delta\Omega_{mi}$ of a pre-defined

discrete direction. It implies that $\frac{w_{LIDAR,1}}{w_{DART,1}} = \frac{\Delta\omega_i(x_1,y_1,z_1)}{\Delta\Omega_{mi}} \approx \frac{A_{LIDAR}}{r^2 \cdot \Delta\Omega_{mi}}$, where r is the distance from a scene element to the LIDAR sensor. The photon weight $w_{LIDAR,i}$ is, consequently, very small. The GLAS satellite LIDAR [62], with $A_{LIDAR} \approx 0.8\ m^2$ and $r = 6\times10^5$ m, has $w_{LIDAR,i}$ of around 10^{-13}. To be able to simulate the acquisition of a single photon with this particular sensor, the use of actual photons without weights would require about 10^{13} scattering events.

Since cells in DART simulated atmosphere are usually bigger than those used for simulating the landscape, a single interception event inside an atmospheric cell that gives rise to a scattering leads to a large uncertainty on the scattering event location defined by the MC random pulling. In order to reduce the associated MC noise without increasing the number of launched photons, K interception events are simulated per interception event along the photon travelling path towards LIDAR FOV. Thus, K photons are sent to the LIDAR, which partially fills the gap of distance recorded based on the random MC pulling with a single scattering event per interception. This approach mimics more closely real behavior of an actual flux of photons, which is continuously intercepted along its path.

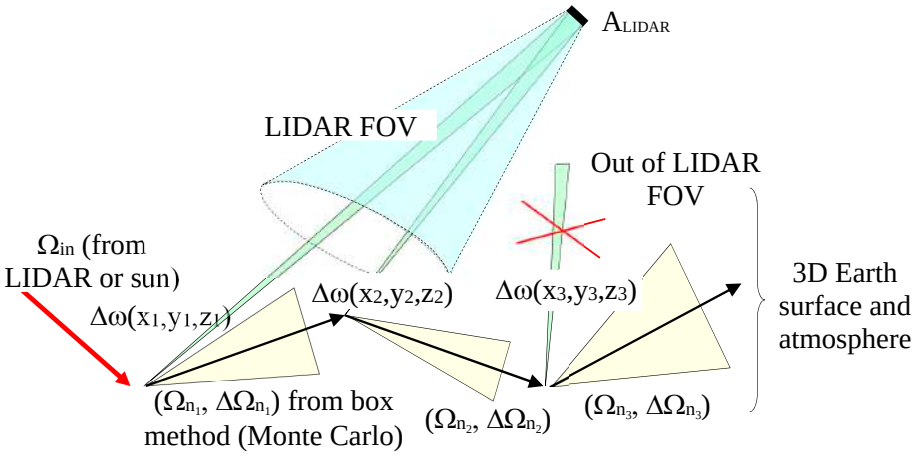

Figure 12. The Ray-Carlo approach for LIDAR simulation, depicted with all several scattering orders.

RT models usually consider the atmosphere as a superimposition of atmospheric layers, each of them being characterized by specific gas and aerosol optical depths. Each layer is defined by constant gas and aerosol extinction coefficients, resulting in a discontinuity of the extinction coefficients at each layer interface. Unlike in case of passive radiometer images, this characterization of the atmosphere leads to inaccurate simulations of LIDAR signals, producing waveforms with discontinuities at the top and bottom of each atmosphere layer. This problem is solved in DART by simulating the atmosphere with vertically continuous gas and aerosol extinction coefficients.

4.2. Box Method: Selection of Photon Scattering Directions

Selection of the discrete direction that corresponds to scattering of a photon incident along a given discrete direction using MC approach is a complex task. Ideally, a function should relate any randomly selected number to a defined discrete direction, and needs to operate between two mathematical spaces: (1)

the positive real numbers within [0, 1] and (2) the N discrete directions, so that any number within [0, 1] corresponds to a unique direction. This means that a bijection map has to be built to link the set of N directions with the corresponding set of N intervals defining the [0, 1] interval.

The probability to select the direction j is defined as:

$$\mathcal{P}(j) = \frac{\int_{\Delta\Omega_i} P(\Omega_s,\Omega_j)d\Omega_j}{\sum_{k=1}^{N}\int_{\Delta\Omega_k} P(\Omega_s,\Omega_k).d\Omega_k} \quad (3)$$

with $\sum_{j=1}^{N} \mathcal{P}(j) = 1$.

A direct method to determine the direction j is to compare a randomly pulled number with each interval representing each direction. This requires performing a maximum of N comparisons per pulling, which is computationally expensive. This problem can be easily solved if the cumulative probability $\mathcal{P}_{cum}(n) = \sum_{j=1}^{N} .\mathcal{P}(j)$ is invertible. Then, random pulling $a \in [0, 1]$ gives directly the direction index $n = \mathcal{P}^{-1}(a)$, which indicates the selected direction. However, $\mathcal{P}_{cum}(n)$ is, in most cases, not invertible. Several inversion methods (e.g., bisection) were tested, but all of them led to large errors, at least for some directions. Therefore, we developed a Box method that can select the scattering direction rapidly with only two random numbers and without any computation of inverse function.

The Box method keeps in memory an array of boxes, where each box represents a tiny interval of $\mathcal{P}_{cum}(n)$ that corresponds to a given direction index (*i.e.*, scattering direction). Subsequently, reading of an array $\mathcal{B}$ with a randomly selected number within [0, 1] provides directly a direction index without any need for further computation. The total number of boxes in $\mathcal{B}$ is ruled by the user-defined size of computer memory used for its storage. A larger memory size implies that more boxes with smaller probability intervals per box can be stored, giving a better accuracy at each random pulling. The number of lines of $\mathcal{B}$ is equal to the N number of incident discrete directions Ω_i and the computer memory is distributed to store the boxes per line of $\mathcal{B}$. A various number of boxes per possible scattering direction $\Omega_{j,i}$ is assigned to a single line i of $\mathcal{B}$, which is proportional to the probability of occurrence $p_{j,i} = \mathcal{P}(j|i)$ of scattering towards the direction j for an incident direction i. The value of each box associated to a given scattering direction $\Omega_{j,i}$ is the index j of that direction. For each line i of $\mathcal{B}$, the least probable scattering direction with probability $p_{1,i}$ is represented by $m_{1,i}$ boxes, which defines the number $M_{j,i}$ of boxes per scattering direction $\Omega_{j,i}$, with total number of boxes $M_i = \sum_{j=1}^{N} M_{j,i}$. Consequently, a random number $m \in [0, M_i]$ defines the scattering direction index. This approach may require quite a large amount of computer memory if the scattering directions have a wide range of occurrence probabilities. For instance, if 10 boxes are used for a scattering direction with a probability of 5×10^{-7}, then 4×10^{6} boxes are needed for a scattering direction with a probability of 0.2.

The requirement of large computer memory and computation time is solved as follows. Scattering directions $\Omega_{j,i}$ are sorted per incident direction Ω_i according to their occurrence probability. Then, sorted adjacent directions are grouped into classes in such a way that the ratio between maximum and minimum probability over all scattering directions $\Omega_{j,i}$ within the same class is smaller than a given threshold γ. Probability P_i^k of a class k is the sum of occurrence probabilities $P_{j,i}^k$ of all scattering directions $\Omega_{j,i}^k$, in class k, *i.e.*, $P_i^k = \sum_j P_{j,i}^k$. Each class k is represented by a number of boxes that depends directly on its probability of occurrence P_i^k for any incident direction Ω_i, and a given number of boxes that is assigned to the class with the lower probability. Since two probability arrays are being used, two successive random pulling values are needed for any scattering event with incident direction Ω_i. The first pulling

derives the class index k from $\{P_i^k\}$, while the second one derives the direction index j from $\{P_{j,i}^k\}$. Finally, the value of γ is optimized such a way that probability arrays $\{P_i^k\}$ and $\{P_{j,i}^k\}$ require a computer memory smaller than the user specified value. Indeed, if γ is increased, the size of $\{P_i^k\}$ decreases with the number of classes, whereas the size of $\{P_{j,i}^k\}$ increases with the number of directions per class.

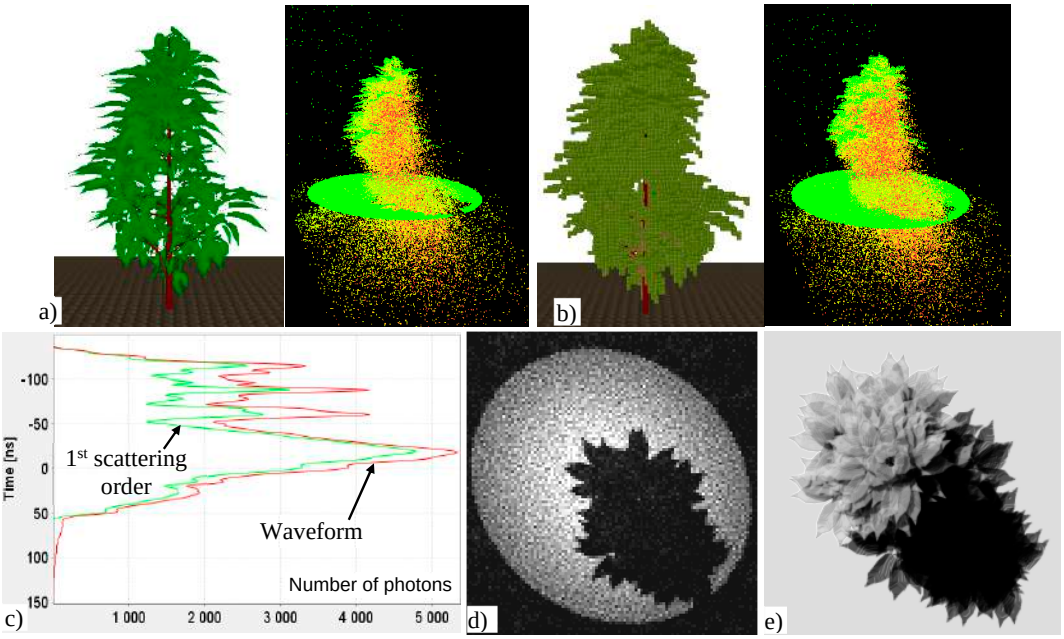

Figure 13. A virtual tree built out of geometrical facets (**a**) and the same turbid-cell tree derived by the facet-to-turbid conversion tool (**b**) with their 3D LIDAR point clouds for an oblique view (θ = 30°, ϕ= 135°) and the 1D waveform with its first scattering order contribution (**c**). The image of photons that reached the ground is showing the last LIDAR echo (**d**) and DART ray tracking provides a high spatial resolution (10 cm) nadir image at λ = 1064 nm.

DART simulations of LIDAR point clouds can be conducted using Ray-Carlo and Box methods for landscapes created with geometrical primitives (facets) and voxels filled with turbid medium. An example of airborne LIDAR sensor viewing a facet based tree created by the AMAP Research Centre under an oblique direction (θ = 30°) at wavelength λ= 1064 nm is presented in Figure 13. High similarity of the two 3D points clouds (*i.e.*, LIDAR echoes) for the two representations, *i.e.*, tree built from facets and transformed into voxels with turbid medium (Figure 13a,b) proves the correct functionality of this timesaving "facet to turbid medium" conversion. 1D waveforms (Figure 13c) display distances measured as time differences between transmission and reception of LIDAR photons. The waveform curve corresponding to multiple scattering orders is significantly larger than the first scattering order curve, which demonstrates high importance of multiple scattering at λ = 1064 nm. It also shows a strong contribution of the ground surface to the simulated signal. Figure 13d shows 2D distribution of photons that reached the ground (*i.e.*, the last echo). As expected, the number of photons tends to be smaller under the tree, relative to the rest of the LIDAR footprint. Finally, Figure 13e presents image of the simulated facet tree as captured by a nadir imaging spectroradiometer at λ = 1064 nm. The 10 cm spatial resolution provides enough details to detect single leaves. It must be mentioned that in addition to mono-pulse LIDAR, DART can also simulate

multi-pulse LIDAR acquisitions for any spectral wavelengths, using a multi-threading algorithm. Such a simulation of the St. Sernin Basilica (Toulouse, France) is shown in Section 5.

Two other LIDAR techniques were implemented in DART, in addition to the airborne/satellite laser scanning: (i) terrestrial LIDAR (TLIDAR), and (ii) photon counting LIDAR. TLIDAR, such as ILRIS-LR can map objects on the ground, resulting in accuracy within millimeters or centimeters. It is increasingly used to assess tree architecture and to extract metrics of forest canopies [63]. TLIDAR simulation within DART is aiming at better understanding of actual data. The photon counting LIDAR is more efficient than conventional LIDAR because it requires only a single detected photon to perform a range measurement. That is why the next ICESat-2 mission [64] will carry a photon counting instrument called the Advanced Topographic Laser Altimeter System (ATLAS). DART simulates photon counting data using the statistical information derived from one or several simulated waveforms. Figure 14 shows an example using a simple bare ground with a vegetation plot and signal of a photon counting LIDAR acquired at λ = 1064 nm along a horizontal sensor path, perpendicular to the vegetation plot. Because, the sun direction was set as oblique (θ_s = 45°), part of the bare ground is in the shade of the vegetation cover. Figure 14b shows the radiance image demonstrating the sun illumination, which is used to compute the solar noise of LIDAR signals. Figure 14c illustrates the photon counting simulation along the sensor path (horizontal axis) and Figure 14d is a subset enlargement of Figure 14c. The continuous point cloud above and below the bare ground level corresponds to the solar noise caused by the sun radiation reflected from the bare ground and the vegetation plot. Solar noise is reaching its maxima at the location of the vegetation plot, because vegetation is more reflective than bare ground at 1064 nm. Similarly, solar noise tends to be minimal in the shaded part of the bare ground, where the sun irradiance is diffuse, and consequently minimal.

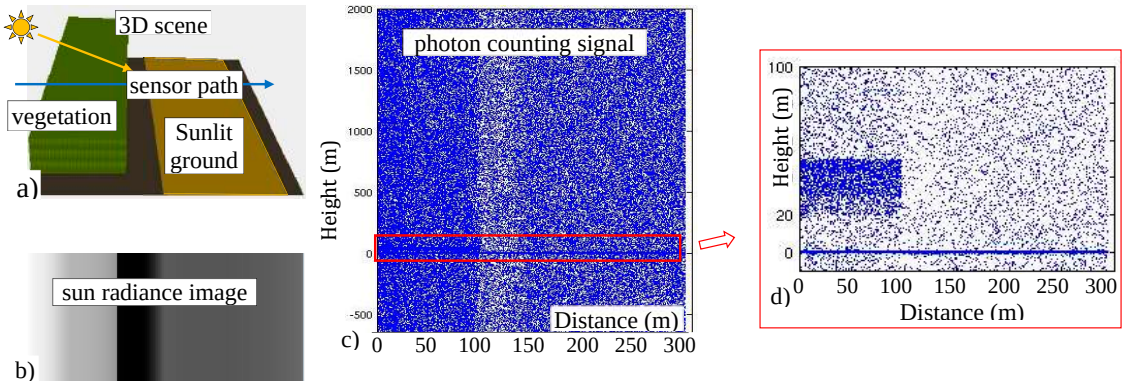

Figure 14. DART simulated photon counting LIDAR with solar noise. (**a**) Bare ground and vegetation plot with an oblique sun irradiation (θ_s = 45°) and a horizontal LIDAR sensor path. (**b**) Radiance image of the scene (*i.e.*, solar noise). (**c**) Simulated photon counting signal. (**d**) An enlarged subset of simulated scene (**c**).

5. Modeling IS Data with the Perspective Projection

RT simulations of BRF are usually based on the assumption that the whole landscape is observed along the same viewing direction. This assumption is acceptable when a relatively small landscape is observed from an altitude ensuring that the divergence of the FOV over the landscape can be neglected.

However, this disqualifies direct comparison of RT modeled images with actual observations that do not meet this assumption. DART was, therefore, improved to properly consider landscape dimensions together with sensor altitude and consequent sensor FOV [65]. This new functionality provides DART images simulated at large scales with realistic geometries, which allows their per-pixel comparability with actual RS acquisitions. Two types of sensor geometries are available: a pinhole camera and an imaging scanner. Pinhole camera acquisitions are modeled with the perspective projection, where the ray convergence point is unique, whereas imaging scanner acquisitions are modeled with the parallel-perspective projection, where the ray convergent point changes with the platform movement.

The perspective projection is modeled for each sensor pixel (x_s,y_s) located within the sensor focal plane. The pixel value is driven by scattering and/or emission of a facet and/or turbid medium volume at location M(x,y,z) in the horizontal plane $\mathcal{P}_{Z_M}$. Its associated sensor pixel is viewed from M(x,y,z) along a flexible direction {ω(M), Δω (M)} under zenith angle θ_v, which depends on the location of the scattering point M(x,y,z) and the geometry of sensor pixel S(x_s,y_s,z_s). A scattering and/or emission event at M(x,y,z) gives rise to local fluxes $W_n(M)$ per discrete direction (Ω_n, $\Delta\Omega_n$) and to a flexible flux W(ω) that heads towards its associated sensor pixel along the direction {ω(M), Δω(M)}. In order to reduce computational time, the scattering phase function for any flexible direction {ω(M), Δω(M)} is similar to the scattering phase function corresponding with the scattering discrete direction {Ω_n, $\Delta\Omega_n$} that contains direction {ω(M), Δω(M)}. Thus, one can write that:

$$W(\Omega_s \rightarrow \omega) = W_n(\Omega_s \rightarrow \Omega_n).\frac{\Delta\omega(M)}{\Delta\Omega_n}, \quad (4)$$

with

$$\omega(M) \subset \{\Omega_n, \Delta\Omega_n\}.$$

The upward flux due to the facet scattering at M(x,y,z), which reaches the BOA plane, is computed as:

$$W^*(M) = T_{M\rightarrow BOA}(\omega) \times \frac{W_n(M)}{\Delta\Omega_n}.\frac{S_{sensor}\cdot\overline{\Omega}_{sensor}\cdot\overline{\omega}(M)}{S_{scatterer}\cdot\overline{\Omega}_{scatterer}\cdot\overline{\omega}(M)} \times Min\{\frac{S_{scatterer}\cdot\overline{\Omega}_{scatterer}\cdot\overline{\omega}(M)}{r^2_{sensor,M}}, \Delta\Omega_{sensor}\} \quad (5)$$

with

$$r^2_{sensor,M} = (x_s - x)^2 + (y_s - y)^2 + (z_s - z)^2 = \left(\frac{z_s - z}{\cos\theta_v}\right)^2$$

where $\Delta\Omega_{sensor}$ is the sensor pixel FOV and $T_{M\rightarrow BOA}(\omega)$ is the path transmittance from the scatterer at location M up to the BOA level (top of the Earth scene).

The condition $Min\{\frac{S_{scatterer}\cdot\overline{\Omega}_{scatterer}\cdot\overline{\omega}(M)}{r^2_{sensor,M}}, \Delta\Omega_{sensor}\}$ ensures that the flux, which arrives to a sensor pixel, is not outside $\Delta\Omega_{sensor}$. If ω(M) is within $\Delta\Omega_{sensor}$, we have:

$$W^*(M) = T_{M\rightarrow BOA}(\omega).\frac{W_n(M)}{\Delta\Omega_n}.\frac{S_{sensor}.\overline{\Omega}_{sensor}.\overline{\omega}(M)}{r^2_{sensor,M}} \quad (6)$$

The term $1/r^2$ stresses that a scattered/emitted flux captured within the sensor pixel FOV decreases with the square of the distance from its scattering/emission point. Fluxes that leave an Earth scene are stored in the horizontal plane $\mathcal{P}_{Z_{min}}$ at the scene minimum altitude z_{min}. To achieve this, scattering facets and volumes are projected along direction ω(M) into $\mathcal{P}_{Z_{min}}$, with M' being the projection of M along ω(M) into $\mathcal{P}_{Z_{min}}$, and $S_{M,xy}$ and $S_{M',xy}$ being the areas of projections along ω(M) of the scattering element M into $\mathcal{P}_{Z_M}$ and $\mathcal{P}_{Z_{min}}$, respectively. Since the projection keeps the radiance constant, one can write:

$$\frac{W^*(M)\cdot r^2_{sensor,M}}{S_M\cdot\cos\theta_v\cdot S_{sensor}\cdot\overline{\Omega}_{sensor}\cdot\overline{\omega}(M)}=\frac{W^*(M')\cdot r^2_{sensor,M'}}{S_{M'}\cdot\cos\theta_v\cdot S_{sensor}\cdot\overline{\Omega}_{sensor}\cdot\overline{\omega}(M')} \quad (7)$$

It implies that: $W^*(M')=W^*(M)\times\frac{\Delta z^2_{sensor,M}\cdot S_{M',xy}}{\Delta z^2_{sensor,M'}\cdot S_{M,xy}}$, with $\Delta z_{sensor,M} = z_S - z_M$ and $\Delta z_{sensor,M'} = z_S - z_{M'}$.

Three sensor projections are considered in DART:

(1) Orthographic projection with parallel rays to the sensor plane: $S_{M',xy} = S_{M,xy}$, resulting in $W^*(M')=W^*(M)\times\frac{\Delta z^2_{sensor,M}}{\Delta z^2_{sensor,M'}}$.

(2) Perspective projection of a pin-hole camera: $S_{M',xy}=S_{M,xy}\times\frac{\Delta z^2_{sensor,M'}}{\Delta z^2_{sensor,M}}$, resulting in $W^*(M') = W^*(M)$.

(3) Combined projection of a scanner: orthographic projection for the axis parallel to the sensor path, and perspective for the other axis. Thus, $S_{M',xy}=S_{M,xy}\times\frac{\Delta z^2_{sensor,M'}}{\Delta z^2_{sensor,M}}$ resulting in $W^*(M')=W^*(M)\times\frac{\Delta z_{sensor,M}}{\Delta z_{sensor,M'}}$.

During the projection process, $W^*(M')$ and the associated projected surface S_M are spread over DART pixels (Δx, Δy) of $\mathcal{P}_{Z_{min}}$. The proportion $\gamma_{M'\to i,j}$ of $W^*(M')$ in pixel (Δx, Δy) is used to compute the total flux from (Δx, Δy) to the sensor pixel (i,j): $W^*_{i,j}=\sum_{M'}\gamma_{M'\to i,j}\times W^*(M')$, leading to pixel radiance $L^*_{i,j}=\frac{\sum_{M'}\gamma_{M'\to i,j}\cdot W^*(M')}{\Delta x\cdot\Delta y\cdot\cos\theta_{v,i,j}\cdot\Delta\omega_{i,j}}$, where $\{\omega_{i,j}(\theta_{v,i,j},\phi_{v,i,j}),\Delta\omega_{i,j}\}$ is the direction under which the sensor is viewed from (i, j). Finally, the sensor image is created by projecting the atmosphere-transmitted radiance onto the sensor plane. Sensor orientation (precession, nutation, and intrinsic angle) is taken into account during this procedure.

A DART modeled airborne camera image of the St. Sernin Basilica (Toulouse, France) is illustrated in Figure 15a. It differs geometrically from the satellite image simulated with an orthographic projection (Figure 15b). As one can see, two surfaces with the same area and orientation, but located at different places, are having, due to perspective projection, different dimensions in the airborne camera image, but equal dimensions in the orthographic projection of the satellite image. This explains why objects, as for instance the basilica tower and the tree next to it look much larger in the camera image.

The fact that pixels in a scanner image correspond to different view directions can strongly affect their radiometric values. This is illustrated by DART simulated scanner images of the Jarvselja birch stand (Estonia) in summer (Figure 16). Jarvselja stand is one of the RAMI IV experiment test sites [38]. It is a 103 m × 103 m × 31 m large forest plot, which was simulated as an image with three spectral bands at 442, 551 and 661 nm, with SKYL (fraction of diffuse-to-direct scene irradiance) equal to 0.21, 0.15 and 0.12, respectively. The scanner followed a horizontal path at three flying altitudes of 0.2 km, 2 km and 5 km. The solar zenith angle was 36.6° (in Figure 16, the solar direction goes from the bottom to the top of images), and the ground spatial resolution was equal to 0.5 m for all three acquisitions. For any altitude, the central view direction of the imaging scanner is the hotspot direction. In the hotspot configuration [66], the sun is exactly behind the sensor. As a result, no shadows occur in the sensor's FOV, providing maximal reflectance values (Figure 16a) represented as a bright horizontal line running parallel to the scanner path of motion (Figure 16b). The hotspot effect (BRF local maximum) is observed in a relatively small angular sector centered in the exact hotspot direction. As expected, the perception

of shadows increases rapidly for viewing directions located far from the hotspot direction. At altitude of 0.2 km, the range of the scanner viewing directions over the whole forest scene is relatively large, ranging from 12.3° to 55.4°, and the hotspot phenomenon is therefore visible only along a narrow line. The range of scanner view directions decreases with increasing altitude. It falls between 34.0° and 39.1° at 2 km altitude and between 36.595° and 36.605° at 5 km altitude, which explains why the hotspot line broadens in case of higher observing altitude of 2 km (Figure 16c), and why the whole forest stand is observed under the hotspot configuration at 5 km altitude (Figure 16d).

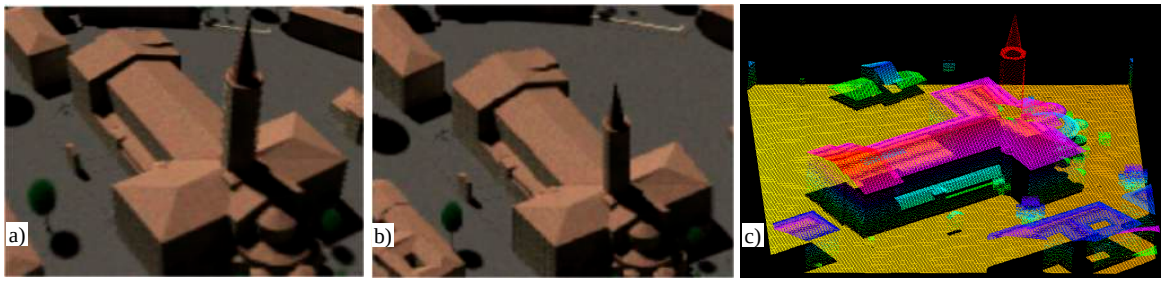

Figure 15. DART simulated products of the St. Sernin Basilica (Toulouse, France). (**a**) Airborne camera image (RGB color composite in natural colors) with the projective projection. (**b**) Satellite image with the orthographic projection. (**c**) Airborne LIDAR scanner simulation, displayed with SPDlib software.

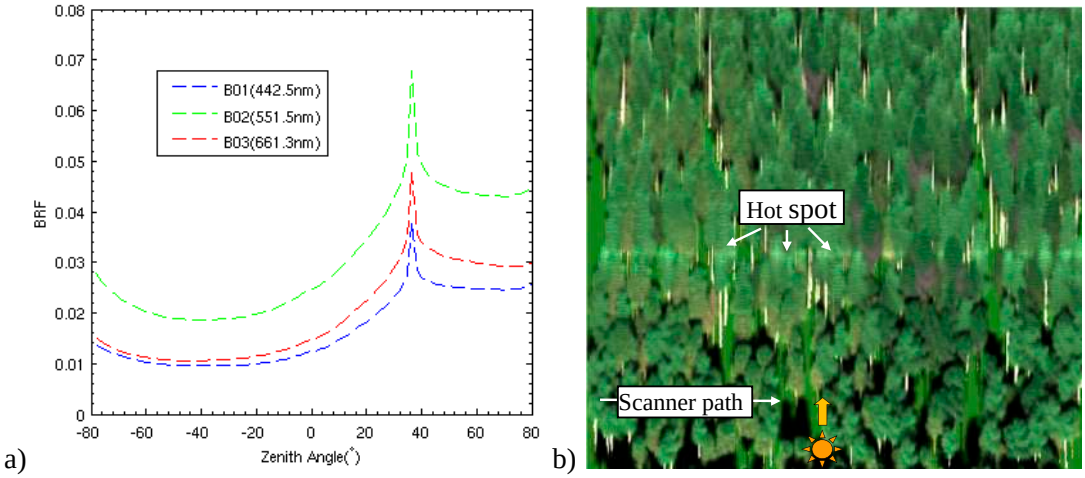

Figure 16. *Cont.*

c) 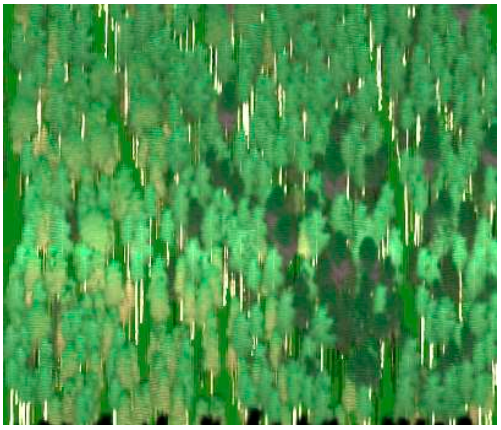 d) 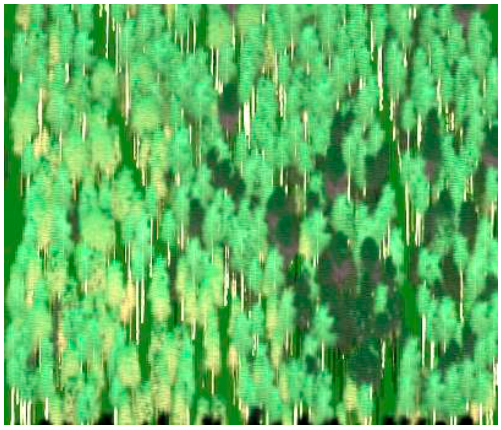

Figure 16. The changing hotspot perception simulated for the Jarvselja birth forest stand (Estonia) in summer: (**a**) DART simulated BRF for three spectral bands (442 nm, 551 nm, 661 nm), with SKYL equal to 0.21, 0.15 and 0.12, respectively, and DART simulated images for an airborne scanner flown at three altitudes: (**b**) 0.2 km, (**c**) 2 km and (**d**) 5 km, with ground resolution of 0.5 m. Dark zones in (**c**) and (d) correspond with occurrences of few pine trees in the birch stand.

Air-/space-borne RS images are usually transformed into orthorectified products that can be superimposed with local maps. DART computes orthorectified RS images directly, without classical orthorectification methods, because the exact location of each scattering/emission event occurring during an image simulation is known [65]. Two types of orthorectified products are produced by DART (Figure 17): ideally orthorectified images and industry orthorectified images, which are similar to RS images derived by industrial orthorectification methods. In the ideal orthorectification, radiance of pixel (i,j) results from the sum of all the fluxes that originate from scattering events occurring within the voxels (i,j,k) from the bottom up to the top of the scene. Selection of two ideal projections is available in DART:

- Orthographic projection (Figure 17a): radiance of pixel (i,j) is $L_{i,j}(\Omega_n) = \frac{\sum_k W_n^*(i,j,k,\Omega_n)}{\Delta x \cdot \Delta y \cdot \overline{\Omega}_g \cdot \overline{\Omega}_n \cdot \Delta\Omega_n}$, with $\overline{\Omega}_g$ the surface normal vector, (Ω_n, $\Delta\Omega_n$) the sensor viewing direction (*i.e.*, DART discrete direction) and k the index of cells above pixel (i,j), and
- Perspective projection (Figure 17b): radiance of pixel (i, j) is $L_{i,j}(\omega_{i,j}) = \sum_k \frac{W^*(i,j,k,\omega_{i,j,k})}{\Delta x \cdot \Delta y \cdot \overline{\Omega}_g \cdot \overline{\omega}_{i,j} \cdot \Delta\omega_{i,j,k}}$, with ($\omega_{i,j,k}$, $\Delta\omega_{i,j,k}$) being the sensor viewing direction for cell (i,j,k) above pixel (i,j).

The industry orthorectification (Figure 17c), which uses altitude of the Earth surface including any 3D object (e.g., trees, man-made objects, *etc*.) from a digital surface model (DSM), is carried out in two successive steps. In the first step, nadir downward ray tracking samples the DSM with a spatial sampling equal to that of the created ortho-image. This step provides the altitude $H_{i,j}$ for each pixel (i, j) of the ortho-image. In the second step, rays are tracked up to the sensor from each $H_{i,j}$. Any upward ray originating from $H_{i,j}$ that is not intercepted within the Earth scene reaches the sensor plane at a point M_{sensor}. In this case, the sensor radiance value at the point M_{sensor} is assigned to the pixel (i, j) of the ortho-image. If an upward ray from $H_{i,j}$ is at least partially intercepted within the Earth scene, then a

value of −1 is assigned to the pixel (i,j), which indicates that this pixel cannot be viewed by the sensor (Figure 17c).

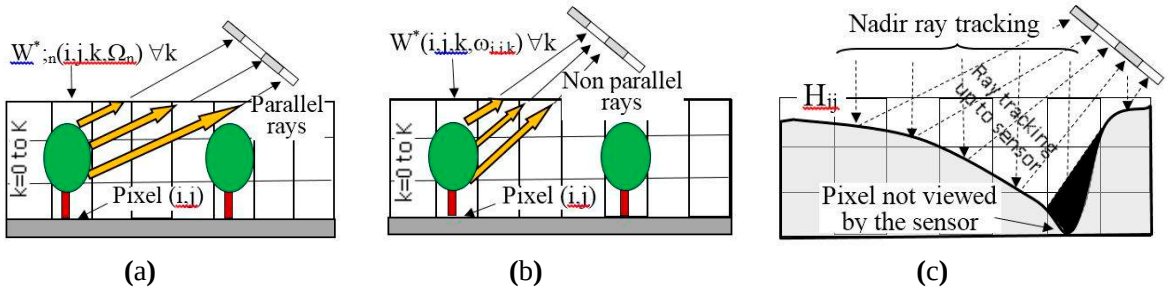

Figure 17. Schematic representation of the DART procedure that simulates orthorectified RS images: an ideal orthorectification with orthographic (**a**) and perspective projection (**b**), respectively, and an industry orthorectification (**c**) with either perspective or orthographic projection.

DART ideal orthorectification with orthographic projection, for a satellite optical sensor observing the Jarvselja birch stand with the central viewing zenith angle of 25° and the illumination direction along the horizontal axis, is illustrated in Figure 18a. The same simulation but for industry orthorectification using a DSM that represents the upper surface of the tree canopy is presented in Figure 18b. Bright color tones in Figure 18b indicate deep occlusion areas of the DSM, indicated in Figure 17c, that sensor cannot see due to the 3D nature of forest canopy. No-signal values are assigned to the corresponding pixels. Figure 18c shows scatterplot of reflectance values of both orthorectified images. Although reflectance images are strongly correlated, one can observe numerous outliers originating from different assumptions about the tree canopy surface. It is considered as a non-opaque medium in the ideal orthorectification, but an opaque surface for the industry orthorectification.

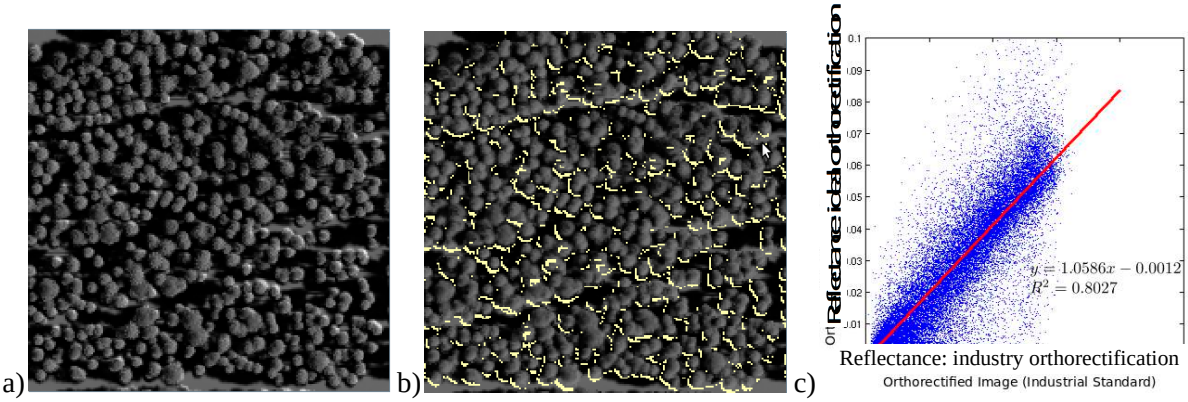

Figure 18. DART simulated orthorectified satellite images of the Jarvselja birth forest stand (Estonia) in summer obtained with ideal (**a**) and industry (**b**) orthorectification (bright tones indicate zones invisible to the sensor, due to the DSM opacity), accompanied by a scatterplot (**c**) displaying linear regression between per-pixel reflectance values of both orthorectified images.

6. Fusion of DART Simulated Imaging Spectroscopy and LIDAR Data

New multi-sensor airborne RS systems, such as the Carnegie Airborne Observatory (CAO) [67,68] and the Goddard's LiDAR, Hyperspectral & Thermal Imager (G-LiHT) [69], are carrying on-board LIDAR and imaging spectrometer instruments simultaneously. The FOV of the instruments are geometrically aligned and both data streams are spatially co-registered. This sensor synergy offers a possibility of an in-flight data fusion, where LIDAR provides structural and geometrical information and imaging spectrometer provides spectral information of observed Earth's objects. This type of fusion can find its use in various RS applications such as land cover/use classifications, monitoring of natural and man-managed ecosystem services or mapping of vegetation bio-diversity and eco-physiological functions.

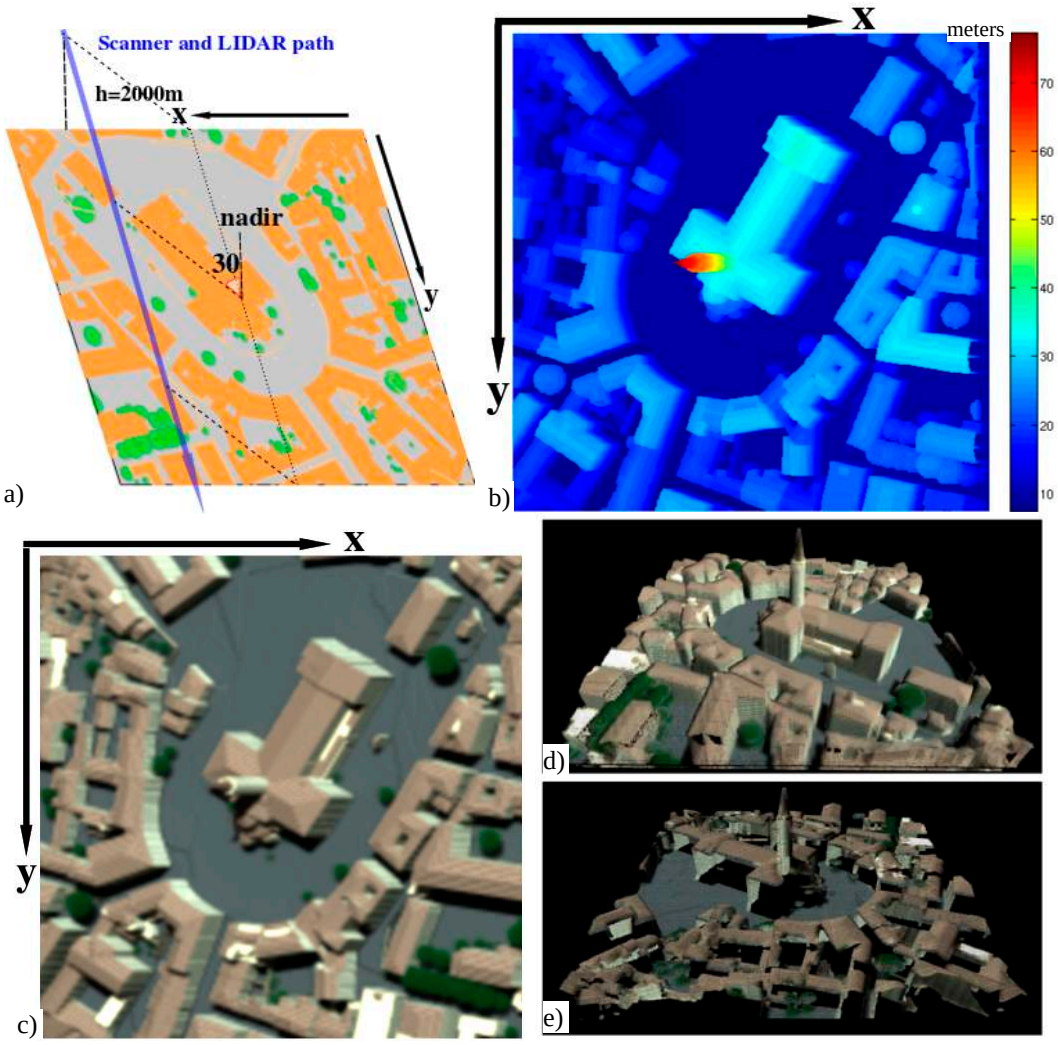

Figure 19. DART fusion of LIDAR and spectral images of St Sernin Basilica (Toulouse, France). (**a**) Acquisition geometry. (**b**) Multi-pulse LIDAR image. (**c**) RGB composition of corresponding spectral image. (**d**) and (**e**) Products of LIDAR-spectral fusion for two opposite viewing directions.

Since DART can apply the ray tracking method to simulate IS and the Ray-Carlo method to simulate LIDAR multi-pulse waveforms of the same landscape in a single run, it can also directly facilitate the in-flight fusion of both simulated datasets. During the first step of this procedure, the position of the LIDAR FOV center at the minimum altitude is recorded per pulse together with corresponding pulse identification number (ID). Then, the imaging scanner image at the minimum altitude is simulated with the parallel-perspective projection. This image is automatically referenced in DART scene coordinate system, which allows the radiance value to be computed in accordance with the FOV center of each recorded LIDAR pulse through a cubic-spline interpolation of the scanner image. The LIDAR output is then converted into the SPD format and processed with the SPDlib software to produce the LIDAR point clouds. Each LIDAR pulse contains *n* returns, which create *n* discrete points in 3D space. These points are linked with radiance value via pulse ID, which results in structural information and spectral information of the simulated landscape objects being achieved through the same path of a given pulse.

The DART in-flight data fusion for the St. Sernin Basilica (Toulouse, France) is illustrated in Figure 19. Figure 19a shows the geometrical configuration of the 250 m × 250 m scene with the x and y axes of the DART coordinate system. The aircraft equipped with a LIDAR sensor (λ = 1064 nm) and an imaging spectrometer (three spectral bands at 450 nm: B, 550 m: G, 650 nm: R) was flown at altitude of 2000 m along the y axis, with an off-nadir viewing angle of 30 degrees from the center of the scene to the left side of the flight path. This set up ensures that the walls of buildings in the scene, which are facing positive values of the x-axis are seen by both the LIDAR and spectrometer. Cell size of 50 cm with an average LIDAR pulse density of 4/m^2 resulted in 250,000 LIDAR pulses, stored in a matrix of 500 × 500 ID items. Figure 19b shows the simulated height image (500 × 500 pixels) of the first returns for each LIDAR pulse, and Figure 19c shows the RGB composition of simulated spectral image, both co-registered via a unique pulse ID. The DART 3D fusion product is then constructed by merging the LIDAR point clouds with spectral radiance image values per pulse ID. Figure 19d illustrates that the walls of the buildings that face the negative x-axis are present, whereas the walls that face the positive x-axis are missing (Figure 19e). This is caused by the off-nadir geometrical configuration allowing the LIDAR and IS sensor to observe only one side of the scene.

7. Conclusions

During more than 20 years of development, DART has reached the stage of a reference RT model in the field of optical RS. Free licenses are provided for research and teaching activities by the Paul Sabatier University (UPS) in Toulouse in cooperation with Centre National d'Etudes Spatiales (CNES, France). More than 100 research organizations and universities use it for designing future satellite sensors, for developing new RS applications for forestry, agriculture, and urbanism, and also for educational purposes, especially for lecturing the physical bases of RS and radiative budget.

This paper demonstrates new DART modeling and functionalities for simulating data of satellite and airborne LIDAR waveform and photon counting sensors, as well as images produced by IS from visible to thermal infrared wavelengths, both for an identical scene containing any vegetation and urban objects. Recent improvements enhanced the capacity of DART to simulate any Earth landscape with any atmosphere conditions from common databases (e.g., AERONET network and ECMWF database). Natural and urban landscapes can be now simulated with geometrically explicit surfaces (facets) and

turbid vegetation/fluid volumes. It addition, DART can import and manage 3D objects (tree, house, *etc.*) in the conventional **.obj* format. Moreover, it can transform part or all of these objects into 3D turbid voxels. Finally, three major improvements in radiation modeling were introduced.

(1) Modeling of satellite and aircraft LIDAR waveform and photon counting signals using the specifically designed Box and Ray-Carlo methods.
(2) Image simulation of spectroradiometers mounted on aircraft or unmanned aerial vehicles in the perspective projection. This simulation is useful to bridge the scaling gap between *in situ* radiometric measurements and satellite observations. The possibility to model LIDAR and spectral image data of the same landscape is highly appealing for RS data fusion techniques.
(3) Simulation of data acquired by an IS aboard a geostationary satellite, for any Earth region, and at any date from sunrise to sunset.

Apart from new scientific functionalities, many technical improvements took place in DART, such as parallelizing computations with the multithread approach or, management of DART outputs as SQL databases. Improvement of DART physics, optimization of its computational performance, and development of new functionalities still continue. The DART developing team is currently working on the following five improvements.

(1) Orthorectification based on digital elevation model in addition to surface model.
(2) Modeling spectral measurements of a sensor within the Earth landscape. Consequently, it will be possible to simulate camera acquisitions that are used to assess the LAI of trees and crops.
(3) Simulation of airborne acquisition according to the actual platform trajectory. This is essential for a pixel-wise comparison with real airborne and satellite images.
(4) Simulation of landscapes with cells of variable dimensions within the same scene for decreasing computational time and computer storage requirements. It will be possible to simulate larger scenes.
(5) RT modeling of water bodies. This modeling relies on 3D distribution of the so-called fluid turbid cells. This new feature is expected to open DART to the scientific community of ocean and inland water remote sensing.

Acknowledgments

This work was supported by the ANR in the frame of the FOLI3D project and by the Centre National d'Etudes Spatiales (CNES) in the frame of the TOSCA projects "Stem-Leaf" and "Geostationary satellite". Part of the work was conducted in the frame of the NASA project "DART-LIDAR". Contribution of J.-B. Féret was supported by a CNES post-doctoral research grant and contribution of Z. Malenovský was supported by the ARC Discovery project DP140101488 "AirLIFT". The authors are grateful for the Toulouse city geo-database provided by Toulouse town hall and thankful to all scientists who contributed to DART development since its first steps in 1992.

Author Contributions

Jean-Philippe Gastellu-Etchegorry plays the leading role for organizing materials, writing background, developing theory, and analyzing simulations in this paper. He has been the principal investigator for the DART team and supervised the DART-related projects for the past 20 years.

Tiangang Yin, Nicolas Lauret, Thomas Cajgfinger, Tristan Gregoire, and Eloi Grau, are members of the DART team. They contribute to DART 5 developments, implementations, and releases in different scientific domains presented in the paper. They include scene parameterization and creation, passive sensor image simulation model, single-pulse and multi-pulse LIDAR model, imaging spectroscopy and LIDAR fusion model, and Atmosphere-Earth coupling model.

Jean-Baptiste Feret, Maïlys Lopes, Jordan Guilleux, and Gérard Dedieu conducted different case studies shown in this paper, e.g., the geostationary satellite simulation in Section 3.2, the urban simulation of sensor fusion in Section 6, *etc*…

Gérard Dedieu (Geostationary satellite), Zbyněk Malenovský (AirLIFT), Bruce Douglas Cook, Douglas Morton, Jeremy Rubio (DART-LIDAR), Sylvie Durrieu, Gregory Cazanave, Emmanuel Martin, Thomas Ristorcelli (Stem-Leaf) are investigators of projects which supported the development of DART5 during the past 5 years. They contributed in designing realistic simulation parameterization in DART5.

Conflicts of Interest

The authors declare no conflict of interest.

References

1. Rouse, J., Jr; Haas, R.; Schell, J.; Deering, D. *Monitoring Vegetation Systems in the Great Plains with ERTS*; Technical Presentations; NASA SP-351; NASA: Washington, DC, USA, 1974.
2. Roujean, J.L.; Leroy, M.; Deschamps, P.Y. A bidirectional reflectance model of the Earth's surface for the correction of remote sensing data. *J. Geophys. Res.: Atmos.* **1992**, *97*, 20455–20468.
3. Wanner, W.; Li, X.; Strahler, A. On the derivation of kernels for kernel-driven models of bidirectional reflectance. *J. Geophys. Res.: Atmos.* **1995**, *100*, 21077–21089.
4. Liu, S.; Liu, Q.; Liu, Q.; Wen, J.; Li, X. The angular and spectral kernel model for BRDF and albedo retrieval. *IEEE J. Sel. Top. Appl. Earth Obs. Remote Sens.* **2010**, *3*, 241–256.
5. You, D.; Wen, J.; Liu, Q.; Tang, Y. The angular and spectral kernel-driven model: Assessment and application. *IEEE J. Sel. Top. Appl. Earth Obs. Remote Sens.* **2014**, *7*, 1331–1345.
6. Rahman, H.; Pinty, B.; Verstraete, M.M. Coupled surface-atmosphere reflectance (CSAR) model: 2. Semiempirical surface model usable with NOAA advanced very high resolution radiometer data. *J. Geophys. Res.: Atmos.* **1993**, *98*, 20791–20801.
7. Martonchik, J.V. Determination of aerosol optical depth and land surface directional reflectances using multiangle imagery. *J. Geophys. Res.: Atmos.* **1997**, *102*, 17015–17022.
8. Engelsen, O.; Pinty, B.; Verstraete, M.; Martonchik, J. *Parametric Bidirectional Reflectance Factor Models: Evaluation, Improvements and Applications*; Technical Report No. EUR 16426 EN; EC Joint Research Centre: Ispra, Italy, 1996.
9. Peddle, D.R.; Franklin, S.E.; Johnson, R.L.; Lavigne, M.B.; Wulder, M.A. Structural change detection in a disturbed conifer forest using a geometric optical reflectance model in multiple-forward mode. *IEEE Trans. Geosci. Remote Sens.* **2003**, *41*, 163–166.

10. Li, X.; Strahler, A.H. Geometric-optical bidirectional reflectance modeling of the discrete crown vegetation canopy: Effect of crown shape and mutual shadowing. *IEEE Trans. Geosci. Remote Sens.* **1992**, *30*, 276–292.
11. Chen, J.M.; Leblanc, S.G. A four-scale bidirectional reflectance model based on canopy architecture. *IEEE Trans. Geosci. Remote Sens.* **1997**, *35*, 1316–1337.
12. Chen, J.M.; Leblanc, S.G. Multiple-scattering scheme useful for geometric optical modeling. *IEEE Trans. Geosci. Remote Sens.* **2001**, *39*, 1061–1071.
13. Leblanc, S.G.; Chen, J.M. A windows graphic user interface (GUI) for the five-scale model for fast BRDF simulations. *Remote Sens. Rev.* **2000**, *19*, 293–305.
14. Dawson, T.P.; Curran, P.J.; Plummer, S.E. LIBERTY—Modeling the effects of leaf biochemical concentration on reflectance spectra. *Remote Sens. Environ.* **1998**, *65*, 50–60.
15. Hapke, B. Bidirectional reflectance spectroscopy: 1. Theory. *J. Geophys. Res.: Solid Earth* **1981**, *86*, 3039–3054.
16. Feret, J.-B.; François, C.; Asner, G.P.; Gitelson, A.A.; Martin, R.E.; Bidel, L.P.; Ustin, S.L.; Le Maire, G.; Jacquemoud, S. PROSPECT-4 and 5: Advances in the leaf optical properties model separating photosynthetic pigments. *Remote Sens. Environ.* **2008**, *112*, 3030–3043.
17. Verhoef, W. Light scattering by leaf layers with application to canopy reflectance modeling: The SAIL model. *Remote Sens. Environ.***1984**, *16*, 125–141.
18. Berk, A. MODTRAN Band Model Transmittance. Available online: www.spectral.com/pdf/MODTRAN4_Multiple_Scattering.pdf (accessed on 16 November 2014).
19. Vermote, E.F.; Tanré, D.; Deuze, J.-L.; Herman, M.; Morcette, J.-J. Second simulation of the satellite signal in the solar spectrum, 6S: An overview. *IEEE Trans. Geosci. Remote Sens.* **1997**, *35*, 675–686.
20. Gastellu-Etchegorry, J.-P.; Demarez, V.; Pinel, V.; Zagolski, F. Modeling radiative transfer in heterogeneous 3D vegetation canopies. *Remote Sens. Environ.* **1996**, *58*, 131–156.
21. Yin, T.; Gastellu-Etchegorry, J.-P.; Lauret, N.; Grau, E.; Rubio, J. A new approach of direction discretization and oversampling for 3D anisotropic radiative transfer modeling. *Remote Sens. Environ.* **2013**, *135*, 213–223.
22. Borel, C.C.; Gerstl, S.A.; Powers, B.J. The radiosity method in optical remote sensing of structured 3-D surfaces. *Remote Sens. Environ.* **1991**, *36*, 13–44.
23. Min, Q. A polarized radiative transfer model based on successive order of scattering. *Adv. Atmos. Sci.* **2010**, *27*, 891–900.
24. Disney, M.; Lewis, P.; North, P. Monte Carlo ray tracing in optical canopy reflectance modelling. *Remote Sens. Rev.* **2000**, *18*, 163–196.
25. Lewis, P. Three-dimensional plant modelling for remote sensing simulation studies using the Botanical Plant Modelling System. *Agronomie* **1999**, *19*, 185–210.
26. North, P. Three-dimensional forest light interaction model using a Monte Carlo method. *IEEE Trans. Geosci. Remote Sens.* **1996**, *34*, 946–956.
27. Govaerts, Y.M.; Verstraete, M.M. Raytran: A Monte Carlo ray-tracing model to compute light scattering in three-dimensional heterogeneous media. *IEEE Trans. Geosci. Remote Sens.* **1998**, *36*, 493–505.

28. Kimes, D.; Kirchner, J. Radiative transfer model for heterogeneous 3-D scenes. *Appl. Opt.* **1982**, *21*, 4119–4129.
29. Myneni, R.; Asrar, G.; Hall, F. A three-dimensional radiative transfer method for optical remote sensing of vegetated land surfaces. *Remote Sens. Environ.* **1992**, *41*, 105–121.
30. Gastellu-Etchegorry, J.; Martin, E.; Gascon, F. DART: A 3D model for simulating satellite images and studying surface radiation budget. *Int. J. Remote Sens.* **2004**, *25*, 73–96.
31. Gastellu-Etchegorry, J. 3D modeling of satellite spectral images, radiation budget and energy budget of urban landscapes. *Meteorol. Atmos. Phys.* **2008**, *102*, 187–207.
32. Gastellu-Etchegorry, J.; Guillevic, P.; Zagolski, F.; Demarez, V.; Trichon, V.; Deering, D.; Leroy, M. Modeling BRF and radiation regime of boreal and tropical forests: I. BRF. *Remote Sens. Environ.* **1999**, *68*, 281–316.
33. Thompson, R.; Goel, N.S. Two models for rapidly calculating bidirectional reflectance: Photon spread (PS) model and statistical photon spread (SPS) model. *Remote Sens. Rev.* **1998**, *16*, 157–207.
34. Pinty, B.; Gobron, N.; Widlowski, J.L.; Gerstl, S.A.; Verstraete, M.M.; Antunes, M.; Bacour, C.; Gascon, F.; Gastellu, J.P.; Goel, N. Radiation transfer model intercomparison (RAMI) exercise. *J. Geophys. Res.: Atmos.* **2001**, *106*, 11937–11956.
35. Pinty, B.; Widlowski, J.L.; Taberner, M.; Gobron, N.; Verstraete, M.; Disney, M.; Gascon, F.; Gastellu, J.P.; Jiang, L.; Kuusk, A. Radiation Transfer Model Intercomparison (RAMI) exercise: Results from the second phase. *J. Geophys. Res.: Atmos.* **2004**, *109*, doi:10.1029/2003JD004252.
36. Widlowski, J.L.; Taberner, M.; Pinty, B.; Bruniquel-Pinel, V.; Disney, M.; Fernandes, R.; Gastellu-Etchegorry, J.P.; Gobron, N.; Kuusk, A; Lavergne, T. Third Radiation Transfer Model Intercomparison (RAMI) exercise: Documenting progress in canopy reflectance models. *J. Geophys. Res.: Atmos.* **2007**, *112*, doi:10.1029/2006JD007821.
37. Widlowski, J.-L.; Robustelli, M.; Disney, M.; Gastellu-Etchegorry, J.-P.; Lavergne, T.; Lewis, P.; North, P.; Pinty, B.; Thompson, R.;Verstraete, M. The RAMI On-line Model Checker (ROMC): A web-based benchmarking facility for canopy reflectance models. *Remote Sens. Environ.* **2008**, *112*, 1144–1150.
38. Widlowski, J.L.; Pinty, B.; Lopatka, M.; Atzberger, C.; Buzica, D.; Chelle, M.; Disney, M.; Gastellu-Etchegorry, J.P.; Gerboles, M.; Gobron, N. The fourth radiation transfer model intercomparison (RAMI-IV): Proficiency testing of canopy reflectance models with ISO-13528. *J. Geophys. Res.: Atmos.* **2013**, *118*, 6869–6890.
39. Gascon, F.; Gastellu-Etchegorry, J.-P.; Lefevre-Fonollosa, M.-J.; Dufrene, E. Retrieval of forest biophysical variables by inverting a 3-D radiative transfer model and using high and very high resolution imagery. *Int. J. Remote Sens.* **2004**, *25*, 5601–5616.
40. Banskota, A.; Wynne, R.H.; Thomas, V.A.; Serbin, S.P.; Kayastha, N.; Gastellu-Etchegorry, J.P.; Townsend, P.A. Investigating the utility of wavelet transforms for inverting a 3-D radiative transfer model using hyperspectral data to retrieve forest LAI. *Remote Sens.* **2013**, *5*, 2639–2659.
41. Durrieu, S.; Cherchali, S.; Costeraste, J.; Mondin, L.; Debise, H.; Chazette, P.; Dauzat, J.; Gastellu-Etchegorry, J.-P.; Baghdadi, N.; Pélissier, R. Preliminary Studies for a Vegetation Ladar/Lidar Space Mission in France. In Proceedings of 2013 IEEE International Geoscience and Remote Sensing Symposium (IGARSS), , Melbourne, Australia, 21–26 July 2013.

42. Bruniquel-Pinel, V.; Gastellu-Etchegorry, J. Sensitivity of texture of high resolution images of forest to biophysical and acquisition parameters. *Remote Sens. Environ.* **1998**, *65*, 61–85.
43. Guillevic, P.; Gastellu-Etchegorry, J. Modeling BRF and radiation regime of boreal and tropical forest: II. PAR regime. *Remote Sens. Environ.* **1999**, *68*, 317–340.
44. Malenovský, Z.; Martin, E.; Homolová, L.; Gastellu-Etchegorry, J.-P.; Zurita-Milla, R.; Schaepman, M.E.; Pokorný, R.; Clevers, J.G.; Cudlín, P. Influence of woody elements of a Norway spruce canopy on nadir reflectance simulated by the DART model at very high spatial resolution. *Remote Sens. Environ.* **2008**, *112*, 1–18.
45. Malenovský, Z.; Homolová, L.; Zurita-Milla, R.; Lukeš, P.; Kaplan, V.; Hanuš, J.; Gastellu-Etchegorry, J.-P.; Schaepman, M.E. Retrieval of spruce leaf chlorophyll content from airborne image data using continuum removal and radiative transfer. *Remote Sens. Environ.* **2013**, *131*, 85–102.
46. Barbier, N.; Couteron, P.; Proisy, C.; Malhi, Y.; Gastellu-Etchegorry, J.P. The variation of apparent crown size and canopy heterogeneity across lowland Amazonian forests. *Glob. Ecol. Biogeogr.* **2010**, *19*, 72–84.
47. Barbier, N.; Couteron, P.; Gastelly-Etchegorry, J.-P.; Proisy, C. Linking canopy images to forest structural parameters: Potential of a modeling framework. *Ann. Forest Sci.* **2012**, *69*, 305–311.
48. Proisy, C.; Barbier, N.; Guéroult, M.; Pélissier, R.; Gastellu-Etchegorry, J.-P.; Grau, E.; Couteron, P. Biomass Prediction in Tropical Forests: The Canopy Grain Approach. Available online: http://hal.ird.fr/ird-00658600/document (accessed on 16 November 2014).
49. Gascon, F.; Gastellu-Etchegorry, J.-P.; Lefèvre, M.-J. Radiative transfer model for simulating high-resolution satellite images. *IEEE Trans. Geosci. Remote Sens.* **2001**, *39*, 1922–1926.
50. Grau, E.; Gastellu-Etchegorry, J.-P. Radiative transfer modeling in the Earth-Atmosphere system with DART model. *Remote Sens. Environ.* **2013**, *139*, 149–170.
51. Nilson, T.; Kuusk, A. A reflectance model for the homogeneous plant canopy and its inversion. *Remote Sens. Environ.* **1989**, *27*, 157–167.
52. Etude des Couverts Forestiers par Inversion de Formes d'onde LIDAR à L'aide du Modèle de Transfert Radiatif DART Développé par le CESBIO. 2010, INSA de Strasbourg. Available online: http://eprints2.insa-strasbourg.fr/645/ (accessed on 16 November 2014).
53. Yin, T.; Gastellu-Etchegorry, J.-P.; Grau, E.; Lauret, N.; Rubio, J. Simulating satellite waveform Lidar with DART model. In Proceedings of Geoscience and Remote Sensing Symposium (IGARSS), 2013 IEEE International, Melbourne, Australia, 21–26 July 2013.
54. Gastellu-Etchegorry, J.-P.; Yin, T.; Grau, E.; Lauret, N.; Rubio, J. Lidar radiative transfer modeling in the Atmosphere. In Proceedings of Geoscience and Remote Sensing Symposium (IGARSS), 2013 IEEE International, Melbourne, Australia, 21–26 July 2013.
55. Bunting, P.; Armston, J.; Lucas, R.M.; Clewley, D. Sorted Pulse Data (SPD) Library. Part I: A generic file format for LiDAR data from pulsed laser systems in terrestrial environments. *Comput. Geosci.* **2013**, *56*, 197–206.
56. Bunting, P.; Armston, J.; Clewley, D.; Lucas, R.M., Sorted pulse data (SPD) library—Part II: A processing framework for LiDAR data from pulsed laser systems in terrestrial environments. *Comput. Geosci.* **2013**, *56*, 207–215.

57. Martin, E. Dart: Modèle 3D Multispectral et Inversion D'images Optique De Satellite—Application Aux Couverts Forestiers. Available online: https://tel.archives-ouvertes.fr/tel-00139368/document (accessed on 16 November 2014).
58. Grau, E. Modélisation DART du transfert Radiatif Terre-Atmosphère pour Simuler les Bilans Radiatif, Images de Télédétection et Mesures LIDAR des Paysages Terrestres. Available online: https://tel.archives-ouvertes.fr/tel-00841795/document (accessed on 16 November 2014).
59. Gastellu-Etchegorry, J.-P.; Grau, E.; Lauret, N. DART: A 3D model for remote sensing images and radiative budget of earth surfaces. Available online: https://hal.archives-ouvertes.fr/ird-00658284/document (accessed on 16 November 2014).
60. Hancock, S.; Disney, M.; Muller, P.L.J.-P. Exploring the Measurement of Forests with Full Waveform LIDAR through Monte-Carlo Ray Tracing. Available online: http://isprsserv.ifp.uni-stuttgart.de/proceedings/XXXVII/congress/1_pdf/38.pdf (accessed on 16 November 2014).
61. North, P.; Rosette, J.; Suárez, J.; Los, S. A Monte Carlo radiative transfer model of satellite waveform LiDAR. *Int. J. Remote Sens.* **2010**, *31*, 1343–1358.
62. Schutz, B.; Zwally, H.; Shuman, C.; Hancock, D.; DiMarzio, J. Overview of the ICESat mission. *Geophys. Res. Lett.* **2005**, *32*, doi:10.1029/2005GL024009.
63. Côté, J.-F.; Fournier, R.A.; Egli, R. An architectural model of trees to estimate forest structural attributes using terrestrial LiDAR. *Environ. Modell. Softw.* **2011**, *26*, 761–777.
64. Abdalati, W.; Zwally, H.J.; Bindschadler, R.; Csatho, B.; Farrell, S.L.; Fricker, H.A.; Harding, D.; Kwok, R.; Lefsky, M.; Markus, T. The ICESat-2 Laser Altimetry Mission. Available online: http://icesat.gsfc.nasa.gov/icesat2/publications/pubs_2010/abdalati_et_al_2010.pdf (accessed on 16 November 2014).
65. Yin, T.; Lauret, N.; Gastellu-Etchegorry, J.-P. Simulation of multi-angle sensor image of the Earth scene by combining 3D radiative transfer modeling with perspective projection. *Remote Sens. Environ.* **2015**, accepted.
66. Morton, D.C.; Nagol, J.; Carabajal, C.C.; Rosette, J.; Palace, M.; Cook, B.D.; Vermote, E.F.; Harding, D.J.; North, P.R. Amazon forests maintain consistent canopy structure and greenness during the dry season. *Nature* **2014**, *506*, 221–224
67. Asner, G.P.; Boardman, J.; Field, C.B.; Knapp, D.E.; Kennedy-Bowdoin, T.; Jones, M.O.; Martin, R.E. Carnegie airborne observatory: In-flight fusion of hyperspectral imaging and waveform light detection and ranging for three-dimensional studies of ecosystems. *J. Appl. Remote Sens.* **2007**, *1*, doi:10.1117/1.2794018.
68. Asner, G.P.; Knapp, D.E.; Boardman, J.; Green, R.O.; Kennedy-Bowdoin, T.; Eastwood, M.; Martin, R.E.; Anderson, C.; Field, C.B. Carnegie Airborne Observatory-2: Increasing science data dimensionality via high-fidelity multi-sensor fusion. *Remote Sens. Environ.* **2012**, *124*, 454–465.
69. Cook, B.D.; Nelson, R.F.; Middleton, E.M.; Morton, D.C.; McCorkel, J.T.; Masek, J.G.; Ranson, K.J.; Ly, V.; Montesano, P.M. NASA Goddard's LiDAR, Hyperspectral and Thermal (G-LiHT) airborne imager. *Remote Sens.* **2013**, *5*, 4045–4066.

Chapter 2

Direction discretization and oversampling

During the recent years, the improvement of RTMs has been mostly focused on improving 3D landscapes simulation and RT mathematical modeling. The angular variable Ω discretization is a much less addressed problem, although it can strongly influence the simulation of satellite signals. The influence of the number, shape and distribution of the discrete directions on the simulation of satellite signals and 3D radiative budget must be addressed. Several methods have been designed to study the anisotropic radiation in the field of heat and mass transfer (Modest, 2003). Among them, the discrete ordinate method (DOM) and the finite volume method (FVM) are extensively used to solve heat transfer problem in steady-state process.

DOM and FVM both have some strong and weak points according to their application in radiative transfer. Several comparisons have been made during the recent years (Kim and Huh, 2000; Mishra et al., 2006). The main disadvantage of DOM arises in anisotropic situations where the distribution of discrete directions can lead to solid angles with unrealistic geometric shapes. In that case, the numerical quadrature made over a surface does not conserve the radiant energy (Raithby, 1999). Instead of using a simple quadrature, an analytical exact integration is proposed in FVM. However, the center (ordinates) and the shape of the angular sector are still not well addressed in FVM, which results in relative large error with small number of directions (Kim and Huh, 2000).

In initial DART versions, simulation of satellite signals was conducted with exact kernel and DOM methods. The 4π space of radiation directions was discretized into N directions (Ω_n, angular sector $\Delta\Omega_n$). These directions were the only possible directions of incident, scattered and emitted radiant fluxes (Kimes and Kirchner, 1982; Myneni et al., 1991). In this chapter, an iterative uniform squared discretization (IUSD) method is presented. This is a new method that combines the advantages of both DOM and FVM, with well defined shape and exact center of each direction. It uses the concept of "squared" angular sector with an analytical expression that allows one to construct the direction with flexible input parameters. With this approach, scattering calculation can combine both numerical quadrature and analytical integration. Different cases are investigated: optimal shape of angular sectors on the 4π sphere, oversampling of planes and angular zones, and use of directions that are not centered on their associated sectors Ω_n for more accurate RT modeling. The IUSD method is elaborated in

Section 2.1

In addition to the uniform distribution of squared solid angles, an algorithm that calculates the cosine-weighted distribution of the squared solid angles (http://sirkan.iit.bme.hu/~szirmay/weight3.pdf) was designed and implemented. Cosine-weighted sampling approach is used in Monte Carlo ray tracing as a weighted importance sampling in shooting algorithms. It is presented in Appendix I.

Furthermore, in DART, any directional products (images, reflectance, temperature, etc...) are bijected to their associated direction. The concept of virtual discrete direction is defined, in order to generate radiance / reflectance / brightness temperature along any set of pre-defined directions. A ray traveling along a virtual direction (a virtual ray) does not contribute to any further scattering event. Optical properties (i.e., scattering transfer functions) associated to all these discrete directions are pre-defined. The virtual direction is the prerequisite of the following chapters of this dissertation. The concept of virtual direction is further extended to non pre-defined virtual discrete directions (also name automated steering virtual direction) for simulating spectro-radiometer images with finite field of view (FOV) (Chapter 3) and for simulating LIDAR waveform (Chapter 4). In both cases, the number of these directions can be very large. For simulating spectro-radiometer images, it is, up to the number of possible scattering points in the atmosphere and Earth scene.

The improvement of discretization of directions is presented in the paper "A new approach of direction discretization and oversampling for 3D anisotropic radiative transfer modeling". Information about the generation of cosine-weighted direction set is given in Appendix I.

2.1 Article: A new approach of direction discretization and oversampling for 3D anisotropic radiative transfer modeling

Remote Sensing of Environment 135 (2013) 213–223

Contents lists available at SciVerse ScienceDirect

Remote Sensing of Environment

journal homepage: www.elsevier.com/locate/rse

A new approach of direction discretization and oversampling for 3D anisotropic radiative transfer modeling

Tiangang Yin *, Jean-Philippe Gastellu-Etchegorry, Nicolas Lauret, Eloi Grau, Jeremy Rubio

CESBIO — CNES, CNRS (UMR 5126), IRD, Universite de Toulouse, 18 avenue, Edouard Belin, bpi 2801, 31401, Toulouse cedex 9, France

ARTICLE INFO

Article history:
Received 22 October 2012
Received in revised form 6 March 2013
Accepted 29 March 2013
Available online 8 May 2013

Keywords:
Discrete ordinate method
3D radiative transfer
Anisotropic scattering
Hot spot
Direction oversampling

ABSTRACT

In radiative transfer modeling, the angular variable Ω discretization can strongly influence the radiative transfer simulation, especially with small numbers of discrete directions. Most radiative transfer models use discrete ordinate method or finite volume method for solving the transport equation. Both of the methods have their own algorithms to discretize the 4π space, under the constraint of satisfying geometric symmetry and specific moments. This paper introduces a new direction discretization and oversampling scheme, IUSD, and compares it with the other methods in simulating satellite signals. This method considers the constraint of geometric shape of angular sector, and iteratively discretizes the 4π space under this constraint. The result shows that IUSD is quite competitive in the accuracy of simulating remote sensing images. Furthermore, the new method provides a flexibility for adding any oversampling angular region, with any number of additional directions, using an optimal approach in terms of the total number of directions. Several case studies are presented. It turns out that the regional oversampling has significant influence for strong anisotropic scattering. This method has been implemented in the latest code of DART 3D radiative transfer model. DART is available for scientific purpose upon request.

1. Introduction

During the recent years, the improvement of radiative transfer (RT) is usually focused on 3D landscape simulation and RT mathematical modeling. In simulating satellite signals, the angular variable Ω discretization is a much less addressed problem, although it can strongly influence the simulation of satellite signals. Therefore, the influence of the number, shape and distribution of the discrete directions on the simulation of satellite signals and 3D radiative budget is interesting to discuss. Several methods have been mentioned to study the anisotropic radiation in the field of heat and mass transfer (Modest, 2003). Among them, the discrete ordinate method (DOM) and the finite volume method (FVM) are extensively used to solve heat transfer problem in steady-state process.

DOM was firstly proposed for atmosphere radiation (Chandrasekhar, 1969) and applied in neutron transport problems (Lathrop, 1966). In recent years, DOM has been applied and optimized for heat transfer problems (Fiveland, 1984, 1987, 1988; Truelove, 1987, 1988). Its representation of 4π space is defined by a number of discrete directions that are centered on the solid angles that discretize the 4π space. The geometric shape of the solid angles is not defined. Each discrete direction is defined by its central zenith and azimuth angles (θ_c, ϕ_c), and by a weight that is specifically computed. S_n DOM approach is normally used as the discrete ordinates. The even number n can be considered as the total number of layers over the sphere ($n/2$ in upper hemisphere), where a layer is made of all angular sectors that have the same zenith coordinate. The ordinates of S_n DOM approach and their respective parameters are provided by Lathrop and Carlson (1965), which are taken as classical references. Integration over angular sectors is approximated by a numerical quadrature.

FVM (Chai et al., 1994; Chui & Raithby, 1993; Raithby & Chui, 1990) is a rather mature spatial discretization technique. Each direction is defined by exact boundaries without overlap, so a full integration over the whole sphere ensures the conservation of energy. There are several available schemes. Raithby and Chui (1990) and Chai et al. (1994) use $N_\phi \times N_\phi$ uniform angular discretization, where the zenith $(0, \pi)$ and azimuth angles $(0, 2\pi)$ are divided by N_θ and N_ϕ, respectively. This leads to a heterogeneous sampling of the 4π space with much smaller solid angles for small zenith angles. This problem is decreased by the distribution scheme called FT_n FVM (Kim & Huh, 2000): the number of discrete directions in 2 successive layers with large zenith angle is multiplied by a factor 4. Here n has the same definition as S_n DOM.

Both DOM and FVM have some strong and weak points according to application in radiative transfer. Several comparisons have been made during the recent years (Kim & Huh, 2000; Mishra et al., 2006). The

* Corresponding author. Tel.: +33 761748944.
E-mail address: tiangang.yin.85@gmail.com (T. Yin).

0034-4257/$ – see front matter © 2013 Elsevier Inc. All rights reserved.
http://dx.doi.org/10.1016/j.rse.2013.03.030

main disadvantage of DOM arises in anisotropic situations where the distribution of discrete directions can lead to solid angles with unrealistic geometric shapes. In that case, the numerical quadrature made over a surface does not conserve the radiant energy (Raithby, 1999). Instead of using a simple quadrature, an analytical exact integration is proposed in FVM. However, the center (ordinates) and the shape of the angular sector are still not well addressed in FVM, which results in relative large error with small number of directions (Kim & Huh, 2000).

In simulating satellite signals, exact kernel and DOM are commonly used in radiative transfer models. They discretize the angular variable Ω into N directions (Ω_n, angular sector $\Delta\Omega_n$) that are the only possible directions of incident, scattered and emitted radiant fluxes (Kimes & Kirchner, 1982; Myneni et al., 1991). Here, an iterative uniform squared discretization (IUSD) method is presented. This is a new method combining the advantages of both DOM and FVM, with well defined shape and exact center of each direction. It uses the concept of "squared" angular sector with an analytical expression that allows one to construct the direction with flexible input parameters. With this approach, scattering calculation can combine both numerical quadrature and analytical integration. Different cases are investigated: optimal shape of angular sectors on the 4π sphere, oversampling of planes and angular zones, and use of directions that are not centered on their associated sectors Ω_n for more accurate RT modeling. We test it with a 3D RT model that uses discrete directions: DART (Discrete Anisotropic Radiative Transfer) (Gastellu-Etchegorry et al., 1996, 2004, 2012). This model simulates vegetation and urban radiative budget and remote sensing images of passive and Lidar systems, for any atmosphere, wavelength and experimental configuration (spatial resolution, etc.…).

2. Algorithm

2.1. Reviews of DOM and FVM

Several basic requirements must be satisfied by any direction discretization method. First, the discretization set must be completely symmetric: the distribution of directions must be invariant after any rotation of 90° along vertical axis. This requirement is necessary for heat transfer modeling along the axes of complicated grids. Moreover, it ensures the exact calculation of boundaries conditions in RT equation. Thus, the total numbers of directions by DOM and FVM are multiples of 8 (4 in upper hemisphere and 4 in lower hemisphere). Then, moments of order 0 and order 1 of both DOM and FVM must verify some equalities. Hereafter, $\hat{s}$ stands for the direction, w stands for the associated quadrature weights, and the direction indices are sorted according to zenith angle:

- Zeroth moment ensures that discretization is exact over the 4π space:

$$\int_{4\pi} d\Omega = \sum_{i=1}^{N} w_i = 4\pi. \tag{1}$$

- First moment and upper hemisphere first moment ensure the conservation of radiant energy:

$$\int_{4\pi} \hat{s}\, d\Omega = \sum_{i=i}^{N} \hat{s}_i w_i = 0 \int_{2\pi} \hat{s} d\Omega = \sum_{i}^{\frac{N}{2}} \hat{s}_i w_i = \pi. \tag{2}$$

Fig. 1 shows several 3D illustrations of the available discretizations. In the DOM, the weight w is calculated to satisfy both the zeroth and the first moments. w corresponds to a solid angle $\Delta\Omega$, but the shape of the estimated angular sector is not defined geometrically. Although the value of w can be determined, one can obtain an inadequate discretization of 4π space. For example, several solid angles may intersect each other or may not be exactly juxtaposed.

Thus, the total integration may lead to problems concerning conservation of energy. In S_n DOM approximation of the DOM (Fig. 1(a)), the sphere is quarterly divided along x and y axes. Starting with 1 direction in the first layer in upper hemisphere, each layer of the hemisphere has a number of directions which are equal to the layer index. Thus, the total number of directions is $n(n+2)$.

In the FVM method, the 4π sphere is discretized explicitly. w is directly taken as the solid angle of each direction. In order to satisfy the first moment, $\hat{s}_i w_i$ is calculated by an integration over the angular sector. Thus, the total integration ensures the conservation of energy. In $N_\theta \times N_\phi$ FVM method, the angular sectors are uniformly divided in both zenith and azimuth axes. However, the zenith and azimuth axes are not in the uniform frame. The vertex of the zenith angle is at the center of the sphere, and that of the azimuth angle is at the center of the circle of the horizontal cross section of the sphere. The zenith angle ranges from 0 to π and the azimuth angle ranges from 0 to 2π. Fig. 1(b) and (c) shows the result of $N_\theta \times N_\phi$ FVM. It can be observed that the generated angular sectors are not perfect by shape: too narrow near the pole and too wide near the equator. This problem is decreased with the FT_n FVM (Kim & Huh, 2000). Same as S_n DOM, n is the number of layers and the layer of index i contains $4i$ directions. Its result is shown in Fig. 1(d).

2.2. Definition of a square direction

A question can be raised: what is the ideal geometric shape of a discrete direction on the 4π sphere? One can think of common figures such as: a circle, an equilateral triangle, a square, or a more complicated image like a regular hexagon. By taking into account that the figure is on the sphere surface, among all the possible shapes, the square is the simplest shape for integration. Therefore, we keep "square" in our mind throughout the whole discretization process and think about how to generate a nearly square angular sector.

Let θ and ϕ be the zenith and azimuth angles in 4π space. Table 1 gives the attributes of any direction (Ω, $\Delta\Omega$). The direction center (θ_c, ϕ_c) is the first attribute to consider. A rectangle is defined by width ($\Delta\theta$) and length ($\Delta\phi$) on a spherical surface. It differs from that on a plane surface. For example, the shape of a direction near the top of the upper hemisphere is more like a triangle, or a trapezoidal rather than a rectangle. Thus, the coordinates that represent any direction (Ω, $\Delta\Omega$) correspond to the centroid of (Ω, $\Delta\Omega$), with a mean azimuth angle $\phi_c = \frac{\phi_0+\phi_1}{2}$, and with a zenith angle θ_c that differs from the mean zenith angle $\left(\frac{\theta_0+\theta_1}{2}\right)$:

$$\theta_c = \arccos((\cos\theta_0 + \cos\theta_1)/2). \tag{3}$$

With this approach, the solid angles "above" and "below" (θ_c, ϕ_c) within the solid angle (Ω, $\Delta\Omega$) are equal. In order to have a square shape, the within solid angle vertical and horizontal arc lengths that cross (θ_c, ϕ_c) must be equal. Therefore, the shape of Ω is nearly a square if the following condition is verified:

$$\Delta\theta = \sin\theta_c \Delta\phi. \tag{4}$$

2.3. Calculation of the number of zenith layers

Unlike the symmetric requirement in heat transfer, the simulation of satellite signal does not contain complex 3D grid. The complete symmetry is replaced by point symmetry relative to the center of the sphere. The directions (Ω, $\Delta\Omega$) that sample the 4π sphere are symmetric relative to the center of the sphere, in such a way that a

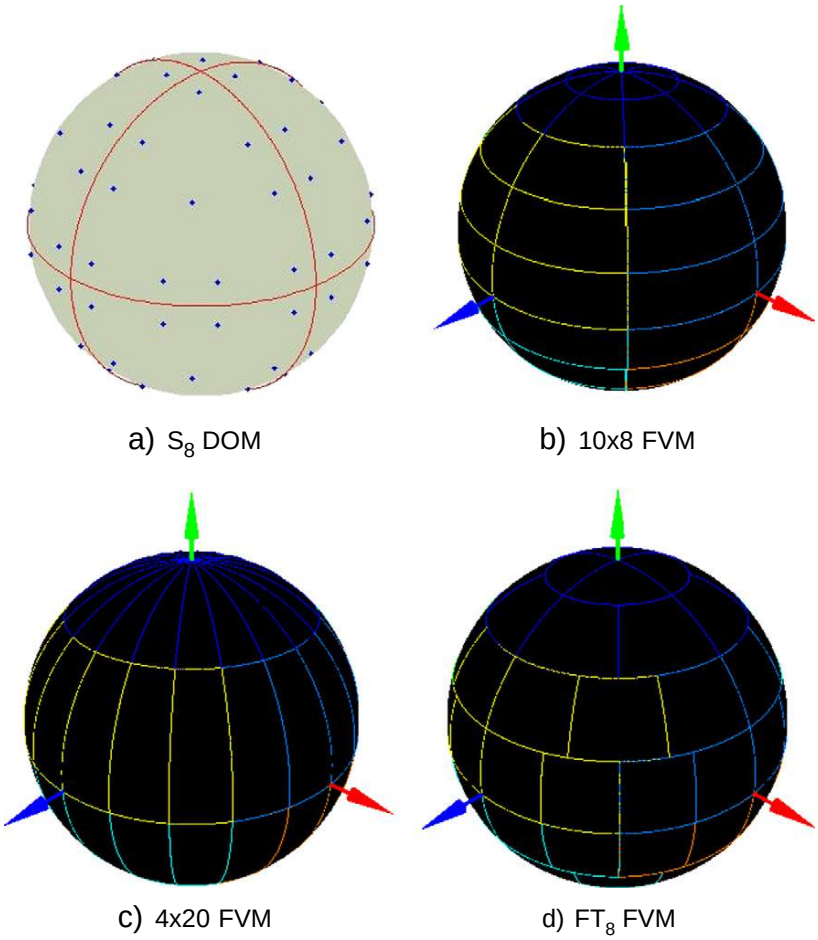

Fig. 1. DOM and FVM direction discretization schemes for $N = 80$.

flux that is intercepted can be backscattered along the direction that is opposite to the incident direction. Therefore, the initialized number of directions (N) is even, and the number of directions of the upper hemisphere (N_{up}) is half the total number of directions ($N_{up} = N/2$). Furthermore, the nadir direction ($\theta_c = 0$, $\phi_c = 0$) is very important for remote sensing, so the top and bottom directions are represented by a circular shape. To facilitate the application of the generated direction list (flux calculation, interpolation, subsampling, etc.…), the 4π sphere is sampled under 4 conditions:

- Directions are created by zenith layer.
- All directions have the same $\Delta\Omega$. Hereafter, this is called $\Delta\Omega_{unit}$.
- The shape of Ω should be nearly a square.

Table 1
Attributes of discrete directions Ω.

Symbol	Expression	Representation
θ_0, θ_1		Upper and lower θ boundaries of Ω
ϕ_0, ϕ_1		Left and right ϕ boundaries of Ω
θ_c	$arccos((cos\theta_0 + cos\theta_1)/2)$	θ of the center of Ω
ϕ_c	$(\phi_0 + \phi_1)/2$	ϕ of the center of Ω
$\Delta\theta$	$\theta_1 - \theta_0$	Difference between the θ boundary values
$\Delta\phi$	ϕ_1, ϕ_0	Difference between the ϕ boundary values
$\Delta\Omega$	$(cos\theta_0 - cos\theta_1) \times \Delta\phi$	Solid angle of Ω

- The distribution of directions on the sphere must be as homogeneous as possible. It implies that the azimuth angle of the directions within different layers must not be coincident.

The algorithm starts with the determination of the directions in the upper hemisphere. The distribution of the directions in the lower hemisphere is the symmetric of the distribution of the directions in the upper hemisphere.

The number of layers (n_L) of the upper hemisphere strongly affects the shape of the generated directions. It is computed with the assumption that $\Delta\theta$ is small (i.e., a relative large N). The constraint of equal solid angles implies that for each direction: $\Delta\Omega_{unit} = \frac{2\pi}{N_{up}}$. Thus, with Eq. (4) and $\Delta\Omega$ expression (Table 1), for each direction Ω, we must have:

$$(\cos\theta_0 - \cos\theta_1)\frac{\Delta\theta}{\sin\theta_c} = \Delta\Omega_{unit}.$$

Combining the cosine functions, we get:

$$2\sin\left(\frac{\theta_0+\theta_1}{2}\right)\sin\left(\frac{\Delta\theta}{2}\right)\frac{\Delta\theta}{\sin\theta_c} = \Delta\Omega_{unit}.$$

Since $\Delta\theta$ is small, we have: $\sin\left(\frac{\Delta\theta}{2}\right) \approx \frac{\Delta\theta}{2}$, and $\sin\left(\frac{\theta_0+\theta_1}{2}\right) \approx \sin\theta_c$. It leads to the approximated value: $\Delta\theta_{app} \approx \sqrt{\Delta\Omega_{unit}}$.

The first layer consists of only a vertical direction with a circular shape. With zenith angle width $\Delta\theta$ being about half of the other

Table 2
Remaining ($_{rem}$) parameter expressions after each iteration n (i.e., the index of layer).

Symbol	Layer 1	Layer n	Representation
N^n_{rem}	$N_{up}-1$	$N^{n-1}_{rem}-N^n_l$	The remaining number of directions
n^n_{Lrem}	n_L-1	$n^{n-1}_{Lrem}-1$	The remaining number of layers
θ^n_{rem}	$\frac{\pi}{2}-\Delta\theta^1$	$\theta^{n-1}_{rem}-\Delta\theta^n$	The remaining θ
$\Delta\Omega^n_{rem}$	$2\pi-\Delta\Omega^1$	$\Delta\Omega^{n-1}_{rem}-\Delta\Omega^n$	The remaining total $\Delta\Omega$
$\Delta\Omega^n_{unit}$	$\frac{\Delta\Omega^1_{rem}}{N^1_{rem}}$	$\frac{\Delta\Omega^n_{rem}}{N^n_{rem}}$	The updated value for unit $\Delta\Omega$ for all remaining directions

layers, the total number of layers is the integer number that is the truncated value of:

$$n_L \approx \frac{\pi/2}{\sqrt{\Delta\Omega_{unit}}} + 0.5 = \frac{\sqrt{2\pi N_{up}}}{4} + 0.5. \quad (5)$$

In a 1st step, the $\Delta\theta$ of each layer is set as:

$$\Delta\theta_{app} = (\pi/2)/(n_L - 0.5). \quad (6)$$

2.4. A new method to generate the discrete directions

Here, a new angular discretization method, called IUSD (Iterative Uniform Square Discretization) is introduced. The directions are iteratively generated by taking into account the remainder of each attribute of last iteration. The number of iterations is equal to the number of layers. Let the superscript n be the layer (iteration) index. First, the top layer with the single direction (Ω^1, $\Delta\Omega^1$) is initialized with:

$$\theta^1_0 = 0 \qquad \theta^1_1 = \theta^2_0 = \Delta\theta^1 = \frac{\Delta\theta_{app}}{2}$$
$$\Delta\Omega^1 = 2\pi\left(1-\cos\theta^1_1\right).$$

Directions of the same layer have the same $\Delta\theta$ and $\Delta\phi$. For layer n, they are called $\Delta\theta^n$ and $\Delta\phi^n$, with $\Delta\phi^n = \frac{2\pi}{N^n_l}$ and N^n_l the number of directions in layer n. It is shown below that it is computed as a round number. After setting the first direction, it remains $N^1_{rem} = N_{up} - 1$ directions and $n^1_{Lrem} = n_L - 1$ layers. Remaining zenith angle is $\theta^1_{rem} = \frac{\pi}{2} - \Delta\theta^1$. Remaining solid angle is $\Delta\Omega^1_{rem} = 2\pi - \Delta\Omega^1$. The updated unit solid angle for the other layers is $\Delta\Omega^1_{unit} = \frac{\Delta\Omega^1_{rem}}{N^1_{rem}}$. These variables ($N^n_{rem}$, n^n_{Lrem}, θ^n_{rem}, $\Delta\Omega^n_{rem}$, $\Delta\Omega^n_{unit}$) are updated at each iteration n (Table 2) following the steps shown below:

- Step 1: Calculate the approximate $\Delta\theta$ for layer index $n > 1$: $\Delta\theta^n_{app} = (\theta^{n-1}_{rem})/n^{n-1}_{Lrem}$. Then, initialize the top θ of layer n with: $\theta^n_0 = \theta^{n-1}_1$.
- Step 2: Calculate the approximate solid angle $\Delta\Omega^n_{app}$ of layer n from $\Delta\theta^n_{app}$:

$$\Delta\Omega^n_{app} = \left(\cos(\theta^n_0) - \cos\left(\theta^n_0 + \Delta\theta^n_{app}\right)\right) \times 2\pi.$$

The actual number of directions N^n_l of the current layer n is calculated as the round integer of $\Delta\Omega^n_{app}/\Delta\Omega^{n-1}_{unit}$.

- Step 3: Compute the actual $\Delta\Omega^n$ and $\Delta\theta^n$, by using the actual N^n_l:

$$\Delta\Omega^n = N^n_l \times \Delta\Omega^{n-1}_{unit}$$
$$\theta^n_1 = \arccos\left(\cos\theta^n_0 - \frac{\Delta\Omega^n}{2\pi}\right) \quad \Delta\theta^n = \theta^n_1 - \theta^n_0.$$

- Step 4: End the current iteration with the update of the remaining parameters N^n_{rem}, n^n_{Lrem}, θ^n_{rem}, $\Delta\Omega^n_{rem}$, and $\Delta\Omega^n_{unit}$ by using the expressions in Table 2.

The iteration ends once the last layer ($n^n_{Lrem} = 0$) is defined and all the remaining parameters (N^n_{rem},θ^n_{rem},Ω^n_{rem}) are 0. Then, a list of layers is generated. After defining the ϕ_0 of the first direction of layer (ϕ^n_0), all other directions can be generated. ϕ^n_0 is 0 only in the top layer. To maximize the distance between all directions, the azimuth angles ϕ^n_0 and ϕ^{n-1}_0 of 2 consecutive layers are shifted:

$$\begin{aligned} \phi^n_0 &= \phi^{n-1}_0 + \frac{\Delta\phi^{n-1}}{2} && \text{if } c<3 \\ \phi^n_0 &= \phi^{n-1}_0 + \frac{\Delta\phi^{n-1}}{2} \times \left(1 + \frac{1}{c^n - 1}\right) && \text{if } c>=3 \end{aligned} \quad (7)$$

where c is the number of adjacent layers with the same number of directions. ϕ^n_0 is shifted by half of the $\Delta\phi^{n-1}$ of last layer multiplied by a constant that depends on c. This constant allows one to take into account the case of multiple successive layers with the same number of directions N^n_l. For instance, let us consider a list of directions of 8 successive layers with N^n_l represented by the set {1 3 3 4 5 6 6 6}, then the corresponding set for c^n is {1 2 2 1 1 3 3 3}.

By applying Eq. (7) to each layer, all directions are generated. They have the same $\Delta\Omega$ except the vertical direction of the top layer, and the shape of each direction is almost square. Then, directions of the lower hemisphere are derived from the directions of the upper hemisphere.

Fig. 2 shows 3 sets of directions with $N = 100$, 500 and 2000. All directions have nearly square shapes on the sphere. Color tones indicate the angular sectors that are used for storing the mean direction

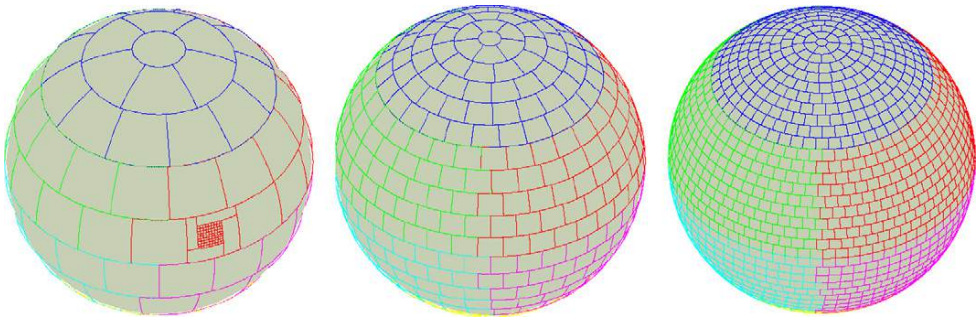

a) 100 directions with region oversampling b) 500 directions c) 2000 directions

Fig. 2. The 3D spherical distribution of directions for 100, 500 and 2000 directions.

of the incident fluxes that are scattered at scattering order larger than 1. They are made of individual DART directions. Their number is smaller or equal to the defined number N of DART discrete directions. Fig. 3 compares the solid angle of discrete direction of FVM method and IUSD method for 3 cases: 24, 48, and 80 directions. The IUSD method gives uniformly distributed directions of equal solid angle with the only exceptions for the top and bottom directions.

2.5. Verification of the first moment

In the IUSD, same as the FVM, the w parameter of the first moment is directly equal to $\Delta\Omega$. As discussed in Section 2.1, since IUSD discretizes the 4π sphere with exact boundaries like the FVM, the first quadrature by integration is automatically verified. In order to verify the conservation of energy in the case of a Lambertian surface, we must verify $\int_0^{2\pi} \cos\theta_c d\Omega = \pi$. The definition of (θ_c,ϕ_c) implies that for each DART direction, we have: $\int_{\Delta\Omega} \cos\theta_c d\Omega = \cos\theta_c \times \Delta\Omega$. Thus, the summation over all DART solid angles, in the case we have n_L layers, leads to:

$$\sum^{N} \cos\theta_c \times \Delta\Omega = 2\pi \sum_{i=1}^{n_L} \cos\theta_c^i \left(\cos\theta_0^i - \cos\theta_1^i\right) = \pi \sum_{i=1}^{n_L} \left(\cos^2\theta_0^i - \cos^2\theta_1^i\right).$$

Substituting $\theta_0^1 = 0$, $\theta_1^{n_L} = \frac{\pi}{2}$, and $\theta_0^i = \theta_1^{i-1}$, we get $\sum_{i=1}^{n_L} \left(\cos^2\theta_0^i - \cos^2\theta_1^i\right) = 1$, then:

$$\sum^{N} \cos\theta_c \times \Delta\Omega = \pi.$$

Therefore, the computation of first moment with numerical quadrature gives the accurate value. This is another advantage of the IUSD over the FVM by defining the direction center to be at the centroid of the shape. In FVM, the direction center is at the mean zenith and azimuth angles (Chui & Raithby, 1993). Therefore, even if it gives an accurate estimation of the flux, FVM does not direct the flux to the accurate direction.

It is very important to pay attention to the calculation of $\cos\theta_c\Delta\Omega$ in IUSD. It can be calculated explicitly except for the nadir direction.

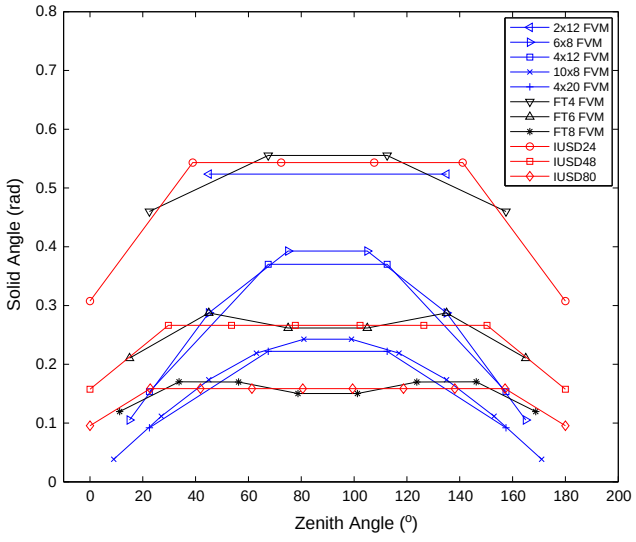

Fig. 3. FVM and IUSD discretized solid angles for 3 cases: 24, 48 and 80 directions.

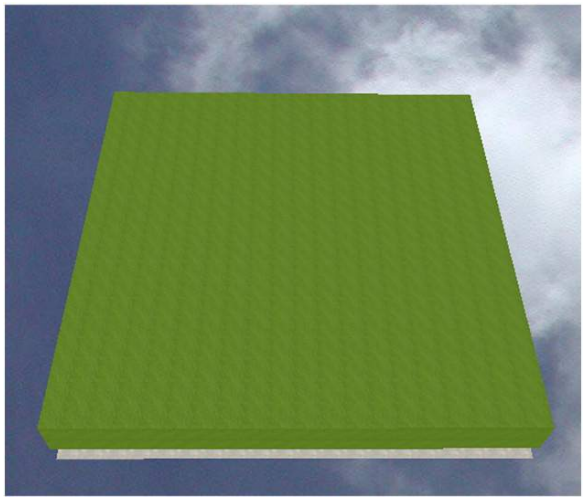

Fig. 4. Simulation of vegetation cover.

This direction is special because in the spherical coordinate system, $\theta_0 = \theta_c = 0$, so $\cos\theta_c\Delta\Omega = \Delta\Omega$, which differs from the expected value $\int \cos\theta d\Omega$. This problem is due to the spherical coordinate system. It happens when the z axis intercepts the spherical surface area of the angular sector. Thus, the expression to calculate $\int \cos\theta d\Omega$ for nadir direction must not use the vertical direction. It is equal to:

$$\int \cos\theta^1 d\Omega = \left(1 - \cos^2\theta_1^1\right) \times \pi.$$

3. Validation and results

The IUSD is validated with a simple simulation shown in Fig. 4. The scene is a homogeneous vegetation cover. The leaf angle distribution (LAD) of the vegetation is spherical, and the mean leaf diameter is 1 cm. The wavelength of simulation is 560 nm. The corresponding leaf reflectance is 0.1017 and the transmittance is 0.0753. The sun position relative to the scene is $(\theta_s = 45, \phi_s = 225)$. DART simulations are conducted in flux tracking mode with 3 different numbers of directions (24, 48, 80) and 3 leaf area indices (LAI = 0.5, 2, 4). The ground is set to be purely absorbing surface with reflectance equal to 0. Therefore, only the radiative interaction with leaves is simulated. Our

Table 3
Nadir reflectance relative error with different discretizations of the 4π space.

Discretization method	Number of directions	Nadir reflectance relative error ($\theta = 0, \phi = 0$) (%)		
		$LAI = 0.5$	$LAI = 2.0$	$LAI = 4.0$
S_4 DOM	24	3.0097	0.3481	3.6590
2 × 12 FVM	24	7.3978	7.3586	7.1021
FT_4 FVM	24	2.6172	3.0530	3.2008
IUSD	24	0.5257	0.3481	0.3988
S_6 DOM	48	0.9453	1.2026	1.1880
4 × 12 FVM	48	2.0920	1.5338	1.4939
6 × 8 FVM	48	1.2059	0.7893	0.7862
FT_6 FVM	48	1.0579	1.4519	1.4958
IUSD	48	0.3624	0.1642	0.1929
S_8 DOM	80	1.0913	1.2275	1.2286
4 × 20 FVM	80	2.0958	1.5427	1.5051
10 × 8 FVM	80	0.5218	0.3052	0.3073
FT_8 FVM	80	0.4881	0.7847	0.8123
IUSD	80	0.2694	0.1630	0.1706

objective is to estimate the accuracy of bidirectional reflectance factor (BRF). The BRF is defined to be the measured reflectance of the scene normalized by the reflectance of a purely white Lambertian surface. In addition to the previously mentioned DART discrete directions, the BRF is also simulated for directions that are in the sun perpendicular plane with 5° step of the zenith angle θ, within the range [−80° 80°]: $\phi = 135°$ and $\theta = \{-80°, -75°, -70°, \cdots -5°, 0°, 5°, \cdots 70°, 75°, 80°\}$, where the negative value of θ represents its reverse at $\phi = 315$. It must be noted that these additional directions do not impact the simulation accuracy. Indeed, they have no impact on radiative transfer. This is explained in Section 4. Because accuracy increases with the number of directions, we assume that simulations conducted with a very large number of directions can be used as a reference for evaluating the accuracy of simulations that are conducted with a smaller number of directions. Here, reference simulations are obtained with 2000 directions for IUSD, 2024 directions for FT_{44} FVM, and 2080 directions for 40 × 52 FVM. The relative differences between the 3 values are less than 0.1%.

Table 3 shows the relative errors of the nadir reflectance. Fig. 5 shows the relative error in the sun perpendicular plane with 5° step. The following points can be observed:

- Accuracies of all methods increase as the number of directions increases, converging towards the reference value. When the number of directions reaches 80, most methods have relative smaller error. (1.23% for DOM, 2.10% for FVM and 0.27% for IUSD.)
- As LAI increases, the chance of multiple scattering increases, with no obvious trend on BRF accuracy.

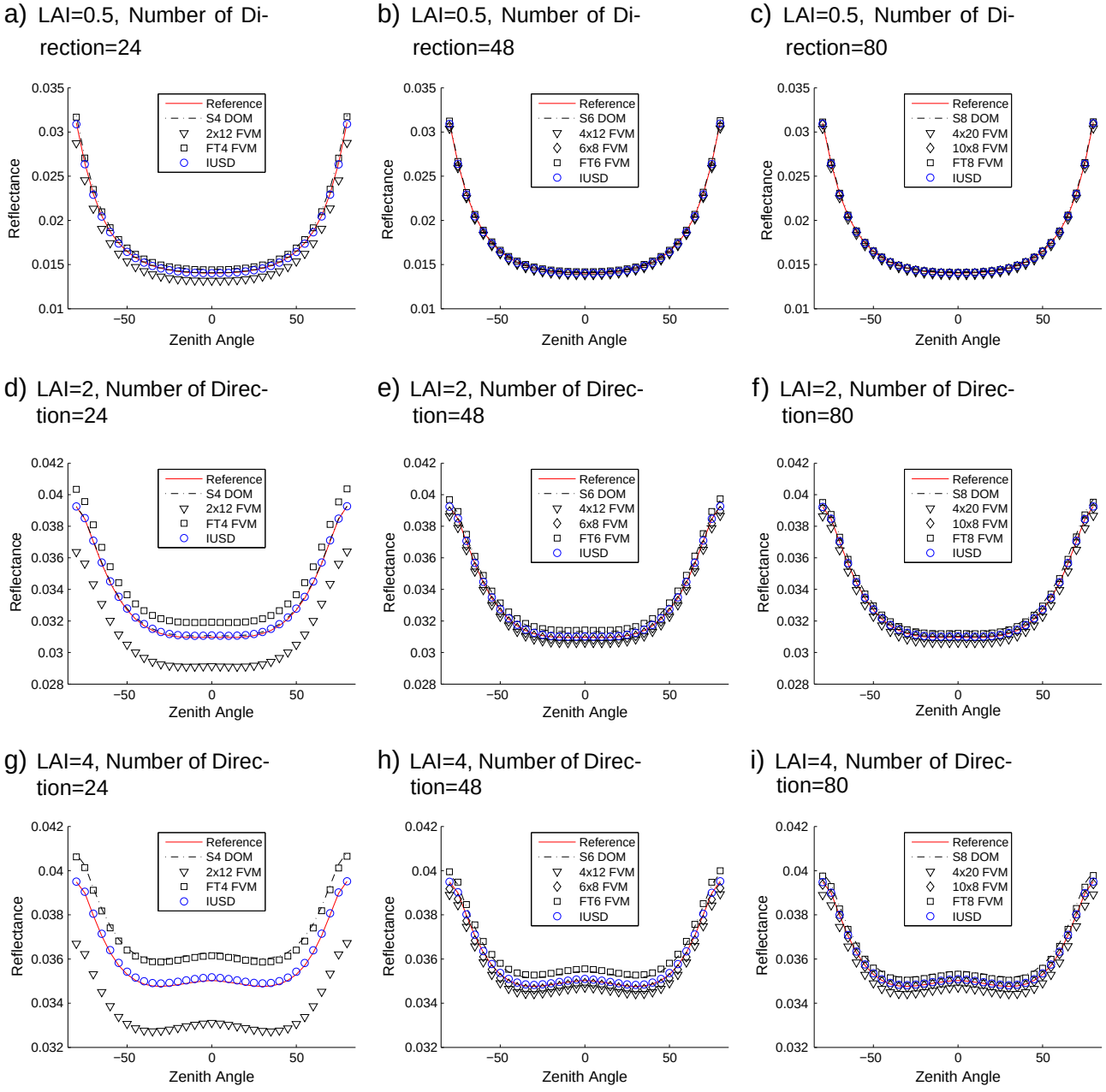

Fig. 5. Reflectance over the perpendicular sun plane (Azimuth = 135°, Zenith step = 5°), for LAI = 0.5, 2, 4 and N = 24, 48, 80.

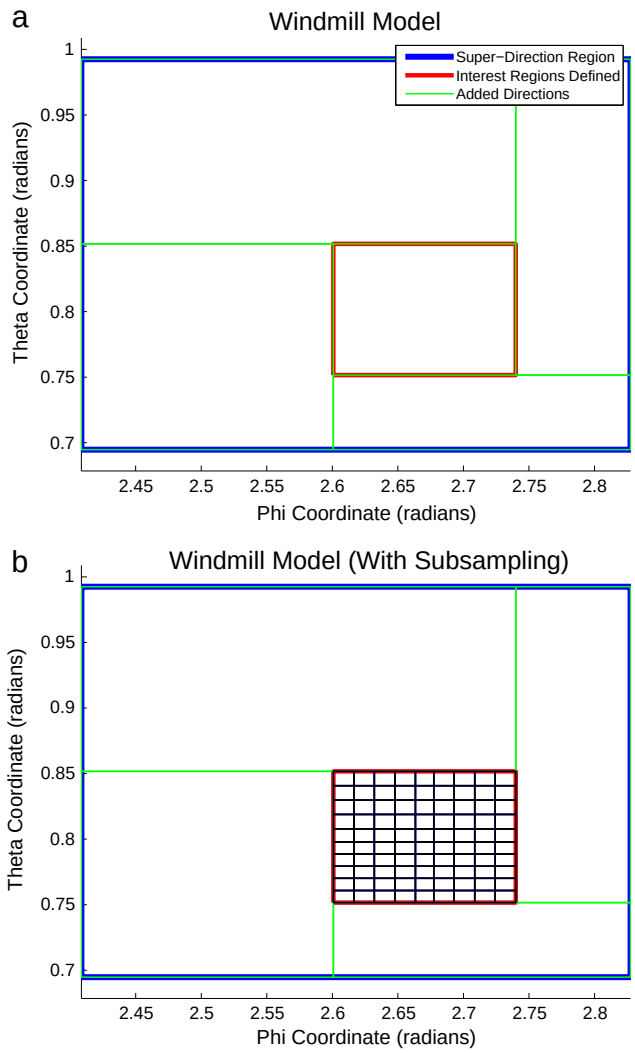

Fig. 6. IUSD-Windmill method adding angular region that corresponds to a single direction (a) or a set of directions (b) that contribute to radiative transfer. Case (b) corresponds to an oversampling.

- The S_n DOM and FT_n FVM are quite stable, with similar result (2.5–3.5% at $N = 24$, 1–1.5% at $N = 48$, 0.5–1% at $N = 80$). The $N_\theta \times N_\phi$ is very unstable with a relatively larger error.
- The IUSD gives better results than all the other methods, with errors less than 0.55% with 24 directions, less than 0.37% with 48 directions, and less than 0.27% with 80 directions.

4. Oversampling technique

It is often necessary to work with discrete directions in addition to the predefined discrete directions that sample homogeneously the 4π space. Such directions can be unique directions (e.g., view direction of a satellite sensor) or a set of directions that sample a given portion of the 4π space (e.g., angular neighborhood of the hot spot and specular directions). Moreover, these additional directions can be defined in such a way that the radiations along these directions do contribute or not to radiative transfer modeling. If there is no contribution, these directions are simply used for providing radiative transfer results. They are not taken into account for computing the moments. This type of additional direction is the view direction that is used in SAIL model (Verhoef, 1984). On the other hand, if there is contribution, for example for improving the accuracy of radiative transfer simulation in presence of anisotropic radiative behaviors, all or part of the originally defined discrete directions must be modified in order to verify the 2 moments. The different cases are presented below.

4.1. Addition of a square direction

The IUSD method can introduce square directions with solid angles that are defined either by their solid angle values $\Delta\Omega$ or by their zenith and azimuth angle ranges.

- Direction $\{\theta_c, \phi_c, \Delta\Omega\}$.

Assume $\delta\theta_0$ and $\delta\theta_1$ are the θ differences from the center to the upper edge and lower edge respectively ($\theta_0 = \theta_c - \delta\theta_0$, $\theta_1 = \theta_c + \delta\theta_1$). $\Delta\Omega$ expression of Table 1 and Eq. (4) leads to:

$$\begin{cases} (\cos(\theta_c - \delta\theta_0) - \cos\theta_c)\dfrac{\delta\theta_0 + \delta\theta_1}{\sin(\theta_c)} = \dfrac{\Delta\Omega}{2} \\ (\cos\theta_c - \cos(\theta_c + \delta\theta_1))\dfrac{\delta\theta_0 + \delta\theta_1}{\sin(\theta_c)} = \dfrac{\Delta\Omega}{2} \end{cases}.$$

There is no analytical solution for these equations. Thus a numerical method is used for finding $\delta\theta_0$ and $\delta\theta_1$. This method works with an equation where $\delta\theta_0$ is the only variable:

$$\begin{aligned} F(\delta\theta_0) = {} & (2(\cos(\theta_c - \delta\theta_0) - \cos\theta_c)) \\ & \times (\delta\theta_0 - \theta_c + \arccos(2\cos\theta_c - \cos(\theta_c - \delta\theta_0))) - \Delta\Omega \\ & \times \sin(\theta_c) = 0. \end{aligned} \quad (8)$$

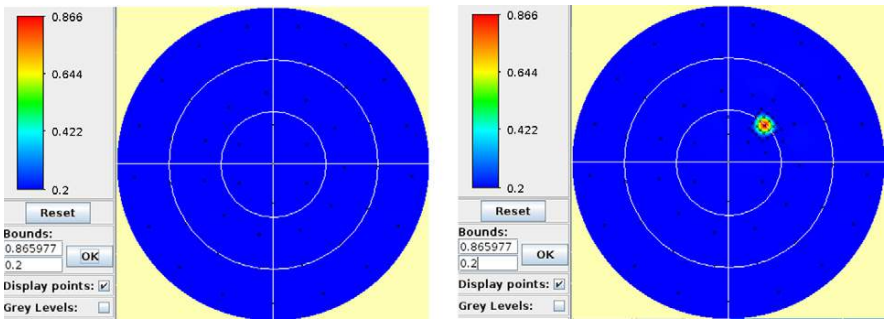

a) Without oversampling b) With oversampling

Fig. 7. Resultant BRF distribution of a specular surface.

Table 4
Vegetation simulation.

Parameter	Value
Scene irradiance ($W \cdot m^{-2} \cdot \mu m^{-1}$)	393.94
Leaf reflectance	0.554
Leaf transmittance	0.410
Number of vertical layers for multiple scattering	10
Leaf diameter (cm)	1
Leaf area index	4
Leaf angle distribution	Spherical
Sun angle Ω_s (θ, ϕ)	(77.1, 58.5)
Oversampling solid angle (sr)	0.003
Number of oversampling directions	25

The bisection method is used to find the value $\delta\theta_0$ that gives $F(\delta\theta_0) = 0$. Once $\delta\theta_0$ is calculated, the other parameters are simply determined.

- Direction $\{\theta_c, \phi_c, (\Delta\theta \text{ or } \Delta\phi)\}$.

This can be solved analytically by using the fact that the solid angle above (θ_c, ϕ_c) is equal to $\Delta\Omega/2$:

$$\delta\theta_0 = \text{acos}(\cos\theta_c / \cos(\Delta\theta/2)) - \Delta\theta/2. \quad (9)$$

Knowing $\delta\theta_0$, one can compute the other attributes.

4.2. IUSD-Windmill oversampling

As already mentioned, if the added directions contribute to radiative transfer, all the original discrete directions that are intersected by at least one added direction must be modified. This is done using the so-called IUSD-Windmill model (Fig. 6(a)). Let D_{in} be the angular region that corresponds to N_{in} added directions. First, an automatic approach searches the initial direction list to find the super direction D_{sup} where D_{in} is included. The approximate unit solid angle of each added direction in D_{in} is:

$$\Delta\Omega_{app} = \frac{\Delta\Omega^{in}}{N_{in}}.$$

We simply have $\Delta\Omega_{app} = \Delta\Omega^{in}$ if $N_{in} = 1$ (Fig. 6(a)). We have an angular oversampling if $N_{in} > 1$ (Fig. 6(b)). Region D_{in} can be defined by one of the two methods presented in Section 4.1. The "100 directions" case in Fig. 2(a) illustrates the possibility to oversample any angular region by using this technique. Indeed, the computation time of RT simulations strongly increases with the number of total directions. This technique avoids to create unnecessary directions. The first moment is verified. This is shown as in Section 2.5.

4.3. IUSD-EO oversampling

The Windmill method increases the number of discrete directions by more than 1 unit, each time one adds a discrete direction. This can be a severe constraint in some cases. In order to decrease this problem, we introduced another oversampling approach when adding directions that contribute to radiative transfer. For that, we consider that there are 3 types of directions that contribute to radiative transfer: the original discrete direction (D), the embedded direction (E), and the occupied direction (O). The directions allow one to verify all the moments and the conservation of energy.

At the beginning, there are only discrete directions (D). If we add directions that contribute to radiative transfer, the direction (Ω_D, $\Delta\Omega_D$) that contains n added directions becomes an occupied direction (O), and the n added directions are called "embedded" directions. (Ω_E, $\Delta\Omega_E$). The occupied direction (Ω_O, $\Delta\Omega_O$) is defined by:

$$\Delta\Omega_O = \Delta\Omega_D - \sum_{i=1}^{n} \Delta\Omega_E^i \quad S_O = S_D - \sum_{i=1}^{n} S_E^i \quad (10)$$

where $S = cos\theta\Delta\Omega$. Thereafter, it does not matter how many "E" directions are added to the list, the conservation condition is always satisfied.

5. Oversampling validation

3 results are shown here in order to illustrate the interest of the IUSD-Windmill sampling method: a surface with specular reflectance, a vegetation landscape and an urban landscape.

5.1. Specular reflection

Specular reflection of a unidirectional flux on a plane surface gives an unidirectional flux that is symmetric to the incident direction relative to the normal of the surface. In order to take into account the surface roughness, the DART model distributes the specular scattered radiation E_{spec} in a cone that is centered on the exact specular direction. The cone has a half angle α_{spec} that depends on surface roughness. E_{spec} is proportional (factor η_{spec}) to the classical Fresnel reflectance coefficient for unpolarized radiation. Here, we consider a surface that has a

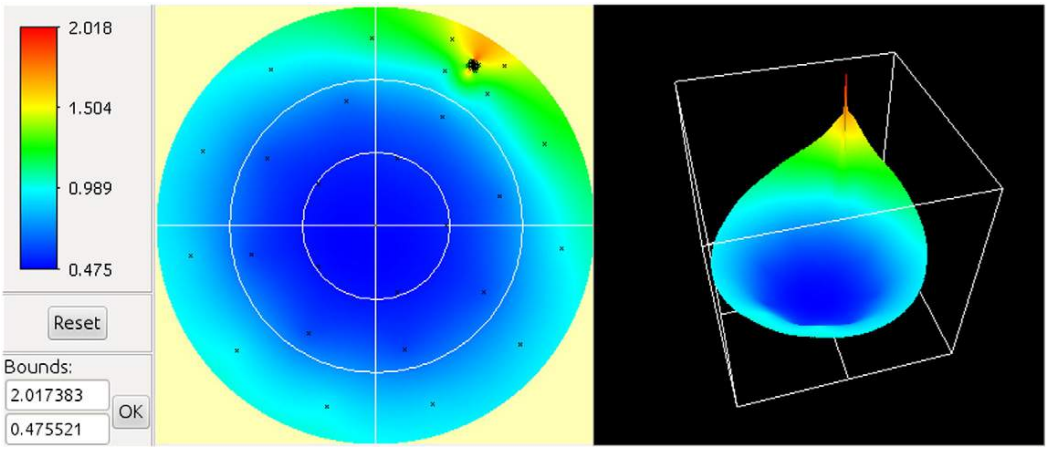

Fig. 8. Directional reflectance of a vegetation cover with hot spot configuration.

Table 5
Simulated exitance and nadir reflectance (Vegetation).

	Nadir reflectance	Exitance ($W \cdot m^{-2} \cdot \mu m^{-1}$)
No HS (50 directions)	0.484	60.233
HS (50 + 25 directions)	0.491	59.673
HS (2000 + 25 directions)	0.490	59.130

Lambertian reflectance (0.2) and a roughness such that $\eta_{spec} = 200$ and $\alpha_{spec} = 0.1$ rad.

Sun position is ($\theta_s = 30$, $\phi_s = 225$). 100 directions are used to discretize the 4π space. In addition, the angular region around the specular direction ($\theta_o = 30$, $\theta_o = 45$) is oversampled with 25 directions. The solid angle of the region is 0.08. Fig. 7 shows the BRF distribution result in polar coordinate system. As expected, specular reflection is not displayed if directions around the specular direction are not simulated (Fig. 7(a)). Use of 25 directions centered on the specular direction allows one to simulate the angular decrease of specular reflectance from the theoretical specular direction (Fig. 7(b)). Here, specular reflection does not influence the reflectance for other directions, because the scattering scene is a 2D surface without any multiple scattering mechanism.

5.2. Vegetation

We illustrate the impact of the 4π space discretization in the presence of multiple scattering. For that, we consider a scene that is a homogeneous vegetation cover. Table 4 summarizes its characteristics. Here, vegetation is simply simulated as the superposition of homogeneous turbid layers.

Usually, the reflectance of vegetation is maximal for the scattering direction that corresponds to sun direction. This is the so-called hot spot configuration (Fig. 8). It corresponds to a strong local anisotropy of scene reflectance. Account of hot spot configuration is important for simulating reflectance values around the hot spot angular region, Hereafter, an overestimation or underestimation of radiation in the hot spot angular region has an impact on radiation along other directions.

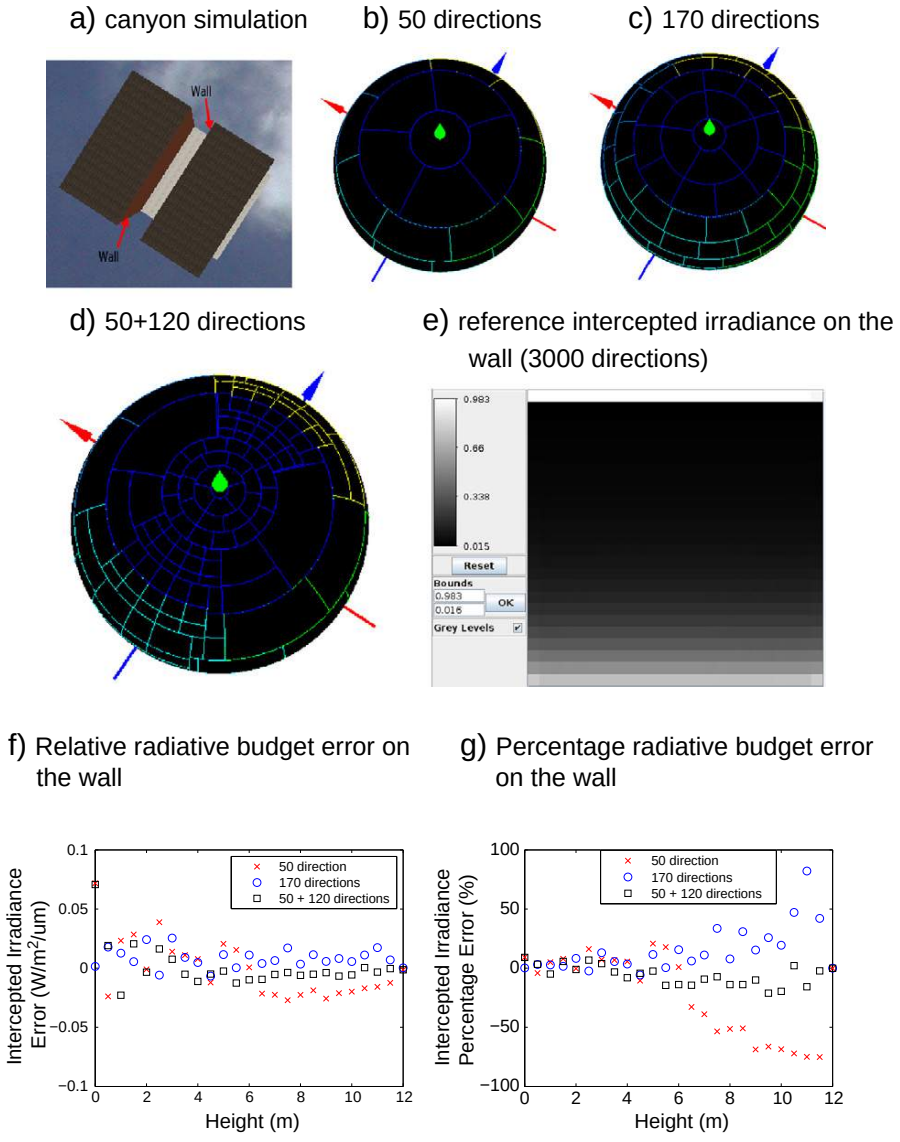

Fig. 9. Simulation of urban canyon.

Table 6
Canyon simulation.

Parameter	Value
Scene irradiance ($W \cdot m^{-2} \cdot \mu m^{-1}$)	1446.99
Wavelength (μm)	0.65
Horizontal resolution (m)	0.2
Vertical resolution (m)	0.5
Sun angle Ω_s (θ, ϕ)	(0, 0)
Building width (m)	5
Building height (m)	12
Roof reflectance (Lambertian)	0.05
Wall reflectance (Lambertian)	0.5
Street reflectance (Lambertian)	0.5
Street width	2

A question is: how to sample the hot spot angular region for simulating landscape exitance and reflectance (e.g., at nadir) with a given accuracy? The way to answer this question is illustrated here with 3 simulations (Table 5): a simulation with 50 directions with 1 direction centered on the hot spot, a similar simulation for which the hot spot angular region is oversampled with 25 discrete directions, and a simulation with 2000 directions, that is used here as a reference simulation. It appears that oversampling the hot spot angular region improves the relative accuracy of nadir reflectance from 1.23% to 0.20% and exitance from 1.87% to 0.92%.

5.3. Urban landscapes

Actual earth scenes can have BRF values with several peaks. In that case it is important to oversample several angular regions. Here, we illustrate such a configuration with the case of an urban landscape.

We consider an urban street that is simulated with a simple canyon shape: a street between 2 vertical walls and 2 horizontal roofs (Fig. 9(a)). Parameters are shown in Table 6. Sun is at nadir. Thus, the walls of buildings only receive the radiation reflected by the street (which is illuminated by the sun directly) and multiple scattering from the opposite wall. With 50 initial directions (Fig. 9(b)), the solid angle of the nadir direction has a lower boundary located at $\theta_1^1 = 12.86$. The top of the walls is seen from the center of the street with a zenith angle equal to $atan(1/12) = 4.76 < < \theta_1^1$ from the center of the street. Therefore, the energy reflected along the nadir direction and all directions in the plane is over-estimated, and the energy received and reflected by the walls is under-estimated.

The same simulation was conducted with an oversampling of angular regions (Fig. 9(d)) with additional 120 directions that sample the angular region that corresponds to the solid angle according to which one sees the sky and the top of the walls from the street center. For comparison, the case with 170 directions is also simulated (Fig. 3). Major differences occur for directions that reach the top of the walls from the street center. It results that it impacts the radiative budget of the walls. The accuracy is decreased as the height of the wall increases, since more pixels are covered by a single large solid angle, and the irradiance distributed to each pixel is hard to be differentiated. This is the reason for the importance of regional oversampling. The reference value considered to be accurate is set to be the simulation with 3000 directions (intercepted irradiance of wall in Fig. 9(e)). Fig. 9(f) and (g) shows the relative and percentage errors of the simulations with and without oversampling. The percentage error of the upper part of the wall is reduced dramatically by the oversampling.

6. Conclusion

A new direction discretization method IUSD for radiative transfer modeling is presented. It defines discrete directions with optimal central directions and solid angle shape that fulfill the condition of squared angular sector. The resultant distribution of directions is quite uniform and satisfies both the zeroth and the first moments. Formulations in the radiative transfer equation are similar to traditional discretization methods (DOM, FVM, etc.). The algorithm has several interesting advantages comparing to other methods. Firstly, any even number of directions can be defined. Also, the number, the shape and solid angle of discrete directions within each zenith layer are adjustable. For example, solid angles can be weighted by the squared cosine of the zenith angle. Furthermore, numerical quadratures are easily applied because the boundaries of each direction are exactly defined, and zenith can be sampled according to its cosine of value to reduce the non-linearity.

Results in this paper show that the IUSD method is more accurate than the S_n DOM, the $N_\theta \times N_\phi$ FVM and the FT_n FVM methods in the case of multiple scattering within turbid medium simulation. 2 oversampling methods based on IUSD are presented: IUSD-Windmill and IUSD-EO, which allow one to add any direction or set of directions on the 4π sphere, and oversample any number of angular regions. The IUSD-Windmill is used to simulate strong anisotropic configurations (specular reflection, hot spot, etc.). For scenes that have a strongly anisotropic radiation region, the method proved to be very useful in order to improve the simulation of scene reflectance and radiative budget. Especially for hot spot configuration, the shape of the hot spot can be extracted from direction oversampling. Another major advantage of this approach is to improve results without a large increase of the number of directions. This is very interesting in terms of computation time. Indeed, computation time increases with the number of discrete directions that contribute to radiative transfer. This method is implemented in the current DART model (http://www.cesbio.ups-tlse.fr/us/dart.html). We believe that heat and mass transfer applications can also benefit from this method.

Acknowledgment

This work is undertaken in the frame of a project of the French Space Center (CNES) “Preparation of a Geostationary satellite with high spatial resolution”.

References

Chai, J. C., Lee, H. S., & Patankar, S. V. (1994). Finite volume method for radiation heat transfer. *Journal of Thermophysics and Heat Transfer*, *8*(3), 419–425.
Chandrasekhar, S. (1969). *Radiative transfer*. : Dover Publications.
Chui, E. H., & Raithby, G. D. (1993). Computation of radiant heat transfer on a nonorthogonal mesh using the finite-volume method. *Numerical Heat Transfer Part B: Fundamentals*, *23*, 269–288.
Fiveland, W. A. (1984). Discrete ordinate methods for radiative transport equation for rectangular enclosures. *Journal of Heat Transfer*, *106*, 699–706.
Fiveland, W. A. (1987). Discrete ordinate methods for radiative heat transfer in isotropically and anisotropically scattering media. *Journal of Heat Transfer*, *109*, 809–812.
Fiveland, W. A. (1988). Three-dimensional radiative heat-transfer solutions by the discrete-ordinates method. *Journal of Heat Transfer*, *2*(4), 309–316.
Gastellu-Etchegorry, J. -P., Demarez, V., Pinel, V., & Zagolski, F. (1996). Modeling radiative transfer in heterogeneous 3-d vegetation canopies. *Remote Sensing of Environment*, *58*, 131–156.
Gastellu-Etchegorry, J. P., Grau, E., & Lauret, N. (2012). DART: A 3D model for remote sensing images and radiative budget of earth surfaces. In Catalin Alexandru (Ed.), *Modeling and Simulation in Engineering*, http://dx.doi.org/10.5772/31315 ISBN: 978-953-51-0012-6, InTech.
Gastellu-Etchegorry, J. -P., Martin, E., & Gascon, F. (2004). Dart: A 3-d model for simulating satellite images and surface radiation budget. *International Journal of Remote Sensing*, *25*(1), 75–96.
Kim, S. H., & Huh, K. Y. (2000). A new angular discretization scheme of the finite volume method for 3-d radiative heat transfer in absorbing, emitting and anisotropically scattering media. *International Journal of Heat and Mass Transfer*, *43*(7), 1233–1242.
Kimes, D., & Kirchner, J. (1982). Radiative transfer model for heterogeneous 3-d scenes. *Applied Optics*, *21*, 4119–4129.
Lathrop, K. D. (1966). Use of discrete-ordinate methods for solution of photon transport problems. *Nuclear Science and Engineering*, *24*, 381–388.
Lathrop, K. D., & Carlson, B. G. (1965). Discrete-ordinates angular quadrature of the neutron transport equation. *Technical information series report LASL-3186.*: Los Alamos Scientific Laboratory.
Mishra, S. C., Chugh, P., Kumar, P., & Mitra, K. (2006). Development and comparison of the dtm, the dom, and the fvm formulations for the short-pulse laser transport

through a participating medium. *International Journal of Heat and Mass Transfer*, *49*, 1820–1832.
Modest, M. F. (2003). *Radiative heat transfer* (2nd ed.).
Myneni, R., Marshak, A., Knyazikhin, Y., & G., A. (1991). Discrete ordinate method for photon transport in leaf canopies, photon-vegetation interactions. *Photon-vegetation interactions: Applications in optical remote sensing and plant ecology* (pp. 45–109).
Raithby, G. D. (1999). Discussion of the finite-volume method for radiation, and its application using 3d unstructured meshes. *Numerical Heat Transfer Part B: Fundamentals*, *35*(4), 389–405.
Raithby, G. D., & Chui, E. H. (1990). A finite-volume method for predicting a radiant heat transfer enclosures with participating media. *Journal of Heat Transfer*, *112*(2), 415–423.
Truelove, J. S. (1987). Discrete-ordinate solutions of the radiation transport equation. *Journal of Heat Transfer*, *109*(4), 1048–1051.
Truelove, J. S. (1988). Three-dimensional radiation in absorbing–emitting–scattering media using the discrete-ordinates approximation. *Journal of Quantitative Spectroscopy and Radiative Transfer*, *39*(1), 27–31.
Verhoef, W. (1984). Light scattering by leaf layers with application to canopy reflectance modeling: The sail model. *Remote Sensing of Environment*, *16*, 125–141.

Chapter 3

Simulation of passive sensor images through finite FOV

Comparison of actual and simulated remotely sensed images is difficult since in many cases, simulated images are not realistic enough in terms of both radiometry and geometry. This chapter presents a modeling approach that aims to provide realistic sensor image simulation. For that, it combines the DART 3D radiative transfer model (RTM) with 3D perspective projection to simulate the image of the Earth scene as acquired by a camera or a cross-track sensor (e.g., scanner, pushbroom). Nowadays, many different types of data acquisition are possible with sensors on board satellites and remote sensing data are available with the fast evolution of sensors on board satellites, planes and unmanned aerial vehicles (UAV). RTM is commonly considered as a classical tool to simulate and validate remote sensing measurement. Most present works on RTMs are focused on mathematical modeling based on 3D landscape simulation, for better simulating the angular distribution of the Earth landscape radiance. This approach is based on the assumption that all parts of the simulated landscape are viewed along the same direction, which is inconsistent with actual measurement where multi-directional acquisition is used within the sensor FOV. Indeed, traditional RTMs cannot account camera model and its image projection geometry, such as classical perspective projection for camera and parallel-perspective projection for cross-track imagers (e.g., linear pushbroom camera, whiskbroom scanner, scanning radiometer, etc.). This situation is particularly problematic for airborne acquisitions with relatively low sensor altitude and wide field of view.

A new modeling approach, the so-called Convergent Tracking and Perspective Projection (CTPP), is designed and implemented in order to solve this problem. The pre-defined virtual direction concept presented in Chapter 2 is extended to the automated steering virtual direction (ASVD). The ASVDs correspond to the already mentioned "non predefined virtual discrete directions". These directions and their associated scattering transfer functions are not pre-computed. They change their directional vectors during ray tracking. Therefore, the virtual fluxes which enter the input aperture of an imaging sensor can come from various directional vectors going through an ASVD. For that, acquisition is simulated for the exact view direction associated with each participating Earth surface element during tracking,

according to the instant positions of both the sensor and the scattering point in the 3D architecture of the Earth landscape.

This new approach improves the usefulness and flexibility of RTMs for simulating actual observations. Both cross-track imager and camera geometries are modeled for most classical configurations. With this implementation, DART provides novel results for many research areas, including:

1. Passive sensor imaging, in presence of finite FOV.
2. Video captured by unmanned aerial vehicle (UAV).
3. Local hot spot (HS) effect in a RS image.
4. Pixel-wise comparison between actual and simulated orthorectified perspective-projection images.
5. Study of radiance variation between images acquired by airborne and spaceborne systems. This is important for inter-calibration purpose and for up-scaling / down-scaling approaches.

These 5 points are illustrated here. Another important application of this method is accurate pixel-wise comparison between simulated and acquired RS data, for any configuration. This potential is illustrated by a few examples in Section 3.1, with the paper "Simulation of multi-view sensor images of the Earth scene by linking 3D radiative transfer modeling with perspective projection".

In Appendix II, DART simulated images are compared with Airborne Prism Experiment (APEX) hyperspectral data. Comparison results show an improvement compared to a previous work (Schneider et al., 2014) that was conducted with DART images that were simulated with the orthographic projection along the average view direction of a swath. This improvement is detailed in the second section of this Chapter, with the Conference proceeding "At-Sensor Radiance Simulation for Airborne Imaging Spectroscopy"

It is interesting to note that the CTPP method is used for simulating LIDAR waveforms and their solar noise (Chapter 4), and also multi-view sensor image fusion (Chapter 5).

3.1 Article: "Simulating images of passive sensors with finite field of view by coupling 3-D radiative transfer model and sensor perspective projection

Remote Sensing of Environment 162 (2015) 169–185

Contents lists available at ScienceDirect

Remote Sensing of Environment

journal homepage: www.elsevier.com/locate/rse

Simulating images of passive sensors with finite field of view by coupling 3-D radiative transfer model and sensor perspective projection

Tiangang Yin *, Nicolas Lauret, Jean-Philippe Gastellu-Etchegorry

Centre d'Etudes Spatiales de la BIOsphere - CNES, CNRS, IRD, Universite de Toulouse, 18 avenue, Edouard Belin, bpi 2801, 31401 Toulouse cedex 9, France

ARTICLE INFO

Article history:
Received 28 July 2014
Received in revised form 17 February 2015
Accepted 20 February 2015
Available online xxxx

Keywords:
Radiative transfer
Perspective projection
DART
Field of view
Camera
Cross-track scanner
Airborne
UAV
Pushbroom imager
Hot spot

ABSTRACT

Comparison of actual and simulated remotely sensed data is difficult if simulated data are not realistic in terms of both radiometry and geometry. This paper presents a modeling approach that considers the multi-directional acquisition within sensor field of view (FOV) in order to simulate realistic images of Earth surfaces, as acquired by passive sensor with a finite FOV. In this approach, the DART (Discrete Anisotropic Radiative Transfer) 3-D radiative transfer model (RTM) is coupled with 3-D perspective projection. Current RTMs assume that all parts of the studied landscape are viewed along the same direction, although all passive imagers acquire energy in a FOV with a nonzero solid angle. In addition, they cannot account camera model and its image projection geometry (e.g., perspective projection for camera and parallel-perspective projection for cross-track imager). This situation is particularly problematic for airborne acquisition with low sensor altitude and wide FOV. Our new modeling approach solves this problem: rays that enter a sensor can come from various directions. For that, during ray tracking, each passive sensor acquisition is simulated for the exact view direction, which is the instant vector from the scattering point to the sensor position. Camera and cross-track imager are both modeled for most classical configurations. With this implementation, DART provides original simulations and assessments for various research domains, including: 1. Passive sensor imaging; 2. Video captured by unmanned aerial vehicle (UAV); 3. Local hot spot (HS) effect in a RS image; 4. Pixel-wise comparison between simulated orthorectified perspective-projection images; and 5. Radiance variation among images acquired by airborne and spaceborne systems with different sensor altitudes. These 5 points are illustrated here. Accurate pixel-wise comparison between simulated and acquired RS data, for any configuration is another important application of this approach.

1. Introduction

Presently, improvements of measurement accuracy and data transfer techniques drive the increasing number of new active and passive sensors mounted on satellites and airplanes to study the Earth's surfaces. Especially, emerging sensors on aircrafts and UAVs are quite favored for their relatively low cost, high spatial/temporal resolution and flexibility. The existing passive sensors used in RS measurements receive signals within their wide FOVs in order to broaden the observing region. Most imaging sensors mounted on satellites and aircrafts are usually cross-track imagers (e.g. linear pushbroom camera, whiskbroom scanner, and scanning radiometer), while those mounted on UAVs are usually frame cameras. A cross-track imager acquires data in parallel cross-track planes, which are usually perpendicular to its platform trajectory and uniformly separated. Within a cross-track plane, the radiance values from a row of across track pixels along different viewing angles are retrieved. For example, NASA's Cloud Absorption Radiometer (CAR) (Gatebe, Dubovik, King, & Sinyuk, 2010; Gatebe et al., 2003; King, Strange, Leone, & Blaine, 1986) has a wide angular FOV up to 190°. Recent developments of the airborne and spaceborne cross-track imager systems tend to use hyperspectral imaging spectroscopy (e.g. the Airborne Prism EXperiment (APEX) of ESA Jehle et al., 2010; Schaepman et al., 2015), and the combination with scanning LIDAR (e.g. Carnegie Airborne Observatory (CAO) Asner et al., 2007 and Goddard's LiDAR, Hyperspectral and Thermal Imager (G-LiHT) Cook et al., 2013). Compared with aircrafts, UAVs are used for observations of relatively smaller areas. Frame cameras are mostly on board UAV and airplanes. They are capable of providing real-time information of the Earth's surfaces and generate images and videos with high resolution (Berni, Zarco-Tejada, Suárez, & Fereres, 2009).

Radiative transfer models (RTM) are extensively applied to simulate the radiation interaction of the Earth's environment in spectral domain from the visible to the thermal. Many works have been devoted for improving RTMs and accurate simulations of the 3-D Earth's surfaces constructed by explicit physical features and elements with associated optical properties. Intercomparison among RTMs is gradually developed with the increasing requirement of modeling accuracy. The RAMI

* Corresponding author.
E-mail address: tiangang.yin.85@gmail.com (T. Yin).

http://dx.doi.org/10.1016/j.rse.2015.02.020
0034-4257/

(Radiative Transfer Model Intercomparison) experiment of the Joint Research Center of European Commission is a typical example (Pinty et al., 2001, 2004; Widlowski et al., 2007; Widlowski, Pinty, Clerici, et al., 2011; Widlowski, Pinty, Lopatka, et al., 2011). This intercomparison has been continuously improved during the past 15 years with 4 phases. It provides reference reflectance values of simple and complex 3-D Earth scenes. One of the main challenges faced by RAMI is the lack of absolute reference standards from actual measurements. Any comparison of RTMs with actual data is quite complicated due to numerous factors, such as errors of geometric construction of 3-D scenes, incomplete object parameterization and sensor noise associated to the measurements. The RAMI defined references are based on the convergent results throughout years of experiments using several "credible" RT models (Widlowski et al., 2008). Another challenge of the intercomparison is the limitation of comparable results provided by RTMs. Most of the comparisons were only done for the scene bidirectional reflectance factor (BRF), albedo (terminology following Schaepman-Strub, Schaepman, Painter, Dangel, and Martonchik (2006)), and to a lesser extent, LIDAR waveform of a single pulse.

There are 3 major constraints for comparing RTM with sensor data:

1. Errors of measurement and data processing: Sensor have systematic errors, and their raw data must go through several processing steps before being suitable for applications. These steps include: radiometric correction, geocoding, orthorectification, atmosphere correction, resampling and interpolation. All steps potentially give rise to errors compared to the physical signal (i.e., ideal RTM) at sensor entrance.
2. Inaccurate account of atmosphere in RTMs: Most RTMs work with partial or no account of the atmosphere radiative coupling with the Earth's surfaces, which lead to inaccurate simulation of neighborhood effects at pixel level.
3. Neglect of sensor geometric configuration in RTM: Mapping 3-D objects onto a 2-D image plane (IP) (a mesh grid with pre-defined size), needs an adaptation method of projection. Usually, classical perspective projection (Sonka, Hlavac, & Boyle, 2008) is applied for cameras, and parallel-perspective projection (Chai & Shum, 2000; Gupta & Hartley, 1997; Zhu, Hanson, & Riseman, 2004) is applied for cross-track imagers. They are crucial in obtaining exact radiance values and their spatial distribution in the IPs. Numerous RTMs utilize a combined method of exact kernel and discrete ordinate method (DOM) to solve the transfer function in steady-state process (Fiveland, 1988; Modest, 2013). In DOM, the 4π space is discretized into a finite number of directions and rays propagate only along these directions. RTMs that use DOM, simulate scene radiance values along a specific direction and the radiance values are orthographically projected onto the IP. This method performs well in calculating scene or pixel reflectance for a given view direction. However, DOM is not appropriate for simulating actual sensor images, since multi-directional acquisitions within sensor FOV and perspective projection are not considered. It results in direction offset for each pixel in simulated image, which makes it extremely difficult to conduct pixel-wise comparisons with actual sensor image. This inconsistency is much amplified with 3-D Earth landscapes, especially if the simulated sensor is at low altitude with a wide FOV.

Discrete anisotropic radiative transfer (DART) (Gastellu-Etchegorry, Demarez, Pinel, & Zagolski, 1996; Gastellu-Etchegorry, Grau, & Lauret, 2012; Gastellu-Etchegorry, Martin, & Gascon, 2004; Gastellu-Etchegorry et al., 2015) can overcome most of the difficulties of the 2nd constraint. In the past 20 years, DART has proved to be one of the most accurate 3-D RT models (Widlowski et al., 2007) to simulate RS data and radiative budget of the Earth's surfaces. DART was the first model to simulate images of orthographic projection for 3-D scenes (Gastellu-Etchegorry et al., 1996) with flexible configurations including spatial resolution, number of bands, and view direction. Its major advantage is to work with any type of 3-D urban and vegetation landscape with topography, for simulating their 3-D radiative budget, active LIDAR signals and radiometric images, from the visible to the thermal infrared spectral domain. Furthermore, the Earth-atmosphere radiative coupling of heterogeneous scenes is implemented (Gastellu-Etchegorry et al., 2004; Grau & Gastellu-Etchegorry, 2013), and validated by comparisons with MODTRAN model (Berk, Bernstein, & Robertson, 1987; Berk et al., 1999). Schneider et al. (2014) carried out a pixel-wise comparison between APEX airborne images and orthographic-projection images (OPImage) simulated by DART over the Laegern forest site (Switzerland). In this study, a high-fidelity test scene (300 m × 300 m) was created from a 3-D forest reconstruction parameterized using airborne, in-situ and laboratory approaches (including airborne and terrestrial LIDAR) (Morsdorf, Kötz, Meier, Itten, & Allgöwer, 2006; Morsdorf, Nichol, Malthus, & Woodhouse, 2009; Morsdorf et al., 2004). The sensor altitude was 4526 m above sea level with the view zenith angle between 3.8° and 9.7° over the scene. The DART simulated image used for comparison was the orthorectified OPImage at the direction of the scene center (view zenith angle = 6.75°). Coefficients of determination for pixel-wise comparisons were 0.55, 0.56, 0.39, and 0.48 for the spectral bands at 533 nm, 570 nm, 680 nm, and 780 nm, respectively. These results are quite encouraging. However, one may wonder if better comparison could be obtained with radiance values that correspond to the precise directions of "object-to-sensor" geometries for each pixel of the image.

Indeed, the OPImage simulated by DART can be considered as a sensor image with the assumption that the sensor is infinitely far away from the Earth and the study area is relatively small, i.e. the FOV is very narrow, which explains that all parts of the study area are approximated to be observed along the same direction. If the solid angle of the FOV cannot be neglected, multi-directional geometry must be considered (e.g. airborne acquisitions), and tracking algorithms adapted to perspective projection must be implemented to simulate images. In a DART simulation, a direction-image bijection map is created. The direction mapped to the perspective-projection image (PPImage) must be adapted to each element in the 3-D landscape that scatters a ray towards the sensor. It leads to the appearance of spatial enlargement and offset of objects in the PPImage compared with the OPImage that corresponds to the view direction at the center of the scene. Furthermore, for each scattering event, the scattering phase function also has to be updated according to the direction towards the sensor during ray tracking. It induces that the radiance value of a defined scattering element on the sensor raw image differs from that on the OPImage. These are the crucial difficulties to overcome the 3rd constraint mentioned above.

In this paper, we present a modeling approach that links DART to 3-D perspective projection to simulate actual sensor acquisitions: the so-called convergent tracking and perspective projection (CTPP). Basically, based on our previous work related to the direction discretization and oversampling method in DART (Yin, Gastellu-Etchegorry, Lauret, Grau, & Rubio, 2013), a concept called automated steering virtual direction (ASVD) is introduced to represent the direction whose vector can be updated during ray tracking according to the point-sensor geometry. Thus, it can account the multi-directional acquisition within the finite FOV of a sensor. CTPP is implemented in the DART release (Version>5.4.7) for both camera mode and cross-track imager mode, and it is applied for evaluations and assessments of several research domains in this paper. By using CTPP, images and videos are efficiently simulated (through multi-thread processing) with various platform altitudes (from 10s of meters for a UAV to 100ks of meter for a satellite), sensor orientations and FOVs. Both raw and orthorectified sensor images can be generated directly by DART.

In addition, local hot spot (HS) effect on a RS image is simulated with CTPP. The HS effect is an optical phenomenon of vegetation that affects RS acquisitions, which depends on the geometry of solar and view direction (Hapke, DiMucci, Nelson, & Smythe, 1996). If the view direction and the solar direction are exactly aligned, any solar ray that is

intercepted and backscattered towards the solar direction reaches the sensor without any further interception. For this particular direction, scatterers fully mask their own shadows, and around this direction, their shadows are partially masked. Therefore, the radiance value for this direction is usually much larger than for other view directions where shadows of leaves can be seen. Around this direction, the enhancement effect gradually dissipates, which induces an angular sector that is influenced by the HS. In traditional RTMs that simulate OPImage, the HS effect is simulated at a fixed view direction, so all parts of the radiance image are equally enhanced by the HS. However, by considering a finite sensor FOV, which is usually much wider than the angular sector influenced by the HS, the radiance enhancement appears only on part of an image. Accurate simulation of this effect can help to better understand the HS apparent greening region on an image, and to filter the HS effect from an image with given solar and sensor geometry (Morton et al., 2014).

Furthermore, CTPP is used to study the variation of radiances acquired by airborne and spaceborne platforms. It is generally accepted that reflectance values of the same Earth's surface are equal for airborne and spaceborne acquisitions if the view directions are the same and if atmospheric effects are negligible or perfectly corrected. Actually, a given Earth's surface with the same overall view direction from a satellite and from an aircraft is not observed with exactly the same FOV configurations: the airborne sensor has a much broader FOV. This can lead to crucial differences since the Earth's surface has an anisotropic directional reflectance. Here, the variation of radiance/reflectance measured by sensors with the same central direction of FOV but different sensor altitude is studied by the CTPP approach. This variation explains the difficulties and the constraints to validate spaceborne products with airborne products, and more generally, to compute sensor measurements acquired under different FOV configurations. For example, it explains the variation of the bidirectional reflectance distribution function (BRDF) product derived from CAR and the Moderate Resolution Imaging Spectroradiometer (MODIS) (Román et al., 2011, 2013).

Nomenclature

ASVD	automated steering virtual direction
BOA	bottom of atmosphere
BRDF	bidirectional reflectance distribution function
BRF	bidirectional reflectance factor
CTPP	converging tracking and perspective projection
DOM	discrete ordinate method
FOV	field of view
HS	hot spot
IP	Image Plane
hIP	horizontal Image Plane
pIP	projection Image Plane
oIP	orthorectification Image Plane
IUSD	iterative uniform squared discretization
LAD	leaf angle distribution
LAI	leaf area index
OPImage	Orthographic-Projection Image
PPImage	Perspective-Projection Image
PTOP	parallel tracking and orthographic projection
RPC	rational polynomial coefficient
RS	remote sensing
RTM	radiative transfer model
UAV	unmanned aerial vehicles

2. Background

The theoretical parts of DART that are used for the present work are discussed below. For other aspects, one is advised to refer to Gastellu-Etchegorry et al. (2004, 2012, 2015). DART simulates heterogeneous scenes with 3-D voxels of uniform size (Δx, Δy, Δz). The voxels are the storage units where radiative interaction occurs. They can contain 2-D facets and combinations of different types of turbid medium (i.e., vegetation, atmosphere or fluids), which are the 2 ways that are used by DART for simulating urban and natural landscapes. Fig. 1 shows the 3-D voxels that are used to construct a DART scene with dimension (X_s, Y_s, Z_s). Turbid medium gives rise to volume interaction. It is used for simulating the atmosphere, vegetation, and any type of fluid, with specific properties (leaf area index (LAI), leaf angle distribution (LAD), aerosol/molecule density, etc.). Facets give rise to surface interaction. They are used for simulating roofs and walls of houses, trunks and branches of trees, foliar elements or part of them, as well as topography, etc. Facets can have any dimension. They are usually small for simulating landscapes with complex architecture. Facet optical properties (specular/isotropic/anisotropic reflectance, direct/isotropic/anisotropic transmittance, absorption, etc.) can be directly specified or indirectly derived through biochemical properties, using the PROSPECT model (Feret et al., 2008). A similar approach is adopted for defining optical properties of turbid media. Vegetation (grass, tree crown, etc.) can be simulated either as turbid medium or as cluster of facets of leaves. Here, we consider the simulation of vegetation as the juxtaposition of 3-D vegetation turbid cells with specified volume properties per cell (LAI, LAD, etc.). It is the optimal approach in terms of computation speed and memory if vegetation is simulated with a very large set of facets. Turbid medium uniformly fills the whole volume of a single voxel. Facets can be embedded inside turbid cells (e.g. branches within tree crown). Radiance attenuation within turbid cells follows Beer's law. For a radiation with radiant intensity $I(r, \Omega_n)$ (unit: W/sr) that propagates in participating media along direction Ω_n at position r, the steady-state discrete 3-D radiative transfer equation is expressed as:

$$\left(\xi\frac{d}{dx}+\eta\frac{d}{dy}+\mu\frac{d}{dz}\right)I(r,\Omega_n) = -\alpha(r,\Omega_n)I(r,\Omega_n)+J_e(r,\Omega_n)+\sum_{m=1}^{N}\alpha_d(r,\Omega_m)\frac{P(r,\Omega_m\rightarrow\Omega_n)}{4\pi}I(r,\Omega_m)\Delta\Omega_m \quad (1)$$

where the terms on the left side of the equation are the divergence of radiant intensity; (ξ, η, μ) are the dot products of unit vector along Ω_n with unit vector of x, y, z axes respectively; $J_e(r, \Omega_n)$ is the emitted radiant flux at position r; α is the total extinction coefficient ($\alpha = \alpha_a + \alpha_d$); α_a and α_d are coefficients of absorption and scattering, respectively; the summation term represents the numerical integration of the scattering from all the incoming radiation with radiant intensity $I(r, \Omega_m)$ over the 4π space, where each direction Ω_m among the N discrete directions sub-divides the 4π space; $\frac{P(r,\Omega_m\rightarrow\Omega_n)}{4\pi}$ is the scattering phase function at position r from Ω_m to Ω_n. All terms of Eq. (1) vary with r in heterogeneous landscapes. The details of the approach used to solve Eq. (1) for volume (i.e., turbid medium) and surface elements are described by Gastellu-Etchegorry et al. (1996).

In the illumination stage of the Earth scene, DART considers both the direct and diffuse radiations that reach the bottom of atmosphere (BOA). The associated directional distribution of radiance is either specified (e.g., SKYL factor: $\frac{diffuse\ \ isotropic\ \ irradiance}{total\ \ irradiance}$), or calculated from ray tracking in the discretized atmosphere cells above the Earth scene. For atmosphere tracking, the properties of the atmosphere cells (aerosol and molecule vertical distribution, phase function, etc.) are either specified or retrieved from SQL database. The Earth scene is illuminated by rays that originate from the centers of sub-divisions (so-called sub-centers) of the top faces of cells on the top of the scene. The number of sub-centers per cell face can be specified, in order to get a more or less dense illumination pattern. In the Earth scene, the direct sun and atmosphere rays are tracked until they are fully intercepted or their energies become lower than a defined threshold.

The scattering process is simulated with an iterative approach until convergence is reached. Starting from the intercepted energy within each cell of previous iteration (illumination stage for the 1st iteration), rays are scattered and tracked from a finite number of points that are

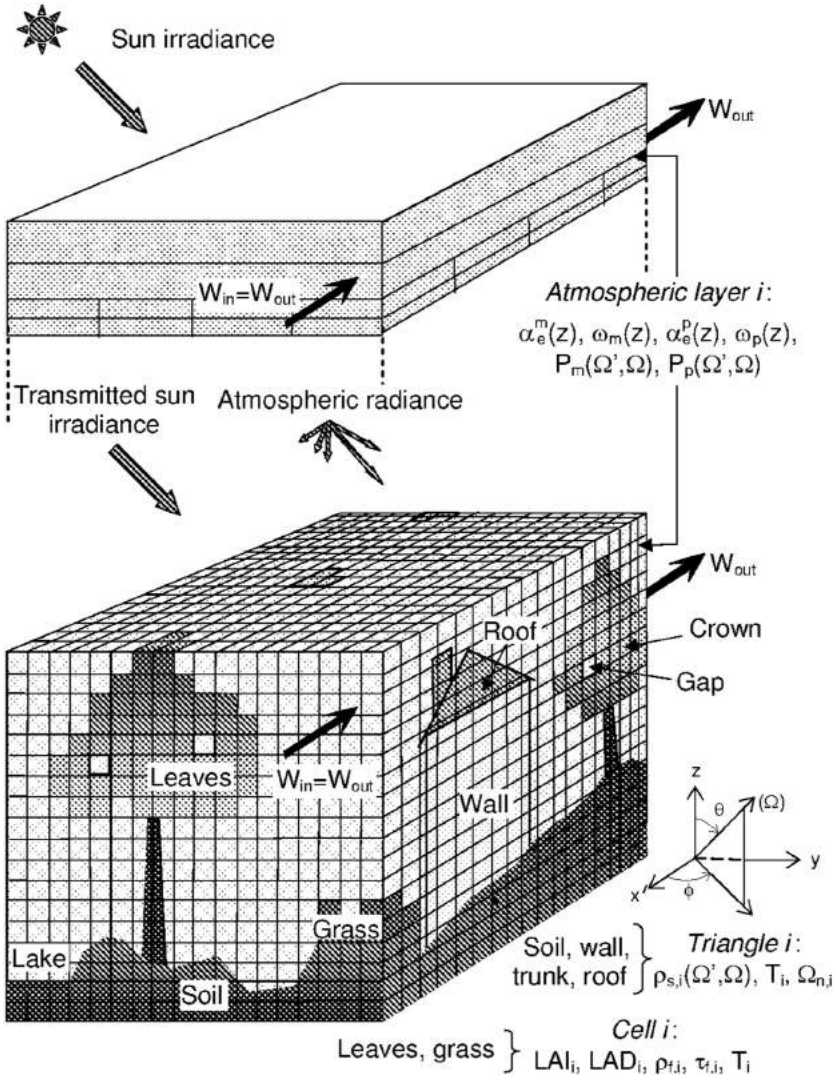

Fig. 1. DART simulated scene system.

pre-defined grids that sub-divide the cell. Scattering occurs with rays towards all the possible directions over the 4π space. The scattered rays experience surface and volume interactions with facets and turbid cells, respectively. Methods are implemented in order to limit the number of interception points to store, and consequently the number of scattering events to compute. This number depends on the number of sub-faces of each cell face and the number of sub-cells of each cell accordingly. For example, with a defined number m of sub-divisions in a cell along one dimension, each cell face is divided into m^2 sub-faces, which results in m^3 sub-cells. For volume interaction, interception points are grouped per incident cell sub-face and per incident angular sector. An angular sector is a set of neighboring discrete directions. Actually, 2 centroids are computed for both upward and downward rays per sub-cell to achieve better accuracy. For surface interaction, the interception points associated to a given facet are grouped per sub-cell and per incident angular sector. The centroids of all interception points per sub-cell are calculated and stored. In each DART iteration, rays are scattered from each centroid within each cell. After being scattered or emitted (thermal mode), rays that cross the face of their original cell are merged per cell sub-face and per discrete direction. Rays that reach the BOA level are projected onto a horizontal IP (hIP). The spatial extent of each ray on the hIP depends on the area of the scattering element that gives rise to the ray. The spatial distribution of ray intensities on the mesh grid of the hIP constitutes an image for the considered upward direction per iteration. The DART iterative process stops if the relative difference of BOA exitance between 2 consecutive iterations is smaller than a defined threshold. Similarly, an individual ray is stopped if its energy becomes too small. Any DART product (i.e., images or 3-D radiative budget) is an exponential extrapolation of the last 3 iterations.

DART pre-calculates the bi-directional phase functions ($\frac{P(r,\Omega_m\rightarrow\Omega_n)}{4\pi}$) of all materials that constitute the Earth scene. They are calculated for all the directions over the 4π space. Recently, a novel direction discretization scheme called iterative uniform squared discretization (IUSD) (Yin, Gastellu-Etchegorry, Lauret, et al., 2013) is implemented in DART. As illustrated in Fig. 2, the IUSD method is able to generate any number of directions (N) of uniform or cosine-weighted distribution of solid angles over the 4π space. The resultant directions satisfy both 0th and 1st moments of classical discretization methods (the S_nDOM (Chandrasekhar, 1969), the finite volume method (FVM) Chai, Lee, & Patankar, 1994). The advantage of the IUSD method over the other discretization methods is that the shape and centroid of a direction

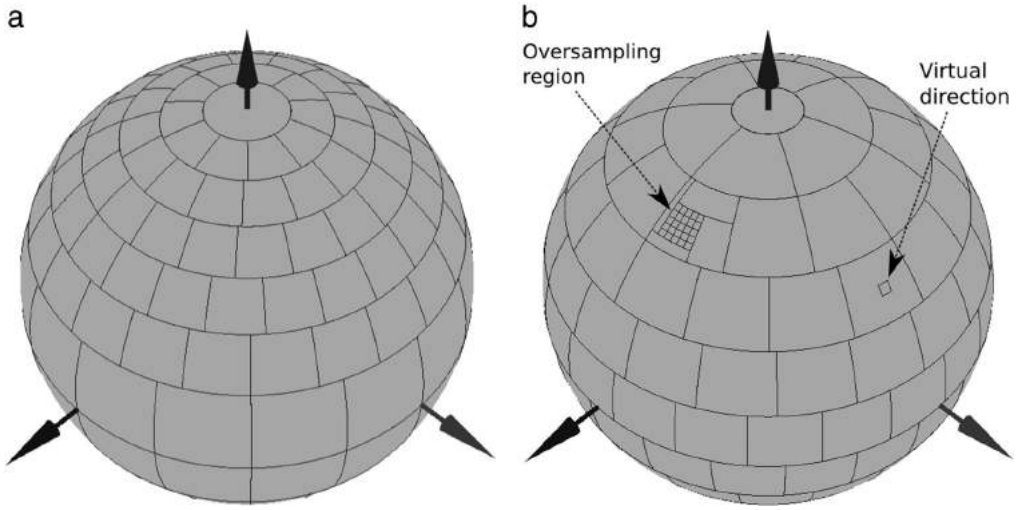

Fig. 2. Examples of IUSD method for direction discretization and oversampling. (a) 216 directions of cosine-weighted distribution of solid angles. (b) 150 directions of uniform distribution of solid angles with an oversampling region ($\theta = 35^{\circ}$, $\phi = 10^{\circ}$, $\Delta\Omega = 0.02sr$) and an additional virtual direction ($\theta = 50^{\circ}$, $\phi = 80^{\circ}$, $\Delta\Omega = 0.002sr$).

(Ω, $\Delta\Omega$) are well defined. The centroid (zenith angle θ_c and azimuth angle ϕ_c) of each direction is calculated such that either the zenith or the azimuth axis passing through it partitions the solid angle $\Delta\Omega$ into 2 equal solid angles ($\frac{\Delta\Omega}{2}$). The boundaries of each direction ensure that the lengths of the arcs which pass through (θ_c, ϕ_c) and are bounded by zenith and azimuth angular range ($\Delta\theta$, $\Delta\phi$), are equal ($\Delta\theta = \sin\theta_c\Delta\phi$). The IUSD method provides more accurate BRF than other methods with the same number of directions. Furthermore, the IUSD method provides two ways of adding additional directions over the pre-defined sampling of the 4π space (Fig. 2(b)) (Section 4 in Yin, Gastellu-Etchegorry, Lauret, et al. (2013)). Both methods are used in the modeling approach that is presented in this work:

1. Adding virtual directions: A ray along a virtual direction (virtual ray) undergoes the same interception as a ray along any discrete direction, except that it does not contribute to scattering after interception. Therefore, without breaking the conservation of energy, these directions are called "virtual". The virtual rays that reach the BOA level contribute to the radiance images which are bijected to the directions they propagate along.
   An advantage of a virtual direction is that it costs much less computation time than a discrete direction. Arbitrary number of virtual directions can be added to a DART simulation to generate arbitrary number of images.
2. Oversampling angular regions: The pre-defined set of discrete directions can be oversampled in one or multiple user-specified angular regions of interest (e.g. around the HS). If the added oversampled region is within a discrete direction, it implies the replacement of that direction with the considered oversampling region and 4 new discrete directions. If the oversampling region overlaps more than one discrete direction, the overlapped sub-region of each occupied discrete direction is divided separately. Any region can be oversampled by any number of additional directions. The set of all the original and added discrete directions makes up the 4π space, and contributes to the RTM. This technique (IUSD-Windmill) has proved to be quite efficient in modeling the directional distribution of specular and HS radiance, as well as radiative budget.

DART pre-computes scattering transfer functions for all these directions. It can simulate images for all discrete and virtual upward directions in each iteration. For that, it uses a method called parallel tracking and orthographic projection (PTOP) (Fig. 3). In order to simulate an image along a certain direction Ω, an associated hIP is created at the minimum altitude of the scene (e.g., the ground $z = 0$), to store the radiations that reach BOA. The reason for using $z = 0$ instead of the BOA altitude ($z = Z_s$) is to keep the scene origin ($x = 0, y = 0, z = 0$) consistent with the image origin (top-left corner). The hIP acts as a bridge between the ray tracking process and the image projection. Each attenuated ray that reaches the BOA is projected onto the hIP along the opposite direction of that ray. As illustrated in Fig. 3(a), according to the shape of the scattering element, the energy carried by a ray is uniformly distributed over the projected area of the element onto the hIP. This projected area on the hIP is determined by point projections of the element's vertices. For turbid cells, the sub-face through which the ray exits the cell is projected. Since the direction is fixed, the projection onto the hIP is parallel. Fig. 3(b) provides a test simulated scene of a single tree, with solar illumination direction ($\theta_s = 30^{\circ}$, $\phi_s = 225^{\circ}$) and view direction ($\theta_v = 45^{\circ}$, $\phi_v = 90^{\circ}$). Fig. 3(c) shows the image generated on the hIP, which uses the coordinate system of the simulated scene. The output OPImage is computed by orthographic projection from the image on the hIP to another IP perpendicular to the view direction, the so-called the projection IP (pIP) (Fig. 3(d)). Fig. 3(e) shows the output OPImage, which uses the local coordinate system of the view direction. Pixels outside the boundaries of the projected area for the whole scene onto the pIP, are set to (− 1) to be distinguished from the pixels within the boundaries.

3. Theory of converging tracking and perspective projection (CTPP)

The sensor is similar to the human eye, whose reception area is much smaller than its observed region at the far field. Radiation that enters a sensor has a converging geometry instead of a parallel geometry for orthographic projection. Perspective projection is generally applied in machine vision and computer graphics. It projects 3-D objects onto the IP along converging lines to the center of projection. The orthographic projection of identical objects onto the IP gives equal areas, regardless of their distance to the IP. However, for perspective projection, a near object has larger projection area onto the sensor IP than an identical distant object. For a RS sensor with a very narrow FOV, the dispersion of the rays that enter the sensor is usually neglected. This corresponds to PTOP in traditional RTMs. However, if the FOV of a sensor cannot be neglected, rays that enter the sensor must be converging instead of being parallel. Here, we present a novel approach which considers perspective projection in RTM, the so-called converging

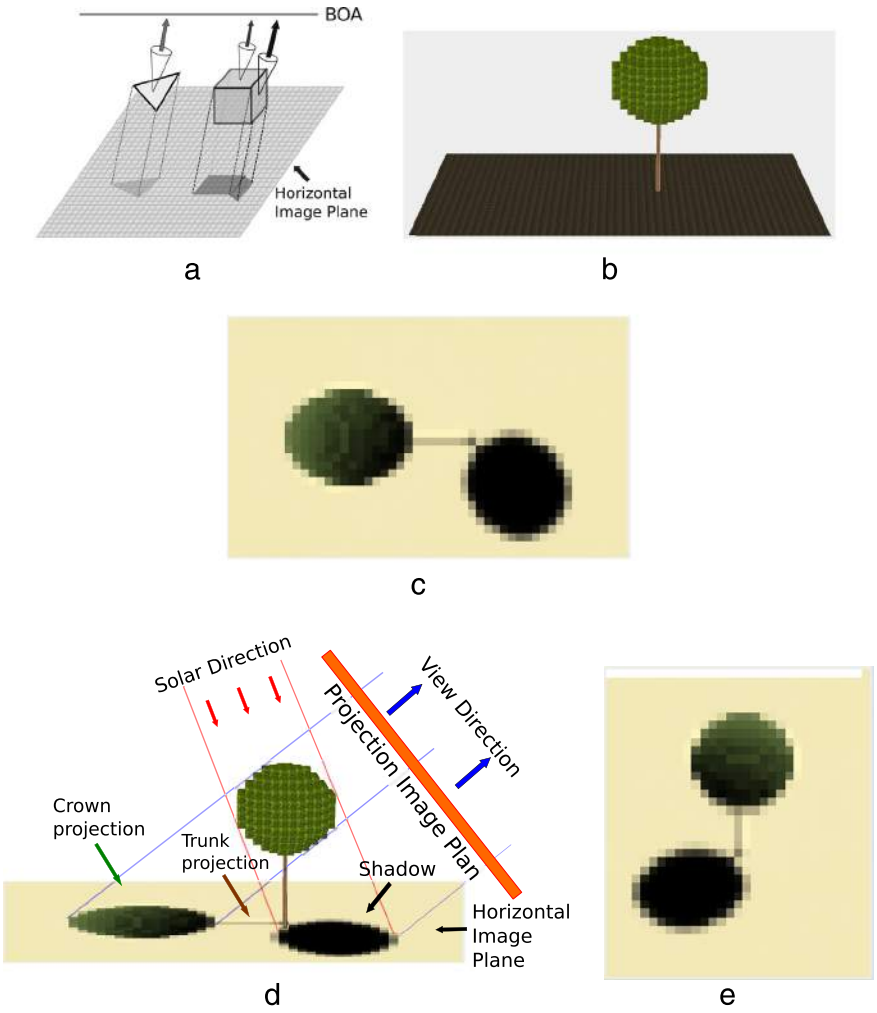

Fig. 3. Parallel tracking and orthographic projection (PTOP) in DART simulation. (a) Orthographic projections of facets and turbid cells onto the hIP. (b) Simulated scene of a tree and ground. (c) Generated radiance image on the hIP through PTOP. (d) Radiance projection onto the hIP, and orthographic projection from the image on the hIP to the pIP. (e) Final OPImage generated on the pIP.

tracking and perspective projection (CTPP). It must be noted that some models such as DIRSIG (http://dirsig.org/) have the capability to simulate airborne sensors. However, these models are not easily accessible to the scientific community.

3.1. Pinhole camera projection model

For a pinhole camera with a long distance from the observed region, the vanishing point of its FOV is assumed to be located at the position of the camera. Any measured ray follows a direction that starts from the location where it was scattered or emitted, to the camera position, possibly with attenuation. Fig. 4 illustrates CTPP for a pinhole camera in the DART simulation. The expanded region of any measured ray is accurately computed as the perspective projection of facets and turbid cells where the ray comes from onto the hIP (Fig. 4(a)). Compared with orthographic projection, the projected region of a scene element is stretched to the positions of the projected vertices. This is illustrated by the same scene shown in Fig. 3(b). In this theoretical case, a camera is assumed located at an altitude that is twice the tree height. It is not a very realistic configuration, but it is a good example for demonstration of perspective projection The image recorded on the hIP is shown in Fig. 4(b). It differs a lot from the result from PTOP (Fig. 3(c)). Indeed, the tree crown appearing on the image is axially extended twice as much. It explains that on the hIP, the tree crown dimension is much larger than the tree shadow, which has the same size as through orthographic projection. The trunk of the tree does not appear on the hIP, since it is behind the crown from the point of view of the camera. Similarly, part of the shadow is masked by the crown. These differences explain that OPImage can differ from the PPImage, when the sensor FOV is not negligible. The pIP is set to be perpendicular to the camera orientation. This orientation is specified in DART by the precession, nutation, and intrinsic rotation angles from nadir view of the carrier platform. In the example of Fig. 4, the camera is looking at the center of the scene and the intrinsic rotation is set to 0°. The image generated on the pIP uses the classical perspective projection of the image on the hIP (Fig. 4(c)).

3.2. Cross-track imager projection model

The swath of a cross-track imager is parallel with the platform trajectory, whereas its cross-track direction is usually perpendicular to the trajectory, but not necessarily. In a classical operating mode, the cross-track plane is vertical, usually with a viewing angle range from the left side to the right side of the nadir direction. Different from a camera, the image acquisition by a cross-track imager uses the parallel-perspective projection, where parallel projection and

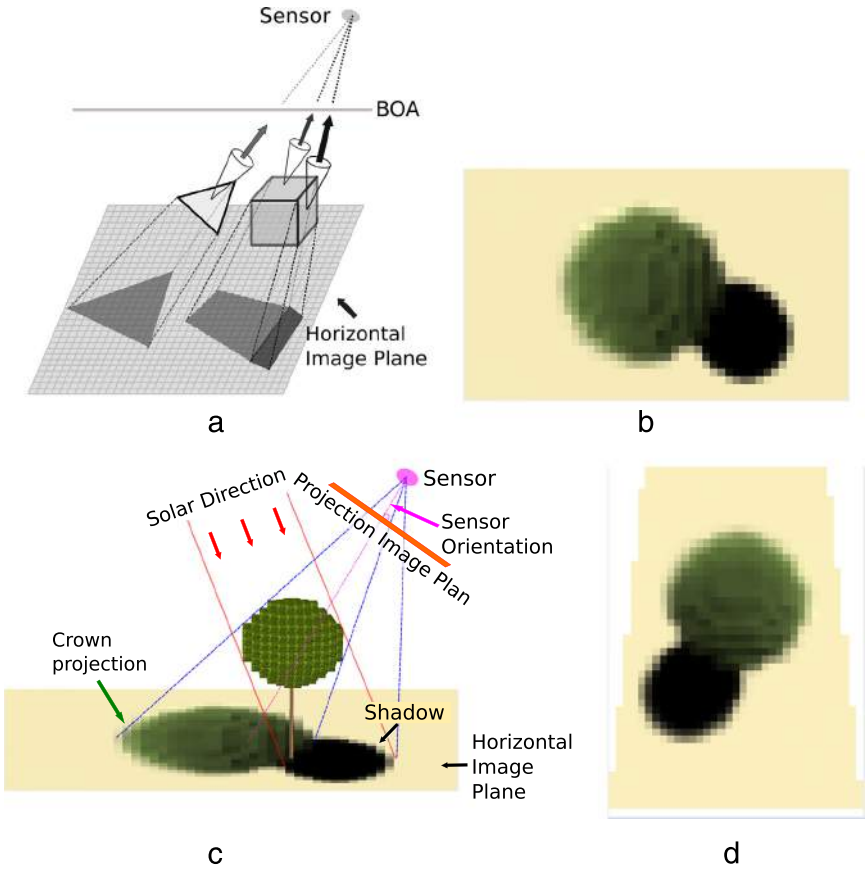

Fig. 4. Converging tracking and perspective projection (CTPP) for a pinhole camera. (a) Perspective projection of facets and turbid cells onto the hIP. (b) Generated radiance image on the hIP through CTPP using the same scene as Fig. 3(b). (c) Radiance expansion by perspective projection onto the hIP and perspective projection from the image on the hIP to the pIP. (d) Final PPImage generated on the pIP.

perspective projection are applied along track and across track, respectively. Fig. 5 illustrates CTPP for a cross-track imager in the DART simulation. When the sensor is moving forward along a straight horizontal flight path, all points of a line lying along track are viewed from the same direction. Therefore, this line is projected onto the hIP with parallel projection. Conversely, for a line lying across track, all points of the line are viewed from different directions. They share the same platform position as the vanishing point. Therefore, this line is projected onto the hIP with perspective projection. The parallel-perspective projection is illustrated by along-track and across-track line cross sections of a facet and a turbid cell in Fig. 5(a). It results that the objects projected onto the hIP are stretched across track (perspective projection), and remain constant along track (parallel projection). An example of projected image onto the hIP is illustrated in Fig. 5(b), using the same DART simulated scene in Fig. 3(b). The platform moving path is a straight horizontal line passing through the same position as the camera shown in

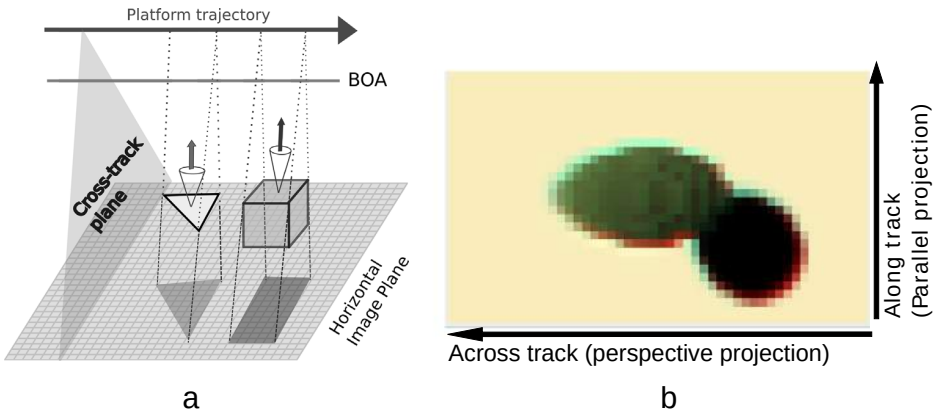

Fig. 5. Converging tracking and perspective projection (CTPP) for a cross-track imager. (a) Parallel-perspective projection of facets and turbid cells onto the hIP. (b) Image generated by DART on the hIP by CTPP using the same scene as Fig. 3(b); parallel-projection is applied along track and perspective-projection is applied across track.

Fig. 4(c). In Fig. 5(b), the tree crown size is stretched across track like that in Fig. 4(b), and remains constant along track like that in Fig. 3(c). The pIP and the hIP are actually identical for cross-track imager, so the generated PPImage on the hIP is directly considered as the sensor raw image. The raw image of a cross-track imager usually has to be orthorectified for RS applications.

3.3. Automated steering virtual direction

In DART, a direction-image bijection map is created to store the simulated images. Before the introduction of CTPP, an upward direction was compulsory for an OPImage in DART. The introduction of CTPP relies on a new type of direction: the so-called automated steering virtual direction (ASVD), which is bijected to a PPImage. The property of a ASVD is virtual, so basically it has all the characteristics of a virtual direction mentioned above. More specifically, the vector representing ASVD is updated during ray tracking, according to the position of each scattering/emitting point of the simulated 3-D scene and the corresponding sensor position. A scattering event in DART is illustrated in Fig. 6. The scattering element is located at position $M(x, y, z)$, with a single-side area A_M. $\Omega_V(x, y, z)$ is an ASVD with solid angle $\Delta\Omega_V(x, y, z)$ to the sensor at position $P_S(x_S, y_S, z_S)$. DART computes the ray $W(x, y, z, \Omega_D)$ from M for each discrete direction $(\Omega_D, \Delta\Omega_D)$ over the 4π space. In addition, it calculates the instantaneous virtual ray through the ASVD $(\Omega_V(x, y, z), \Delta\Omega_V(x, y, z))$. One should notice that the vector of the ASVD is updated for each particular scattering event. The updated unit vector of the ASVD from M is:

$$\overrightarrow{\Omega_V} = norm\left(\overrightarrow{P_S} - \overrightarrow{M}\right) \tag{2}$$

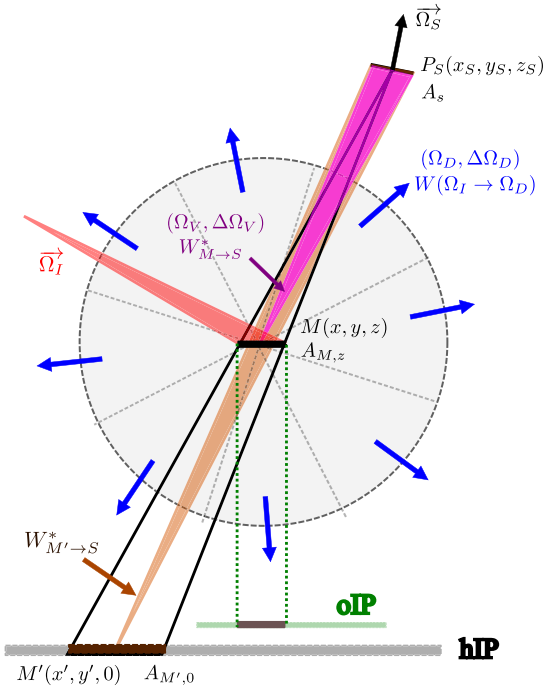

Fig. 6. Diagram of ray projection in a scattering event through CTPP. An incident ray through direction Ω_I arrives at a scattering element located at M with area $A_{M,z}$. The scattered rays through a set of discrete ordinates Ω_D that sample the 4π space are represented by $W(\Omega_I \to \Omega_D)$. A virtual ray $W_{M\to S}^*$ is sent towards the sensor through an updated ASVD Ω_V. It is projected backward onto the hIP (projected area $A_{M',0}$), with equivalent ray $W^*_{M'\to S}$ sent towards the sensor to generate the same radiance value as $W_{M\to S}^*$ does. During DART orthorectification, $W_{M\to S}^*$ is orthographically projected onto the oIP.

The distance $R_{M,S}$ from M to the sensor, and the solid angle $\Delta\Omega_V$ are also updated:

$$R_{M,S} = |\overrightarrow{P_S} - \overrightarrow{M}| \tag{3}$$

$$\Delta\Omega_V = \frac{A_S \cdot \overrightarrow{\Omega_V} \cdot \overrightarrow{\Omega_S}}{R^2_{M,S}} \tag{4}$$

where A_S is the area of the sensor aperture, and $\overrightarrow{\Omega_S}$ represents the sensor orientation unit vector (θ_S, ϕ_S).

For a pinhole camera, P_S is a constant, while for a cross-track imager, $P_S(x_S, y_S, z_S)$ depends on $M(x, y, z)$. In order to define a horizontal linear trajectory of a cross-track imager, a point on the trajectory $P_{sc}(x_{sc}, y_{sc}, z_S)$ and the along-track direction (expressed by platform azimuth angle ϕ_p) must be defined. The horizontal trajectory is expressed as:

$$-\sin\phi_p \cdot (x_S - x_{sc}) + \cos\phi_p \cdot (y_S - y_{sc}) = 0 \tag{5}$$

If the cross-track plane is not perfectly perpendicular to the along-track direction, an offset azimuth angle (ϕ_o) can be taken into consideration. The equation of the horizontal line that represents the cross-track direction passing through (x_S, y_S) is:

$$\cos\left(\phi_p + \phi_o\right)(x_S - x) + \sin\left(\phi_p + \phi_o\right)(y_S - y) = 0 \tag{6}$$

By combining Eqs. (5) and (6), the cross-track imager horizontal coordinate x_S and y_S is given by the intersection of the two lines:

$$\begin{aligned} x_S &= \frac{\left(\sin\phi_p \cdot x - \cos\left(\phi_p + \phi_o\right) \cdot y\right)\sin\left(\phi_p + \phi_o\right) - \left(\cos\phi_p \cdot x_{sc} + \sin\left(\phi_p + \phi_o\right) \cdot y_{sc}\right) \cdot \cos(\phi_p + \phi_o)}{\sin\phi_p \cdot \sin\left(\phi_p + \phi_o\right) + \cos\phi_p \cdot \cos\left(\phi_p + \phi_o\right)} \\ y_S &= \frac{\left(\cos\left(\phi_p + \phi_o\right) \cdot y - \sin\phi_p \cdot x\right)\cos\phi_p + \left(\cos\phi_p \cdot x_{sc} + \sin\left(\phi_p + \phi_o\right) \cdot y_{sc}\right)\sin\phi_p}{\sin\phi_p \cdot \sin\left(\phi_p + \phi_o\right) + \cos\phi_p \cdot \cos\left(\phi_p + \phi_o\right)} \end{aligned} \tag{7}$$

then, Eqs. (2), (3) and (4) are applied to update the virtual cross-track imager direction.

3.4. Convergent ray tracking

The discrete directions that partition the 4π space possibly with a number of additional ordinary virtual directions, as well as their associated scattering functions for each type of materials are pre-computed by DART. However, this is not the case for ASVDs. Indeed, the vector of an ASVD is changing during the tracking and the pre-calculations for the ASVD are over-numerous, since the order of magnitude of pre-calculations depends on the total number of potential scattering events in the 3-D scene. Similarly, DART does not pre-calculate the scattering functions for the ASVDs. For an incident ray from direction Ω_I, irregular grid interpolation method (e.g. radial basis function (RBF) interpolation) could be applied on the pre-calculated scattering functions each time to calculate the exact scattered energy towards the AVSD. However, such interpolation is quite a burden for computation speed if it is called for all scattering events (Press, 2007). In order to accelerate the computational speed, the virtual ray through the ASVD (Fig. 6) is expressed as:

$$W^*_{\Omega_I \to \Omega_V} = W(\Omega_I \to \Omega_D) \cdot \frac{\Delta\Omega_V}{\Delta\Omega_D} \tag{8}$$

where Ω_D represents the discrete direction which has Ω_V within its boundaries. The ray along Ω_V is calculated as the scattering energy along Ω_D multiplied by the fraction of the solid angles.

By substituting Eq. (4) into Eq. (8), we get the attenuated ray that reaches the sensor:

$$W^*_{M\to S} = \tau_{M\to S}\cdot\frac{W(\Omega_I\to\Omega_D)}{\Delta\Omega_D}\cdot\frac{A_S\cdot\overrightarrow{\Omega_V}\cdot\overrightarrow{\Omega_S}}{R^2_{M,S}} \tag{9}$$

by using the transmittance $\tau_{M\to S}$ from M to the sensor.

3.5. Energy projection on the hIP

The energy of a ray which enters the sensor is firstly projected onto the hIP and then onto the pIP. Both projections are calculated in such a way that the radiance value remains constant from the scattering point to the hIP and from the hIP to the pIP.

The projection for the scattering element at M onto the hIP is a 2-D surface. This surface is considered to "emit" a ray which gives rise to a radiance value at sensor level that is equal to the radiance value provided by the ray with power $W^*_{M\to S}$ from the element M. The radiance value added to the sensor image by $W^*_{M\to S}$ as shown in Fig. 6 is:

$$L^*_{M\to S} = \frac{W^*_{M\to S}}{A_{M,z}\cdot\cos\theta_V\cdot\Delta\Omega_V} \tag{10}$$

where $A_{M,z}$ is the projected area of the object onto a horizontal layer at altitude z, and θ_V is the zenith angle of the view direction Ω_V.

Let M' be the projected region of the object on the hIP with position $(x', y', 0)$ and area $A_{M',0}$. $W^*_{M'\to S}$ represents the virtual ray from $M'(x', y', 0)$ to the sensor. The equivalence of radiance implies:

$$\frac{W^*_{M\to S}\cdot R^2_{M,S}}{A_{M,z}\cdot\cos\theta_V\cdot A_S\cdot\overrightarrow{\Omega_V}\cdot\overrightarrow{\Omega_S}} = \frac{W^*_{M'\to S}\cdot R^2_{M',S}}{A_{M',0}\cdot\cos\theta_V\cdot A_S\cdot\overrightarrow{\Omega_V}\cdot\overrightarrow{\Omega_S}} \tag{11}$$

where $R_{M',S}$ is the distance from M' to sensor.

Eq. (11) leads to:

$$W^*_{M'\to S} = \frac{W^*_{M\to S}\cdot\Delta z^2_{M,S}\cdot A_{M',0}}{z^2\cdot A_{M,z}} \tag{12}$$

where $\Delta z_{M,S}$ and z are the altitude differences from the sensor to M and M', respectively.

For a pinhole camera (Fig. 4), the projected area of the object onto hIP is extended towards both axes. We have

$$A_{M',0,camera} = \left(z/\Delta z_{M,S}\right)^2\cdot A_{M,z} \tag{13}$$

Substitution of Eq. (13) into Eq. (12) implies that the fluxes from M and M' to the camera are actually equal:

$$W^*_{M'\to S,camera} = W^*_{M\to S,camera} \tag{14}$$

On the other hand, for a cross-track imager (Fig. 5), the projected area is extended along the cross-track plane, and keeps the same along the moving direction. We have:

$$A_{M',0,scanner} = \left(\Delta z_{M',S}/\Delta z_{M,S}\right)\cdot A_{M,z} \tag{15}$$

Substitution of Eq. (15) into Eq. (12) leads to:

$$W^*_{M'\to S,scanner} = \frac{\Delta z_{M,S}}{\Delta z_{M',S}}\cdot W^*_{M\to S,scanner} \tag{16}$$

3.6. Generation of PPImages and orthorectification

The projection of $W^*_{M'\to S}$ is distributed according to the mesh (pixel) size of the hIP $(\Delta x, \Delta y)$. The projected area of each object may occupy several pixels on the hIP. Let $\gamma_{i,j}$ be the fraction of projected area $A_{M',0}$ within pixel (i, j) on hIP. Let $\{M\}$ be the set of the scattering objects whose projection onto the hIP is at least partly within pixel (i, j), then the total power $W_{total,i,j}$ from pixel (i, j) is the summation: $W_{total,i,j} = \sum_{\{M\}}\gamma_{i,j}\cdot W^*_{M'\to S}$. The radiance value of pixel (i, j) is:

$$L\left(i,j,\Omega_{V,i,j}\right) = \frac{\sum_{\{M\}}\gamma_{i,j}\cdot W^*_{M'\to S}}{\Delta x\cdot\Delta y\cdot\cos\theta_{V,i,j}\cdot\Delta\Omega_{V,i,j}} \tag{17}$$

where $(\Omega_{V,i,j}, \Delta\Omega_{V,i,j})$ is the updated ASVD from the center location of pixel (i,j) to the sensor, and $\theta_{V,i,j}$ is the corresponding zenith angle.

The final step of projection from the hIP to the pIP is a classical perspective projection according to the defined sensor orientation (precession, nutation, and intrinsic angles). The precession angle and nutation angle have the same geometric definition as the sensor zenith and azimuth angles (θ_S, ϕ_S), respectively. The intrinsic angle r is the self rotation of the sensor, which is restricted by the center of the pIP. One needs to note that usually for a cross-track imager, the pIP is horizontal ($\theta_S = 0$, $\phi_S = 0$, and $r = \phi_p$). Detail of the projection algorithm can be found in Sonka et al. (2008) and Gupta and Hartley (1997).

Orthorectification is a classical technique which creates an image of nadir orthographic view from a sensor image that is acquired with various directions within its FOV. The orthorectification of images acquired by one or several sensors with different geometries produces images that are superimposed and registered, which facilitates their combined analysis. During orthorectification, the 3-D object is vertically orthoprojected to a fictive horizontal IP, the so-called orthorectified IP (oIP). The orthorectified image preserves the radiance value for each pixel associated to its original view direction. The classical orthorectification method is a post processing step after acquisition. It requires a rational polynomial coefficient (RPC) model built from the platform trajectory and direction of each acquisition and a reference surface model (e.g. digital elevation model or digital surface model), in order to map the raw image pixels to the geo-coordinate system. In DART, a rather straightforward approach is implemented. Indeed, the exact location of each scattering event that enters the sensor is known. Therefore, the ray is vertical-orthographically projected onto the oIP during tracking (Fig. 6). Let (i', j') be a pixel on oIP with dimension $(\Delta x'\cdot\Delta y')$, and $\gamma'_{i',j'}$ be the area fraction of $A_{M',0}$ over the pixel (i', j'). The radiance value of pixel (i', j') derived from Eq. (10) is:

$$L_{ortho}\left(i',j'\right) = \frac{\sum_{\{M\}}\gamma_{i',j'}\cdot W^*_{M\to S}}{\cdot\cos\theta_V\cdot\Delta\Omega_V}\Big/\Delta x'\cdot\Delta y' \tag{18}$$

where the summation is over $\{M\}$ which represents the set of all the scattering elements that have their projection part lying within pixel (i', j'). Pixels of oIP which are not seen by the sensor are set to a specific value (-1). This DART orthorectified image is too theoretical compared to actual orthorectified image. Thus it is correct but cannot be achieved from real RS data.

3.7. Adaptation to actual sensors

The ideal pinhole camera and cross-track imager (moving along a straight line) have theoretical configurations in DART compared to the actual measurement configuration. For example, the trajectory of a cross-track imager is usually not a straight line because of aircraft fluctuation and steering. In the previously presented method, the direction

from any location in the scene to the sensor must be known to calculate the radiance and projection of an object. Therefore, a general method is designed for determining iteratively the sensor direction for each position M in 3-D scene. This method requires a distribution map consisting of the view directions for all points of the ground surface. Hence, the question becomes how to determine the direction vector on a 3-D point $M(x, y, z)$ in the scene with known 2-D distribution $(\theta_{i,j}, \phi_{i,j})$ of sensor view directions on the ground. The process is divided into 5 steps:

1. From position $M(x, y, z)$, the coordinate of vertical projection of M on the ground $(M'(x, y))$ is calculated.
2. With interpolation of M' on the direction distribution map, the direction vector at M' is determined $(\overrightarrow{r'_M})$.
3. The projected position from M' along $\overrightarrow{r'_M}$ to the horizontal plane of altitude z is computed $(M_n(x', y', z))$.
4. The displacement vector from M_n to M is calculated $(D(x' - x, y' - y))$ and subtracted by position M' on the ground $(M' = (x - \lambda D_x, y - \lambda D_y))$, where $\lambda <= 1$ is a coefficient which slows down the convergence to avoid local minimums.
5. Go back to step 2, and start another iteration until $D(x' - x, y' - y)$ is smaller than a defined threshold.

With this approach, a direction vector can be determined for each scattering event in the 3-D scene. The vertices of scattering objects can be determined for the projection on IPs. In addition to the 2-D distribution of view directions, the sensor altitude needs to be known for each pixel. Furthermore, in actual acquisitions, the area of the projection of an object onto hIP does not follow Eq. (13) or Eq. (15). Consequently, the simplified Eqs. (14) and (16) cannot be used. Indeed, the implemented method uses Eq. (12) to calculate the ray from hIP.

4. Evaluations, assessments and tests

4.1. Image and video from a camera

DART simulates radiative transfer in a 3-D scene that is usually larger than the region for which one intends to simulate the acquisition by a digital camera or a cross-track imager. In order to simulate a camera FOV extent in the 3-D scene, 4 additional parameters need to be known to define this region: the location of the vanishing point of the camera (P_S), the camera orientation $(\Omega_S(\theta_S, \phi_S, r))$, the shape of the sensor detector array and the distance from the plane of detector array to the convergence point. For a detector array with a rectangular shape, the FOV extent on a horizontal plane at any altitude is a quadrilateral with irregular shape for oblique views. This quadrilateral is composed of 4 straight lines that are intersections of the horizontal plane with the 3-D FOV volume (tetrahedron shape). For a scattering event, $M(x, y, z)$ is checked with the 4 lines at altitude z to determine whether M is inside the quadrilateral. If the answer is yes, a virtual ray is calculated and delivered along the updated ASVD towards the camera.

Fig. 7 shows an example of the Saint-Sernin Basilica of Toulouse, France. The scene is a sub-region of the urban database from the CAPITOUL experiment (Masson et al., 2008). Fig. 7(a) illustrates the 3-D scene. The scene dimension is 300 m × 300 m × 80 m with voxel size of 1 m × 1 m × 1 m. The basilica (80 m high) is located at the center of the scene. An oversampling is applied on the hIP and pIP with a mesh grid size (pixel resolution) of 0.5 m × 0.5 m. The image captured in the FOV of a video camera has 400 × 300 pixels. The 4 lines of the quadrilateral projected onto the ground are displayed in Fig. 7(b) with the camera orientation: $\theta_S = 50^\circ$, $\phi_S = 0^\circ$, $r = 0^\circ$. The red circle is the projection of the center of the image, according to the camera orientation. The camera altitude is $z_S = 140$m. Fig. 7(c) shows the DART simulated reflectance images as RGB band combination (650 nm, 550 nm, 450 nm

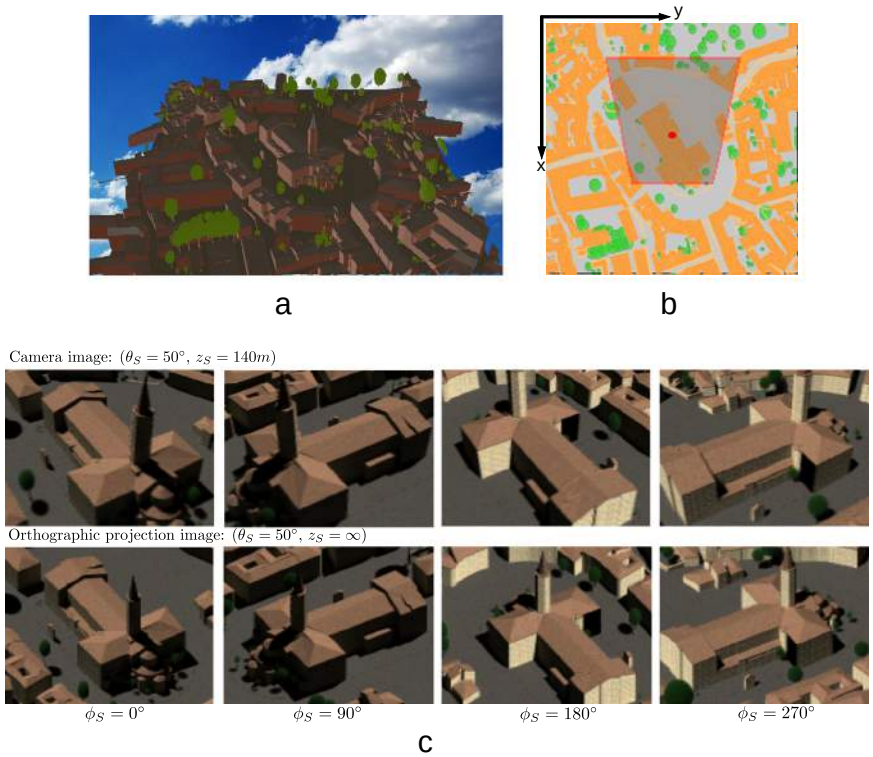

Fig. 7. DART simulated OPImages and camera images of Saint-Sernin Basilica (Toulouse, France). (a) Simulated 3-D scene. (b) FOV extent on the ground for a camera ($\theta = 50^\circ$, $\phi = 0^\circ$, $r = 0^\circ$, $z_S = 140$m). (c) Simulated camera images with sensor altitude $z_S = 140$m (top row) and OPImages (bottom row), for 4 different camera orientations ($\theta_S = 50^\circ$ and $\phi_S = 0^\circ, 90^\circ, 180^\circ, 270^\circ$). The solar direction has $\theta_s = 30^\circ$ and $\phi_s = 225^\circ$.

with bandwidth of 20 nm), with fixed solar direction ($\theta_s = 30^\circ, \phi_s = 225^\circ$) over the scene. The subfigure at the top-left corner is the simulated PPImage through CTPP with a defined camera orientation ($\theta_S = 50^\circ$, $\phi_S = 0^\circ, r = 0^\circ$). The bottom-left subfigure is the corresponding simulated OPImage of the same region through PTOP. The OPImage can be considered as the measurement of a camera with an altitude that is infinitely high.

From left to right, Fig. 7(c) shows the simulated camera images and the OPImages with various ϕ_S (0°, 90°, 180°, 270°). The top images correspond to the acquisition by an UAV camera with a circular trajectory around the basilica. The effect of perspective projection can be observed by comparing between the top and the bottom images. For example for $\phi_S = 0^\circ$ and 90°, the basilica tower (near field) is closer to the camera than the other side of the basilica (far field). By comparison between the camera image and the OPImage, the tower appears larger in the camera image than in the OPImage, whereas the other side of the basilica has the same size. This effect is reversed for $\phi_S = 180^\circ$ and 270°, since the near field and the far field are reversed.

Another example is taken from one of the actual canopy simulations of the RAMI-4 experiment: the Jarvselja Pine Stand (Summer) experiment. The detailed scene parameters are presented on the dedicated web page of RAMI-4 (http://rami-benchmark.jrc.ec.europa.eu/HTML/RAMI-IV/RAMI-IV.php). The scene has 1120 trees with optical properties in 19 bands provided for each tree species. The scene dimension is 103.2m × 103.2m × 18.8m with voxel size of 0.4m × 0, 4m × 0.4m (Fig. 8(a)). Facets representing the tree leaves are converted into turbid media. The distribution of the tree positions is shown in Fig. 8(b). Here, we show the simulation results for 3 bands ($B01 = 442.5$nm, $B02 = 551.5$nm, $B03 = 661.3$nm). The RGB combination ($R = B03$, $G = B02$, $B = B01$) creates the color images. Fig. 8(c) is the orthographic image created at nadir view with solar direction ($\theta_s = 36.6^\circ, \phi_s = 299.06^\circ$). Different from the original setting of the experiment, the isotropic diffuse component is removed from illumination ($SKYL = 0$), so only direct sun illumination is used in the simulation. PPImages with similar camera configurations as above are generated, with $z_S = 140$m, $\theta_S = 36.6^\circ, r = 0^\circ$, and 4 different sensor azimuth angles to define camera orientations (Fig. 8(e)). As expected, the aspects of the simulated PPImages depend on the camera orientation. For example, pixel values (i.e., reflectance) are much lower for $\phi_S = 90^\circ$ than for $\phi_S = 0^\circ$ and 270°. Indeed, for these 2 cases, the acquisitions are generally with the backscattering configuration, which is closer to the HS configuration (Hapke et al., 1996). Each pixel value of the camera image depends on its location. For example, the left side of the camera image for $\phi_S = 270^\circ$ is much brighter than the right side. It corresponds to the fact that the left side is closer to the HS configuration.

Unlimited number of ASVDs can be added in a DART simulation, so the same number of bijected PPImages can be simulated at the same time in a DART simulation. With many ASVDs, processing speed is the most crucial concern. For that, multi-thread processing with Boost C++ library is implemented in DART. With 4 threads, the processing speed is accelerated by approximately 3 times (some thread-specific attributes slow down the processing). The possibility to simulate large sequences of sensor PPImages is illustrated here with the Saint-Sernin and the Jarvselja scenes. We simulated 360 camera images with ϕ_S ranging from 0° to 359°. Both simulations took less than 60 min on a server with 24 parallel threads. The resultant images were converted into video frames, and joined together into a video of 24 s, with 15 frames per second. They can be downloaded from the DART website (http://www.cesbio.ups-tlse.fr/dart/license/en/dartResults.php).

4.2. Hot spot regional enhancement in passive sensor images

With turbid media, DART simulates the HS using the approach of Kuusk (1991). In this approach, the extinction coefficient α_e for 1st order scattering along the view direction Ω_v depends on the solar direction (Ω_s), the apparent leaf dimension $s_f(\Omega_v)$, and the path $\delta s_i(\Omega_v)$ along direction Ω_v from the scattering event position M_s:

$$\alpha_e = u_f \cdot G(\Omega_v) \times \left(1 - \sqrt{\frac{G(\Omega_s)\cdot\mu_v}{G(\Omega_v)\cdot|\mu_s|}} \cdot exp\left(\frac{-\Delta(\Omega_s,\Omega_v)}{s_f(\Omega_v)} \cdot \delta s_i(\Omega_v)\cdot\mu_v\right)\right) \quad (19)$$

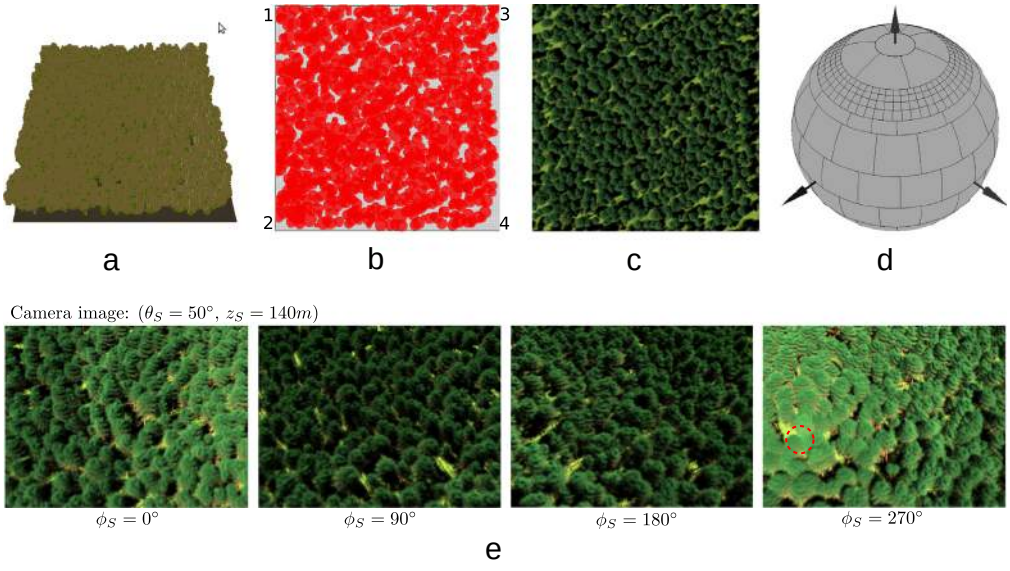

Fig. 8. DART camera images simulation over the Jarvselja pine stand forest site in summer (Estonia). (a) Simulated 3-D scene. (b) Distribution of the trees over the scene. (c) Simulated nadir OPImage by DART. (d) Direction discretization (317 directions) to simulate camera images with $\theta_S = 50^\circ$, $z_S = 140$m, and $\phi_S \in [0\ 360]$. (e) Simulated camera images with sensor altitude $z_S = 140$m for 4 different camera orientations ($\theta_S = 50^\circ$ and $\phi_S = 0^\circ, 90^\circ, 180^\circ, 270^\circ$). The solar direction has $\theta_s = 36.6^\circ$ and $\phi_s = 299.06^\circ$.

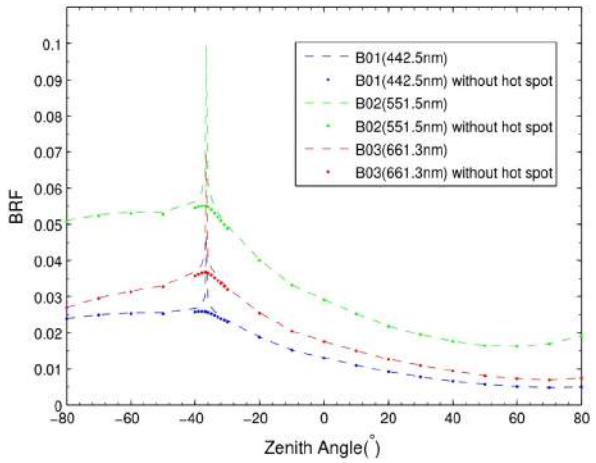

Fig. 9. Calculated BRF distribution of the Jarvselja forest site in the sun principal plane ($\phi_v = 299.06^{\circ}$) with ($d_f = 0.1cm$, dashed lines) and without (dotted lines) HS effect. Negative θ_{vp} represents backscattering (with the HS located at $\theta_{vp} = -36.6 = -\theta_s$).

where u_f is the leaf volume density of the cell; $G(\Omega)$ is the mean projection of a unit leaf along direction Ω; $\mu_s = \cos\theta_s$; $\mu_v = \cos\theta_v$; and:

$$\Delta(\Omega_s, \Omega_v) = \sqrt{\frac{1}{\mu_v^2} + \frac{1}{\mu_s^2} - \frac{2cosg}{|\mu_s||\mu_v|}}$$

where $cosg = \overrightarrow{\Omega_s} \cdot \overrightarrow{\Omega_v}$. For random distribution of circular leaves according to normalized leaf angle distribution $\frac{g_f(\Omega_f)}{2\pi}$:

$$s_f(\Omega_v) = \frac{\pi \cdot d_f \cdot G(\Omega_v)}{4\mu_v} \int_{2\pi} \int_{\frac{\pi}{2}} \frac{g_f\left(\Omega_f\right)}{2\pi \cdot \sqrt{1 + \tan^2\theta_f \sin^2\phi_f}} d\theta_f d\phi_f$$

where d_f is the leaf diameter, Ω_f is the leaf orientation, and $\frac{g_f(\Omega_f)}{2\pi}$ is the normalized leaf angle distribution function.

Fig. 9 illustrates the calculated BRF plot of the Jarvselja forest site in the principal plane ($\phi_v = 299.06$) with and without HS effect. It corresponds to reflectance values that would be measured by a satellite at an infinite altitude (i.e. orthographic projection). The range of view zenith angle on the principal plane θ_{vp} is from -80° to 80°, with negative values associated to backscattering. The subscript p highlights that it corresponds to the ordinary direction if $\theta_{vp} > 0$ and to the direction with opposite azimuth angle ($|\theta_{vp}|$, $\phi_v + \pi$) if $\theta_{vp} < 0$. By setting d_f to 1 cm, a peak in the BRF appears near $\theta_{vp} = -36.6^{\circ}$. The shape of the peak depends on d_f. The dashed plot in Fig. 9 allows us to show the angular range of BRF that is influenced by the HS. If d_f increases, the HS peak becomes smoother. The BRF distribution without HS effect is shown by the dotted plots in Fig. 9. For the absence of the HS, the BRF is much less dependent on the solar-view configuration which is more adapted for image inversion in terms of the Earth's surface parameters such as LAI.

In RS images, the HS configuration provides the appearance of regionally enhanced reflectance. For example, the Amazon forest green up in the dry season derived from MODIS observation (Huete et al., 2006) was recently found to be a "green illusion" caused by the effect of sun-sensor geometry (Morton et al., 2014). Most RTMs can simulate the HS effect on BRF by orthographic projection. The orthographic projection is usually assumed to be accurate enough for dealing with satellite images. However, one may question its accuracy when dealing with strongly anisotropic features such as the HS. This is investigated here with the Jarvselja forest site. Indeed, by using CTPP, DART can simulate actual satellite images influenced by HS with regionally enhanced reflectance.

Since each pixel of a sensor image is associated to a specific view angle, the Earth's surface that is impacted by the HS has a circular/elliptical shape in camera image, and a straight-belt shape in a cross-track imager image. The location and size of the HS in the image reflect the BRF distribution shown in Fig. 9. Below, we illustrate the HS effect with 2 classical acquisition configurations (camera and cross-track imager) at various sensor/platform altitudes. Fig. 10 presents the geometric configurations. For each configuration, the scene boundaries

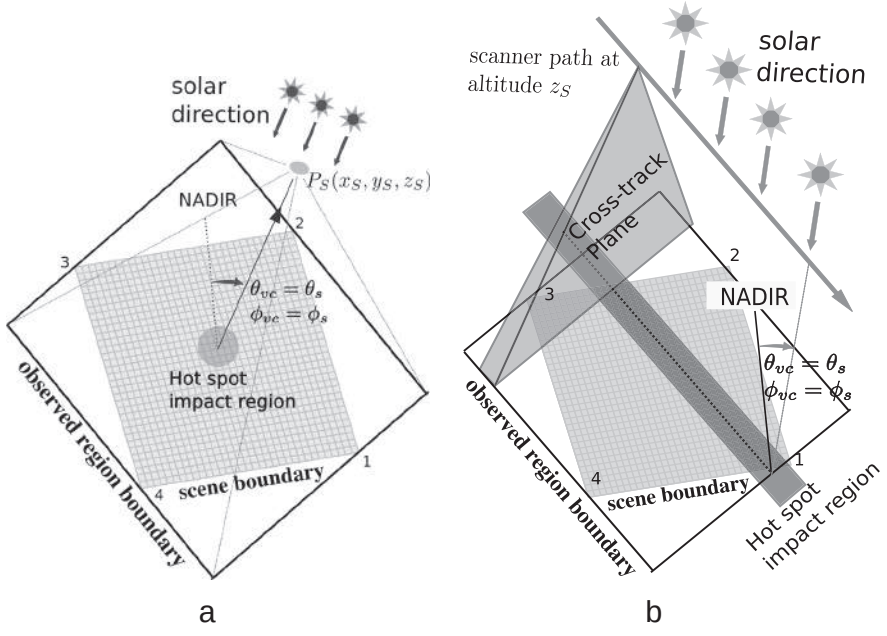

Fig. 10. Configuration of HS regional enhancement simulations on the Jarvselja forest site. (a) For a camera. (b) For a cross-track imager.

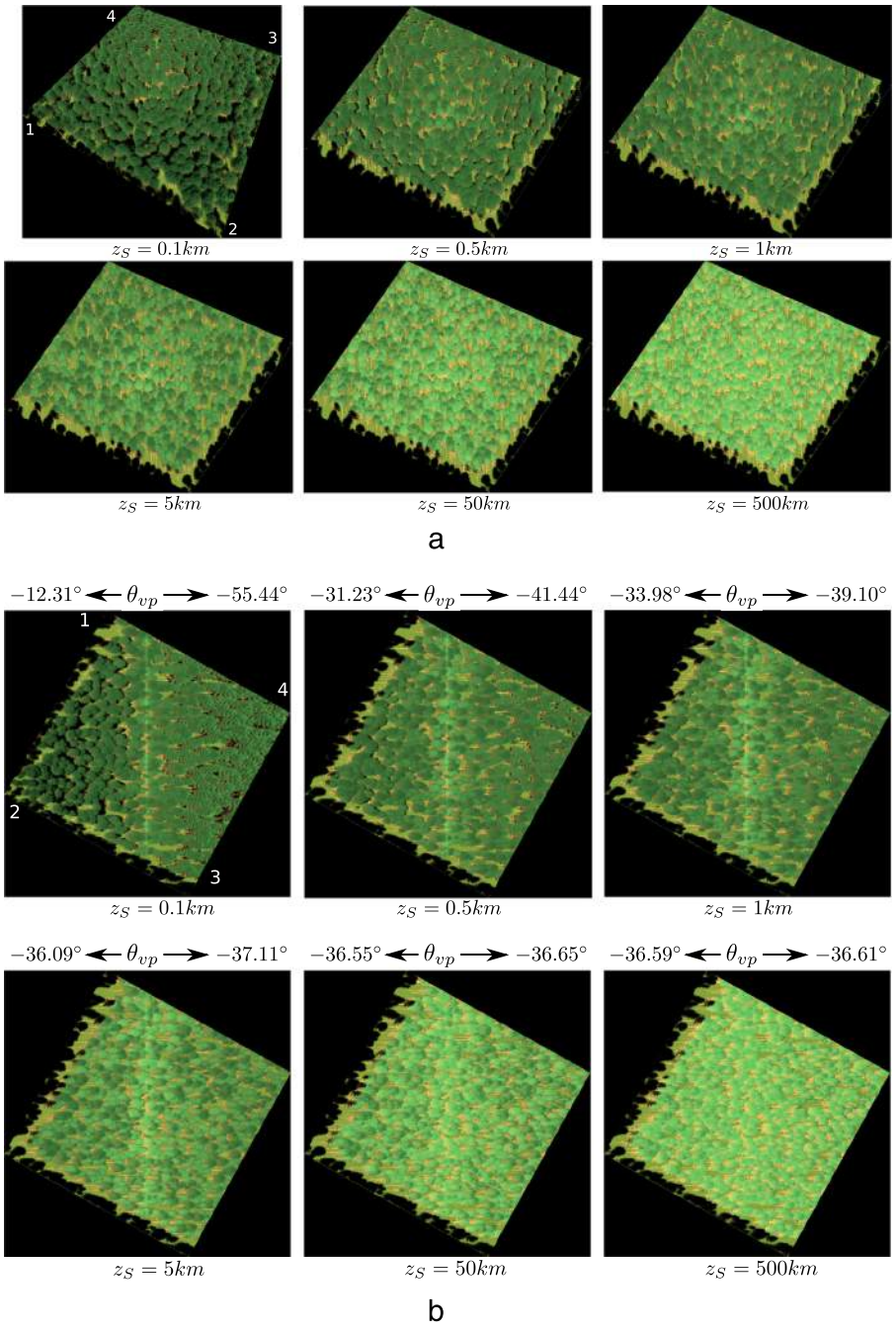

Fig. 11. Simulated sensor images with HS of the Jarvselja forest site, for a sensor/platform at different altitudes (0.1km, 0.5km, 1km, 5km, 50km, 500km). Color components of DART images in blue, green, and red bands. (a) For a camera. (b) For a cross-track imager (θ_{vp} range is shown on top of each image). (For interpretation of the references to color in this figure legend, the reader is referred to the web version of this article.)

and sensor observed region (image of sensor frame) boundaries on the ground are represented by 2 quadrilaterals. The whole scene is enclosed in the image of sensor frame, with the locations of the 4 indexed corners marked according to Fig. 8(b). For cameras (Fig. 10(a)), the view direction at the center of the scene and the camera orientation are manually chosen to be aligned with the solar direction ($\theta_{vc} = \theta_S = \theta_s$, $\phi_{vc} = \phi_S = \phi_s$). Camera intrinsic rotation is set to 0°. For cross-track imagers (Fig. 10(b)), the direction of the platform path is perpendicular to the solar azimuth angle ($\phi_p = 119.06°$). The direction of acquisitions on the cross-track plane is associated with the sun principal plane (Fig. 9).

Fig. 11(a) presents the PPImages of a camera with HS configuration at different altitudes without orthorectification ($\theta_s = 36.6°$, $\phi_s = 299.06°$). The geometric correspondences of the 4 indexed corners of the scene are marked in the image corners according to Fig. 8(b). As the altitude of the camera increases (from top-left to bottom-right 0.1 km, 0.5 km, 1 km, 5 km, 50 km, and 500 km respectively), the HS influenced region also expands gradually from the central point of the scene and finally covers the whole image at the higher altitudes. Fig. 11(b) shows the PPImages of a cross-track imager that are simulated for the same altitude configurations, without orthorectification.

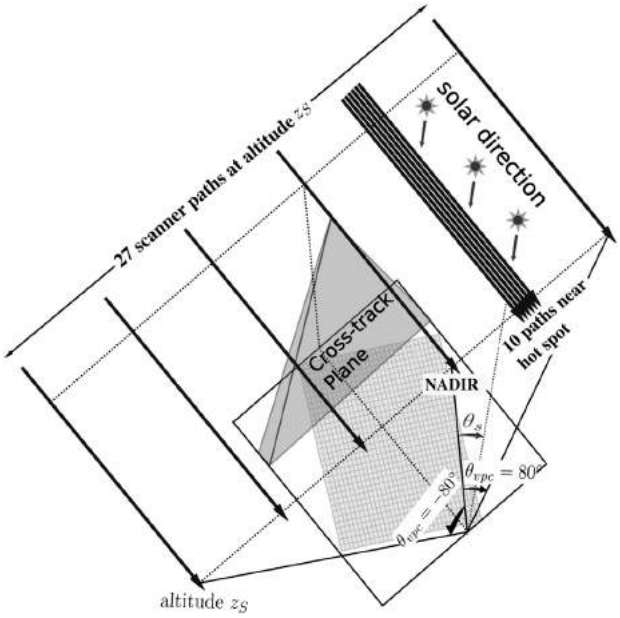

Fig. 12. Simulation to study the reflectance variability of the Jarvselja scene measured by scanner for different altitudes. This figure illustrates the geometry of the simulation for a given altitude z_S.

Instead of a circular spot, the influenced region has a shape of straight belt, since along the moving trajectory, a HS influenced region is persistently observed at the same θ_{vp} range for each cross-track acquisition line (e.g. http://earthobservatory.nasa.gov/IOTD/view.php?id=83048). As the sensor altitude increases, the θ_{vp} range of the cross-track plane decreases and converges to approach the solar direction itself ($\theta_s = 36.6^\circ$) as shown in Fig. 11(b). Therefore, the HS belt width also increases with sensor altitude until the peak reflectance covers the whole image at $z_S = 500$km. This belt is actually discontinuous, since the HS effect only appears on the vegetation part of the heterogeneous scene. For the ground which is simulated with a Lambertian surface, there is no obvious difference whether the region is influenced by the HS or not. However, in reality, the ground surface is usually far away from Lambertian. With appropriate anisotropic parameterization (e.g. the RPV model Rahman, Pinty, & Verstraete, 1993), a reasonably strong HS effect should also be observed. The BRF variation in the sun principal plane, as shown in Fig. 9, corresponds to the reflectance variation from the corner 2 to the corner 4 on the images in Fig. 11(b).

4.3. Pixel-wise comparison and study of variation between simulated aircraft and satellite images

PPImages of a cross-track imager are simulated at different altitudes with different view zenith angle ranges in the sun principal plane. Fig. 12 illustrates the geometry that is used to simulate images for a given altitude. For each altitude, images are simulated with 27 trajectories perpendicular to the solar azimuth angle. These parallel trajectory directions are associated with the similar configuration in Fig. 10(b) of Section 4.2. Let θ_{vpc} represent the θ_{vp} on the principal plane at the scene center, where negative value represents backscattering and positive value represents forwardscattering. It is usually considered in actual data as the representative θ_{vp} of the whole swath. For each sensor altitude, the step of θ_{vpc} is 10° from − 80 to 80°, and 1° around the HS region ($\theta_{vpc} \in [-39^\circ$ to $-31^\circ]$). Together with the exact HS configuration

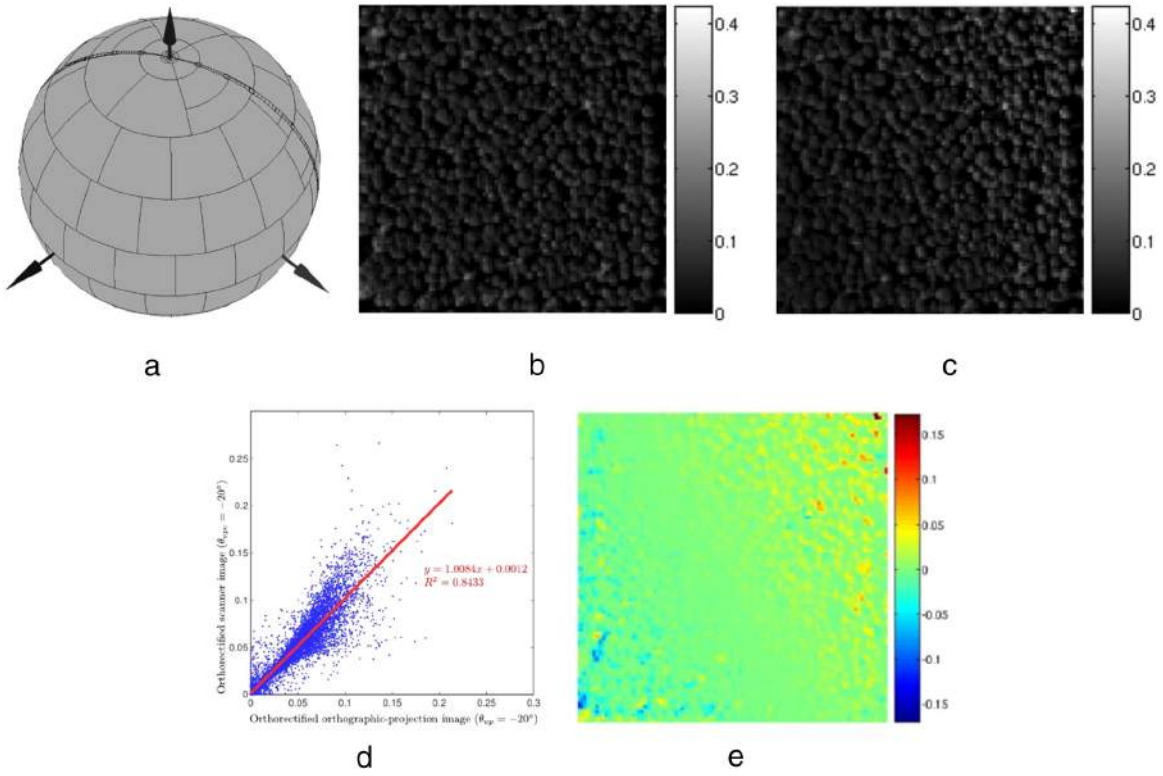

Fig. 13. Parameters of IUSD and pixel-wise comparison of the simulated images of the Jarvselja scene. (a) The IUSD discretization for simulating scanner images of multiple paths with θ_{vpc} range in the sun principal plane. (b) Orthorectified orthographic-projection images (reflectance) for $\theta_{vpc} = -20^\circ$. (c) Orthorectified scanner image (reflectance) at $z_S = 0.2$km. (e) Linear regression analysis of the pixel values in (b) and (c). (d) The pixel-wise reflectance difference of the orthorectified perspective-projection Image and orthorectified orthographic-projection image at $\theta_{vp} = -20^\circ$ (*PPImage* − *OPImage*).

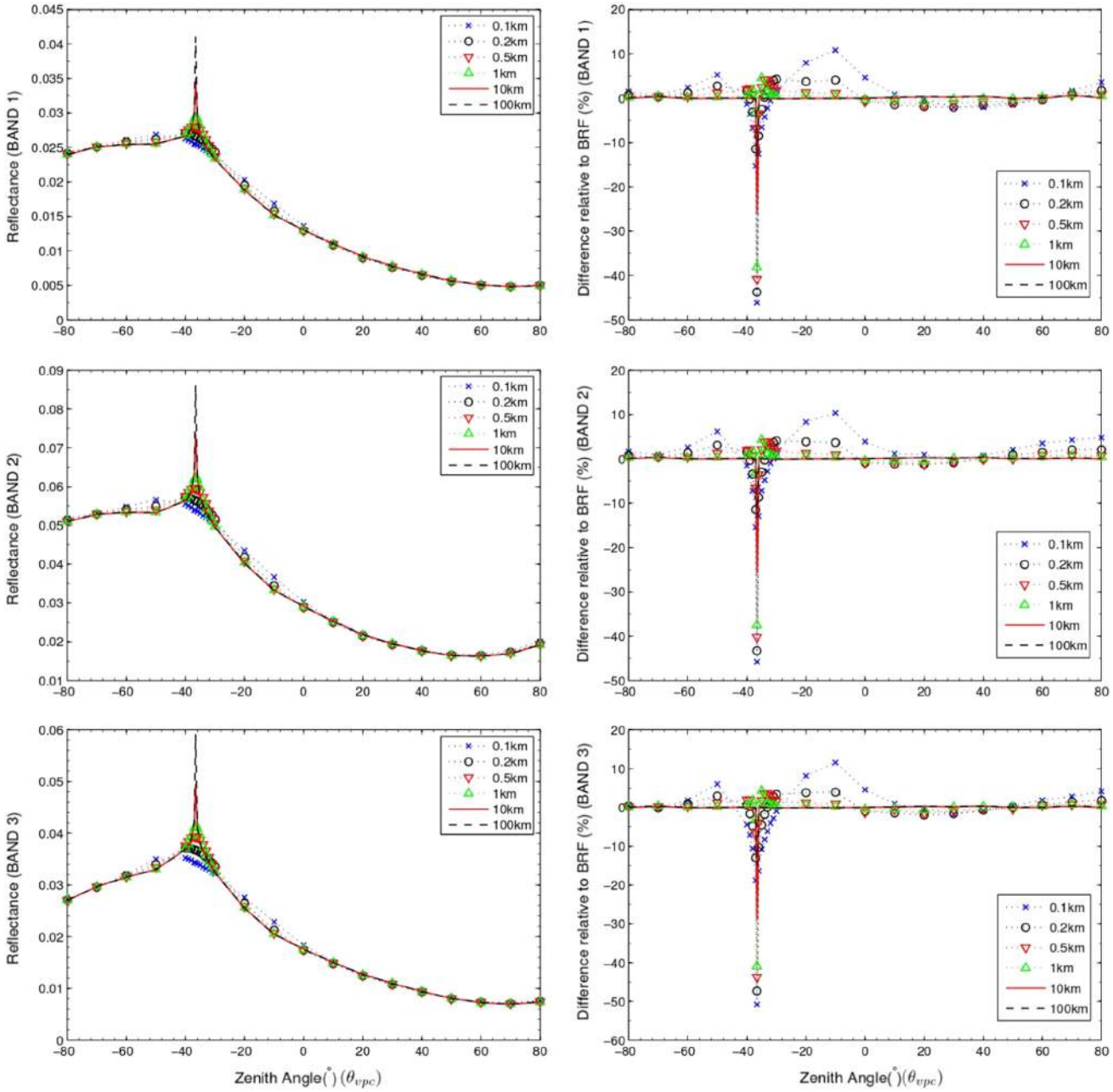

Fig. 14. Plot of average reflectance of the simulated orthorectified PPImages of the Jarvselja scene (3 figures on the left) and the difference with the scene BRF of θ_{vpc} (3 figures on the right).

($\theta_{vpc} = -\theta_s$), 27 images are created for each altitude from airborne to spaceborne acquisitions: 0.1 km, 0.2 km, 0.5 km, 1 km, 10 km and 100 km.

Fig. 13(a) illustrates the IUSD oversampling along the principal plane. This oversampling reduces the error when a scattering function is assigned to the nearest neighbor direction for a ASVD. All images are orthorectified in order to make pixel-wise intercomparison between each other. For example, Fig. 13(b) and (c) illustrates for $\theta_{vpc} = -20^{\circ}$, the *B*02 orthorectified OPImage and PPImage at $z_S = 0.2$km, respectively. The linear regression of pixel values between them (Fig. 13(d)) gives $R^2 = 0.8433$, which proves that they are highly correlated. The pixel-wise difference between the orthorectified images (*PPImage* − *OPImage*) is shown in Fig. 13(e). It can be observed that along a straight line ($\phi_v = 29.06^{\circ}$, $\theta_{vp} = -20^{\circ}$) that crosses the center of the image, the differences between pixels are almost 0. This is due to the fact that along this line, the difference of view angles between the two images is small, so is the reflectance difference. At the top-right part of the image where $\theta_{vp} < -20^{\circ}$, the reflectance tends to be larger for *PPImage* than for *OPImage*. Conversely, for the other side of the image where $\theta_{vp} > -20^{\circ}$, the reflectance tends to be smaller for *PPImage* than for *OPImage*. This is coherent with the BRF distribution around $\theta_{vp} = -20^{\circ}$ in Fig. 9. As mentioned above, differences occur only on vegetation, because the ground is simulated as a Lambertian surface.

Totally 807 orthorectified images were simulated, for the same 3 bands (RGB). Fig. 14 plots the average of all the pixels for each orthorectified reflectance image ($R(\theta_{vpc}, z_S)$) simulated per band, and the corresponding percentage differences to the calculated BRF of θ_{vpc}

in Fig. 9 ($\frac{R-BRF}{BRF}$). Maximum difference occurs at the HS configuration. By comparing the results of the same band with different altitudes, it can be observed that as the platform altitude increases, the differences converge to 0. Indeed, because the scene has a fixed dimension, as the distance from the sensor to the scene increases, the upper and lower boundaries of θ_{vp} range over the whole scene converge to θ_{vpc} (same tendency as θ_{vp} ranges shown in Fig. 11(b)), and the scene reflectance tends to be the exact BRF value. The distribution of the differences over the θ_{vp} axis can be divided into 3 segments depending on the sensor altitude. For example with $z_S = 0.1$km, the 3 segments are:

- HS influenced segment (e.g. $\theta_{vpc} \in (-45^\circ, -27^\circ)$): The BRF inside the region is influenced by the HS. At low altitude, the θ_{vp} range covered by sensor is relatively wide. The HS influenced region corresponds to a belt in the image similar to Fig. 11(b). The major part of the image is outside the HS influenced region. Therefore, in this segment, the average scene reflectance is smaller than the BRF value.
- Near HS segment (e.g. $\theta_{vpc} \in (-70^\circ, -45^\circ) \cup (-27^\circ, 10^\circ)$): The BRF at θ_{vpc} inside this region is away from the HS peak, so it is not influenced by the HS effect. However, the HS influenced region is present in the sensor image. Therefore, the resultant average reflectance is larger than the BRF value.
- Far segment (e.g. $\theta_{vpc} \in (-90^\circ, -70^\circ) \cup (10^\circ, 90^\circ)$): The BRF region is far away from the HS on the plot. The average reflectance of the sensor image can be larger or smaller than the BRF value but the difference is small since the BRF distribution is relatively smooth inside this region. The sign of the difference depends on the 2nd derivative of the BRF distribution inside the angle range.

A similar study using actual data is the variability of the BRDF product investigated by Román et al. (2011) through comparing the CAR measurement with the MODIS measurement. The authors mentioned that one possible reason that causes the differences is the shadow of foliage and canopy components at a spatial resolution >90 m (caused by the HS and the sensor-object geometry). The above "3 segments" explanation can be used to reproduce and analyze this kind of data.

5. Conclusions and prospects

In order to build a bridge between simulated and actual RS measurements, an approach combining image perspective projection with 3-D RTM, the so-called converging tracking and perspective projection (CTPP) is implemented in DART. It uses ASVD and the IUSD method to assign a specific direction vector and phase function for each scattering/emission event. The simulated sensor image stores radiance values that depend on the pixel-sensor geometry. Evaluations and tests of the approach are presented and discussed: simulation of images of camera and cross-track sensors for various altitude and configuration, video generation, HS regional enhancement on sensor images, pixel-wise comparison of orthorectified images, and variation of reflectance between airborne and spaceborne measurements. The approach needs further improvement to better consider the actual measurement configurations. For example, we started studying how to import into DART the actual platform trajectory and direction distribution of image pixels. Work is also conducted on improving the accuracy of simulations for the image boundaries where the iterative method (Section 3.7) may fail. Furthermore, the DART atmosphere tracking algorithm (Grau & Gastellu-Etchegorry, 2013) has been improved to adapt the CTPP approach. The distance from each pixel location on the image to the sensor through the atmosphere varying according to the pixel-sensor geometry, the atmosphere direct transmittance needs to be calculated for each pixel. We interpolate the DART computed transfer functions, from the top Earth scene up to sensor altitude, for each direction incident onto the sensor. However, accuracy and processing speed require further optimizations.

CTPP application with actual remote sensing data continues with the comparison between APEX and DART orthorectified images of the Laegern site. Previous results obtained with the orthographic projection method (Schneider et al., 2014) are much improved with CTPP (Schneider, Yin, Gastellu-Etchegorry, Morsdorf, & Schaepman, in press). With the help of multi-threading, we are now considering simulations and comparisons with larger scenes (1km × 1km) including atmosphere. Solar noise simulation in airborne laser scan (ALS) data is another ongoing CTPP application. ALS is an active multi-pulse technique with a similar geometric configuration as passive cross-track imager. Using the so-called Ray-Carlo method, DART simulates LIDAR data, with atmosphere (Gastellu-Etchegorry, Yin, Grau, Lauret, & Rubio, 2013; Gastellu-Etchegorry, Yin, & Lauret, in preparation; Yin, Gastellu-Etchegorry, Grau, Lauret, & Rubio, 2013; Yin, Gastellu-Etchegorry, & Lauret, in preparation). By segmenting the sun induced radiance image of a cross-track imager according to each LIDAR FOV pulse, solar noise can be estimated simultaneously for millions of LIDAR pulses, for each LIDAR pulse. Solar noise is a major concern for LIDAR photon counting. Its simulation is implemented in present DART release. Other applications can benefit from DART and its CTPP approach, including algorithm validation of 3-D vision from airborne measurements. For example, the parallel-perspective airborne stereo mosaic (Zhu et al., 2004) from multiple simulated sensor images. Since DART simulates both LIDAR and airborne images, algorithms of sensor fusion can be tested using DART simulations. Comments and suggestions by DART users are welcome for further improvement and application. Free DART license is provided by Paul Sabatier University for scientific works (http://www.cesbio.ups-tlse.fr/dart/license/en/index.php).

Acknowledgment

This work was supported by the ANR (Agence Nationale de la Recherche) in the frame of the project FOLI3D and by the CNES (Centre National d'Etudes Spatiales) in the frame of the projects STEM-LEAF and Hypertropik. We are very thankful to the team of scientists of CESBIO (Centre d'Etudes Spatiales de la Biosphere) who contribute to the continuous developments of DART. We thank also the scientists for their valuable remarks and advices, especially F. Schneider (Remote Sensing Laboratories, University of Zurich, Switzerland). We appreciate the anonymous reviewers for their very detailed and valuable remarks and corrections. We thank also M. E. Bauer and B. Schiefelbein at Remote Sensing of Environment for handling the reviewing process.

References

Asner, G. P., Knapp, D. E., Kennedy-Bowdoin, T., Jones, M. O., Martin, R. E., Boardman, J., et al. (2007). Carnegie airborne observatory: In-flight fusion of hyperspectral imaging and waveform light detection and ranging for three-dimensional studies of ecosystems. *Journal of Applied Remote Sensing, 1*(1), 013536–013536-21.

Berk, A., Anderson, G. P., Bernstein, L. S., Acharya, P. K., Dothe, H., Matthew, M. W., et al. (1999). MODTRAN4 radiative transfer modeling for atmospheric correction. *Proc. SPIE's international symposium on optical science, engineering, and instrumentation* (pp. 348–353). International Society for Optics and Photonics.

Berk, A., Bernstein, L. S., & Robertson, D. C. (1987). MODTRAN: A moderate resolution model for LOWTRAN. *Tech. rep., DTIC document*.

Berni, J., Zarco-Tejada, P. J., Suárez, L., & Fereres, E. (2009). Thermal and narrowband multispectral remote sensing for vegetation monitoring from an unmanned aerial vehicle. *IEEE Transactions on Geoscience and Remote Sensing, 47*(3), 722–738.

Chai, J. C., Lee, H. S., & Patankar, S. V. (1994). Finite volume method for radiation heat transfer. *Journal of Thermophysics and Heat Transfer, 8*(3), 419–425.

Chai, J. -X., & Shum, H. -Y. (2000). Parallel projections for stereo reconstruction. *Computer vision and pattern recognition, 2000. Proceedings. IEEE conference on, Vol. 2*. (pp. 493–500). IEEE.

Chandrasekhar, S. (1969). *Radiative transfer*. Dover Publications.

Cook, B. D., Corp, L. A., Nelson, R. F., Middleton, E. M., Morton, D. C., McCorkel, J. T., et al. (2013). NASA Goddard's LiDAR, hyperspectral and thermal (G-LiHT) airborne imager. *Remote Sensing, 5*(8).

Feret, J. -B., François, C., Asner, G. P., Gitelson, A. A., Martin, R. E., Bidel, L. P., et al. (2008). PROSPECT-4 and 5: Advances in the leaf optical properties model separating photosynthetic pigments. *Remote Sensing of Environment, 112*(6), 3030–3043.

Fiveland, W. (1988). Three-dimensional radiative heat-transfer solutions by the discrete-ordinates method. *Journal of Thermophysics and Heat Transfer*, *2*(4), 309–316.
Gastellu-Etchegorry, J. -P., Demarez, V., Pinel, V., & Zagolski, F. (1996). Modeling radiative transfer in heterogeneous 3-D vegetation canopies. *Remote Sensing of Environment*, *58*, 131–156.
Gastellu-Etchegorry, J. -P., Grau, E., & Lauret, N. (2012). *Modeling and simulation in engineering*. Ch. DART: A 3D model for remote sensing images and radiative budget of earth surfaces. Oxford: Intech.
Gastellu-Etchegorry, J. -P., Martin, E., & Gascon, F. (2004). DART: A 3-D model for simulating satellite images and surface radiation budget. *International Journal of Remote Sensing*, *25*(1), 75–96.
Gastellu-Etchegorry, J., Yin, T., Grau, E., Lauret, N., & Rubio, J. (2013, July). Lidar radiative transfer modeling in the atmosphere. *Proc. geoscience and remote sensing symposium (IGARSS), 2013 IEEE international* (pp. 4554–4557).
Gastellu-Etchegorry, J. -P., Yin, T., & Lauret, N. (2015). Simulation of LIDAR data by DART model (I): A quasi-Monte Carlo ray tracing mode in DART and waveform simulation in Earth-Atmosphere system. *Remote Sensing of Environment* (in preparation).
Gastellu-Etchegorry, J. -P., Yin, T., Lauret, N., Cajgfinger, T., Gregoire, T., Grau, E., et al. (2015). Discrete Anisotropic Radiative Transfer (DART 5) for modeling airborne and satellite spectroradiometer and LIDAR acquisitions of natural and urban landscapes. *Remote Sensing*, *7*(2), 1667–1701 (URL http://www.mdpi.com/2072-4292/7/2/1667).
Gatebe, C., Dubovik, O., King, M., & Sinyuk, A. (2010). Simultaneous retrieval of aerosol and surface optical properties from combined airborne-and ground-based direct and diffuse radiometric measurements. *Atmospheric Chemistry and Physics*, *10*(6), 2777–2794.
Gatebe, C. K., King, M. D., Platnick, S., Arnold, G. T., Vermote, E. F., & Schmid, B. (2003). Airborne spectral measurements of surface–atmosphere anisotropy for several surfaces and ecosystems over southern Africa. *Journal of Geophysical Research*, *108*(D13).
Grau, E., & Gastellu-Etchegorry, J. -P. (2013). Radiative transfer modeling in the Earth-atmosphere system with DART model. *Remote Sensing of Environment*, *139*, 149–170.
Gupta, R., & Hartley, R. I. (1997). Linear pushbroom cameras. *IEEE Transactions on Pattern Analysis and Machine Intelligence*, *19*(9), 963–975.
Hapke, B., DiMucci, D., Nelson, R., & Smythe, W. (1996). The cause of the hot spot in vegetation canopies and soils: Shadow-hiding versus coherent backscatter. *Remote Sensing of Environment*, *58*(1), 63–68.
Huete, A. R., Didan, K., Shimabukuro, Y. E., Ratana, P., Saleska, S. R., Hutyra, L. R., et al. (2006). Amazon rainforests green-up with sunlight in dry season. *Geophysical Research Letters*, *33*(6).
Jehle, M., Hueni, A., Damm, A., D'Odorico, P., Weyermann, J., Kneubiihler, M., et al. (2010, Nov). APEX — Current status, performance and validation concept. *Proc. sensors, 2010 IEEE* (pp. 533–537).
King, M. D., Strange, M. G., Leone, P., & Blaine, L. R. (1986). Multiwavelength scanning radiometer for airborne measurements of scattered radiation within clouds. *Journal of Atmospheric and Oceanic Technology*, *3*(3), 513–522.
Kuusk, A. (1991). The hot spot effect in plant canopy reflectance. *Photon–vegetation interactions* (pp. 139–159). Springer.
Masson, V., Gomes, L., Pigeon, G., Liousse, C., Pont, V., Lagouarde, J. -P., et al. (2008). The Canopy and Aerosol Particles Interactions in TOulouse Urban Layer (CAPITOUL) experiment. *Meteorology and Atmospheric Physics*, *102*(3-4), 135–157. http://dx.doi.org/10.1007/s00703-008-0289-4.
Modest, M. F. (2013). *Radiative heat transfer*. Academic Press.
Morsdorf, F., Kötz, B., Meier, E., Itten, K., & Allgöwer, B. (2006). Estimation of LAI and fractional cover from small footprint airborne laser scanning data based on gap fraction. *Remote Sensing of Environment*, *104*(1), 50–61.
Morsdorf, F., Meier, E., Kötz, B., Itten, K. I., Dobbertin, M., & Allgöwer, B. (2004). LIDAR-based geometric reconstruction of boreal type forest stands at single tree level for forest and wildland fire management. *Remote Sensing of Environment*, *92*(3), 353–362.
Morsdorf, F., Nichol, C., Malthus, T., & Woodhouse, I. H. (2009). Assessing forest structural and physiological information content of multi-spectral LiDAR waveforms by radiative transfer modelling. *Remote Sensing of Environment*, *113*(10), 2152–2163.
Morton, D. C., Nagol, J., Carabajal, C. C., Rosette, J., Palace, M., Cook, B. D., et al. (2014). Amazon forests maintain consistent canopy structure and greenness during the dry season. *Nature*, *506*(7487), 221–224.
Pinty, B., Gobron, N., Widlowski, J. -L., Gerstl, S. A. W., Verstraete, M. M., Antunes, M., et al. (2001). Radiation transfer model intercomparison (RAMI) exercise. *Journal of Geophysical Research*, *106*(D11), 11937–11956.
Pinty, B., Widlowski, J. -L., Taberner, M., Gobron, N., Verstraete, M. M., Disney, M., et al. (2004). Radiation Transfer Model Intercomparison (RAMI) exercise: Results from the second phase. *Journal of Geophysical Research*, *109*, D06210.
Press, W. H. (2007). *Numerical recipes 3rd edition: The art of scientific computing*. Cambridge University Press.
Rahman, H., Pinty, B., & Verstraete, M. M. (1993). Coupled surface-atmosphere reflectance (CSAR) model: 2. Semiempirical surface model usable with NOAA advanced very high resolution radiometer data. *Journal of Geophysical Research: Atmospheres (1984–2012)*, *98*(D11), 20791–20801.
Román, M. O., Gatebe, C. K., Schaaf, C. B., Poudyal, R., Wang, Z., & King, M. D. (2011). Variability in surface BRDF at different spatial scales (30 m–500 m) over a mixed agricultural landscape as retrieved from airborne and satellite spectral measurements. *Remote Sensing of Environment*, *115*(9), 2184–2203.
Román, M. O., Gatebe, C. K., Shuai, Y., Wang, Z., Gao, F., Masek, J. G., et al. (2013). Use of in situ and airborne multiangle data to assess MODIS-and Landsat-based estimates of directional reflectance and albedo. *IEEE Transactions on Geoscience and Remote Sensing*, *51*(3), 1393–1404.
Schaepman, M. E., Jehle, M., Hueni, A., D'Odorico, P., Damm, A., Weyermann, J., et al. (2015). Advanced radiometry measurements and Earth science applications with the Airborne Prism Experiment (APEX). *Remote Sensing of Environment*, *158*, 207–219.
Schaepman-Strub, G., Schaepman, M., Painter, T., Dangel, S., & Martonchik, J. (2006). Reflectance quantities in optical remote sensing definitions and case studies. *Remote Sensing of Environment*, *103*(1), 27–42.
Schneider, F. D., Leiterer, R., Morsdorf, F., Gastellu-Etchegorry, J. -P., Lauret, N., Pfeifer, N., et al. (2014). Simulating imaging spectrometer data: 3D forest modeling based on LiDAR and in situ data. *Remote Sensing of Environment*, *152*, 235–250.
Schneider, F. D., Yin, T., Gastellu-Etchegorry, J. -P., Morsdorf, F., & Schaepman, M. E. (2014s). At-sensor radiance simulation for airborne imaging spectroscopy. *IEEE WHISPERS 2014* (in press).
Sonka, M., Hlavac, V., & Boyle, R. (2008). *Image processing, analysis, and machine vision*, *Vol. 3*, Toronto: Thomson.
Widlowski, J. -L., Pinty, B., Clerici, M., Dai, Y., Kauwe, M. D., de Ridder, K., et al. (2011). RAMI4PILPS: An intercomparison of formulations for the partitioning of solar radiation in land surface models. *Journal of Geophysical Research*, *116*, G02019.
Widlowski, J. -L., Pinty, B., Lopatka, M., Atzberger, C., Buzica, D., Chelle, M., et al. (2011). The fourth radiation transfer model intercomparison (RAMI-IV): Proficiency testing of canopy reflectance models with ISO-13528. *Journal of Geophysical Research*, *118*, 6869–6890.
Widlowski, J. -L., Robustelli, M., Disney, M., Gastellu-Etchegorry, J. -P., Lavergne, T., Lewis, P., et al. (2008). The RAMI On-line Model Checker (ROMC): A web-based benchmarking facility for canopy reflectance models. *Remote Sensing of Environment*, *112*(3), 1144–1150.
Widlowski, J. -L., Taberner, M., Pinty, B., Bruniquel-Pinel, V., Disney, M., Fernandes, R., et al. (2007). Third Radiation Transfer Model Intercomparison (RAMI) exercise: Documenting progress in canopy reflectance models. *Journal of Geophysical Research*, *112*, D09111.
Yin, T., Gastellu-Etchegorry, J., Grau, E., Lauret, N., & Rubio, J. (2013, July). Simulating satellite waveform Lidar with DART model. *Proc. geoscience and remote sensing symposium (IGARSS), 2013 IEEE international* (pp. 3029–3032).
Yin, T., Gastellu-Etchegorry, J. -P., & Lauret, N. (2015). Simulation of LIDAR data by DART model (II): Multi-pulse airborne and terrestrial laser scan, photon counting data generation, and solar noise assessment. *Remote Sensing of Environment* (in preparation).
Yin, T., Gastellu-Etchegorry, J. -P., Lauret, N., Grau, E., & Rubio, J. (2013). A new approach of direction discretization and oversampling for 3D anisotropic radiative transfer modeling. *Remote Sensing of Environment*, *135*, 213–223.
Zhu, Z., Hanson, A. R., & Riseman, E. M. (2004). Generalized parallel-perspective stereo mosaics from airborne video. *IEEE Transactions on Pattern Analysis and Machine Intelligence*, *26*(2), 226–237.

Chapter 4

Simulation of LiDAR data

The term LiDAR indicates an active remote sensing technology that measures distance by illuminating a target with a laser and analyzing the reflected light. LiDAR works on the same principle as RADAR, while it uses much shorter wavelengths than RADAR. Therefore, it allows the detection and analysis of much smaller objects, such as aerosols and cloud particles. LiDAR technology originated in the 1930s with the launch of light pulses into the atmosphere to calculate the altitude of clouds through measurement of the light pulse round-trip time. This was the first application of atmospheric LiDAR. In 1950, a French physicist Alfred Kastler (Nobel Prize for Physics 1966) proposed the method of optical pumping, which led to the completion of the theory of lasers. Today LiDAR most commonly refers to the use of laser radiation detection.

LiDAR can be either ground-based or onboard RS platforms (planes, satellites, helicopters, air balloons, as well as UAVs). It was only with the deployment of differential Global Positioning Systems (GPS) in the 1980s, allowing the precise positioning of aircraft, that LiDAR made airborne surveying of Earth surfaces possible. The GPS and inertial measurement unit (IMU) data recorded on a flying platform are combined with the laser pulse range measurements to produce point data with horizontal locations and vertical elevation (ASPRS, 2006). The IMU helps control and record the roll, pitch, and yaw of the aircraft while the LiDAR system is scanning (Campbell et al., 2007). LiDAR has many military and civil applications, for example to make high-resolution maps, with applications in geomatics, atmospheric physics, forestry, archeology, geography, geomorphology, etc. (Vierling et al., 2008). The use of LiDAR continues to increase as LiDAR datasets are made available to the public and the price of new data acquisitions decreases. Despite the various applications and availability of data, LiDAR processing remains a significant challenge (Chen, 2007). Height filtering, the process of classifying the data into ground and non-ground returns, is an essential but difficult step in most analyses (Liu, 2008).

A LiDAR pulse is usually in the near-infrared and visible spectral domains, typically with wavelength of ND-YAG laser $\lambda = 1064nm$ where vegetation reflectance is high, and at its double frequency $\lambda = 532nm$ for shallow penetration into water and retrival of atmosphere constituents. Some LiDAR devices also operate in the ultraviolet or SWIR spectral domain (Govaerts, 1996). For example, the ILRIS-LR terrestrial LiDAR demonstrated in Figure 5 of Section 4.2 utilizes 1535nm wavelength for

better distinguished branches and leaves through the apparent reflectance. Basically, a LiDAR device launches very narrow band pulses to a target and records the delayed time interval of energy return to the source to measure the distance to the target (the so-called time of flight). The time interval multiplied by the speed of light gives the distance between the sensor and the target. When observing Earth surfaces, it can measure both the horizontal distribution and vertical height of vegetation communities (Lefsky et al., 2002). The diameter of circular region at ground level, that is illuminated by a LiDAR pulse at nadir is called footprint size. It is usually smaller than the circular region at ground level that is observed. The diameter of this region is called the LiDAR FOV size. Small footprint airborne LiDAR typically has a pulse diameter of $0.2m$-$1m$.

LiDAR systems can be classified into discrete-return, waveform system, and photon counting system.

- Discrete-return systems (usually with small footprint size) can receive either single or multiple return pulses, which leads to a high resolution, three-dimensional point-cloud of raw elevation data that depicts the Earth's surface with centimeter to decimeter absolute vertical accuracy (Campbell, 2007) (Harding et al., 2008). Sampling density on the ground (e.g., $1-20$ points $/m^2$) depends on the detector sensitivity, response time, and detection threshold, the system pulse rate and scan angle, and the platform speed and height of the aircraft. Discrete-return LiDAR data can be interpolated to create surface elevation models and bare-earth digital elevation models or used to estimate a variety of vegetation metrics such as biomass, height, crown size, LAI, and vertical canopy structure (Bater and Coops, 2009). The estimations of these various vegetation metrics are typically based on their height above a LiDAR-derived digital elevation model.

- There are more complicated LiDAR systems that record the time varying backscattered intensity in temporal bins (i.e., multiple echoes per pulse) (Lefsky et al., 2002). The output that stores this information is called a waveform and the associated sensors are called the waveform LiDARs (wLiDAR). Footprint can be 5 m or larger (Campbell, 2007). WLiDAR systems can transmit thousands of pulses per second that are directed by a rotating or scanning mirror across a specified swath width below the aircraft, generally $< \pm 20^\circ$ off-nadir (Ackermann, 1999) (Campbell, 2007).

- Photon-counting LiDAR (pcLiDAR) is an emerging technology that fires low energy photons with high frequency. It offers the potential for low energy expenditure and potential high altitude operation allowing extended laser lifetime and large area coverage (Rosette et al., 2011). Low laser energy output ensures eye safety of these instruments despite operating at a visible wavelength. A high pulse repetition rate and photon detection probability produces a high point density even whilst flying at greater altitudes whilst a narrow pulse duration ($< 1ns$) allows photons to be located with greater vertical precision. One significant factor resulting from the green wavelength is that photons returned from the emitted pulse cannot be obviously distinguished from detected photons resulting from ambient noise. A small detector field of view and narrow optical band-pass filter are two important elements to reducing the background noise as much as possible. Much of

the remaining background can be eliminated by coincidence filtering. Acquiring data at dusk or night would further reduce the background noise.

Among all these devices, wLIDAR records the most detailed signals for each LiDAR pulse. It can be converted into discrete-return data by decomposition, and into pcLiDAR data by simulating the physics of photon counting detector (Yin et al., 2015a).

A general-purpose simulation tool of wLiDAR can help to evaluate the influences of instrumental and experimental configurations on retrieved waveform, and further help to develop inversion algorithms for specific system. Several models have been developed to simulate LiDAR waveform from medium to large footprints. Semi-empirical models (Blair and Hofton, 1999; Chauve et al., 2007) considered waveform as a sum of Gaussian or Lognormal profiles. These profiles are calculated through convolution with reflection of hit objects of the simulation and spatial distribution (2D Gaussian profile) of pulse energy. The simulated scenes were composed of facets with limited reflectance model, and complicated interactions of ray transfer between the scene elements are not simulated. Sun and Ranson (2000) developed a analytical model to simulate waveform of heterogeneous vegetation landscape consists of turbid medium. Ni-Meister et al. (2001) used the geometric optical and radiative transfer (GORT) model to estimate waveform in one-way hot spot configuration. These analytical models provide fast and somehow accurate estimation of waveform. However, in these models, only first-order scattering returns are considered. The multiple scattering events within LiDAR FOV which induce a slow decay after vegetation canopy signal in waveform, is neglected. Furthermore, geometric optical description of simulated scene is based on simplifying hypotheses for representing interaction phenomena. For example, computation of scene fractions of sunlit canopy, sunlit background, and shadows, is potential source of modeling inaccuracy.

3D RTMs which rely on radiative transfer equation, model the changes of radiations (rays) along its path according to local absorptions, scatterings and thermal emissions. The simulated scene is represented with realistic and detailed description of every element which constituents the Earth's landscape. Monte Carlo ray tracing (MCRT) approach is used in some 3D RTMs to solve the radiative transfer equation. It is a powerful tool because they allow multiple scattering processes to be simulated as a succession of exactly modeled single scattering processes (Disney et al., 2000). In the field of LiDAR waveform simulation, North, et al, 2010, implemented a waveform simulation tool based on a well known MCRT radiative transfer model, the FLIGHT model (North, 1996). The simulated waveforms were validated with the reflectance calculated by FLIGHT and the waveforms from GLAS measurements. Other models like n-Dimensional Estimation of Lidar Signals (DELiS) (Ristorcelli, 2013; Ristorcelli et al., 2014), also uses the MCRT approach. Since MCRT simulate rays in terms of multiple simulated photons, trade-off exists between the simulated accuracy and the number of launched simulated photons. Computational time is the major constraint with Monte Carlo methods, especially if the phase functions of scene elements are anisotropic and complex. FLIGHT achieves processing time around 1s for single pulse waveform simulation. In reality, a wLiDAR system has a pulse repetition frequency up to hundreds hertz. Point cloud generated over an observation area consists of up to millions point. Further

acceleration is called due to the application and evolution of multi-pulse simulation. The fast development of LiDAR technologies requires efficient and accurate simulation tool for both single pulse and multiple pulses to validate existing measurements and to prepare future devices.

In Section 4.1, we present a general-purpose LiDAR waveform simulation tool from the DART 3D radiative transfer model. Some of its theories and applications have already been introduced in previous works (Gastellu-Etchegorry et al., 2013; Grau, 2012; Yin et al., 2013a). A quasi Monte Carlo Ray Tracing approach to simulate photon propagation is introduced in DART. Based on that, 2 new approaches, the so-called Box method and Ray Carlo method, are implemented to provide robust simulation of LiDAR waveform with any geometrical configuration, any footprint size, as well as any simulated landscape and atmosphere distribution. The box method optimizes and enormously accelerates the selection of scattering direction of a photon during interaction with materials of anisotropic properties. The Ray Carlo method utilize the virtual ray and the ASVD concepts presented in Chapter 2 and Chapter 3. It brings DART traditional ray tracking into Monte Carlo simulation, which increases significant signals received by LiDAR with reduced number of initially launched simulated photons. Combination of these 2 methods devotes to provide fast and accurate simulation of LiDAR pulse waveform, so that it is applied to multi-pulse simulation and integrated analysis of received data. Simulated results are validated with reflectance value generated by traditional DART ray tracking.

Most existing models are incapable or inconvenient for efficient and accurate simulation of multiples pulses. In Section 4.2, we present the second part of LiDAR data simulation of DART model. We develop a systematic multi-pulse model of airborne and terrestrial laser scan acquisitions from extension of the previous work of the single-pulse model. With the advantage of inherited efficiency and accuracy from single-pulse model, the design of this multi-pulse model is also optimized in both efficiency and practicability. The implementation of the model avoids repetitive loading of simulated scene, which is a common source factor of slow speed when single-pulse model is called iteratively for each simulated pulse. The parameterization of device and platform supports both abstract configurations such as platform path, zenith angle ranges, and angular/distance separation between pulses, etc..., as well as the importation of instantaneous LiDAR position and orientation per pulse to facilitate actual data comparison. Therefore, platform and sensor based simulation can be created for existing or future systems to produce and validate their data. Each pulse is independently simulated with its own sensor geometries, so algorithmic multi-threading processing is implemented to enormously improve the processing speed. The output data is converted into an industrial LiDAR format, the sorted pulse data (SPD) (Bunting et al., 2013b) format through python binding, and hence processed into point cloud by the associated open-source data processing software, the SPDlib (Bunting et al., 2013a).

In addition, an approach is developed to simulate pcLiDAR data through conversion from waveforms. PcLiDAR exploit single-photon detector for signal acquisition. The acquisition of single-photon detector is simulated with defined sensor parameters like quantum efficiency, dark count rate, and detector dead time, etc... The number of photons in each bin of waveform data is converted into probability of detection and driven by random number generations to find out whether a photon is detected. Case

studies are carried out under various simulated Earth's scene with atmosphere database, and conditions of solar illumination. Furthermore, based on the at-sensor radiance image simulations for cameras and pushbroom imagers which are elaborated in Section 3, a new method for simulation of solar noise in LiDAR waveform is initially developed. Solar noise is a minor problem for data processing of the existing wLiDARs, since the high pulse energy reduces its weight in the return signal, but pcLiDAR is much more sensitive to solar noise than wLiDAR because of its low pulse energy. In addition, solar noise does play an important role in LiDAR sensor design in order to optimize the signals measurements at daytime. Instead of 1 source and 1 sensor system in traditional RTMs, 2 sources and 1 sensor system is developed. In this system, 2 simulations are created for both wLiDAR and passive sensor. The passive sensor radiance image is converted into FOV-localized number of photons per bin and combined with the simulated waveform.

Examples are demonstrated with LiDAR configurations for various existing and future platforms, including CAO (Asner et al., 2012, 2007), ILRIS terrestrial LiDAR, MABEL (McGill et al., 2013), and the ATLAS (Anthony et al., 2010).

4.1 Article: Simulation of satellite, airborne and terrestrial LiDAR with DART (I): waveform simulation with quasi-Monte Carlo ray tracing

Simulation of satellite, airborne and terrestrial LiDAR with DART (I): waveform simulation with quasi-Monte Carlo ray tracing

Jean-Philippe Gastellu-Etchegorry [1]*, Tiangang Yin [1], Nicolas Lauret [1], Eloi Grau [1], Jeremy Rubio [1,2], Bruce D. Cook [2], Douglas C. Morton [2], Guoqing Sun [2]

1. Centre d'Etudes Spatiales de la BIOsphère (CESBIO) - UPS, CNES, CNRS, IRD, Université de Toulouse, 31401 Toulouse cedex 9, France.
2. NASA Goddard Space Flight Center, Greenbelt, MD 20771, USA.

* Email: jean-philippe.gastellu-etchegorry@cesbio.cnes.fr

Abstract: LIght Detection And Ranging (LiDAR) provides unique data on the 3-D structure of atmosphere constituents and the Earth's surface. Simulating LiDAR returns for different laser technologies and Earth scenes is fundamental for evaluating and interpreting signal and noise in LiDAR data. Different types of models are capable to simulate LiDAR waveforms of Earth surfaces. Semi-empirical and geometric models are not very accurate because they rely on very simplified simulations of Earth surfaces and light interaction mechanisms. On the other hand, Monte Carlo Ray Tracing (MCRT) models are potentially very accurate, but require very long computational time. Here, we present a new LiDAR waveform simulation tool that is based on the introduction of a quasi-Monte Carlo ray tracing approach in the Discrete Anisotropic Radiative Transfer (DART) model. Two new approaches, the so-called "box method" and "Ray Carlo method", are implemented to provide robust and accurate simulations of LiDAR waveforms for any landscape, atmosphere and LiDAR sensor configuration (view direction, footprint size, pulse characteristics, etc.). The box method accelerates the selection of scattering direction of a photon in presence of scatterers with non-invertible phase function. The Ray Carlo method brings traditional ray-tracking into MCRT simulation, which makes computational time independent of LiDAR field of view (FOV) and reception solid angle. Both methods are fast enough for simulating multi-pulse acquisition. Sensitivity studies with various landscapes and atmosphere constituents are presented, and simulated LiDAR signals compare favorably with their associated reflectance images and Laser Vegetation Imaging Sensor (LVIS) waveforms. The LiDAR module is fully integrated in DART, enabling more detailed simulations of LiDAR sensitivity to specific scene elements (e.g., atmospheric aerosols, leaf area, branches, or topography) and sensor configuration for airborne or satellite LiDAR sensors.

Keywords: LiDAR, DART, radiative transfer model, multiple scattering, LVIS, Monte Carlo ray tracing, Ray Carlo, box method

1. INTRODUCTION

Sampling the Earth's atmosphere and surface features with LiDAR sensors provides detailed data on topography, vegetation architecture, aboveground biomass, and novel approaches for change detection in vegetated and urban areas (Vosselman and Maas, 2010). Waveform LiDAR sensors (wLiDAR) provide ranging information based on the return energy in the backscattered signal which is discretized into short sampling intervals. In addition to the distance from the vegetation canopy and ground surface, wLiDAR data captures energy returned from the diffuse media (e.g., the atmospheric column and vegetation profile). Thus, the inversion of waveform signal can be used to infer the distribution of sub-canopy elements, and distribution of atmospheric constituents. wLiDAR sensors are usually categorized according to platform, beam divergence and footprint,

sampling method, laser wavelength and pulse width, and method of detection and digitization. Airborne wLiDAR systems typically utilize a small footprint (<1 m diameter) infrared or green laser beam, and a scanning or multi-faceted mirror for distributing laser pulses in the cross-track direction (Asner et al., 2007, 2012). Space-based wLiDAR devices usually have been profiling systems with large footprints: the Geoscience Laser Altimeter System (GLAS) LiDAR had a 50-60 m diameter footprint (Zwally et al., 2002) and a 25 m diameter footprint is planned for the Global Ecosystem Dynamics Investigation (GEDI) waveform LiDAR (Krainak et al., 2012, Dubayah et al., 2014).

A general-purpose simulation tool of wLiDAR can help to evaluate the influences of instrument characteristics and environmental conditions on LiDAR waveforms, including the development of inversion algorithms for specific systems. Several models have been developed to simulate wLiDAR from medium to large footprints. Semi-empirical models (Blair and Hofton, 1999, Chauve et al., 2007) consider waveform as a sum of Gaussian or Lognormal profiles computed by convolving the target objects' reflectance and pulse energy spatial distribution (2-D Gaussian profile). The analytical model of Sun and Ranson (2000) simulates waveforms of heterogeneous vegetation landscapes made of turbid medium. Ni-Meister et al. (2001) used a geometric optical and radiative transfer (GORT) model to estimate waveform in the hot spot configuration (Kuusk, 1991). These analytical models provide computationally efficient estimations of waveforms. However, the modeling approaches provide less accurate waveform data because they consider only first-order scattering returns. Simulation of multiple scattering mechanisms that occur in the LiDAR FOV is particularly important for near infrared (NIR) LiDAR systems over vegetation, given the high reflectance and transmittance of foliage in typical LiDAR wavelengths (1064 nm). Furthermore, previous models also work with very simplified simulations of Earth surfaces.

Three-dimensional (3-D) radiative transfer models (RTM) rely on radiative transfer equations to simulate local absorption, scattering and thermal emission. Many RTMs can work with detailed scenes with realistic geometry and optical properties. Some 3-D RTMs use a MCRT approach to solve the radiative transfer equation. MCRT models are powerful tools because they simulate multiple scattering processes as a succession of exactly modeled single scattering processes (Disney et al., 2000). In the field of wLiDAR simulation, (North et al., 2010) implemented a waveform simulation tool based on the well-known MCRT FLIGHT model (North, 1996). They validated it with the reflectance calculated by FLIGHT and waveforms from GLAS measurements. Since MCRTs simulate rays in terms of multiple simulated photons, an inherent trade-off exists between the simulation accuracy and the number of simulated photons. Computational time is the major constraint with MCRTs, especially if the scene element phase functions cannot be inverted, a typical case because common scattering elements have anisotropic and complex phase functions. A 1s processing time for a single pulse waveform is very limiting, as many actual wLiDAR systems have a pulse repetition frequency up to hundreds of kHz.

In this paper, we present a new quasi-MCRT model that simulates wLiDAR in an accurate and computationally efficient manner. It is implemented in the Discrete Anisotropic Radiative Transfer (DART) model (Gastellu-Etchegorry et al., 1996, 2004, 2012, 2015). It is a general-purpose model for any LiDAR configuration (footprint size, pulse energy, spatial and temporal pulse distribution, view direction, etc.), for any urban or vegetation landscape, including topography. MCRT within atmosphere is also implemented and coupled, which does not exist in most Earth surface RTMs. Section 2 of this paper reminds DART background. Section 3 presents a new approach, called box method, for fast selection of photon scattering direction for any scattering event, which is the fundamental method for the quasi-MCRT model in DART. Section 4 explains the implementation of the quasi-MCRT model in LiDAR simulation, with the introduction of a new approach called

Ray Carlo method. For each scattering event, this method tracks a fraction of the radiation returned in the direction of the sensor to reduce the total number of simulated photons, greatly improving simulation accuracy and processing speed. Section 4 also presents sensitivity studies for different landscape and atmosphere conditions, including a comparison with Laser Vegetation Imaging Sensor (LVIS) waveforms for a temperate forest. Section 5 highlights atmosphere tracking, with specific accelerating techniques that reduce MCRT noise. A companion paper presents DART-LiDAR applications for simulating multiple pulse acquisitions, terrestrial LiDAR, and photon counting LiDAR systems. Nomenclature of this paper is shown in **Appendix A**.

2. THE BACKGROUND OF DART MODEL THEORY

DART is a 3-D RTM that is developed since 1992. It simulates 3-D radiative budget and airborne and satellite images of urban and natural landscapes from visible to thermal infrared domains (Gastellu-Etchegorry et al., 1996, 2004, 2008, 2015). It simulates any 3-D experimental landscape configuration (forest stand, agricultural crop, atmosphere, topography, sun direction or date) and instrument specification (e.g., spatial and spectral resolutions, sensor viewing direction, platform altitude).

A 3-D scene (Figure 1) is the superposition of three rectangular volumes: the high atmosphere (HA), the mid atmosphere (MA), and the Earth scene, with topography. Scene simulation is independent from the RT modelling, which allows one to simulate several sensors with the same landscape. Major DART simulated scene elements are: trees, grass and crop canopies, urban features, and water bodies. Additionally, DART can import scene elements from external libraries to simulate Earth scenes of varying complexity. Atmosphere cells are defined by their gas and aerosols contents and spectral properties (i.e., scattering phase functions, vertical profiles, extinction coefficients, spherical albedos, etc.) that are user defined, or imported from internal or external databases such as AERONET (http://aeronet.gsfc.nasa.gov/). Atmospheric RT modelling includes the Earth-atmosphere radiative coupling.

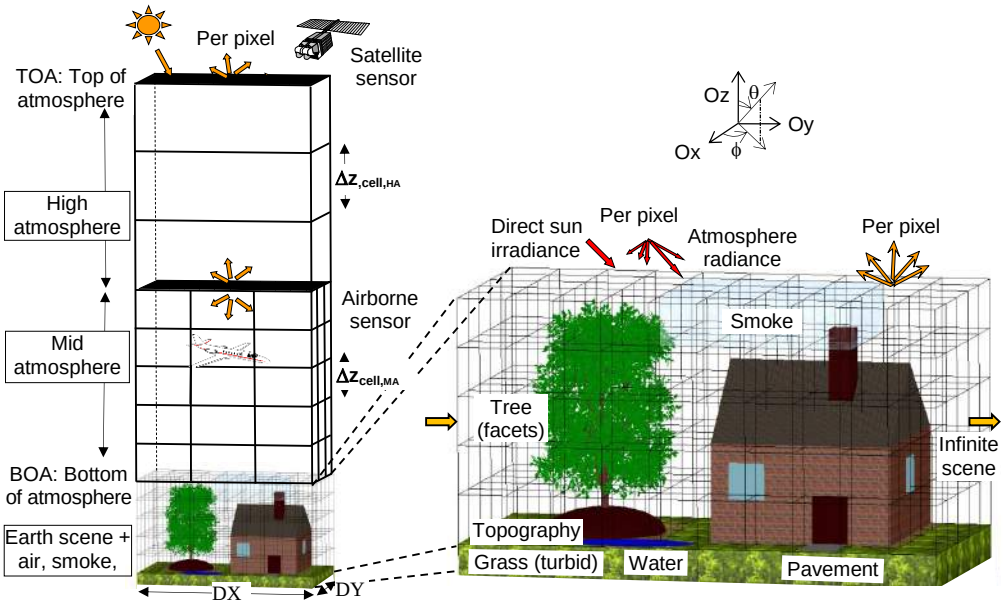

Figure 1. DART simulated Earth / atmosphere scene (Gastellu-Etchegorry et al., 2015).

An Earth scene is an array of 3-D cells (Δx, Δy, Δz) where any scene element is created with a dual approach as a set of cells that contain turbid media or a set of geometric primitives (triangles) called "facets". Turbid medium is a statistical representation of matters that are used to simulate fluids (air, soot, water, etc.) and vegetation foliage. A fluid turbid medium is a volume of homogeneously distributed particles defined by their density (particles / m^3), cross section (m^2 / particle), single scattering albedo, and scattering phase function. Turbid vegetation medium is a volume of leaf elements simulated as infinitely small flat surfaces defined by their orientation, i.e. leaf angle distribution $\frac{g(\Omega_f)}{2\pi}$ (LAD; sr^{-1}), volume density u_f (m^2/m^3), and isotropic transmittance and reflectance, with a specular component.

A facet is a surface element defined by its orientation Ω_n in space, area and optical properties: direct transmittance t_{dir}, diffuse transmittance t_{diff} and reflectance ρ, with $t_{diff} + \rho \leq 1$. A ray of light incident on a facet interacts with the front side, which is defined by a normal vector, but it does not interact with the facet's backside. Thus, depending on the type of object, any surface can be simulated using only 1 facet or 2 facets with opposite normal vectors, and optionally different optical properties. For an energy flux W along Ω_s, the direct transmittance along Ω_s is $t_{dir}^{1/|\Omega_s \cdot \Omega_n|}$; the scattered flux is $W \cdot (1 - t_{dir}) \cdot \rho$; and the transmitted diffuse flux is $W \cdot \left(1 - t_{dir}^{1/|\Omega_s \cdot \Omega_n|}\right) \cdot t_{diff}$. Reflectance ρ can be Lambertian, Hapke (Hapke, 1981), RPV (Rahman et al., 1993), etc., with a specular component that is defined by the facet refraction index, an angular width and a multiplicative factor. Facets are used to build virtual houses, plant leaves, tree trunks and branches, etc. Vegetation canopies are therefore simulated as assemblies of turbid medium voxels or facets or combination of both.

Rays $W(r, \Omega)$ are tracked with the so-called ray-tracking method: they propagate in space r along discrete directions, with each one being characterized by its vector Ω and solid angle ΔΩ (sr). They are iteratively tracked until convergence is achieved: rays intercepted in the previous iteration are scattered and tracked towards all relevant N_{dir} discrete directions in the current iteration, which corresponds to multiple scattering. Three types of discrete directions are used:

- $N_{dir,nv}$ pre-defined directions. They cover the 4π space: $\sum_{i=1}^{N_{dir,nv}} \Delta\Omega_i = 4\pi$. They can oversample angular sectors such as the hot spot (Kuusk, 1991) and penumbra (Dare, 2005) configurations. They are used for simulating the radiative budget and sensor images with orthographic projection (Yin et al., 2013b).
- $N_{dir,vd}$ pre-defined virtual directions. Their properties are set to "virtual" because rays along these directions cannot be scattered along other directions. They are used for simulating remote sensing images with orthographic projection (Yin et al., 2013b).
- $N_{dir,vnd}$ non pre-defined virtual directions. They are used for simulating LiDAR signal and passive sensor images (camera, cross-track imager), with multi-angle acquisition within the sensor FOV, through perspective projection. Their vectors vary to scatter-to-sensor direction per scattering event. Their number (e.g., 10^6) is more or less equal to the number of emitting and scattering elements in the scene (Yin et al., 2015).

Facets and turbid volume cells give rise to 2-D and 3-D ray interactions (i.e., scattering and absorption), respectively. A ray $W_{int}(\Omega_i)$, incident along direction Ω_i that is intercepted by a facet or a turbid medium of type k gives rise to scattered rays along pre-defined and not pre-defined discrete directions $(\Omega_i, \Delta\Omega_i)$:

$$W_{scat}(\Omega_j) = T(k, \Omega_i, \Omega_j) \cdot W_{int}(\Omega_i) \quad (1)$$

where $T(k, \Omega_i, \Omega_j)$ is the scattering transfer matrix. It is pre-computed for each type of volume and surface scene element, for pre-defined directions Ω_i only. For a volume of turbid vegetation of type k, we have:

$$T(k, \Omega_i, \Omega_j) = \frac{1}{G(k, \Omega_i)} . \int_{\Delta\Omega_j} \int_{2\pi} \frac{g_f(k, \Omega_f)}{2\pi} . |\Omega_i . \Omega_f| . F(k, \Omega_f, \Omega_i \rightarrow \Omega_j) . d\Omega_f . d\Omega_j \quad (2)$$

with

$$G(k, \Omega_i) = \frac{1}{2\pi} \int_{2\pi} g_f(k, \Omega_f) . |\Omega_i . \Omega_f| . d\Omega_f \quad (3)$$

where $G(k, \Omega_i)$ is the mean projection of a unit foliage area of type k on a surface unit perpendicular to direction Ω_i (Ross, 1981). $F(k, \Omega_f, \Omega_i \rightarrow \Omega_j)$ is the probability that a ray, intercepted along Ω_i by a foliar element with orientation Ω_f, is scattered towards Ω_j. It corresponds to Lambertian transmittance and reflectance, possibly with a specular component that depends on foliar refraction index and roughness.

For a ray intercepted along Ω_i, the probability of scattering along a non virtual direction Ω_j is:

$$p_{ij,k} = \frac{T(k, \Omega_i, \Omega_j)}{\sum_{j=1}^{N_{dir,nv}} T(k, \Omega_i, \Omega_j)}, \text{ with } j \in [1 \ N_{dir,nv}] \text{ and } \sum_{j=1}^{N_{dir,nv}} p_{ij,k} = 1 \quad (4)$$

Facet scattering matrices $T(\Omega_i, \Omega_j)$ are defined by the facet transmittance t_{diff} and reflectance ρ. During radiation tracking, scattering matrices are handled differently for facets and turbid vegetation, where leaf distribution is statistically known. Indeed, any facet has a specific orientation Ω_n that must be considered when computing its radiation interaction. This is done in 3 steps. 1) Coordinates of the incident photon are transformed from the scene reference system to the facet reference system. 2) Application of $T(\Omega_i, \Omega_j)$ in the facet reference system for computing the direction of the scattered photon. 3) Coordinates of the scattered photon are transformed from the facet reference system to the scene reference system.

Gas and aerosol scattering matrices $T(\Omega_i, \Omega_j)$ are computed with their respective single scattering albedo ω and normalized scattering phase functions: Rayleigh function $\frac{P_{gas}(\Omega_i, \Omega_j)}{4\pi}$ for gasses and double Henyey-Greenstein function $\frac{P_{aerosol}(\Omega_i, \Omega_j)}{4\pi}$ for aerosols. The strong anisotropy of aerosol scattering explains that $T(\Omega_i, \Omega_j)$ is computed as integral over the solid angles of the incident and scattered direction, using the Newton-Cotes numerical integration:

$$T(\Omega_i, \Omega_j) = \frac{1}{\Delta\Omega_i} . \omega . \int_{\Delta\Omega_i} \int_{\Delta\Omega_j} \frac{P(\Omega_i, \Omega_j)}{4\pi} . d\Omega_i . d\Omega_j$$

$$\frac{P_{gas}(\Omega_i, \Omega_j)}{4\pi} \approx \frac{1}{4\pi} . [0.7552 + 0.7345 \cos^2 \Psi_{i,j}] \quad (5)$$

$$\frac{P_{aerosol}(\Omega_i, \Omega_j)}{4\pi} = \frac{a . (1 - g_1^2)}{[1 + g_1^2 - 2g_1 \cos \Psi_{i,j}]^{1.5}} + \frac{(1 - a) . (1 - g_2^2)}{[1 + g_2^2 + 2g_2 \cos \Psi_{i,j}]^{1.5}}$$

$\Psi_{i,j}$ is the angle between directions Ω_i and Ω_j and (a, g_1, g_2) are parameters of the double Henyey-Greenstein function. They depend on aerosol size and wavelength.

DART forward simulation of vegetation reflectance was successfully verified by real measurements (Gastellu-Etchegorry et al., 1999) and cross-comparisons against independently designed 3-D reflectance models (e.g., FLIGHT (North, 1996), Sprint (Thompson and Goel, 1998), Raytran (Govaerts and Verstraete, 1998) in the RAdiation transfer Model Intercomparison (RAMI) experiment (Pinty et al., 2001, Widlowski et al., 2007, 2008, 2013). To date, DART has been successfully employed in many scientific applications: design of inversion methods for airborne and satellite reflectance images (Gascon et al., 2004, Banskota et al., 2013), design of satellite sensors (e.g., NASA DESDynl, CNES Pleiades), impact studies of canopy structure on satellite image texture (Bruniquel-Pinel and Gastellu-Etchegorry, 1998, Barbier et al., 2010, 2012, Proisy et al., 2011) and reflectance (Gastellu-Etchegorry et al., 1999, Malenovskýet al., 2008) , modelling of 3-D photosynthesis distribution and primary production rate in vegetation canopy (Guillevic and Gastellu-Etchegorry, 1999), design of new chlorophyll vegetation index (Malenovskýet al., 2013), among others.

Two novel modelling approaches are introduced into DART for simulating terrestrial, airborne and satellite LiDAR signals (i.e., waveform, photon counting). They combine Monte Carlo (MC) and ray-tracking methods (UEBERSCHLAG, 2010, Gastellu-Etchegorry et al., 2013, Yin et al., 2013a). They are presented in Section 3 and 4.

3. PROPAGATION AND INTERACTION OF PHOTONS

MC methods are used to assess an expected result as an integration of a large number N of random samples. These unbiased methods converge to the exact solution with an error proportional to $1/\sqrt{N}$. This low convergence rate explains the frequent use of variance reduction techniques such as stratified sampling, Russian roulette integration and quasi-MC methods (Suykens, 2002). In DART, illumination energy is simulated as discretized tiny samples referred to as simulated photons (SP). Three parameters (W_{sp}, $\overrightarrow{r_{sp}}$, $\overrightarrow{\Omega_{sp}}$) define the state of each SP. W_{sp} is a weight factor which defines the energy quantity (unit: Joule) that a SP carries. $\overrightarrow{r_{sp}}$ is the SP position and $\overrightarrow{\Omega_{sp}}$ is the unit direction vector. The paths of individual SPs are tracked through successive interactions, starting from the illumination source (e.g., sun, sky, laser beam, etc.). An individual SP can undergo many interactions with various elements in a simulated system. At each interaction, it is transmitted, absorbed or scattered. This is simulated by considering the probability $P_X(0 < P_X < 1)$ of any event X, with $P_X(t) = F_X(t) - F_X(a)$, where $F_X(t) = \int_a^t f_X(t)$ is the cumulative distribution function (CDF) of event X, $f_X(t)$ is the probability distribution function (PDF) and t is a variable (e.g., SP path before interception, selected scattering direction, etc.) bounded by its limits a and b. We have $\sum_x P_X(b) = 1$. The comparison of a randomly generated number p ($0 < p < 1$) with the transmission, absorption and scattering CDFs is used to select an event. Then, the inverse function of the selected CDF is applied on p, to retrieve the value of the variable t (i.e., $t = F_X^{-1}(p)$) that is used to update the SP state. Functions F_X and $f_X(t)$ depend on the interacting elements.

3.1 Interception

If a SP enters a cell along $\overrightarrow{\Omega_{sp}}$, the longest possible path δl_{sp} along $\overrightarrow{\Omega_{sp}}$ is computed, and the intercepted facets and turbid media along the path are shortlisted. If this list of elements is empty, the only possible event is transmission through the cell. Then:

$$\overrightarrow{r_{sp}} = \overrightarrow{r_{sp}} + \overrightarrow{\Omega_{sp}} \times \delta l_{sp} \quad (6)$$

It brings the SP to the next cell, with δl_{sp} equal to its path distance.

If there are facets along the SP path, and if the cell is not filled with turbid medium, δl_{sp} in Eq. (6) is replaced by the distance δl from the current SP position to the first facet in the list. The interaction of the SP with the facet gives rise to 2 possible events: direct transmission or interception. Different transmission corresponds to the fact that the SP simply crosses a semi-transparent facet along $\overrightarrow{\Omega_{sp}}$ (e.g., windows in buildings). On the other hand, the SP can be intercepted, and be further absorbed, or scattered. For a facet direct with transmittance t_{dir}, interception occurs if a randomly generated number p verifies the inequality: $p < 1 - t_{dir}$. If the SP is transmitted, it is directed to the next facet of the list for another interaction test.

If the cell contains a turbid medium, turbid interaction must be considered before the SP is moved to a facet or exits the cell. Again, the SP can either be transmitted or intercepted. Transmittance along the ray path is used to statistically determine if an interception occurs. This transmittance is computed using pre-computed extinction coefficients $\alpha(\overrightarrow{\Omega_l})$. For molecules or aerosols in atmosphere, $\alpha(\overrightarrow{\Omega_l})$ is isotropic.

For vegetation turbid cell with K vegetation types: $\alpha_v(\overrightarrow{\Omega_l}) = \sum_{k=1}^{K} G(k, \overrightarrow{\Omega_l}) . u_f(k)$, where each vegetation type k has a parameter $G(k, \overrightarrow{\Omega_l})$ (Eq. (3)) and leaf volume density $u_f(k)$. For an initialized SP along the illumination source direction $\overrightarrow{\Omega_l}$, for first order scattering, $\alpha_v(\overrightarrow{\Omega_l})$ takes into account the finite dimension d_f of leaves for simulating the hot spot effect (Kuusk, 1991). Indeed, the extinction coefficient for first order scattering $\alpha_v^1(\overrightarrow{\Omega_j})$ depends on $\overrightarrow{\Omega_l}$. For example, if $\overrightarrow{\Omega_l}$ and $\overrightarrow{\Omega_j}$ are exactly opposite, a ray scattered along $\overrightarrow{\Omega_j}$ will not be intercepted, which corresponds to $\alpha_v(\overrightarrow{\Omega_j} = -\overrightarrow{\Omega_l}) = 0$. This effect occurs also, with less intensity, for scattering directions near $-\overrightarrow{\Omega_l}$. The hot spot is simulated with Kuusk approach (1991):

$$\alpha_v^1(\overrightarrow{\Omega_j}) = u_f . G(\overrightarrow{\Omega_j}) \left(1 - \sqrt{\frac{G(\overrightarrow{\Omega_l}) . \mu_j}{G(\overrightarrow{\Omega_j}) . |\mu_i|}} \right) . \exp\left(\frac{-\Delta(\overrightarrow{\Omega_l}, \overrightarrow{\Omega_j})}{s_f(\overrightarrow{\Omega_j})} . \Delta l(\overrightarrow{\Omega_j}) . \mu_j \right) \quad (7)$$

where $\mu_i = \cos\theta_i$, $\mu_j = \cos\theta_j$, $\Delta(\overrightarrow{\Omega_l}, \overrightarrow{\Omega_j}) = \sqrt{\frac{1}{\mu_i^2} + \frac{1}{\mu_j^2} - \frac{2\cos g}{|\mu_i . \mu_j|}}$ with $\cos g = \overrightarrow{\Omega_l} . \overrightarrow{\Omega_j}$, $\Delta l(\overrightarrow{\Omega_j})$ is the path length along $\overrightarrow{\Omega_j}$ and $s_f(\overrightarrow{\Omega_j})$ is the apparent leaf dimension:

$$s_f(\overrightarrow{\Omega_j}) = \frac{\pi . d_f . G(\overrightarrow{\Omega_j})}{4\mu_j} \int_{2\pi} \int_{\frac{\pi}{2}} \frac{g_f(\Omega_f)}{2\pi . \sqrt{1 + \tan^2\theta_f . \sin^2\phi_f}} . d\theta_f . d\phi_f \quad (8)$$

where Ω_f is the leaf orientation, and $g_f(\Omega_f)$ is the LAD.

The probability that a SP is intercepted along a path length Δl within a turbid cell is:

$$P(\Delta l) = 1 - e^{-\alpha(\overrightarrow{\Omega_{sp}}) . \Delta l} \quad (9)$$

A random number p is compared with $P(\Delta l)$ to state if the SP is intercepted or transmitted. If it is transmitted, Eq. (6) is applied to move it with $\delta l_{sp} = \Delta l$. If the SP is intercepted, Eq. (9) is inverted to calculate the distance before the interception:

$$\delta l_{sp} = -\frac{\ln(1-p)}{\alpha(\overrightarrow{\Omega_{sp}})} \tag{10}$$

Then, the SP is moved by distance δl_{sp} (Eq. (6)) before being absorbed or scattered.

The DART quasi-MCRT method differs from other MCRT models because scattered SPs propagate only along the $N_{dir,nv}$ discrete directions that sample the 4π space. This simplifying hypothesis is acceptable if the divergence of a vector within each pre-calculated discrete direction can be neglected, which is valid only if scattering is isotropic or if $N_{dir,nv}$ is large (i.e., small solid angle per discrete direction). This approach allows one to work with pre-computed quantities such as scattering matrices $T(\Omega_i, \Omega_j)$, which greatly accelerates simulations. For example, direction-based parameters such as $G(\overrightarrow{\Omega})$ (Eq. (3)), $\omega(\overrightarrow{\Omega})$, $\alpha(\overrightarrow{\Omega})$ and $T(\Omega_i, \Omega_j)$ are pre-calculated for any direction, whereas in other MCRT models, they are calculated each time for each new $\overrightarrow{\Omega}$, which is very computationally demanding.

3.2 Scattering

A SP that is intercepted is absorbed or scattered with a proportion that depends on local single scattering albedo ω. This albedo is pre-calculated for facets and turbid media (atmosphere, vegetation, fluid). For a facet, with a SP incident along Ω_i:

$$\omega(\Omega_i) = \frac{1}{\pi} . \int_{2\pi} \rho(\Omega_i, \Omega_j) . |\Omega_n . \Omega_j| \, . \, d\Omega_j + t_{diff} \tag{11}$$

where Ω_n is the facet normal, t_{diff} is the facet isotropic transmittance, and $\rho(\Omega_i, \Omega_j)$ is the facet directional reflectance. The integral is over the hemisphere where $\Omega_n . \Omega_j > 0$.

For vegetation turbid medium:

$$\omega(\Omega_i) = \frac{\int_{4\pi}\int_{2\pi} \frac{g_f(\Omega_f)}{2\pi} . |\Omega_i . \Omega_f| F(\Omega_f, \Omega_i, \Omega_j) \, . \, d\Omega_f \, . \, d\Omega_j}{G(\Omega_i)} \tag{12}$$

Most MCRT models generate a random number p and compare it with ω to state if the SP is absorbed or scattered. In DART, scattering occurs if $\omega > 0$ and the weight W_{sp} of the scattered SP is the weight of the intercepted SP multiplied by ω.

$$W_{sp} = W_{sp} \times \omega(\Omega_i) \tag{13}$$

By this approach, a SP is never eliminated by absorption, except if $\omega = 0$, and the total number of launched SPs is much reduced compared with pure MCRT models to achieve the same accuracy. For example, a facet with $\omega = 0.01$ in a pure MCRT model would eliminate 99% of SPs that reached the facet. This model behavior is particularly interesting in the presence of multiple scattering events.

Common MCRT models as FLIGHT (North, 1996) assume an isotropic scattering to the 4π space. Thus, for any incident direction Ω_i, the zenith θ_j and azimuth ϕ_j angles of the scattering vector Ω_j ($\Delta\Omega_j = 0$) is calculated with 2 random numbers p_1 and p_2:

$$\theta_j = \cos^{-1} p_1 \qquad \phi_j = 2\pi \times p_2 \tag{14}$$

Depending on models, a SP can have a weight W_{sp}. Then, during a scattering event, the weight of the scattered SP is updated by multiplying it with scattering probability density p_{ijk} (Eq. (4)) from direction Ω_i to direction Ω_j:

$$W_{sp} = W_{sp} . p_{ij,k} \tag{15}$$

This approach is less accurate if scattering phase functions are not isotropic because the use of an isotropic phase function induces inadequate sampling for directions Ω_i with large $p_{ij,k}$ values, and over sampling for directions with small $p_{ij,k}$ values.

In addition, the random generation of Ω_j implies to compute $p_{ij,k}$ frequently during SP tracking, using complex computation (Eq. (2)-(5)) and changing summation terms into integration terms with $\Delta\Omega_j = 0$. This is inefficient in terms of computation time. Thus, back-tracking algorithms are often implemented to track rays from the sensor (Disney et al., 2000), considering scattering events up to a limited scattering order.

During a SP scattering event, DART uses an exact probability of scattering to redirect the SP. Moreover, the incident Ω_i and scattered Ω_j directions are restricted to be pre-defined discrete directions. Therefore, terms (Eq. (2)-(5)) that traditional MCRT must calculate frequently can be pre-calculated in DART. It should be noted that $p_{ij,k}$ represents a cumulative probability with non-zero solid angle $\Delta\Omega_j$, instead of the probability density in Eq. (15). Thus, probabilities of scattering towards each discrete direction over the 4π space are represented by fractional intervals that sum to unity. Thus, it is possible to invert a random number p to determine Ω_j:

$$\overrightarrow{\Omega_j} = F_X^{-1}(p) \tag{16}$$

where F_X is piece-wise CDF with $p_{ij,k}$ being the probability of each interval. Usually, F_X cannot be inverted analytically, which implies that p must be numerically compared with F_X. Classical solving methods such as the bisection method can be very slow. Thus, a specific search method, hereafter called box method, was designed for fast selection of Ω_j. This selection relies on two random numbers only.

The box method uses an array B_k that is created per element type k in computer memory. B_k stores the anisotropic scattering probabilities $p_{ij,k}$ (Eq. (4)). For a turbid medium, it has $(N_{dir,nv} + 1)$ lines and $N_{dir,nv}$ columns (Figure 2). For each line i of B_k, we have: $\sum_{j=1}^{N_{dir,nv}} p_{ij,k} = 1$. A basic approach would be to transform each $p_{ij,k}$ into $X_{b,i,j,k}$ probability intervals (boxes), each one storing the index j of a scattering direction, with the number $X_{b,i,j}$ of boxes for a scattering direction j being proportional to probability $p_{ij,k}$. The total number of boxes of a line i is $\sum_j X_{b,i,j} = X_{b,i}$. Thus, a random number p, between 0 and 1, defines the box $p.X_{b,i}$, and the value of this box gives the index of the scattering direction to consider. Actually, this direct approach is unsuitable because it can require too much computer memory. Indeed, scattering probabilities are converted to integer numbers of boxes, which can require very large numbers of boxes, if the range of $p_{ij,k}$ probabilities is very large. For example, if 10 boxes are assigned to a scattering direction with probability of 5×10^{-7}, then a scattering direction with a 0.2 probability must occupy 4×10^{6} boxes.

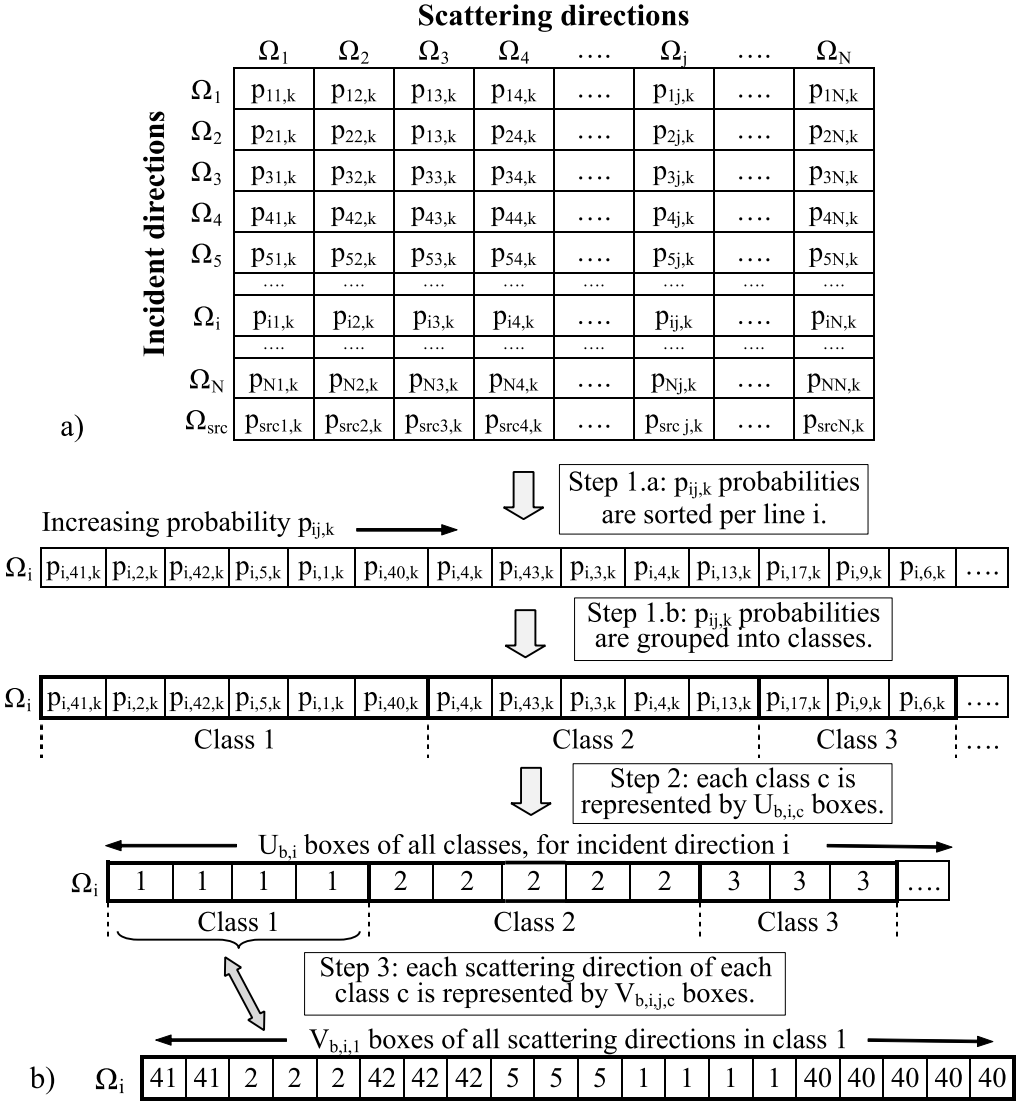

Figure 2 : Box method. a) Array B_k of probabilities $p_{ij,k}$. Ω_i is the illumination source direction. b) The 3 steps of the box method.

Thus, in order to optimize memory management, the box method (Figure 2) uses an array B_k that is created with 3 steps:

- Step 1: Probabilities $p_{ij,k}$ of each line i of B_k are sorted and grouped into classes that have similar probabilities. This grouping is such that the range of probabilities of scattering directions within the same class is less than a given threshold $\gamma \geq 1$. Thus, for any two scattering directions Ω_j and Ω_j in the same class c, with $p_{ij,k} \geq p_{ij',k}$, we have always: $p_{ij,k} \leq \gamma . p_{ij',k}$. With this approach, each line i has C_i classes.
- Step 2: Any class c is represented by $U_{b,i,c}$ boxes. Thus, the set of classes of each line i is represented by $U_{b,i} = \sum_{c=1}^{C(i)} U_{b,i,c}$ boxes.
- Step 3: Each scattering direction of a class c is represented by $V_{b,i,c,j}$ boxes. Thus, the selection of one direction Ω_j in class c relies on a representation of class c by a number of boxes equal to $V_{b,i,c} = \sum_j V_{b,i,c,j}$.

Thus, $\sum_{c=1}^{C(i)}(U_{b,i,c} + V_{b,i,c}) \ll \sum_j X_{b,i,j}$ $\forall$ line i, and the scattering direction is selected with 2 random numbers p_1 and p_2. First, $p_1 . U_{b,i}$ gives a box the value of which is the class c, and then $p_2 . V_{b,i,c}$ gives a box the value of which is the scattering direction.

Another advantage of the box method is that the computation time for selecting the scattering direction does not depend on the number of discrete directions $N_{dir,nv}$. $N_{dir,nv}$ can be very large, for instance for sampling very accurately the 4π space, yet the required computer memory increases with $N_{dir,nv}$. Let us consider an Earth scene with a single scene element. The required computer memory is defined and assigned per line of B. With an available memory M, the memory per line is $M_l = \frac{M}{n_l}$, where n_l is the total number of lines of B. We have $n_l = N_{dir,nv} + 1$ for any turbid medium, $n_l = \frac{N_{dir,nv}}{2} + 1$ for any opaque facet with anisotropic reflectance, and $n_l = 1$ for isotropic facet. In presence of n_{turb} turbid mediums and n_{facet} anisotropic facets, $n_l = (N_{dir,nv} + 1) . n_{turbid} + \left(\frac{N_{dir,nv}}{2} + 1\right) . n_{facet}$.

Sizes of arrays $V_{b,i,c}$ and $U_{b,i,c}$ depend on threshold γ. For example, if the direction with the smaller probability in any class c is represented by $V_{b,i,c,min}$ boxes, then, any scattering direction in the any class is represented by a number of boxes between $V_{b,i,c,min}$ and $\gamma . V_{b,i,c,min}$. Thus, the mean number of boxes that is needed for representing all scattering directions of the C(i) classes is about:

$$V_{b,i,c,min} . \frac{\gamma + 1}{2} . N_{dir,nv} \quad (17)$$

On the other hand, the number of classes C(i), and hence the number of boxes that represent all classes, is inversely proportional to γ. For optimizing computer memory, γ must be selected to minimize the total size of the arrays $V_{b,i,c}$ and $U_{b,i,c}$. This is achieved with an iterative optimization method that considers that the worst solution (i.e., largest number of boxes) occurs for $\gamma = 1$. Then, the total number of boxes per line i is $X_{b,i}$. This optimization is conducted independently for each incident direction because the scattering directions are assumed to be independently distributed per incident direction. The accuracy of the box method is discussed in the **Appendix B**.

3.3 Case study and self-validation

The DART quasi-MCRT mode was tested against simulated bi-directional reflectance factor (BRF) and reflectance image of the most heterogeneous site in the RAMI4 experiment (Widlowski et al., 2013): the $100m \times 100m$ Jarvselja birch stand (Kuusk et al., 2009). This site has 7 tree species with heights ranging from 5.9 to 30.51m. 18 trees are constructed by 3-D facets representing branches, trunks and leaf elements. Optical properties are given per type of element on RAMI4 website (http://rami-benchmark.jrc.ec.europa.eu/HTML/RAMI-IV/RAMI-IV.php). DART BRFs of this test site were validated in the RAMI4 experiment. Figure 3a shows a $20m \times 20m$ DART simulation (center: (65m, 55m)), with $0.2m \times 0.2m \times 0.1m$ cell size. Being too numerous ($> 3 \times 10^7$) to be simulated as such, leaf and branch facets were converted into turbid medium for much faster processing, with leaf area index (LAI) and LAD being calculated per cell. Computer time can be divided by more than 10, depending on the number of facets and the size of DART cells. Figure 3b shows the simulated scene 3-D representation. The IUSD method (Yin et al., 2013b) was applied to create 11 discrete directions with 0.4 sr solid angles and 15^o view zenith angle (VZA) step in the zenith plane defined by 90^o view azimuth angle (VAA) (Figure 3c). These view directions are used for studying BRF variation in the plane ($VAA = 90°$) with different SP numbers for illumination. The simulated LiDAR wavelength was λ=532nm ($\Delta\lambda$=0.03μm). Sun was positioned at nadir.

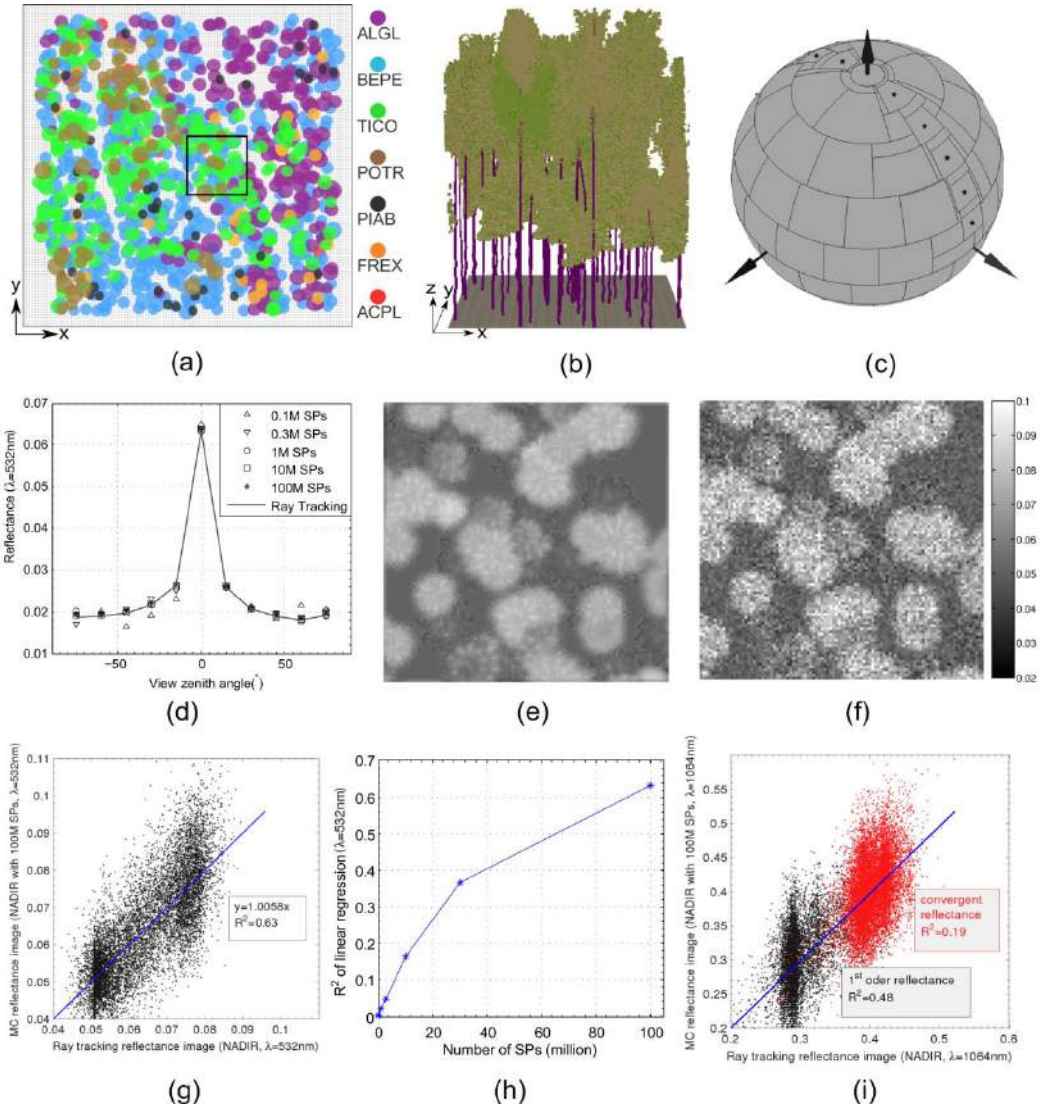

Figure 3. Quasi-MCRT validation with DART ray-tracking, for RAMI4 Jarvselja birch site. a) Tree species map and the simulated $20m \times 20m$ scene. b) 3-D simulated scene. c) IUSD discretization with 11 directions in the plane VAA=90°-270°. d) BRF of the 11 directions, simulated with ray-tracking and quasi-MRCT with 5 SP numbers (λ=532nm). Negative VZA is for the half plane VAA=270°. e, f) Ray-tracking and quasi-MCRT (10^8 SPs) nadir reflectance images. g) Scatterplot of images (e) and (f). h) R^2 values with increasing SP number. i) Same as h) with (λ=1064nm).

Based on the above pre-defined parameters, BRFs and reflectance images of the Jarvselja site were simulated with DART quasi-MCRT and ray-tracking modes. In the quasi-MCRT mode, 7 simulations are run with 7 SP numbers: 0.1, 0.3, 1, 3, 10, 30, 100×10^6 SPs. Each SP carries an energy equal to sun irradiance divided by the SP surface density. The maximal number of scattering events was set to 150. On average, the time required for simulating interactions of each SP is $\approx 4.1\ 10^{-4}$ s, with a 3.07 GHz processor. In total, the processing time per simulation ranged from 41 s to 11.4 h. Figure 3d shows the BRF values for the 11 selected directions and the 7 SP numbers. The BRF values (solid line) simulated with DART ray-tracking mode are used as the reference, because they were validated in the RAMI experiment (Widlowski et al., 2007). BRF values converge to the reference as the number of SPs increases, demonstrating that with enough SPs, the quasi-MCRT

method can be very accurate. The hot spot effect in the nadir view direction always occurs. The images simulated in the ray-tracking (Figure 3e) and MRCT modes were also compared per pixel, with different SP numbers. Figure 3f shows the MRCT reflectance image with 10^8 SPs, and Figure 3g shows the close correspondence between the two images ($y = 1.0058x$, $R^2 = 0.63$). It improves only slightly if only the 1st order reflectance is compared ($R^2 = 0.66$). The relationship improves logarithmically as the number of SPs increases (Figure 3h), demonstrating that DART ray-tracking images corresponding to MRCT images can be computed in much less time. For example, the ray-tracking image (Figure 3e) required ≈ 45 mn with 20 threads to simulate, whereas the image in Figure 3f requires 11.4 h and has a large noise content.

The quasi-MCRT method was also validated in the NIR with (λ=1064nm, $\Delta\lambda$=0.1nm) and the above experimental conditions. Figure 3h shows the scatterplot of the ray-tracking image versus the quasi-MRCT image that was simulated with 10^8 SPs, for 1st order reflectance (dark points) and total (i.e., convergence) reflectance. The strong reduction of R^2 value from 0.48 for 1st order reflectance down to $R^2 = 0.19$ for convergence reflectance, is due to the strong multiple scattering in NIR. Thus, the number of SPs must be increased to get a larger R^2 value.

The relationship between 1st order reflectance in the NIR band ($R^2 = 0.48$) is less than in the green band ($R^2 = 0.66$). Here, it is explained with a schematic scene that is made of a grass understory with backscattering reflectance $\rho_{gr,\lambda}(\Omega, -\Omega)$ along direction Ω at wavelength λ below a tree canopy, with a direct transmittance $t_{dir,\lambda}(\Omega)$ and a 1st order back-scattering phase function $P_{\lambda,1}(\Omega, -\Omega)$. In this scene, 1st order back-scattered reflectance for direction (Ω) is: $\rho_{\lambda,1,fp}(\Omega, -\Omega) \approx t_{dir,\lambda}(\Omega).\rho_{gr,\lambda}(\Omega, -\Omega) + \left(1 - t_{dir,\lambda}(\Omega)\right).P_{\lambda,1}(\Omega, -\Omega)$. The 1st term represents grass scattering, and the 2nd term represents vegetation canopy scattering. In DART ray-tracking mode, both of the terms are calculated exactly. In the quasi-MCRT mode, the 2 terms are not assessed with the same accuracy. For having the same accuracy, the 2 terms should be estimated with numbers of SPs weighted on the values of these 2 terms. However, DART estimates each term with number of SPs weighted on $t_{dir,\lambda}(\Omega)$. In the Jarvselja site, $t_{dir,\lambda}(\Omega)$ is very small, with $\rho_{gr,\lambda}(\Omega, -\Omega)$ small in the visible and very large in the NIR. Thus, grass reflectance has a small impact on $\rho_{\lambda,1,fp}(\Omega, -\Omega)$ in the visible, independent of associated Monte Carlo noise, and a large impact in the NIR. In real canopies, interactions with branches and trunks makes the situation even more complicated.

4. LiDAR WAVEFORM SIMULATION

This section presents the simulation of wLiDAR, for any instrument configuration (sensor orientation, footprint and FOV sizes, etc.) and Earth-atmosphere system.

4.1 LiDAR geometry and simulated photon initialization.

DART simulates more realistic configurations than previous LiDAR models. For example, scene elements are not represented as simplified geometric objects. Figure 4 illustrates how DART simulates LiDAR geometry. In LiDARs, laser pulses are reflected by a rotating / oscillating mirror towards the observed region. The left part of Figure 4 shows a LiDAR pulse with nadir illumination (footprint) and acquisition (FOV) at ground level. The spatial width of transmitted laser beam is neglected: the source of pulse transmission is a single point, which is the LiDAR position $P_L(x, y, H)$, where H is the height above the scene reference minimum altitude (SRMA: elevation model smaller altitude). P_L is also the location of the acquisition telescope, with radius r_t and area $A_t = \pi r_t^2$. Footprint and FOV are constant parameters for a LiDAR with height H, which defines

the illumination and reception regions in nadir direction. They are represented by half dispersion angle β_{fp} and β_{FOV} respectively, which are constant parameters for a LiDAR. The footprint and FOV give circular regions on the plane at SRMA (C_{fp} and C_{FOV}), with radii $r_{fp} = \frac{H}{\tan\beta_{fp}}$ and $r_{FOV} = \frac{H}{\tan\beta_{fp}} + r_t$, respectively.

For oblique LiDAR orientation $\overrightarrow{\Omega_L}$ (right part of Figure 4), with look angle θ_L, the circular illumination and reception regions at SRMA level in LiDAR local coordinate system (frame according to $\overrightarrow{\Omega_L}$) correspond to elliptical regions (E_{fp} and E_{FOV}) in the simulated system frame. The short (perpendicular) radii of the ellipses are $r_{\perp,ilm} = H.\frac{\tan\beta_{fp}}{\cos\theta_L}$ and $r_{\perp,rcp} = H.\frac{\tan\beta_{FOV}}{\cos\theta_L} + r_t$, respectively. The long radii are $r_{\parallel,ilm} = H.\frac{\tan\beta_{fp}}{\cos^2\theta_L}$ and $r_{\parallel,rcp} = \frac{H\cdot\tan\beta_{fp}/\cos\theta_L + r_t}{\cos\theta_L}$, respectively.

Cross-beam energy W can have any spatial distribution. Default cross-beam energy $W(r)$ follows Gaussian law $\exp(-\frac{r^2}{2\sigma^2})$, where r is the distance to the center of footprint circle C_{fp} and standard deviation σ is derived from the user defined energy fraction of Gaussian maximum at C_{fp} boundary ($r = r_{fp}$). Energy outside C_{fp} is neglected. The associated SP spatial distribution is a squared illumination cell grid on a plane perpendicular to $\overrightarrow{\Omega_L}$ in the LiDAR local frame. The energy to launch per cell grid at a distance r_{sub} to the pulse center, within footprint region C_{fp}, is:

$$W_{sub} = W_L \times P_{sub} \quad \text{with } P_{sub} = \frac{\exp(-\frac{r_{sub}^2}{2\sigma^2})}{\sum_{fp}\exp(-\frac{r_{sub}^2}{2\sigma^2})} \tag{18}$$

where the summation is over all cell grids within footprint region C_{fp} and W_L is the total energy of a pulse within its footprint. Basically, the total number of photons to be launched per cell grid is proportional to the cell grid energy W_{sub}. Let $N_{sp,apr}$ be the user defined value that represents the approximated total number of SPs within footprint. Then, for each cell grid, the number of SPs to fire is:

$$N_{sp,sub} = \begin{cases} N_{sp,apr}.P_{sub} & \text{if } N_{sp,apr}.P_{sub} > N_{sp,sub,min} \\ N_{sp,sub,min} & \text{if } N_{sp,apr}.P_{sub} < N_{sp,sub,min} \end{cases} \tag{19}$$

with $N_{sp,sub,min}$ the minimum number of SP to fire per cell grid to ensure that enough SPs are launched at footprint boundary. Each SP in a cell grid has the energy $W_{sp} = \frac{W_{sub}}{N_{sp,sub}}$. Thus, $N_{sp} = \sum_{grid} N_{sp,sub}$ SPs must be fired, with $N_{sp} \geq N_{sp,apr}$.

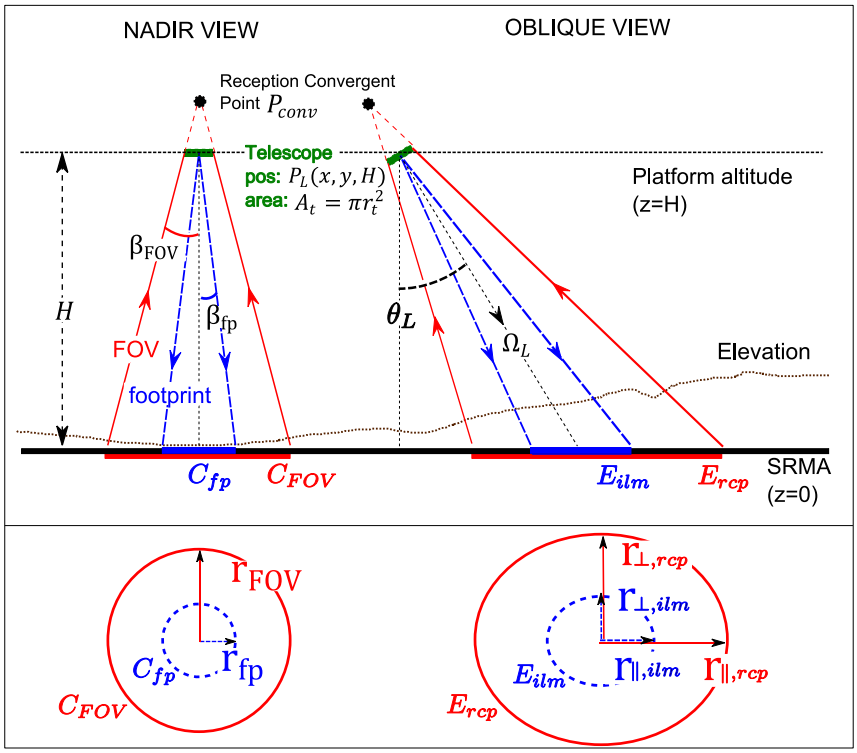

Figure 4: LiDAR pulse geometry for nadir (left) and oblique (right) orientations, with the illumination and reception areas at the horizontal plane "z = 0".

For each SP to be fired from a cell grid, 2 random numbers are generated to select its position in the cell grid. This position defines the SP direction vector in the LiDAR frame. This vector is multiplied by the rotation matrix of LiDAR orientation $\overrightarrow{\Omega_L}$ to get the photon direction $\overrightarrow{\Omega_{sp}}$ in the scene coordinate system, which initializes the SP. After its launch, the SP state (W_{sp}, $\overrightarrow{r_{sp}}$, $\overrightarrow{\Omega_{sp}}$) is updated at each interaction (Eq. (6), (13), (16)) for setting its new weight W_{sp}, position r_{sp} and direction Ω_{sp}.

4.2 Ray Carlo method for waveform retrieval

The Ray Carlo method relies on adaptations of stratified sampling and quasi-MCRT methods. N_{sp} SPs are launched in sequence, and the traveled distance and energy of all backscattered SPs that enter LiDAR are recorded to create the waveform signal. The probability that a SP scattered in P enters the LiDAR is proportional to the solid angle $(\overrightarrow{\Omega_{p2l}}, \Delta\Omega_{p2l})$ from P to LiDAR FOV convergent point (P_{conv}), with $\overrightarrow{P_{conv}} = \overrightarrow{P_L} - \frac{r_t}{\tan \beta_{FOV}} . \overrightarrow{\Omega_L}$ and r_t is LiDAR telescope radius. With d_{p2l} the distance from P with intersection of A_t along $\overrightarrow{\Omega_{p2l}}$, we have: $\Delta\Omega_{p2l} = A_t \cdot \frac{-\overrightarrow{\Omega_{p2l}} \cdot \overrightarrow{\Omega_L}}{d_{p2l}^2}$, which is usually extremely small. Thus, the chance that a SP enters LiDAR by pure MCRT is very low.

To increase the number of measured SPs, a method called Ray Carlo was designed. Figure 5 illustrates it with 3 scattering events of a SP. At each scattering event in P, the direction $\overrightarrow{\Omega_{sp}}$ of the incident SP is updated to one of the pre-calculated discrete directions $\overrightarrow{\Omega_D}$, and an additional SP is

initialized and fired towards LiDAR if P is within LiDAR FOV ($-\overrightarrow{\Omega_{p2l}}.\overrightarrow{\Omega_L} < \cos\beta_{FOV}$). Moreover, for entering the telescope, SPs must have incident angles smaller than the LiDAR aperture angle β_{FOV}, which requires $\text{atan}\left(\frac{r_t}{d_{p2l}}\right) < \beta_{FOV}$ and reduces $\Delta\Omega_{p2l}$. Actually, this reduction is significant only for very close range scattering. For turbid medium the scattering space is 4π. For facets, it is the hemisphere that is defined by $\overrightarrow{\Omega_{p2l}}.\overrightarrow{\Omega_f} > 0$ for reflection, and $\overrightarrow{\Omega_{p2l}}.\overrightarrow{\Omega_f} < 0$ for diffuse transmission.

The additional SP towards LiDAR is called "virtual SP" because it corresponds to a virtual ray (Yin et al., 2013a). The energy of the virtual SP is $W_{p2l} = W_{sp}.\Delta\Omega_{p2l}.T(\overrightarrow{\Omega_i}, \overrightarrow{\Omega_{p2l}})$, where $T(\overrightarrow{\Omega_i}, \overrightarrow{\Omega_{p2l}})$ is the scattering probability towards $\overrightarrow{\Omega_{p2l}}$. To simplify calculation, scattering is assumed to be isotropic within each pre-calculated scattering discrete direction. Thus, we can write $T(\overrightarrow{\Omega_i}, \overrightarrow{\Omega_{p2l}}) = \frac{T(\overrightarrow{\Omega_i}, \overrightarrow{\Omega_{s(\overrightarrow{\Omega_{p2l}})}})}{\Delta\Omega_{s(p2l)}}.\Delta\Omega_{p2l}$ where $s(\overrightarrow{\Omega_{p2l}})$ is the index of the discrete direction that contains $\overrightarrow{\Omega_{p2l}}$ in its angular sector, which leads to:

$$W_{p2l} = W_{sp}.\frac{\Delta\Omega_{p2l}}{\Delta\Omega_{s(\overrightarrow{\Omega_{p2l}})}}.T(\overrightarrow{\Omega_i}, \overrightarrow{\Omega_{s(p2l)}}) \quad (20)$$

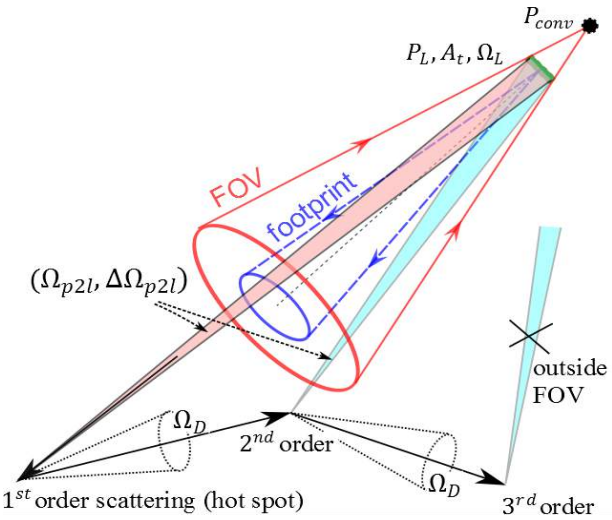

Figure 5 : Illustration of Ray Carlo method for simulating LiDAR acquisition with multiple scattering orders.

The tracking of a virtual SP is equivalent to multiplying its energy by the direct transmittance along the path to the LiDAR. With the assumption that LiDAR position does not change during acquisition, 1st order scattering is under an exact hot spot condition (Eq. (7)); for vegetation turbid medium: $\alpha_v^1(\overrightarrow{\Omega_{sp}} = -\overrightarrow{\Omega_{sr}}) = 0$. In short, the Ray Carlo method (virtual ray and MCRT) greatly increases the number of measured SPs by a factor more or less equal to $\frac{\Delta\Omega_{nv}}{\Delta\Omega_{p2l}}$, which can be as large as 10^{10}, depending on LiDAR altitude and solid angle $\Delta\Omega_{nv}$ of non virtual directions.

In DART, all SPs are fired at the same time, and the received signal is divided into temporal bins, the size of which depends on the acquisition rate. The waveform of a wLiDAR device with an emitted laser pulse, is simulated as a temporal convolution of the pulse temporal profile with the DART simulated signal. The temporal profile can be a Gaussian profile with its full wave at half

maximum and a duration equal to a number of standard deviations, or an imported temporal profile from an actual wLiDAR device. The retrieval distance range of the LiDAR signal is also defined depending on the spatial region of interest, which depends on the scientific objective (DEM generation, vegetation structure, or atmosphere constituent's analysis). It can be restricted to the Earth landscape (usually less than 100m range above and below SRMA) or atmosphere range (thousands of meters above the Earth scene).

4.3 DART LiDAR products and self-validations

Figure 6 illustrates a LiDAR waveform that is simulated with the DART Ray Carlo method and a small-footprint configuration, for a scene that consists of a single 3-D object from the Jarvselja birch stand (Figure 6a). The LiDAR altitude is H=10km , with device configuration given in Table 1, which is very close to the LiDAR system onboard the Carnegie Airborne Observatory (CAO) platform (Asner et al., 2012). The emitted pulse and detector are characterized by λ=1064nm and $\Delta\lambda$=0.1nm. The LiDAR acquisition rate is 1ns. Thus, the absolute distance stored per bin is $\approx$15cm.

Since DART has the information of each SP that enters the sensor (e.g., SP energy, traveled distance, scattering order and direction, etc.), the expected position of scattering of each SP can be back-tracked. Figure 6b shows the associated original DART output. Green points show the scattering positions of the SPs that enter the sensor through 1st order scattering. They are located on the surface of scattering elements. Other colors indicate SPs that have undergone multiple scattering events. Thus, they are not located on the surface of their last scattering element. Thus, they can be located below the ground and between the ground and the crown canopy. Figure 6c gives the full waveform (blue line) and the waveform due to 1st order scattering (red line). The vertical axis represents the recorded time and distance according to the ground return. The horizontal axis gives the actual number of photons acquired per bin of acquisition (1ns in the simulation). Signals from the ground (last waveform peak) and the tree crown (other peaks) are well separated. Peaks from the tree crown are somewhat correlated with the horizontal levels of branches and leaves. In actual wLiDAR devices, the photon count is converted into electrical voltage by analog signal detectors. The multiple scattering contribution to the waveform (Figure 6c) is the difference between the total and 1st order waveforms. The large NIR optical properties of vegetation explain that NIR multiple scattering is important in vegetation. It increases if LiDAR FOV increases. Multiple scattering is usually a source of difficulty for analyzing measured waveforms. Indeed, it prevents from relating each waveform bin to a unique Earth scene element. This difficulty stresses the need to have a good estimate of the fraction η of multiple scattering in LiDAR waveforms ($\eta = \frac{full\ waveform - 1^{st}\ order\ waveform}{full\ waveform}$). An example of assessment of η is presented in the **Appendix C** for a schematic vegetation cover. It quantifies the impact of 3 parameters (foliar spherical albedo ω_f, LAI, footprint size r_{fp}) on η. In these cases, ω_f is the predominant parameter.

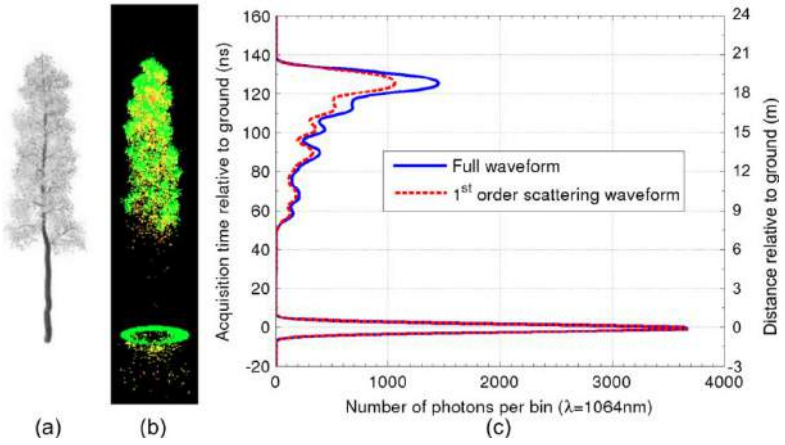

Figure 6. DART waveform of a LiDAR pulse. (a) The scene is a Linden tree from the RAMI-4 experiment. (b) 3-D plot: each point indicates the distance traveled per acquired photon. (c) 1st order (red dashed line) and full (blue line) waveforms.

Table 1. Configuration of the simulated LiDAR.

Parameters	Symbols	Values
Sensor area	A_t	0.1m^2
Time step per bin	δt_{bin}	1 ns
Footprint divergence half angle	β_{fp}	0.25 mrad
FOV divergence half angle	β_{FOV}	0.4 mrad

The Ray Carlo method to simulate LiDAR waveform was validated with the Jarvselja birch site (Figure 7), with similar methodology as in Section 3.4. LiDAR FOV and footprint centers (Figure 7a) are located at (65m, 55m), which is the center of the simulated scene in Figure 3a and b. LiDAR device configuration is set by Table 1, with ($\lambda = 532\text{nm},\ \Delta\lambda = 0.03\text{nm}$) as in Section 3.4. The acquired waveform is simulated for 5 sensor altitudes (H=2km, 5km, 10km, 20km, 35km), which gives the corresponding r_{fp} of small footprint to middle footprint configuration (r_{fp}=0.68m 1.43m 2.68m 5.18m and 8.93m). LiDAR pulse energy is set to 1mJ for H=35km as a reference. For the other cases with different altitudes, it is proportional to H^2 for having approximately the same W_{p2l} received through $\Delta\Omega_{p2l}$ (inversely proportional to H^2), with the same scene elements. Thus, waveforms can be cross-compared (Figure 7b). For each case, 0.1M SPs are fired from LiDAR to calculate the waveform. On average, the time period for simulating each SP is about 4.6×10^{-4} s (46 s per simulation), using Ray Carlo method, which is larger than the 4.1×10^{-4} s in the quasi-MCRT in Section 3.4 because of the tracking of W_{p2l}.

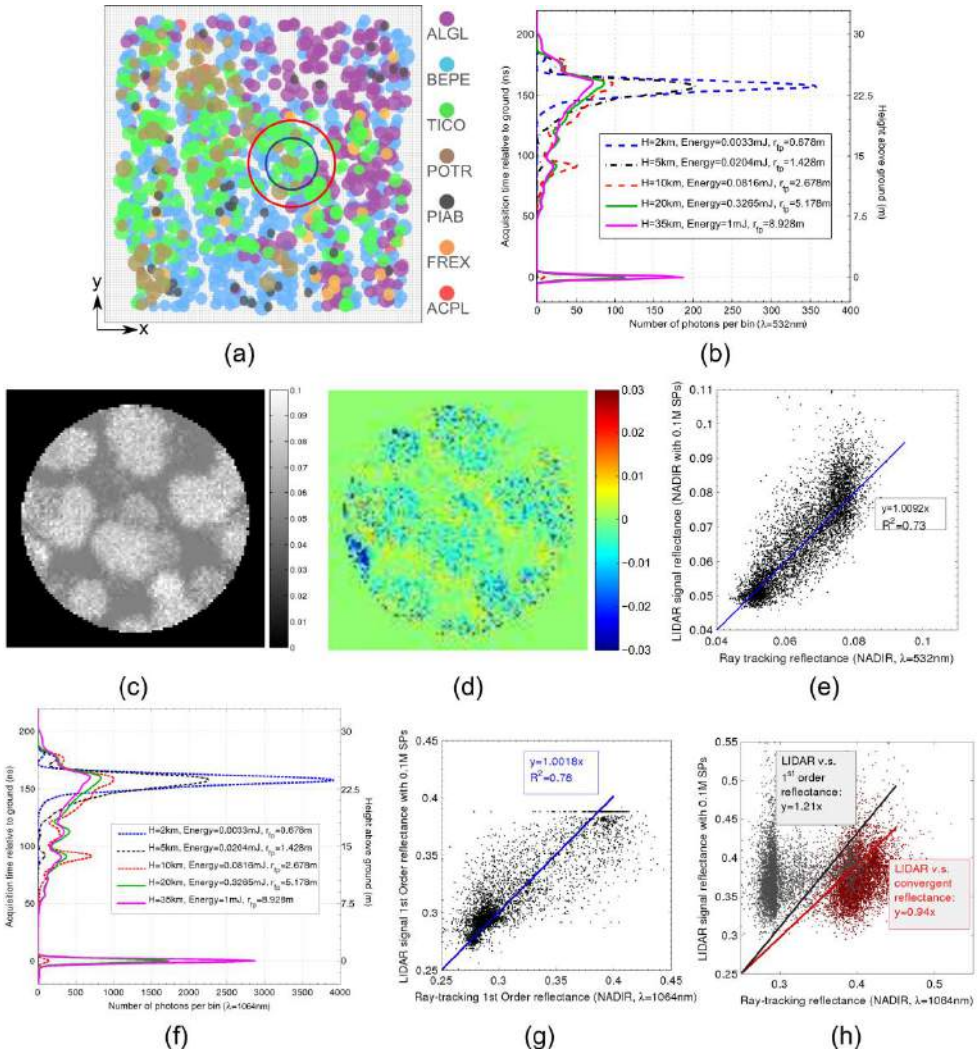

Figure 7. LiDAR simulation and validation with Jarvselja birch stand. (λ=532nm) in (a-e) and (λ=1064nm) in (f-h). a) Tree species map with C_{fp} and C_{FOV} centered at (65m, 55m). b) Simulated waveforms with parameters of Table 1 and different altitudes (H), pulse energy and ground projected footprint radii (r_{fp}). c) LiDAR derived reflectance image for H=35km (r_{fp} = 8.926m). d) Difference image: subtraction of ray-tracking (Figure 3e) and LiDAR (c) reflectance images within C_{fp}. e) Linear regression: ray-tracking and LiDAR reflectance images within C_{fp}. f) Simulated waveforms at 1064 nm. g) Linear regression: 1st order LiDAR and ray-tracking reflectance images (y=1.0018x). h) Linear regression: LiDAR image versus 1st order (y=0.94x) and convergent (total: y=1.21x) ray-tracking images.

Figure 7b shows the generated waveforms for the 5 cases. For the case with H=2km, the whole C_{fp} covers part of the crown of a poplar with 25m height. The LiDAR pulse is attenuated within the crown with dense leaves and branches, and no SP reaches the ground, which explains that the sensor cannot acquire ground signals. Thus, the waveform concentrates in the range between 18m to 25m above the ground. As the altitude increases, firstly an obvious peak is observed between 10m to 15m, which corresponds to the lindens around the 2 poplars. As the altitude further increases, several lindens with height range from 5.9m to 20.7m and birches with height from 19.9m to 30.5m are profiled by the waveform. In addition, from H=10km, SPs start to reach the ground and are

backscattered to LiDAR, through vegetation gaps and space between tree crowns. As the area of C_{fp} increases more signals from the ground contribute to the waveforms.

With the aim to validate the LiDAR received signals, DART creates automatically a reflectance "image" by projecting the spatial distribution of received SP energies onto a plane centered on the SRMA and perpendicular to the LiDAR orientation. The reflectance value of pixel (i,j) on the plane is:

$$\rho_{i,j} = \frac{E_{i,j,rcp} \times \pi}{\Delta\Omega_{i,j,p2l} \times E_{i,j,ilm}} \quad (21)$$

where $E_{i,j,rcp}$ is the received energy within the pixel, and $E_{i,j,ilm}$ is the illumination energy on the pixel; $\Delta\Omega_{i,j,p2l}$ is the solid angle from the pixel to the LiDAR sensor. This reflectance image is a novel DART product which is not produced by usual wLiDARS. Figure 7c shows the LiDAR reflectance image generated in the case with H=35km. It is shown within a $20\text{m} \times 20\text{m}$ window that contains C_{fp}. This is to facilitate the pixel-wise comparison with the reflectance image (Figure 3e) that is simulated with DART tracking mode. Figure 7d shows the difference image by subtracting Figure 7c from Figure 3e. It can be observed that within C_{fp}, the difference is very small. Linear regression of Figure 7c versus Figure 3e is plotted by selecting only the pixels within C_{fp} in Figure 7e. We get $y = 1.0024x$ and $R^2 = 0.73$, with processing time of 58 seconds. This R^2 value is better than the R^2 that is obtained with the quasi-MCRT method with 100M SPs, without the Ray Carlo method, which takes about 11 hours.

The Ray Carlo method is also validated with NIR band ($\lambda = 1064\text{nm}, \Delta\lambda = 0.1\text{nm}$). Figure 7f plots waveforms that are simulated with the same experimental condition as Figure 7b. As expected, the vegetation and ground responses are much higher in the NIR band than in the visible (Figure 7b). Figure 7g plots the linear regression of LiDAR generated reflectance image and DART ray-tracking 1st order reflectance image. The fit is rather good: $y = 1.0018x$ and $R^2 = 0.78$. It cannot be perfect because illumination conditions differ: sun illumination is homogeneous over the studied scene, whereas LiDAR illumination has a spatial Gaussian distribution centered on the scene. Thus, here the larger LiDAR 1st order reflectance, compared to 1st order ray-tracking reflectance, can be explained by the fact that the central part of the observed scene has a larger reflectance than the mean scene reflectance. Figure 7h plots convergent LiDAR generated reflectance values versus 1st order (red dots: y=1.21x) and convergent (grey dots: y=0.94x) ray-tracking reflectance images. LiDAR reflectance image values are larger than 1st order ray-tracking image reflectance values due to both single and multiple scattering events. On the other hand, LiDAR reflectance image values are smaller than convergent ray-tracking image reflectance values because in LiDAR mode the observed scene surroundings are not illuminated, whereas in ray-tracking mode, sun illumination is homogeneous, and then the scene surrounding is illuminated as the observed scene itself. Compared to the visible domain (Figure 7e), multiple scattering is much larger, which explains that in ray-tracking mode the illumination of the observed scene has a much larger multiple scattering component. Given the potential differences between the LiDAR 1st order reflectance image values and convergent ray-tracking reflectance image, the LiDAR simulations compare quite favorably.

4.4 Comparison with LVIS data

For validation, DART LiDAR waveforms were compared with actual airborne waveforms from the LVIS sensor (Blair et al., 1999) for a $200\text{m} \times 150\text{m}$ mixed hardwood and softwood forest plot (Figure 8) in Howland Forest, Maine (45°15'N, 68°45'W), part of the Northern Experimental Forest (www.nrs.fs.fed.us/ef/). Field measurements took place in 1990, and again in 2003-2004 and

2006. Every tree with a diameter larger than 3cm was measured for its location, diameter at breast height and species (coniferous: hemlock or deciduous: aspen). Tree height and crown dimensions were derived from allometric relationships. Tree crowns were assumed to be cones for coniferous (hemlocks) and ellipsoids for deciduous (aspen). The site has a tree height distribution between 2m and 26m, fractional cover of ≈75%, and LAI=4 ($LAI_{deciduous} = 0.4$ and $LAI_{coniferous} = 3.6$). Mean volume density of foliar elements u_f was computed using tree crown dimensions: $u_{f,deciduous} = 0.14$ and $u_{f\,coniferous} = 0.30$. A total of 89 LVIS full waveforms were acquired along 2 flight tracks (Figure 8) over the site in the summer of 2003 as part of a NASA Terrestrial Ecology Program aircraft campaign. There was nearly no overlap between the footprints along track.

In the absence of accurate ground and foliar optical properties, a normalization was applied to DART and LVIS waveforms. Most DART and LVIS waveforms were similar (Figure 9). The correlation coefficients of LVIS and DART waveforms ranged from 0.09 to 0.97, with a mean $R^2 = 0.52$. The major cause of differences is inaccuracies in forest plot simulation. For instance, tree crowns are simply simulated as ellipsoidal or conical volumes without branches. Actually, DART can simulate trees very accurately with any crown shape and branches, if branches and foliar elements are simulated with facets (Gastellu-Etchegorry et al., 2015). However, this detailed information was not available. Additional work, not shown here, showed that DART LiDAR simulations are more realistic if branches are simulated. A suggestion for future works is to simulate trees with "mean" branch systems, combined with "mean" crown shapes (ellipsoidal, etc.). The fact that optical properties based on environmental conditions for ground and foliar elements cannot be exact is also a source of differences between the LVIS and DART waveforms.

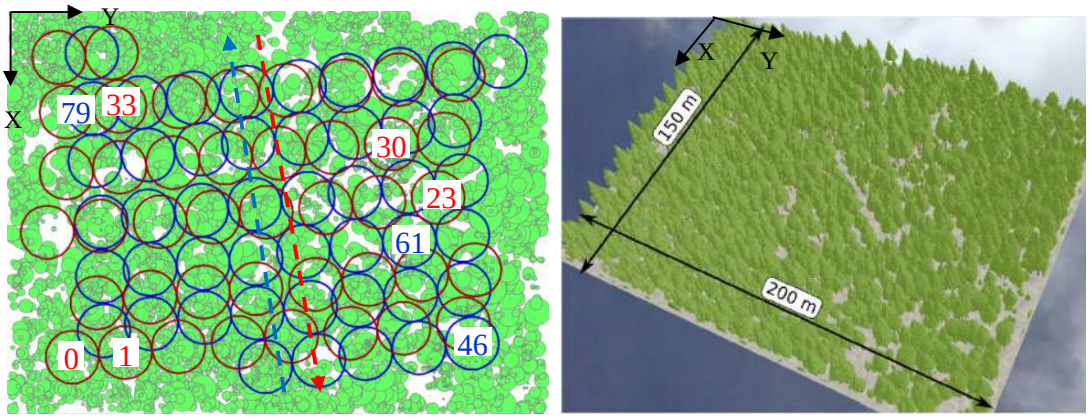

Figure 8: a) Howland forest study area and the 89 LVIS footprints acquired along the 2 flight tracks (red and blue arrows). Local DART reference system (X,Y) is shown. b) DART forest scene used for simulating waveforms.

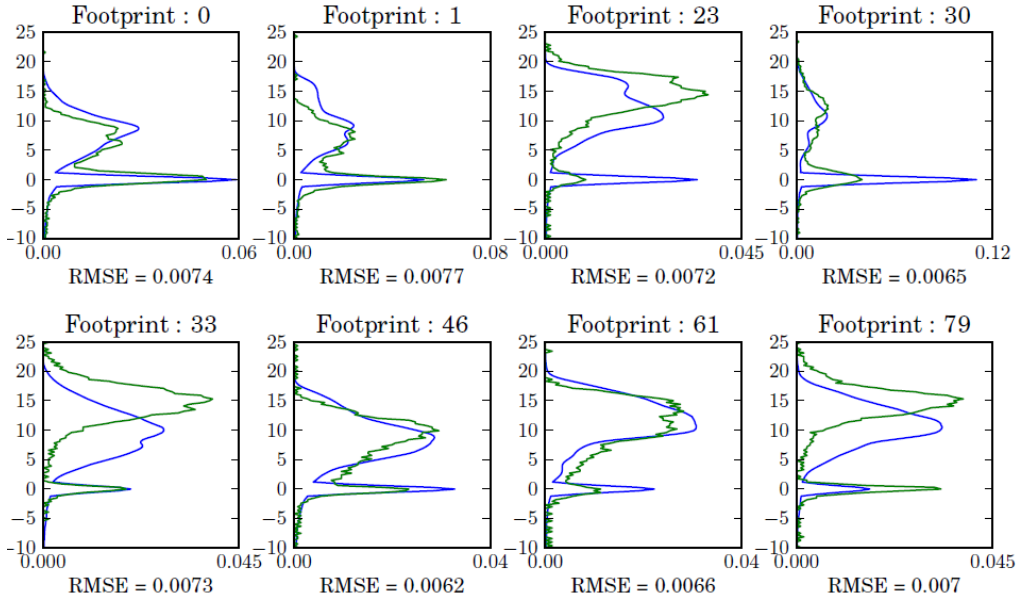

Figure 9: Measured (LVIS, green) and simulated (LVIS, blue) LiDAR footprints with their RMSE. See Figure 8 for the location of footprints in the study area.

Table 2 : LVIS characteristics (Blair et al., 1999) used for DART simulations.

Telescope aperture	20 cm	**Altitude**	2.5 km
Telescope total FOV	110 mrad	**Laser pulse width**	10 ns (FWHM)
Detector FOV	8 mrad	**Pulse repetition rate**	100-500 Hz
Digitiser sampling rate	500 Msamp/s: 2 ns	**Laser output wavelength**	1064 nm
Laser output energy	5 mJ	**Footprint diameter**	20 m

5. WAVEFORM SIMULATION WITH ATMOSPHERE

In addition to solar radiation scattering, the atmosphere has 3 major impacts on LiDAR waveforms: 1) Interception of the LiDAR pulse before it reaches the Earth's surface, 2) Interception of the signal that is backscattered from the Earth's surface, and 3) Backward and forward scattering of LiDAR photons intercepted by the atmosphere, which depends on the altitudes of scattering events as well as the atmosphere density and optical properties. The Ray Carlo method simulates these effects.

5.1 Theory

Similar to most atmospheric models, the extinction coefficient $\alpha(z)$, with z being the altitude, was initially assumed to be a constant per atmosphere layer. In that case, the optical depth that a ray meets along a direction of zenith angle θ in an atmosphere layer n of thickness Δz_n and extinction coefficient α_n is $\delta\tau = \alpha_n . \Delta z_n / \cos\theta$. The SP travel distance is calculated with Eq. (9) and (10) and a random number.

Atmosphere layers can be very thick, up to several kilometers for the top layers. However, even for these layers, the assumption of constant $\alpha(z)$ is not a source of inaccuracy for simulating the signals of optical passive sensors. Indeed, these signals depend on each layer optical depth and not on the

layer vertical distribution of $\alpha.(z)$. For LiDAR, signals, the situation is very different because a waveform is a temporal profile of continuous signal which varies with the atmosphere vertical density. Thus, simulating the atmosphere with density discontinuity, which implies a discontinuity of α, implies a discontinuity of the simulated waveform. A solution could be to simulate the atmosphere with layers the depths of which are smaller than the distance associated to LiDAR acquisition rates of several nanoseconds (i.e., 15cm/ns). However, this solution is not realistic with DART, because it requires a tremendous number of atmosphere layers. It can be noted that this discontinuity problem occurs also in vegetation turbid cells in the simulated Earth landscapes. However, it is negligible because vegetation cells have very small dimensions. DART solves the atmosphere discontinuity problem by simulating $\delta\tau$ and α as continuous profiles. For that, 3 conditions are verified per layer: exact layer optical depth and exact extinction coefficients at the 2 layer boundaries. In addition, for simplifying photon tracking in LiDAR modeling, the vertical variation of $\delta\tau(z')$ in each layer must be an invertible function in order to replace the relationship $\delta\tau(\delta l) = \alpha.\delta l$ that is used with constant α. The selected invertible function is a third-order polynomial:

$$\delta\tau(z') = c_3 z'^3 + c_2 z'^2 + c_1 z' + c_0 \quad (22)$$

where z' is the relative altitude in an atmosphere layer: $z' \in [0\ \ \Delta z]$ with $z' = 0$ at the bottom of the layer, and $z' = \Delta z$ at the top of the layer. The extinction coefficient $\alpha(z')$ is derived from the relationship $\delta\tau(z') = \int_{\Delta z}^{z'} \alpha(z')\, dz'$:

$$\alpha(z') = -3c_3 z'^2 - 2c_2 z' - c_1 \quad (23)$$

Let n be the index of an atmosphere layer. With pre-defined total optical depth of the layer $\delta\tau_n$, and the extinction coefficients at the bottom and top of the layer α_{n0} and α_{n1}, respectively. Four equations must be verified:

$$\delta\tau(\Delta z_n) = 0,\ \ \delta\tau(0) = \delta\tau_n,\ \ \alpha(\Delta z_n) = \alpha_{n1},\ \ \alpha(0) = \alpha_{n0} \quad (24)$$

Solving Eq. (24) gives a set of 4 coefficients $[c_3, c_2, c_1, c_0]$ per atmosphere layer and constituent (gasses and aerosols). These coefficient sets are pre-computed.

Consider a SP along direction $\overrightarrow{\Omega_{sp}}(\theta_{sp}, \phi_{sp})$ at position $\overrightarrow{r_{sp}}$ (relative altitude z'_{sp} in the layer). If this SP has been determined to be intercepted, using a random number p, the interception occurs at an optical depth $\delta\tau(z')$ that is defined by:

- $\frac{\delta\tau(z'_{sp}) - \delta\tau(z')}{|\cos\theta_{sp}|} = \ln(1-p)$ for downward $\overrightarrow{\Omega_{sp}}$.
- $\frac{\delta\tau(z') - \delta\tau(z'_{sp})}{|\cos\theta_{sp}|} = \ln(1-p)$ for upward $\overrightarrow{\Omega_{sp}}$.

z' is derived from $\delta\tau(z')$, using Eq. (22). Numerical solutions can be obtained with methods such as bisection or Newton's methods. However, these methods are very computer intensive because they must be applied to each photon. Therefore, z' is analytically computed with Cardan method (Nickalls, 1993). With the change of variable $z' = x - \frac{c_2}{3c_3}$, we can write:

$$x^3 + q_1.x + q_0 = 0 \quad (25)$$

where $q_1 = \frac{c_1}{c_3} - \frac{c_2^2}{3c_1^2}$, and $q_0 = \frac{c_0 - \delta\tau(z')}{c_1} - \frac{c_2 \cdot c_1}{3c_3^3} + \frac{2c_2^3}{27c_1^3}$.

It leads to 3 configurations:

- $4q_1^3 + 27q_0^2 > 0$ implies 1 real root and 2 complex roots.
- $4q_1^3 + 27q_0^2 = 0$ implies 1 real root and 1 real double root.
- $4q_1^3 + 27q_0^2 < 0$ implies 3 real roots.

Usually, $4q_1^3 + 27q_0^2 > 0$ is verified. Thus, Eq. (25) and (22) lead to:

$$z' = \sqrt[3]{-\frac{q_0}{2} - \frac{1}{2}\sqrt{\frac{4q_1^3 + 27q_0^2}{27}}} + \sqrt[3]{-\frac{q_0}{2} + \frac{1}{2}\sqrt{\frac{4q_1^3 + 27q_0^2}{27}}} - \frac{c_2}{3c_1} \quad (26)$$

Rarely, we get $4q_1^3 + 27q_0^2 \leq 0$. In that case, there is usually only 1 solution in the atmosphere layer ($0 < z' < \Delta z$). Very rarely, all solutions are outside the layer, which means that the layer optical depth profile is not well described by the 3rd order polynomial. If this situation occurs, α is set as a constant in the layer. Once z' is known, the traveled distance of the SP before interception is calculated: $\delta l = \frac{z'_{sp} - z'}{|\cos\theta_{sp}|}$ for downward $\overrightarrow{\Omega_{sp}}$, and $\delta l = \frac{z' - z'_{sp}}{|\cos\theta_{sp}|}$ for upward $\overrightarrow{\Omega_{sp}}$.

The above method considers the gas and aerosol extinction coefficients for absorption and scattering. Let us assume that interception occurs at z' and that gas and aerosol extinction coefficients for scattering are $\alpha_{m,sca}(z')$ and $\alpha_{a,sca}(z')$, respectively. The Ray Carlo Equation (Eq. (20)) for the energy of virtual SP generated is weighted by the instantaneous extinction coefficients for atmosphere scattering:

$$W_{p2l} = W_{sp} . \frac{\Delta\Omega_{p2l}}{\Delta\Omega_{s(\overrightarrow{\Omega_{p2l}})}} . \frac{\alpha_{m,sca}(z') . T_m\left(\overrightarrow{\Omega_l}, \overrightarrow{\Omega_{s(\overrightarrow{\Omega_{p2l}})}}\right) + \alpha_{a,sca}(z') . T_a\left(\overrightarrow{\Omega_l}, \overrightarrow{\Omega_{s(\overrightarrow{\Omega_{p2l}})}}\right)}{\alpha_{m,sca}(z') + \alpha_{a,sca}(z')} \quad (27$$

where T_m and T_a are gas and aerosol scattering phase functions, respectively.

The large thickness of atmosphere layers explains that many SP must be scattered to the LiDAR in order to reduce the Monte Carlo noise due to the fact that photons are scattered from a small number of locations in the layer. An approach was designed for improving this situation without launching a larger number of photons: if a SP is assumed to be scattered, $N_{v,sp}$ SPs are scattered from the layer to the LiDAR. For that, each time a SP is determined to be scattered, $N_{v,sp}$ random numbers ($p_n, n \epsilon [1\ N_{v,sp}]$) are generated. These numbers are multiplied by the probability threshold of interception $P(\Delta L) = [1 - \exp\left(-\frac{\delta\tau_n}{|\cos\theta|}\right)]$ in order to make sure all the $p_n . P(\Delta L)$ can be inverted to get the $N_{v,sp}$ values $\delta\tau(z')$. Then, application of Eq. (26) gives $N_{v,sp}$ values of z' for scattering. Finally, W_{p2l} calculated from Eq. (27) is divided by $N_{v,sp}$ to assign the correct energy to each virtual SP. This approach reduces the noise level by a factor equal to $\sqrt{N_{v,sp}}$.

5.2 Validation

The validity of the DART simulated 1st order waveform was tested with the summation of the analytical expression of the 1st order waveform for all atmosphere layers. This analytical expression considers that the atmosphere is divided into many tiny layers with a thickness that corresponds to the acquisition bin $\Delta z = c.\frac{\nu}{2}.\cos\theta_L$, where ν is the LiDAR acquisition frequency. Therefore, all

photons measured by LiDAR from 1st order scattering within a layer $[z\ z+\Delta z]$ belong to the same waveform bin. The 1st layer is just above the ground. Let $\Delta\tau_m$ and $\Delta\tau_a$ be the total gas and aerosol optical depths of the atmosphere, respectively, and $\Delta\tau_{m,sca}$ and $\Delta\tau_{a,sca}$ the associated optical depths for scattering. In addition, the gas and aerosol vertical distributions are defined by height factors H_m and H_a, respectively. Thus:

$$\begin{cases} \delta\tau_m(z) = \Delta\tau_m \exp\left(\frac{-z}{H_m}\right) \\ \alpha_{m,sca}(z) = \frac{\Delta\tau_{m,sca}}{H_m}\exp\left(\frac{-z}{H_m}\right) \end{cases} \quad \begin{cases} \delta\tau_a(z) = \Delta\tau_a \exp\left(\frac{-z}{H_a}\right) \\ \alpha_{a,sca}(z) = \frac{\Delta\tau_{a,sca}}{H_a}\exp\left(\frac{-z}{H_a}\right) \end{cases}$$

The mean altitude of layer $[z\ z+\Delta z]$ is $\bar{z} = z + \Delta z/2$. Thus, the mean scattering extinction coefficients of gasses and aerosols are $\alpha_{m,sca}(\bar{z})$ and $\alpha_{a,sca}(\bar{z})$, with the associated optical depths $\delta\tau_m(\bar{z})$ and $\delta\tau_a(\bar{z})$, respectively. Let N_{tot} be the number of photons in the emitted pulse ($N_{tot} = \frac{W_L}{hc/\lambda}$). The number of photons that undergo 1st order scattering in layer $[z\ z+\Delta z]$ and that enter the LiDAR, is:

$$N_{[z\ z+\Delta z]} = N_{tot}.\exp\left(-2\frac{\delta\tau_m(\bar{z}) - \delta\tau_m(H) + \delta\tau_a(\bar{z}) - \delta\tau_a(H)}{\cos\theta_L}\right) .\left[\alpha_{m,sca}(\bar{z}).\frac{T_{m,b}}{4\pi} + \alpha_{a,sca}(\bar{z}).\frac{T_{a,b}}{4\pi}\right].\frac{\Delta z}{\cos\theta_L}.\frac{A_t.\cos\theta_L}{(H-z)^2} \quad (28)$$

The exponential term is the double path direct transmittance to LiDAR at altitude H. $T_{m,b}$ and $T_{a,b}$ are gas and aerosol backscattered phase functions, respectively (i.e., $\Psi_{i,j} = 180°$ in Eq. (5).

Table 3. Configuration of simulated GLAS device.

Parameters	Symbols	Values
Sensor area	A_t	$0.785m^2$
Wavelength	λ	532 nm
Bandwidth	$\Delta\lambda$	0.03 nm
Sensor altitude	H	600 km
Pulse energy		36 mJ
Time step per acquisition	δt_{bin}	500 ns
Depth per acquisition	Δz	37.5 m
Footprint divergence half angle	β_{fp}	0.05835 mrad
Footprint radius	r_{fp}	35.01 m
FOV divergence half angle	β_{FOV}	0.08 mrad
FOV radius	r_{FOV}	48 m

Table 4. Experimental configuration for atmosphere validation.

Parameters	Symbols	Values
Depth of atmosphere layer	Δz_n	5000 m

Molecule optical depth of scattering	$\Delta\tau_{m,sca}$	0.1
Molecule transmittance		0.9048
Molecule scale factor	H_m	8400m
Aerosol total optical depth	$\Delta\tau_a$	0.3
Aerosol albedo	ω	0.947
Aerosol scale factor	H_a	2000m
Henyey Greenstein parameters	a	0.95
	g_1	0.79
	g_2	0.4
Ground reflectance		0

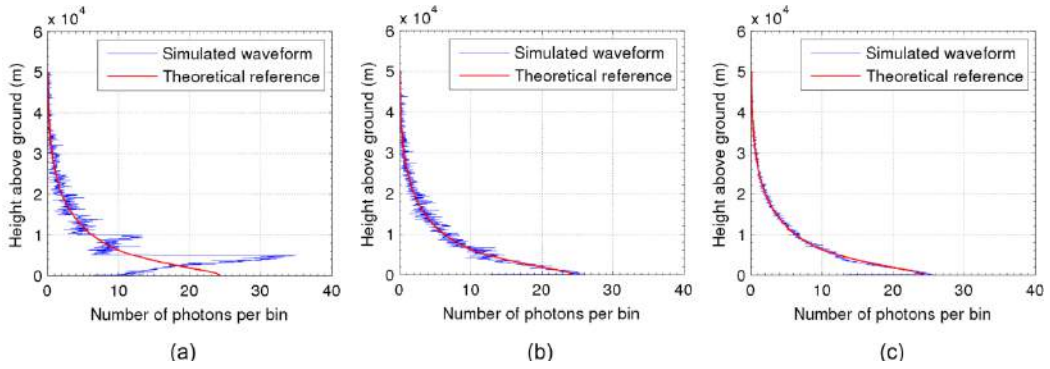

Figure 10. Comparison of DART simulated GLAS (Table 3) (blue curve) and analytically calculated (Eq. (28)) (red curve) 1st order atmosphere waveforms, with experimental configuration from

Table 4 shows the atmosphere parameters. **Figure 10** shows the theoretically predicted (red line) and DART simulated (blue line) 1st order atmosphere responses. Totally, 50K SPs are launched, which requires ≈0.4 s to run the simulation with maximum scattering order that is set to 3. **Figure 10**a shows DART results with constant extinction coefficient α per atmosphere layer, and with a single scattered SP per scattering event ($N_{v,sp} = 1$). Within each layer, the LiDAR pulse attenuation follows Beer's law with the extinction coefficient α. As expected, discontinuities appear at layer boundaries due to α discontinuity. **Figure 10**b shows DART simulations with optical depth and extinction coefficient that are fitted with polynomials for each layer (Eq. (22) and (23)). In such case, α is continuous at each layer boundary, which explains that the atmosphere response is no more discontinuous, and the simulated result fits the theoretical prediction with some Monte Carlo noise. The noise level depends on the number of fired SPs. To reduce this noise, here, $N_{v,sp}$ is set to 10. Thus, 10 SPs are sent per scattering event towards the detector. As shown in **Figure 10**c, the noise level is much reduced, as if 500K SPs are fired, yet firing 500K SPs requires 4 s, whereas firing 50K SPs requires 1.5 s.

The above simulation method is adapted to any atmosphere profile hat cannot be analytically managed (Eq. (28)). DART has integrated most of the atmosphere molecule and aerosol models

from MODTRAN, and it can any import atmosphere vertical profile. In addition, it provides a possible prototype to a future model where clouds can exist in a simulated atmosphere system.

6. CONCLUSION

DART model was extended for simulating airborne and satellite LiDAR acquisitions. Thus, DART can now simulate LiDAR waveforms of any Earth landscape, including urban and vegetation canopies, for any set of experimental (e.g., atmosphere, vegetation growth state, etc.) and instrumental (e.g., LiDAR FOV and footprint sizes, view direction, pulse energy, etc.) conditions. Earth scenes are simulated as the combination of facets, to simulate surface elements (e.g., ground, tree trunk, foliar element, etc.) that give rise to surface scattering, and volume elements (e.g., fluids, vegetation, atmosphere) that are filled with turbid medium and give rise to volume interaction. The fact that DART LiDAR mode works with the same Earth scenes as the DART ray-tracking mode that is used to simulate radiometer acquisitions from the visible to the thermal infrared domain, is very useful for multi-sensor approaches.

DART modeling of single pulse waveform relies on a new modeling method that is called quasi Monte Carlo Ray Tracing (quasi-MCRT). It was designed to track efficiently photon propagation in any Earth scene and atmosphere. Basically, LiDAR signal propagation is simulated as a flux of tiny energy elements called simulated photons (SP), with each SP being characterized by its propagation direction and a weight that indicates its energy. The modeling approach is based on 2 new methods, the so-called Box method and the Ray Carlo method. The Box method provides fast selection of direction of SPs that are scattered. The Ray Carlo method combines classical Monte Carlo and DART ray-tracking methods for modeling SP propagation and interaction. The use of SPs with weights is very efficient. For example, computational time can be reduced by factors as large as 10^{10}, compared to direct Monte Carlo methods that manage actual photons. In short, results show that the combination of the 2 methods can provide fast and accurate simulation of waveform.

DART wLiDAR modeling was successfully tested with three approaches.

- Monte Carlo method. The validity of its implementation in DART was analyzed by comparing radiometer images that are simulated with this method and with the already validated DART ray-tracking method. It was verified that Monte Carlo images converge towards ray-tracking images if many photons are fired.
- Quasi-MCRT method. Its validity was tested by comparing LiDAR derived reflectance images (i.e., MCRT images) and classical ray-tracking reflectance images. Generally speaking, 1st order MCRT images converge to the ray-tracking images if the number of fired SPs increases.
- LVIS data of a forest stand in Howland Forest. LVIS and DART waveforms were compared and correspondence was good: differences were mostly explained by inaccurate forest allometry and spectral attributes.

DART wLiDAR modeling approach considers the atmosphere, with two original modeling approaches: continuous vertical profile of gas and aerosol extinction coefficients for avoiding discontinuities in waveforms, and scattering of several SPs per scattering event for decreasing Monte Carlo noise. These advances are critical to provide realistic simulations of satellite LiDAR systems over conditions with aerosol contamination.

Preliminary results illustrate that DART is a fast and accurate modeling tool for simulating actual LiDAR signals. For example, its multithreaded modeling approach that uses SPs with weights takes advantage of the accuracy of Monte Carlo simulations while retaining the small computation time

of classical ray-tracking methods. Moreover, DART modeling is adapted to any experimental (e.g., Earth landscape and atmosphere) and instrumental (e.g., LiDAR device and platform) configuration. Consequently, it is consistent with DART simulation of satellite and airborne radiometers. Another practical advantage of the DART model is the user friendly graphic user interface.

DART efficiency is a key factor for extending it to LiDAR applications. The integrated approach to model LiDAR signals in the DART environment provides a seamless opportunity to simulate solar noise impacts on LiDAR signals and actual instrument configurations such as multi-pulse acquisitions by satellite, airborne and terrestrial LiDAR devices. Solar noise is an important concern for LiDAR devices with low energy pulses, which is the case of photon counting devices. DART extension to the simulation of solar noise, multi-pulse satellite, airborne and terrestrial devices, as well as photon counting devices, is presented in a companion paper. Free DART licenses can be obtained from Paul Sabatier University (www.cesbio.ups-tlse.fr/dart/license/en/getLicense.php) for scientific research.

7. ACKNOWLEDGEMENT

This work was supported by the ANR in the frame of the FOLI3D project and by the Centre National d'Etudes Spatiales (CNES) in the frame of the TOSCA projects 'Stem-Leaf' and 'Hypertropik'. Part of the work was conducted in the frame of the NASA project "DART-LiDAR". The authors are thankful to Audrey Ueberschlag who initiated the first comparison with LVIS data and to all scientists who contributed to DART development since its first steps in 1992.

Appendix A: Nomenclature

Acronyms

BRF	Bidirectional Reflectance Factor
CDF	Cumulative Distribution Function
DART	Discrete Anisotropic Radiative Transfer
FOV	Field Of View
LAD	Leaf Angle Distribution
LAI	Leaf Area Index
LiDAR	LIght Detection and Ranging
wLiDAR	waveform LiDAR
MCRT	Monte Carlo Ray Tracing
NIR	Near Infrared
PDF	Probability Density Function
RTM	Radiative Transfer Model
SP	Simulated Photon
SRMA	Scene Reference Minimum Altitude
VAA	View azimuth angle
VZA	View zenith angle

Symbols

$(\Omega, \Delta\Omega)$	Discrete direction with unit vector Ω and solid angle $\Delta\Omega$.
$(\overrightarrow{\Omega_{p2l}}, \Delta\Omega_{p2l})$	Direction of a virtual SP that is scattered to the LiDAR.
a, g_1, g_2	Coefficients of the double Henyey-Greenstein function that fits the scattering phase function of a given type of aerosols.
A_t	LiDAR telescope area.

B_k	Array of scattering direction probabilities, in box method for material type k.
c_3, c_2, c_1, c_0	3^{rd} order polynomial coefficients to fit the gas or aerosols extinction coefficient $\alpha(z)$ of a given atmosphere layer.
C_{fp}, C_{FOV}	Circular footprint and FOV regions at SRMA (nadir LiDAR).
d_f	Leaf dimension.
d_{p2l}	Distance from point P to LiDAR.
E_{ilm}, E_{rcp}	Elliptical illumination and view regions at SRMA (oblique LiDAR).
f_X	Probability density function of an event X.
F_X	Cumulative probability distribution function of an event X.
$F(\Omega_f, \Omega_i, \Omega_j)$	Probability to scatter along vector Ω_j a ray that is incident along vector Ω_i and that is intercepted by a facet with orientation Ω_f.
g_f	Leaf angle distribution.
$G(\Omega_i)$	Relative leaf cross section for vector Ω_i in a vegetation turbid medium
H_m H_a	Gas and aerosol scale height factors of $\alpha(z)$ in the atmosphere 1^{st} order analytical LiDAR model.
M	Computer memory usage.
n_l	Number of incident lines (i.e., incident directions) in array B.
$N_{sp,sub}$	Number of SPs per illumination cell grid in LiDAR local frame.
$N_{dir,nv}$	Number of pre-defined (pre-calculated) non virtual discrete directions.
$N_{dir,vd}$	Number of pre-defined (pre-calculated) virtual discrete directions.
$N_{dir,vnd}$	Number of non pre-defined virtual directions.
p	A random generated number ($0 < p < 1$).
$p_{ij,k}$	Probability of an intercepted ray along Ω_i, scattered towards Ω_j in medium k. For given i and k, $\sum_{j=1}^{N_{dir,nv}} p_{ij,k} = 1$.
P_X	Probability of an event X.
$P_L(x, y, H)$	LiDAR position with altitude H.
P_{conv}	LiDAR reception convergent point.
$P(\Omega_i, \Omega_j)$	Scattering phase function from Ω_i towards Ω_j
$\overrightarrow{r_{sp}}$	Position vector of a SP.
r_t	LiDAR telescope radius.
r_{fp}, r_{FOV}	Radii of C_{fp} and C_{FOV}.
$r_{\perp,ilm}$, $r_{\parallel,ilm}$	Short (perpendicular) and long (parallel) radii of E_{ilm}.
$r_{\perp,rcp}$, $r_{\parallel,rcp}$	Short (perpendicular) and long (parallel) radii of E_{rcp}.
r_{sub}	Distance "cell grid center - center of LiDAR pulse spatial distribution".
s_f	Leaf apparent dimension.
t_{dir}	Facet direct transmittance.
t_{diff}	Facet diffuse transmittance.
$T(\Omega_i, \Omega_j)$	Fraction of flux intercepted along Ω_i that is scattered along Ω_j.
u_f	Leaf volume density.
$U_{b,i,c}$	With incident direction i, the number of boxes to store the probability of certain scattering directions which are categorized in class index c.

$V_{b,i,c,j}$	With incident direction i, the number of boxes to store the probability scattering towards j, where j is categorized in class index c.
W_{sp}	Energy that is carried by a SP.
W_L	Energy carried by a LiDAR pulse.
W_{sub}	Total energy of SPs per illumination cell grid in LiDAR local frame.
W_{p2l}	Energy of a scattered virtual SP in Ray Carlo method.
$X_{b,i,j,k}$	Number of boxes to store the probability for ray interaction with material k, with incident direction i, and scattering direction j.
$\alpha(z)$	Gas and aerosol extinction coefficient per absorption and scattering, at altitude z.
α_{n0}, α_{n1}	Extinction coefficients at the bottom and top of an atmosphere layer with index n.
β_{fp}, β_{FOV}	Half dispersion angle of LiDAR footprint and FOV.
γ	Threshold used for optimizing computer memory.
δl	Displacement of a SP along its propagation direction.
$\delta\tau_n$	Total optical depth of an atmosphere layer with index n.
$\delta\tau(z')$, $\alpha(z')$	Optical depth and extinction coefficient with relative altitude z' in an atmosphere layer.
ΔL	Path length of a SP from its current position.
$\Delta\Omega_{s(p2l)}$	Solid angle of the discrete direction that contains $\overrightarrow{\Omega_{p2l}}$.
η	Fraction of signals contributed by multiple scatterings in a LIDAR waveform.
θ, ϕ	Zenith and azimuth angles.
$\Psi_{i,j}$	Angle between direction Ω_i and direction Ω_j.
$\rho(\Omega_i, \Omega_s)$	Facet directional reflectance factor from Ω_i towards Ω_s.
ω	Scattering albedo.
$\overrightarrow{\Omega_{sp}}$	Propagation direction vector of a SP.
$\overrightarrow{\Omega_L}(\theta_L, \phi_L)$	LiDAR orientation.

Appendix B: Accuracy of the box method

MC techniques aim to give results that approach the expected value as the number of photons goes to infinity. In reality, computation time always limits the number of photons. Thus, one must assess the maximal error that the box method can introduce because the number of boxes that represents a probability as an integer, whereas this probability is a real number. For example, let us consider two scattering directions Ω_1 and Ω_2 with probabilities $p_1 = 0.1$ and $p_2 = 0.273$, respectively. If Ω_1 is represented by 1 box, Ω_2 requires 3 boxes, which leads to a strong bias because the ratio of boxes differs from the probability ratio. On the other hand, if Ω_1 is represented by 10 boxes, then Ω_2 is represented by 27 boxes, which leads to a smaller bias because the ratio of boxes is closer to the ratio of probabilities.

Let us consider an incident direction Ω_i. The probability to select a class c and to select a direction j in this class c of line i is:

$$p = \frac{U_{b,i,c}}{U_{b,i}} . \frac{V_{b,i,c,j}}{V_{b,i,c}}$$

with $U_{b,i,c}$ the number of boxes that represent class c, $U_{b,i}$ the number of boxes that represent all classes, $V_{b,i,c,j}$ the number of boxes that represent direction Ω_j in class c, and $V_{b,i,c}$ the number of boxes that represent all directions in class c. We have:

$$\frac{dp}{p} = \frac{dU_{b,i,c}}{U_{b,i,c}} + \frac{dV_{b,ij,c}}{V_{b,ij,c}} - \frac{dU_{b,i}}{U_{b,i}} - \frac{dV_{b,i,c}}{V_{b,i,c}}$$

The maximum relative error is:

$$\frac{\varepsilon(p)}{p} = \frac{\varepsilon(U_{b,i,c})}{U_{b,i,c}} + \frac{\varepsilon(V_{b,i,c,j})}{V_{b,i,c,j}} + \frac{\varepsilon(U_{b,i})}{U_{b,i}} + \frac{\varepsilon(V_{b,i,c})}{V_{b,i,c}}$$

The maximum rounding error on $U_{b,i,c}$ and $V_{b,i,c,j}$ is one box. The error on $U_{b,i}$ is maximal if the maximal rounding error occurs for each class of line i, except for the first class because its number of boxes is set to an exact number of boxes (i.e., $V_{b,i,c,min}$). With C(i) the number of classes in line i, the maximal rounding error on $U_{b,i}$ is:

$$\epsilon(U_{b,i}) = 0.5.[C(i) - 1]$$

We always have $U_{b,i} > C(i).V_{b,i,c,min}$. Thus, we have:

$$\frac{\varepsilon(U_{b,i})}{U_{b,i}} < \frac{0.5}{V_{b,i,c,min}}$$

The same approach applied to $V_{b,i,c}$, using directions instead of classes, leads to:

$$\frac{\varepsilon(V_{b,i,c,j})}{V_{b,i,c,j}} < \frac{0.5}{V_{b,i,c,min}}$$

Finally, the maximal relative error on p is:

$$\frac{\varepsilon(p)}{p} < \frac{2}{V_{b,i,c,min}}$$

Thus, with $V_{b,i,c,min} = 1000$, the maximum relative error on p_j is smaller than 2.10^{-3}, an acceptable level compared to the usual satellite sensor accuracy.

Rounding errors do not occur on the least probable class and direction. Indeed, errors arise only if some rounding takes place. Thus, $V_{b,i,c,min}$ is needed at most only from the second least probable class or direction. It explains that the number of boxes of the least probable direction and class is computed with a simple proportionality relationship. For example, if $p_{c,2}$ is the probability of the second least probable class, the number of boxes of the least probable class (probability $p_{c,1}$) is calculated with:

$$U_{b,i,c=1} = \text{ceil}(V_{b,i,c,min}.\frac{p_{c1}}{p_{c2}})$$

Then, each number of boxes $U_{b,i,c=2}$, $U_{b,i,c=3}$,… is computed with the proportionality relationship. We can note that we have always: $U_{b,i,c=2} > V_{b,i,c,min}$.

Appendix C:

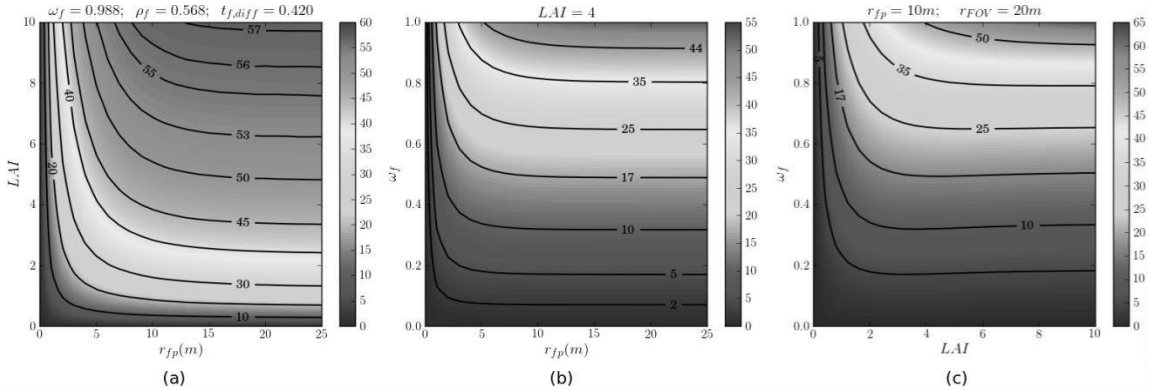

Figure C1. Multiple scattering fraction $\eta(\%)$ in LiDAR waveform of a vegetation layer with no ground. a) $\eta(LAI, r_{fp})$ with $\omega_f = 0.988$. b) $\eta(\omega_f, r_{fp})$ with $= 4$. c) $\eta(\mathrm{LAI}, \omega_\mathrm{f})$ with $r_{fp} = 10m$.

The contribution of within vegetation multiple scattering in LiDAR waveform under variable experimental and instrumental conditions is assessed with DART simulations. The studied scene is a simple 10m height turbid vegetation layer with spherical leaf angle distribution and an horizontal ground the reflectance of which is null. It is simulated with $0.5m \times 0.5m \times 0.5m$ cells. The LiDAR is at 10km altitude with nadir orientation. The contribution of multiple-scattering in waveforms is assessed with η. Three varying experimental and instrumental conditions are considered: the LAI, the footprint/FOV size (r_{fp} and r_{FOV}), and the foliar spherical albedo $\omega_f = \rho_f + t_{f,diff}$, where ρ_f represents the first integration term on the right hand side of Eq. (11). By default, we set $r_{FOV} = 2r_{fp}$. The sensitivity study includes the following 3 cases:

1. $\eta(r_{fp}, LAI)$ with $LAI \in [0\ 10]$, $r_{fp} \in [0\ 25m]$ and $\omega_f = 0.988$ ($\rho_f = 0.568$, $t_{f,diff} = 0.429$). This case corresponds to NIR band. Figure C1a shows that with a large ω_f, the fraction of multiple scattering η can be very large. It is small if both LAI and r_{fp} are small (e.g., $\eta \approx 10\%$ if $r_{fp} = 2m$ and $LAI = 1$), and it increases if LAI and/or r_{fp} increase, especially for small r_{fp} and LAI values. We can note its relative quick saturation with r_{fp}. For example, $\eta \approx 20\%$ with ($r_{fp} = 3m$, $LAI = 2$), $\eta \approx 50\%$ with ($r_{fp} = 10m$, $LAI = 6$), and $\eta \approx 56\%$ with ($r_{fp} \geq 10m$, $LAI = 9$).
2. $\eta(r_{fp}, \omega_f)$ with $r_{fp} \in [0\ 25m]$, $\omega_f \in [0\ 1]$ ($\rho_f = t_{f,diff} = \frac{\omega_f}{2}$) and LAI= 4. Figure C1b shows that the fraction of multiple scattering η increases strongly with ω_f. It increases also with r_{fp}, with a relatively fast convergence, as noted for $\eta(r_{fp}, LAI)$. For example, $\eta \approx 2\%$ with ($r_{fp} = 5m$, $\omega_f = 0.8$), $\eta \approx 10\%$ with ($r_{fp} = 5m$, $\omega_f = 0.38$), and $\eta \approx 35\%$ with ($r_{fp} = 5m$, $\omega_f = 0.85$).
3. $\eta(LAI, \omega_f)$ with $LAI \in [0\ 10]$, with $\omega_f \in [0\ 1]$ ($\rho_f = t_{f,diff} = \frac{\omega_f}{2}$) and $r_{fp} = 10m$ ($r_{FOV} = 20m$). Figure C1c shows that η increases strongly with ω_f and that η converges up to a value that depends on ω_f. For example, $\eta \approx 5\%$ with ($LAI = 4$, $\omega_f = 0.2$), $\eta \approx 34\%$ with ($LAI \geq 4$, $\omega_f = 0.8$).

In short, for the studied cases, the foliar scattering albedo ω_f is the predominant parameter, although LAI and r_{fp} play also a role. This type of information is useful for analyzing measured waveforms and also for devising LiDAR systems. In that case, the homogeneous vegetation layer must be replaced with a more realistic vegetation or urban landscape.

4.2 Article: Simulation of satellite, airborne and terrestrial LiDAR with DART (II): ALS and TLS multi-pulse acquisitions, photon counting, and solar noise

Simulation of satellite, airborne and terrestrial LiDAR with DART (II): ALS and TLS multi-pulse acquisitions, photon counting, and solar noise.

Tiangang Yin *, Nicolas Lauret, Jean-Philippe Gastellu-Etchegorry,

Centre d'Etudes Spatiales de la BIOsphère (CESBIO) - UPS, CNES, CNRS, IRD, Université de Toulouse, 31401 Toulouse cedex 9, France.

*Email: tiangang.yin.85@gmail.com

Abstract: Light Detection And Ranging (LiDAR) devices are increasingly used to provide data on Earth's landscapes structures and atmosphere constituents. Their fast development, especially with scanning and multi-beam systems that launch pulses along different directions, requires efficient and accurate simulation tools to analyze existing data and to design future systems. A few radiative transfer models (RTM) can simulate LiDAR waveform of a single pulse. Based on that, efficient and accurate multi-pulse modeling must be developed. This paper presents an efficient, flexible and user-friendly approach that extends the LiDAR single pulse modelling functionality of the Discrete Anisotropic Radiative Transfer (DART) model to actual multi-pulse systems. Actual acquisition configurations (platform positions and orientations) can be imported and simulated waveforms can be output to industrial data format and processed by real-world data processing software. Application of multi-pulse modeling to airborne and terrestrial devices is presented. DART was also extended to simulate photon counting LiDAR data, using single-photon detector physical principles and waveform simulation. In addition, it computes solar noise for any atmosphere configuration through a combined simulation of LiDAR waveforms and passive sensor radiance images. Its multi-threading algorithm eases its application to simulate actual acquisition. With these improvements, DART has become a unique tool for satellite, airborne and terrestrial LiDAR multiple pulse systems. It is illustrated with theoretical configurations of existing and future devices, including CAO, ILRIS, MABEL and ATLAS.

Keywords: LiDAR, DART, radiative transfer, ALS, TLS, multiple pulses, photon counting, solar noise

1. INTRODUCTION

LiDAR devices are increasingly used in remote sensing and terrestrial systems for many applications: topography (Hladik et al., 2013), vegetation architecture and dimensions (Popescu et al., 2011, Yang et al., 2013, Montesano et al., 2015), urban mapping (Yan et al., 2015), bathymetry (Quadros et al., 2008), atmosphere constituents (Zhang et al., 2011), etc. Waveform LiDAR (wLiDAR) does the time of flight measurement of returned signals, transforms signals into analog electrical counts in volts, and records them as continuous temporal bins (Shan and Toth, 2008). The distance from LiDAR position to the scattering elements along laser path can be estimated from recorded waveforms. Waveform acquisition associated to the emission of multiple pulse along different directions leads to 3-D (three dimensional) points cloud that reveal both optical properties and locations of the scattering elements which give rise to the measured signals (Wagner et al., 2006). Laser generator pulse repetition frequency (PRF) of wLiDARs can be large. For example, it is 400 kHz for the wLiDAR on board the AtoMS system (Airborne Taxonomic Mapping System) of the Carnegie Airborne Observatory (CAO) (Asner et al., 2007, 2012).

Among multi-pulse wLiDAR devices, airborne laser scan (ALS) uses small-footprint LiDAR for acquisition over a swath that is defined by the platform and sensor configuration (Mallet and Bretar,

2009). The term "small-footprint" refers to the combination "Small pulse divergence - Low platform altitude". Thus, the vertical illumination region of the pulse on the Earth's surface is relatively small (usually less than 5m in diameter). For example, the CAO has a footprint diameter which is less than 1m if platform altitude is less than 2km. The decomposed points from ALS pulses can be classified into Earth surface types (ground, vegetation canopy, etc.) (Zhang et al., 2003). Further integrated analysis of the 3-D points gives topography, canopy height, as well as landscape biophysical parameters. On the other hand, terrestrial laser scan (TLS) is a ground-based device. Its pulse distribution can be very dense, which explains why it is increasingly used for tree structure retrieval through the calculation of the location of the observed scattering elements (Rosell et al., 2009). TLS points can be classified into branches, leaves, trunk and ground according to the energy and position of each return. Points from TLS acquisitions of the same object from different locations and directions can be combined. For example, they can lead to precise 3-D tree representations that can be used further by computer graphics software for visualization and by RTMs (Côté et al., 2009 , 2011) to simulate remotely sensed data. RTM simulations with this 3-D vegetation representation (Schneider et al., 2014) is more accurate than with common vegetation representation with turbid medium (Ross, 1981).

The rapid development of wLiDAR technology calls for modeling tools that can simulate its data efficiently and accurately, to validate present systems and to prepare future systems. RTMs are common tools for simulation, validation and inversion of remote sensing measurements. Currently, many existing semi-empirical or geometric optical models can simulate LiDAR waveform of a single pulse (Blair and Hofton, 1999, Chauve et al., 2007, Sun and Ranson, 2000, Ni-Meister et al., 2001). However, these models are based on strong simplifications for simulating landscapes (e.g., geo-optical description) and/or ray propagation within landscapes. For example, they often treat landscapes as turbid media and consider first-order scattering only. On the other hand, Monte Carlo ray tracing (MCRT) methods can be very accurate because they can work with realistically simulated landscapes without simplifying hypotheses on multiple scattering mechanisms (North et al., 2010). However, they must compromise with the trade-off between simulation accuracy and computational speed. A companion paper (Gastellu-Etchegorry et al., 2015a) presents an extension of the Discrete Anisotropic Radiative Transfer (DART) model (Gastellu-Etchegorry et al., 1996, 2004, 2012) to simulate accurately and quickly single pulse LiDAR waveform with atmosphere using a quasi-MCRT approach. The approach tackles most theoretical and experimental bottlenecks of existing models with 2 novel methods: the box method and the Ray Carlo method. The box method accelerates the weighted random selection of the discrete direction of a scattered photon by partitioning discrete directions with similar scattering probabilities and by taking advantage of computer memory usage. The Ray Carlo method tracks partial radiation (*i.e.*, weighted photon) towards the LiDAR sensor for each scattering event. This method reduces the total number of launched simulated photons, and further improves simulation accuracy and processing speed. The whole simulation process is optimized in terms of mathematical algorithms, computer processor efficiency and memory usage. Waveforms generated by this approach have been successfully validated with traditional DART simulated reflectance for total energy received in the LiDAR FOV, analytical expression of atmosphere LiDAR signal, and actual data of the Laser Vegetation Imaging Sensor (LVIS) system (Blair et al., 1999).

This paper presents an extension of the single pulse LiDAR component of DART model to simulate multi-pulse data with concentration on airborne and terrestrial acquisitions. It is optimized in terms of efficiency and practicability. For example, the multi-pulse simulation is not an iterative loop on the single-pulse model per simulated pulse, which avoids the repetitive loading of a simulated scene, and the computation time avoids unnecessary increment. In addition, the device and platform parameterization supports abstract configurations (*e.g.*, platform path, zenith angle range,

angular/distance separation between pulses, etc.) and the importation of actual configurations (*e.g.*, LiDAR position and orientation per pulse) to facilitate comparison with actual data. The objective is to simulate any existing or future system. Moreover, algorithmic multi-threading processing is implemented, which greatly improves processing speed. It uses the fact that each pulse is independently simulated with its own sensor geometry. Another practical advantage is that the output data can be converted into an industrial LiDAR format, the sorted pulse data (SPD) (Bunting et al., 2013b), and hence processed into point cloud by the associated open-source data processing software, the SPDlib (Bunting et al., 2013a).

The DART extension simulates also photon counting LiDAR (pcLiDAR) (Degnan et al., 2013, Montesano et al., 2015), i.e., single-photon detection. The approach relies on the available simulated waveforms. The acquisition of single-photon detector is defined with sensor parameters like quantum efficiency, dark count rate, and detector dead time, etc. The number of photons in each waveform bin is converted into probability of detection, which is used to find out if a photon is detected. Furthermore, existence of solar noise in LiDAR signal is simulated. The approach utilizes the at-sensor radiance image simulation for pinhole camera and linear pushbroom imager which was recently implemented in DART (Yin et al., 2015). This reflected radiance image is converted into photons per bin, for each LiDAR FOV. During daytime, solar noise is usually a minor problem for wLiDARs with high pulse energy and a major problem for pcLiDARs, because of their low pulse energy. Thus, it must be considered for analyzing LiDAR data and also for designing future devices. Simulating solar noise in LiDAR systems is a "2 sources - 1 sensor" configuration, conversely to the "1 source - 1 sensor" configuration handled by traditional RTMs.

Finally, DART LiDAR modelling is illustrated with the simulation of a few systems, including the wLiDAR system of the CAO, the ILRIS terrestrial LiDAR system of Optech Inc, the Multiple Altimeter Beam Experimental LiDAR (MABEL) (McGill et al., 2013) of NASA's Goddard Space Flight Center, as well as the Advanced Topographic Laser Altimeter System (ATLAS, Yu et al. (2010)) which will be onboard the upcoming 2nd generation of NASA Ice, Cloud, and Land Elevation Satellite (ICESat-2) (Abdalati et al., 2010). Nomenclature of this paper is shown in **Appendix A**.

2. MULTI-PULSE SIMULATION

2.1 Multi-pulse geometries and configurations

The laser system of an ALS or TLS wLiDAR device generates pulses that are reflected by a rotating/oscillating mirror towards the observed region. The previous companion work (Gastellu-Etchegorry et al., 2015b) presents the theory and methodology of DART model for simulating single-pulse waveform, with realistic ALS settings. Figure 1 illustrates the general configuration. LiDAR position $P_L(x, y, H)$ depends on the LiDARaltitude H relative to the scene reference minimum altitude (SRMA), which depends on the simulated scene. P_L is the laser point source, with the assumption that the cross section of the laser beam that exits the LiDAR laser generator is negligibleLiDAR. A laser ray is transmitted from P_L along the LiDAR orientation $\overrightarrow{\Omega_L}$ in a usually very small solid angle that is defined by footprint divergence half angle β_{fp}. The telescope for signal reception is defined by a circular surface (radius r_t, area $A_t = \pi r_t^2$) with its center located at P_L, and its orientation $\overrightarrow{\Omega_L}$. The telescope reception cone is defined by FOV divergence half angle β_{FOV}.

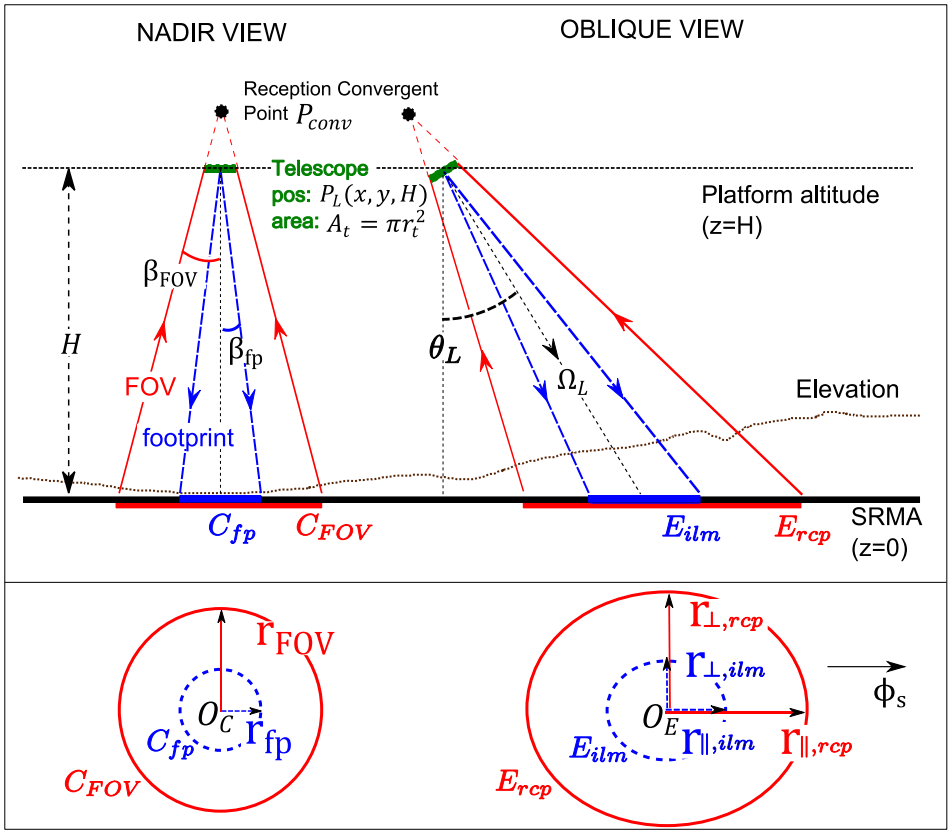

Figure 1: ALS geometric configuration of a LiDAR pulse for nadir and oblique orientation, with corresponding footprint and FOV projected regions at the horizontal SRMA plane. (Gastellu-Etchegorry et al., 2015b)

For a given LiDAR device, parameters $\{r_t, A_t, \beta_{fp}, \beta_{FOV}\}$ are constant terms, whereas P_L and $\overrightarrow{\Omega_L}$ are variables during multi-pulse acquisition. The footprint and FOV of the ALS system are shown on the left part of Figure 1. They correspond to circular projected regions (C_{fp} and C_{FOV}) on the plane at SRMA, with their radii calculated as:

$$r_{fp} = H \cdot \tan \beta_{fp} \qquad r_{FOV} = H \cdot \tan \beta_{FOV} + r_t \tag{1}$$

If $\overrightarrow{\Omega_L}$ is oblique with look angle θ_L (*cf.* right part of Figure 1), the illumination and reception circular regions on the SRMA plane in LiDAR local coordinate system (frame projected $\overrightarrow{\Omega_L}$) give rise to ellipse regions (E_{fp} and E_{FOV}) in the simulated coordinate system frame. Short and perpendicular ellipse radii are:

$$r_{\perp,ilm} = \frac{H \cdot \tan \beta_{fp}}{\cos\theta_L} \qquad r_{\perp,rcp} = \frac{H \cdot \tan \beta_{FOV}}{\cos\theta_L} + r_t \tag{2}$$

Long and parallel radii along the cross-track scan direction, defined by the azimuth angle ϕ_s, are:

$$r_{\parallel,ilm} = \frac{H \cdot \tan \beta_{fp}}{\cos^2\theta_L} \qquad r_{\parallel,rcp} = \frac{\dfrac{H \cdot \tan \beta_{FOV}}{\cos\theta_L} + r_t}{\cos\theta_L} \tag{3}$$

The footprint and FOV projected regions on the SRMA plane can be calculated for any LiDAR position P_L and orientation $\overrightarrow{\Omega_L}$, with Equation (1), (2) and (3).

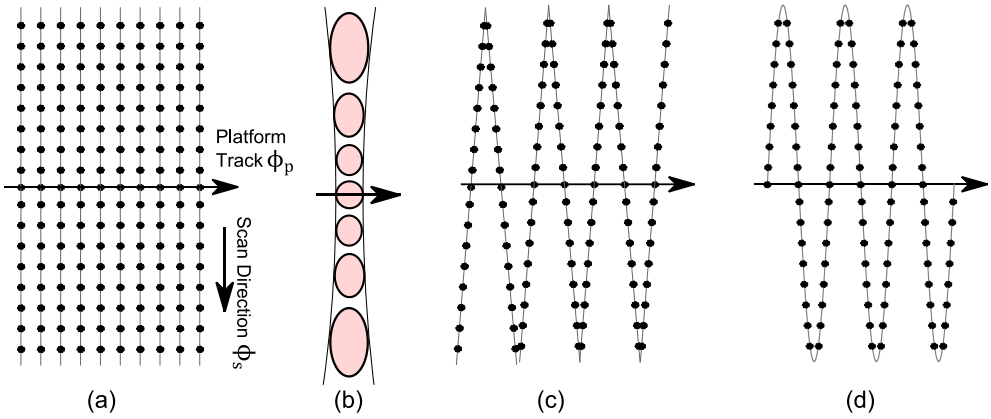

Figure 2: ALS scan patterns for three rotating and oscillating mirror systems. (a) Pattern of rotating polygon mirror, with ϕ_{off}=0°. (b) Projected FOV regions for a single scan line from rotating polygon mirror, with ϕ_{off}=0°. (c) Pattern of saw-toothed oscillating mirror. (d) Pattern of sinusoidal oscillating mirror.

Accurate and efficient account of varying P_L and $\overrightarrow{\Omega_L}$ per pulse is the major difficulty for simulating multi-pulse acquisition. Centers (O_C, O_E in Figure 1) of projected regions are located at the interception of each line (P_L, $\overrightarrow{\Omega_L}$) with the SRMA plane. They define the scan pattern of the rotation or oscillation of the reflecting mirror that redirects pulses. ALS devices can use different scan patterns: rotating polygon (Figure 2(a)), saw-toothed (Figure 2(c)) and sinusoidal (Figure 2(d)) oscillating mirror, etc. The rotating polygon is the default mode for DART multi-pulse simulation. Its scan pattern is a series of parallel lines. Two horizontal axes play a specific role (Figure 2(a)): platform track axis $\overrightarrow{\phi_p}$ defined by an azimuth angle ϕ_p towards forward path direction, and scan (cross-track) axis $\overrightarrow{\phi_s}$ defined by the scan azimuth angle ϕ_s with direction towards the right side of the platform track. They are usually nearly perpendicular to each other. Here, we consider an offset angle ϕ_{off}, such that: $\phi_s = \phi_p + \phi_{off} - 90°$. Pulses of a scan line share the same P_L. Thus, for an arbitrary position along the laser path of a given pulse, P_L horizontal coordinates (x, y) are computed as the intersection of platform track along $\overrightarrow{\phi_p}$ and a line crossing the position along $\overrightarrow{\phi_s}$. The ray transmission direction $\overrightarrow{\Omega_L}(\phi_s, \theta_L)$ reflected by a rotating polygon is defined by ϕ_s and look angle θ_L, with θ_L negative on the platform track left side ($-\overrightarrow{\phi_s}$ direction) and positive on the right side ($+\overrightarrow{\phi_s}$ direction). Thus, ALS multi-pulse scan pattern of rotating polygon is defined by 2 parameters in DART: distance step δd_s between scan lines along platform track and look angle step $\delta\theta_L$ between pulses in a scan line. We have $\delta d_s = v_P/f_s$ with platform velocity v_P and scan (line) frequency f_s. The number of pulses per scan is $n_s = PRF/f_s$, and the look angle step between pulses in a scan is:

$$\delta\theta_L = \frac{2\theta_{L,max,scan} \cdot f_s}{PRF} \tag{4}$$

with $\theta_{L,max,scan}$ the maximum look angle per scan, which is system-based. δd_s and $\delta\theta_L$ can be directly specified in DART. $\delta\theta_L$ sets the pulse density on the SRMA plane. The pulse density is larger around nadir ($\theta_L \approx 0°$) than for oblique directions (Figure 2(b)). Let the total distance of a swath along $\overrightarrow{\phi_p}$ be Δd, and the difference between maximum and minimum look angles within the swath be $\Delta\theta_{L,swath}$.Then, the total number of simulated pulses N_p, and the average density of pulses ρ_p are:

$$N_p = \frac{\Delta d}{\delta d_s} \cdot \frac{\Delta \theta_{L,swath}}{\delta \theta_L} \qquad \rho_p = \frac{N_p}{A_{swath}} \tag{5}$$

with A_{swath} the swath area on the SRMA plane. For each pulse, $\{P_L, \overrightarrow{\Omega_L}\}$ is derived from the multi-pulse parameters $\{\theta_{L,max}, \delta\theta_L, \Delta d, \Delta d_s\}$ and a known control point. Geometrical configurations and illumination / reception projections are calculated for all pulses with Equation (1), (2) and (3).

For TLS (Figure 3), there are no footprint and FOV projected regions on the SRMA plane. P_L is a constant. $\overrightarrow{\Omega_L}$ is defined by classical zenith angle θ_{tls} and azimuth angle ϕ_{tls} in the coordinate system of the studied scene. The illumination and reception range of each pulse are specified by β_{fp} and β_{FOV}, respectively. For multi-pulse simulation, the region of TLS observation is defined by zenith angle range $\Delta\theta_{tls}$ and azimuth angle range $\Delta\phi_{tls}$. The angle step between pulses in zenith and azimuth ranges are $\delta\theta_{tls}$ and $\delta\phi_{tls}$, respectively. Therefore, an acquisition corresponds to $N_p = \frac{\Delta\phi_{tls}}{\delta\phi_{tls}} \cdot \frac{\Delta\theta_{tls}}{\delta\theta_{tls}}$ pulses.

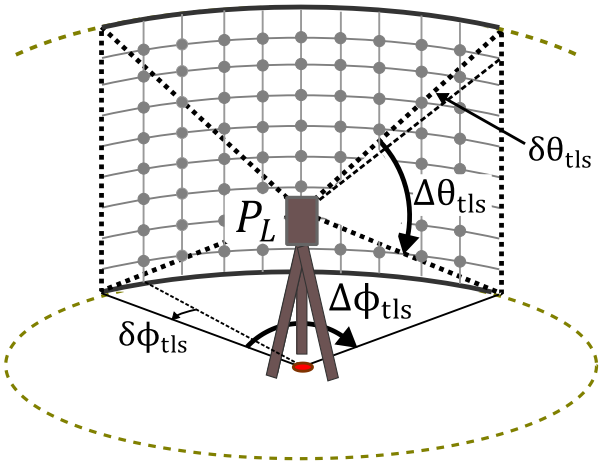

Figure 3: Scanning pattern of a terrestrial LiDAR

Multi-pulse modeling is implemented in such a way that computation time is minimized. For example, the scene and the associated memory loading for quantifying phase functions in the box method (Gastellu-Etchegorry et al., 2015b) are computed once, only. Moreover, waveform simulation is independent between pulses. Each pulse is referred by 2 indices {i, j}. For ALS, i is the index of scan line along the platform track, and j is the pulse index in scan line i. For TLS, i is the zenith angle index, and j is the azimuth angle index. Simulations are accelerated using algorithmic multithreading with BOOST library (Demming and Duffy, 2010). With N_{th} threads, N_p/N_{th} pulses are assigned per thread. Thus, the acceleration factor is about N_{th}. Waveforms are simulated with DART quasi-MCRT method (Gastellu-Etchegorry et al., 2015b).

2.2 Output data format conversion and processing into point cloud

All simulated waveforms are processed and then, stored in a binary file the format of which is shown in Table B1 in **Appendix B**. A single file stores all data, which eases the access to pulse information. DART uses this file to display the waveform of any selected pulse. The data design methodology is optimized to store only the information which is relevant to data processing. Parameters irrelevant to data processing (PRF, sensor speed, etc.) are not stored.

In actual ALS or TLS wLiDAR data processing, waveforms are usually decomposed into points, which are estimated locations where transmitted laser pulses are scattered by scene elements. Then, these points are usually classified for various applications like digital elevation model (DEM) generation, canopy structure retrieval, etc. DART has no LiDAR data processing functionality such as waveform decomposition, classification, etc. Thus, simulated LiDAR data are transformed into a format compatible with industrial software that processes actual wLiDAR data. Several formats are used to store ALS and TLS data. The American Society for Photogrammetry and Remote Sensing (ASPRS) develops and supports the LAS format. For a long period, it has been employed to store traditional discrete return LiDAR data as a binary file with point indexing and compression. Since version 1.3, LAS supports waveform storage. However, its management of waveforms is not efficient. Waveforms are generally stored and indexed as points without reference to individual pulses. Waveform data associated to a given point are linked by offset in bytes or stored in another file, which is difficult to manage and to support. Furthermore, some current open source libraries of LAS format (*e.g.*, libLAS: http://www.liblas.org/) do not support waveform reading and writing.

DART LiDAR outputs are converted into a newer industrial format, the Sorted Pulse Data (SPD) format. SPD uses version 5 Hierarchy Data Format (HDF5) for storing waveform data (Bunting et al., 2013b). HDF5 is an open-source and self-describing database format with full input/output support through many programs and libraries. SPD uses a pulse-based model with better storage management than the LAS format. A SPD file stores waveforms with pulse indexing in arrays with various categories of associated parameters per pulse. The DART-to-SPD conversion is through python binding of the associated open-source library SPDlib (Bunting et al., 2013a)Most parameters stored in a multi-pulse output binary file (Table B1) can be mapped accordingly in a SPD file. DART stores waveforms defined by photon number per bin. However, actually measured waveforms are stored in analog digital number per bin. The conversion formula is:

$$V_{bin} = V_{off,bin} + g.\, N_{ph,bin} \tag{6}$$

with V_{bin} the recorded digital number (*e.g.*, 8 bits positive integer from 0 to 127), $V_{off,bin}$ the offset, and g the simulated gain which converts waveform intensity unit from number of photons per bin $N_{ph,bin}$ into digital number. $V_{off,bin}$ and g are fixed parameters in waveform recording per pulse. The conversion can use a constant g for all pulses, or a value per pulse or group of pulses to adjust the maximum value. For example, if $N_{ph,max,bin}$ is the maximum number of photons per bin for the waveform of a reference pulse, the gain is $g = (V_{max,bin} - V_{off,bin})/N_{ph,max,bin}$, with $V_{max,bin} \in [1\ 127]$ in an 8 bits system, which is roughly corresponding to the automatic gain control of the detector in an actual wLiDAR.

Pulse information from different threads is stacked with the producer-consumer pattern (Demming and Duffy, 2010). Thus, simulations of LiDAR pulses managed by different threads are not completed in the same sequence as their original indexing. SPD uses a grid based sorting algorithm for optimizing memory usage and access speed to fast display all or part of the retrieved points. SPD file also supports data compression using deflate algorithm, which produces more than 50 times smaller size file than the original DART output.

SPDlib (Bunting et al., 2013a) can decompose SPD waveform data into point cloud, and classify the points into different categories (ground, vegetation canopy, etc.). DEMs can be generated from ALS ground returns, and tree heights are retrieved from differences of elevation between DEMs and LiDAR canopy returns. SPDlib can also subset and merge LiDAR points from different measurements, and create industrial file of surface model from points, which can be used for geographical information system application. Python binding script for data conversion is provided

with DART latest release (V5.5.3). However, its use requires SPDlib pre-installation under LINUX system.

2.3 ALS example

DART participated to the 4 RAMI experiments (http://rami-benchmark.jrc.ec.europa.eu/HTML/) over the last 15 years (Widlowski et al., 2007, 2008, 2013) and proved to be one of the accurate BRF models. Some RAMI4 3-D tree and scenes that are simulated with facets, are used below to illustrate DART outputs. In particular, the Jarvselja pine stand (during summer) (110m × 110m) in Estonia is used to illustrate ALS simulation. Most trees are scots pines. There are 1114 pines from 10 tree species that have the same leaf and trunk optical properties, but different tree heights (10.21m to 18.56m), crown radii (0.48m to 3.70m), and one-side total leaf area (1.2975m^2 to 79.0104m^2). Figure 4(a) shows the pine distribution in the simulated scene. Each pine is indicated as a circle with an area proportional to its crown size. Facet representation of all foliar elements of a single tree requires tremendous computer memories, which forbids the simulation of the whole pine stand with facets. Thus, for simulating this stand, DART converts "foliar" facets within each rectangular cell of the simulated scene into turbid medium (Ross, 1981). Here, we consider 0.4m × 0.4m × 0.4m cells. Two horizontal coordinate systems are used (Figure 4(a)): the simulated scene global system (x-y axes), and wLiDAR system (platform-track $\overrightarrow{\phi_p}$ axis (+x direction, $\phi_p = 0°$) and cross-track $\overrightarrow{\phi_s}$ axis (-y direction, $\phi_s = 270°, \phi_{off} = 0°$)). The platform path crosses the scene center at altitude $H = 500\text{m}$. The wLiDAR has a rotating mirror polygon that gives a 108m × 108m swath area. The look angle θ_L ranges from $-6.16°$ on the platform track left side to $6.16°$ on the other side ($\Delta\theta_{L,swath} = 12.32°$). This instrumental configuration mimics the LiDAR onboard the CAO AtoMS system as illustrated in Table 1 (Asner et al., 2012). Unpublished parameters are set to DART default setting (*e.g.*, 2ns pulse duration, 36.8% of pulse spatial energy at footprint boundary, etc.). From Equation (1), we get $r_{fp} = 0.25\text{m}$ and $r_{FOV} = 0.4\text{m}$. From Equation (5), we get $N_p = 167478$ (309 scans along track, and 542 pulses per scan), and $\rho_p = 14.35$ pulses/m^2. Since multiple scattering plays an important role with vegetation in near infrared band, 5000 simulated photons are transmitted per pulse, and processing time is 0.78 second per pulse per thread. With 20 parallel threads of 3.07 GHz processors, the whole simulation takes about 110 minutes.

Table 1 : Instrumental parameters that mimic the wLiDAR onboard the AtoMS system of the Carnegie Airborne Observatory

Parameters	Symbols	Values
Sensor area	A_t	0.1m^2
Wavelength	λ	1064 nm
Pulse energy		1 mJ
Time step per bin	δt_{bin}	1 ns
Distance step per bin	δd_{bin}	30 cm
Footprint divergence half angle	β_{fp}	0.25 mrad
FOV divergence half angle	β_{FOV}	0.4 mrad
Pulse Repetition Frequency	PRF	400 kHz
Scan frequency	f_s	140 Hz
Maximum look angle	$\theta_{L,max,scan}$	32.5 ^{o}

Platform speed	v_p	49 m/s (95.24 knots)
Along-track distance step per scan	δd_s	0.35 m
Look angle step per pulse	$\delta\theta_L$	0.02275 ^{o}

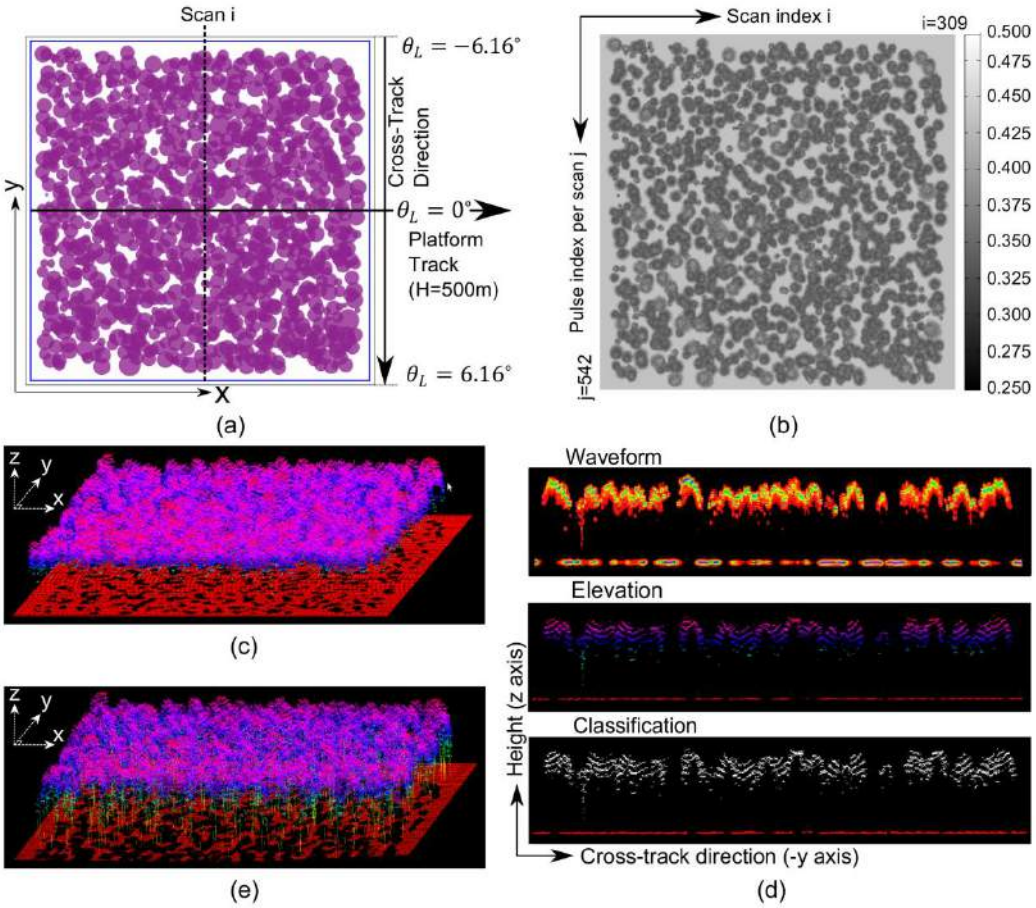

Figure 4: ALS simulation of Jarvselja pine stand. (a) Pine distribution and wLiDAR platform geometrical configuration ($H = 500m, \theta_L \in [-6.16°, 6.16°]$). (b) Reflectance image per pulse. (c) Point cloud displayed by SPDlib. (d) Points of scan i in (a). From top to bottom: waveform, elevation, and ground classification (red: ground, white: no ground). (e) Another example of generated point cloud by configuring the platform path to make $\theta_L = +45°$ at the center of the swath with the same configuration of altitude and platform direction as (a).

DART maps (Figure 4(b)) the reflectance $R_{i,j}$ associated to each DART generated pulse. This reflectance is calculated with:

$$R_{i,j} = \frac{N_{ph,rcp,i,j} \cdot \pi}{\cos\theta_{L,i,j} \cdot \delta\Omega_{O_E,i,j} \cdot N_{ph,ilm}} \quad (7)$$

with $N_{ph,rcp,i,j}$ the number of photons in the waveform, $\delta\Omega_{O_E,i,j} = A_t . \cos^2\theta_{L,i,j} / H^2$ the solid angle through which O_E sees the LiDAR telescope, and $N_{ph,ilm}$ the total number of transmitted photons. The original size of the reflectance image is consistent with the number of LiDAR pulses (309 ×

542 pixels). The image in Figure 4(b) is rescaled according to the swath dimension. Reflectance distribution in the map is generally correlated with the pine leaf area index distribution.

Output data are converted into SPD format with gain g=2.3 10^{-6} volts/photon. Figure 4(c) shows the SPDlib processed point cloud. In all, 393926 points are retrieved by Gaussian decomposition (≈ 2.35 points / pulse). Color indicates the elevation. Ground signal is discontinuous because some pulses have no ground return. Figure 4(d) shows 3 vertical sections for the scan of index i in Figure 4(a): waveforms (amplitude / bin), elevation, and classification, from top to bottom. Pine trunks give sparse returns. Indeed, θ_L range being around nadir direction, very few photons can reach trunks. Another configuration is assessed with θ_L at 45° at the scene center. Then, trunk returns appear clearly in the generated point cloud (Figure 4(e)), and ground returns are much smaller. It illustrates that DART can simulate any ALS experimental geometric configuration.

2.4 TLS illustration

TLS simulation is illustrated with a citrus tree object (identifier CISI6 in RAMI4) from a Wellington Citrus Orchard site, South Africa. Figure 5(a) shows this tree and a 3-D reference frame. It is 3.26m high, with 1.23m maximum crown radius. Total leaf area is 15.3m^2 and total wood area is 6.29m^2. Here, the simulated TLS mimics configurations of the ILRIS-LR (Table 2) of Optech Inc. (www.optech.com). Côté et al. (2009) used this device for tree object reconstruction. Its operation wavelength (1535nm) allowed them to distinguish leaves (reflectance: 0.43) and wood (reflectance: 0.765). The terrestrial LiDAR is 5.5m away from the citrus vertical axis along the –x axis. It is 1.7m above ground, with a FOV center along x axis. The scan FOV covers a 40° × 40° window (4m × 4m cross section region at citrus center location). In all, about 1.777 million (1333 × 1333) pulses are simulated. The measured distance range is set to 4-8 m from the LiDAR position to cover the whole object volume. The laser beam divergence is very small (0.075 mrad). Thus, multiple scattering is very small, and as little as 150 photons are fired per pulse. Simulation time is 0.093 seconds per pulse. With 20 threads, the simulation takes 138 minutes.

Table 2 : Instrumental configurations that mimic ILRIS-LR terrestrial LiDAR

Parameters	Symbols	Values
Sensor area	A_t	0.1024m^2
Wavelength	λ	1535 nm
Pulse energy		1 mJ
Time step per bin	δt_{bin}	0.05 ns
Distance step per bin	δd_{bin}	15 mm
Laser divergence half angle	β_{fp}	0.075 mrad
FOV divergence half angle	β_{FOV}	0.1 mrad
Zenith angle step per pulse	$\delta\theta_{tls}$	0.03 ^{o}
Azimuth angle step per pulse	$\delta\phi_{tls}$	0.03 ^{o}

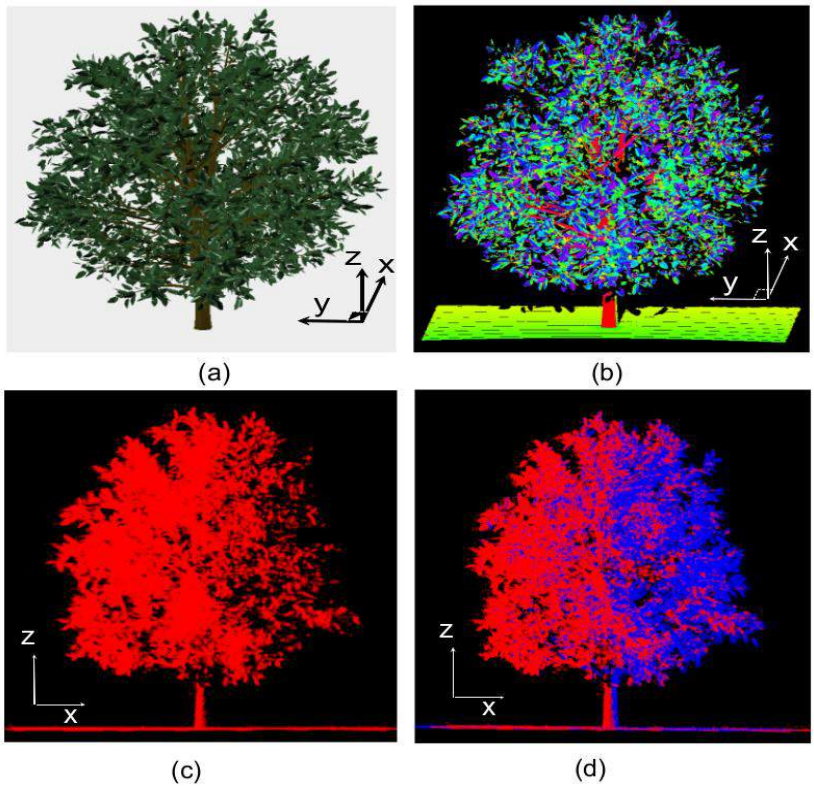

Figure 5 : TLS simulation for a citrus object. (a) The simulated tree object. (b) Forward view of the decomposed point cloud with amplitude. (c) Side view of the point cloud (red points). (d) Side view of merged point cloud with another simulation from reverse direction (blue points).

Conversion into SPD format is done with $g = 7.58 \times 10^{-5}\ volts/photon$. In all, 823754 points are extracted by SPDlib. This number is much smaller than the number of transmitted laser pulses, because many pulses are not intercepted or give rise to returns that are outside the measured distance range. Figure 5(b) shows the 3-D points with color indicating each return energy. The viewpoint of the 3-D display is the same as Figure 5(a), along LiDAR mean orientation (+x direction). Returns from the facets of branches (red), leaves (blue, green, purple) and ground (yellow) can be distinguished through their energy, and tree objects can be reconstructed from these points. Figure 5(c) shows a point cloud side view (along +y direction). Point density is much larger on the LiDAR-illuminated side than on the opposite side, since laser pulses can be intercepted along their within crown paths. In actual acquisitions, LiDAR data from several directions are merged to solve this problem (Rosell et al., 2009, Côté et al., 2009), which leads to complete and accurate tree and leaf distributions. Figure 5(d) shows the merged resulting point cloud from another simulation: the LiDAR is 5.5m away along +x direction and measures the citrus towards –x direction. This measurement is complementary to the original points and fills most of the missing points from the opposite side.

3. PHOTON COUNTING DATA SIMULATION

Photon counting LiDAR (pcLiDAR) is a novel technology which uses single-photon detector instead of traditional analog electronics detector. Compared with wLiDAR, pcLiDAR pulses usually have much lower energy (10's-100's µJ), higher PRF (Spinhirne, 1993, McGill et al., 2002),

and smaller β_{fp} and β_{FOV}. Three key parameters of a single-photon detector are considered here: the quantum efficiency P_Q (the probability to detect a photon that reaches the detector), the detector dead time t_{dead} (the period needed by the detector to recover from a detection event, before another photon can be detected), and the dark count rate f_{dark}(the detector's minimum count rate without light source). Bin time width δt_{bin} for single-photon detector is usually small (100's ps, which gives ≈10's mm accuracy in distance measurement). The theoretical distance accuracy is better than wLiDAR for which δt_{bin} is around a few nanoseconds (*i.e.*, around 10 cm accuracy in distance measurement). Moreover, single-photon detector can avoid the wLiDAR acquisition analog signal noise. Presently, a few airborne pcLiDARs are operational. Some of them are used to prepare future space missions. For example, MABEL (McGill et al., 2013) and Swath Imaging Multi-polarization Photon-counting LiDAR (SIMPL) (Dabney et al., 2010, Harding et al., 2007) are both prototypes for the next ATLAS (Yu et al., 2010) onboard ICESat-2 (Abdalati et al., 2010).

pcLiDAR and wLiDAR data acquisition and interpretation differ a lot. Instead of waveform data continuous profile, which needs post processing, pcLiDAR data can be directly seen as scattering events locations. Actually, waveforms indicate the probabilities of occurrence of photon detection events, thus it can be converted into pcLiDAR data with implementation of single-photon detector physical mode. The approach presented below converts DART simulated single or multiple pulses waveforms, for any instrumental configuration, into detected photons of single-photon detector.

Assume that N_p photons reach a single-photon detector during a short time period Δt. Then, the probability that a photon is detected is:

$$P(\Delta t) = 1 - \left(1 - P_Q\right)^{N_p + f_{dark}.\Delta t} \tag{8}$$

where $f_{dark}.\Delta t$ is the number of background photons associated to the dark count rate during an acquisition period. Let t_{pc} be a cursor that indices the waveform time axis within the pre-defined record time period from $\frac{t_{min}}{2}$ to $\frac{t_{max}}{2}$, in order to test detection event. This time period corresponds to the actual distance of scattering points to the LiDAR, which is half of the recorded distance. The increase of t_{pc} with time step Δt (cf. Figure 6) represents the time flow. Then, photon detection is modeled in the single-photon detector for each t_{pc} value. At the initial state, $t_{pc} = \frac{t_{min}}{2}$ and $\Delta t = \delta t_{bin}$. With $P(\Delta t)$ from Equation (8) and a random number p ($0 < p < 1$), the following rule states for each t_{pc} value if there is photon detection:

- If $p > P(\Delta t)$: no photon is detected, and t_{pc} is updated with $t_{pc} = t_{pc} + \frac{\Delta t}{2}$
- If $p < P(\Delta t)$: a photon is detected at a position defined by $t_{pc} + \frac{p}{P(\Delta t)} \cdot \frac{\Delta t}{2}$, and t_{pc} is updated with $t_{pc} = t_{pc} + \frac{p \cdot \Delta t}{2P(\Delta t)} + \frac{t_{dead}}{2}$. (9)

Initially, t_{pc} is at a time bin left boundary (Figure 6), and $\Delta t = \delta t_{bin}$. Once, a photon is detected ($p < P(\Delta t)$, t_{pc} is no more located at a bin boundary. Then, Δt is set to the time period to the next bin boundary, which is smaller than δt_{bin}, and Equation (9) can be applied again.

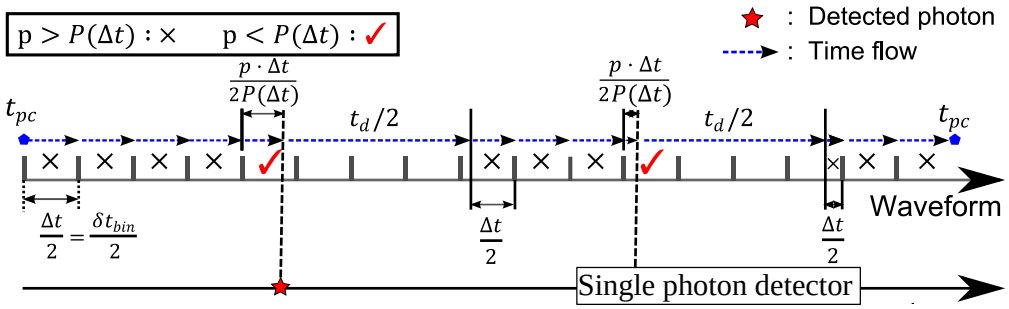

Figure 6 : Illustration of photon counting simulation

Here, the photon counting method is used to simulate MABEL instrumental configuration (McGill et al., 2013) for the RAMI4 Jarvselja Pine Stand test site (Figure 4(a)). Conversely to rotating/oscillating mirrors that reflect pulses towards targets, MABEL splits each laser pulse through 24 optical fibers to generate 16 beams at 532 nm and 8 beams at 1064 nm. The pulses of these beams have the same PRF and much smaller energies than the generated pulse, and $\delta d_s = v_p/PRF = 2cm$. Platform altitude is 20 km, which gives $r_{fp} = 1m$ and $r_{FOV} = 2.16m$ on the SRMA. Night conditions with clear atmosphere are considered with a rural (23km visibility) aerosol model and a US standard gas model (1976). Thus, the laser generator of MABEL is the only source of photons.

Pulses of two beams of MABEL at 532nm and 1064nm are simulated along scan i (Figure 4(a)) with nadir Ω_L. Figure 7 illustrates results: sub-figure (a) for 532nm and (b) for 1064nm. The upper figures of each sub-figure show the detected photons over the wide vertical range (-2000m, 10000m). Points above the Earth's scene are from the atmosphere, whereas photons below the ground are mostly from the dark count rate f_{dark}. The lower figures are enlargements for the vertical range (-5m, 25m). They mainly show photons from the Earth's scene. Photons from ground and vegetation are clearly distinguished. Their spatial distribution is coherent with that of the associated wLiDAR data (Figure 4(d)). We distinguish 3 regions: (25m, 10000m) above the Earth scene, (-5m, 25m) in the Earth scene, and (-2000m, -5m) below the scene. For 532nm band, the vertical photon detection rate is 0.95 photons/m vertically above the scene, from atmosphere scattering and dark count rate, 119.23 photons/m within the scene, from the scene elements, and 0.60 photons/m below the scene (from the detector dark count rate). Conversely, for 1064nm, the photon detection rate is 0.0625 photons/m above the scene, 266.9 photons/m within the scene, and 0.0564 photons/m below the scene. As expected, atmosphere returns are more numerous for 532nm. The large near infrared reflectance of vegetation explains that returns are more numerous for 1064nm, although quantum efficiency is larger for 532nm. The horizontal distribution of atmosphere photons is rather uniform in both figures, because the atmosphere was assumed to be horizontally homogeneous.

Table 3 : Instrumental configurations that mimic MABEL

Parameters	Symbols	Values
Wavelength	λ	532 nm / 1064 nm
Bandwitdth	Δλ	0.03 nm / 0.4 nm
Pulse energy		6 µJ
Time resolution	δt_{bin}	0.083 ns

Distance step per bin	δd_{bin}	24.9 mm
Footprint dispersion half angle	β_{fp}	0.05 mrad
FOV dispersion half angle	β_{FOV}	0.105 mrad
Pulse Repetition Frequency	PRF	10 kHz
Number of beams		16 / 8
Platform speed	v_p	200 m/s
Quantum efficiency	p_Q	12.5% / 1.5%
Detector dead time	t_d	2.5 ns
Dark count rate	f_{dark}	100 kHz

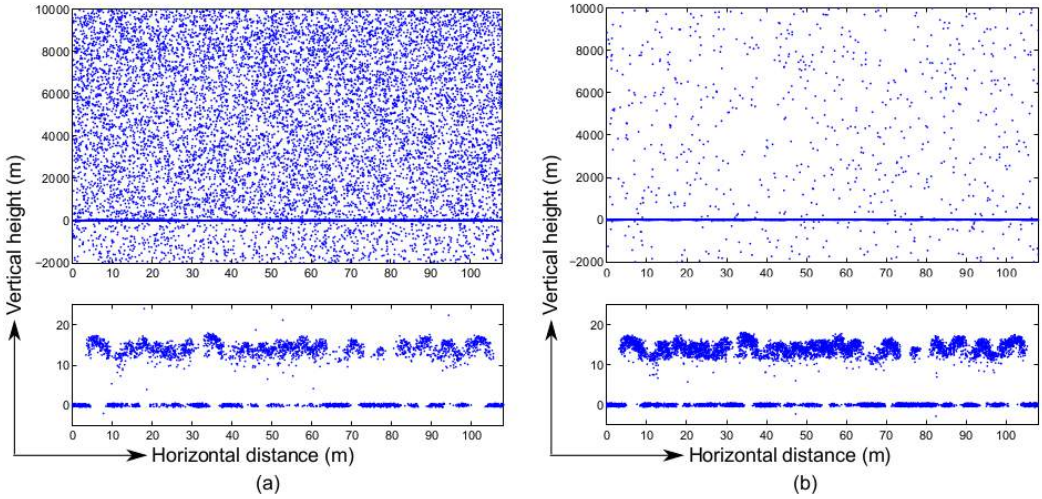

Figure 7 : Along track MABEL simulated photon counting data, for Jarvselja Pine Stand test site (scan i in Figure 4(a)). (a) 532nm band. (b) 1064nm band.

4. SOLAR NOISE SIMULATION

4.1 Modeling method

Solar noise refers to sun rays which are scattered into the LiDAR sensor by the atmosphere and the Earth's surface during daytime. A novel DART method simulates LiDAR data with solar noise. It relies on the combination of 2 DART modeling modes:

a) Quasi-MCRT mode. It simulates noiseless LiDAR waveforms. LiDAR is both the source and the sensor.

b) Ray-tracking mode. Sun is the source and LiDAR is the sensor. The at-sensor radiance image is simulated as if LiDAR is a passive imaging radiance sensor (pinhole camera or linear pushbroom imager). Then, radiance within the FOV of each pulse is converted into number of photons and added to each noiseless waveform as the solar noise for each pulse.

The ray-tracking mode is an iterative process in the Earth scene (Gastellu-Etchegorry et al., 1996) and atmosphere (Grau and Gastellu-Etchegorry, 2013). In the illumination stage, atmosphere and/or sun rays that enter the Earth scene are tracked along pre-defined downward directions that sample

the 2π hemisphere. They undergo surface and volume interactions (absorption, scattering) with facets and turbid cells that simulate the Earth scene, respectively. In each iteration n, radiation intercepted at iteration (n-1) is scattered through the pre-defined directions that sample the 4π space (Yin et al., 2013), and directions that head to an eventual pinhole camera or linear pushbroom imager (Yin et al., 2015). Rays that reach pre-defined altitude levels are recorded for creating radiance, reflectance and/or brightness temperature images. Iterations stop if relative increase of the Earth scene exitance between successive iterations is smaller than a user specified threshold.

When a ray reaches the top of a simulated scene, its intensity and its source element (within cell facet or sub-face of turbid cell) are projected onto a horizontal image plane (HIPlane) with altitude at the SRMA (Yin et al., 2015). Depending on the sensor product to simulate, one of three types of projections is applied:

1. Orthographic projection for sensors at infinite distance. The divergence of rays that enter the sensor is neglected. All pixels of the same image are viewed along the same direction, for each simulated direction.
2. Perspective projection for pinhole cameras. The sensor is a single point, and rays that enter it are converging to this point. The source element is projected onto the HIPlane along lines defined by the pinhole camera and the vertices of the source element.
3. Parallel-perspective projection for linear pushbroom imagers. Pushbroom imager acquisition geometry is similar to the rotating polygon scan pattern (Figure 2(a)): orthographic projection along platform track, and perspective projection along the scan axis (Gupta and Hartley, 1997). The source element and sensor locations, and platform track are linked similarly as P_L with known ϕ_p, ϕ_s and a control point (Section 2.1). Thus, a point is projected onto the HIPlane by finding first the corresponding scan line and the sensor position, and then applying perspective projection along $\overrightarrow{\phi_s}$.

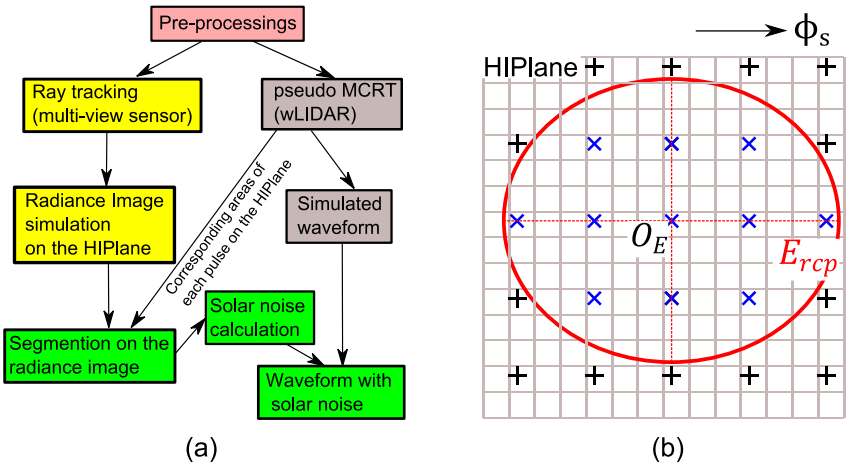

Figure 8: LiDAR solar noise simulation in DART. (a) Workflow of solar noise simulation. (b) Segmentation and interpolation for estimating solar noise on the HIPlane. The mesh grid represents the radiance image generated on the HIPlane. The red ellipse is the LiDAR reception area on the HIPlane. Symbols × and + show the initial selected points inside and outside the LiDAR FOV, respectively.

wLiDAR with solar noise is simulated for single and multiple pulse configurations with a dual-simulation approach (Figure 8(a)), which includes 3 processing steps:

1) Pre-processing. DART pre-calculation steps are performed: discrete directions definition, scene simulation and scattering phase function calculation per type of scene element for all directions, including solar and LiDAR illumination directions.

2) Dual simulation. The LiDAR waveform and the passive sensor radiance image on the HIPlane are simulated with the quasi-MCRT DART and ray tracking methods, respectively. The passive sensor image is simulated with the wLiDAR geometry configuration (P_L , ϕ_p , ϕ_s , etc.), wavelength λ , bandwidth $\Delta\lambda$, using pinhole camera mode for single-pulse simulation and pushbroom imager mode for multi-pulse simulation. The region of E_{rcp} on the SRMA plane is stored per pulse, during wLiDAR simulation.

3) Reception radiance calculation. The radiance image HIPlane and wLiDAR SRMA are in the same plane. Thus, the radiance image, without orthorectification to preserve each pixel view direction, can be segmented per LiDAR reception region E_{rcp} (Figure 1) for computing the average radiance $L_{i,j}$ per pulse. Let us consider a region E_{rcp}, with a center O_E, a grid of defined dimensions along ϕ_s and its perpendicular axis, and points (×) of the radiance image within E_{rcp} (Figure 8(b)). $L_{i,j}$ is derived from cubic spline interpolation on points (×). Its accuracy depends on the grid dimension. O_E can differ from HIPlane pixel centers, which allows one to work with extreme cases such as radiance image with pixel size larger than E_{rcp}.

The average radiance per pulse $L_{i,j}$ (unit: W/sr/m^2/nm) is converted into a number of solar noise photons per waveform per bin:

$$N_{ph,SN,i,j,bin} = L_{i,j} \cdot \Delta\lambda \cdot A_{E,rcp} \cdot cos\,\theta_{L,i,j} \cdot \Delta\omega \cdot \delta t_{bin} \cdot \frac{\lambda}{h.c} \quad (10)$$

δt_{bin} is the time step per bin in the simulated waveform. $\Delta\omega = A_t.cos^2\,\theta_{L,i,j}/H^2$ is the solid angle through which the center of projection O_E sees the LiDAR telescope. $A_{E,rcp} = \pi \cdot r_{\perp,rcp} \cdot r_{\parallel,rcp}$ is the area of E_{rcp}, where $r_{\perp,rcp}$ and $r_{\parallel,rcp}$ are calculated by Equation (2) and (3). h is the Plank's constant. c is the speed of light.

$N_{photon,SN,i,j}$ photons are added to each bin of the pulse waveform. We assume that $H \cdot tan\,\beta_{FOV} / cos\,\theta_{L,i,j} \gg r_t$, which is usually valid for long range detection. In that case, the r_t term can be removed from Equation (3), and Equation (10) becomes:

$$N_{ph,SN,i,j,bin} \approx L_{i,j} \cdot \Delta\lambda \cdot \pi^2 \cdot tan^2\,\beta_{FOV} \cdot A_t \cdot \delta t_{bin} \cdot \frac{\lambda}{h \cdot c} \quad (11)$$

As expected, solar noise depends on $L_{i,j}$, and thus on scene spectral reflectance, atmosphere spectral transmittance and solar spectra. Its absolute value is reduced if A_t, δt_{bin} and β_{FOV} are reduced. Variation of $\Delta\lambda$ can change $L_{i,j}$ at the same time, so there is no direct trend. The pure LiDAR signal is proportional to A_t and δt_{bin}, so the ratio of pure LiDAR signal over solar noise is not improved by changing A_t and δt_{bin}. Reduction of β_{FOV} can improve this ratio. The value of β_{FOV} is limited by technique bottle neck of detector design.

Solar zenith angle and surface reflectance affect a lot solar noise. It is illustrated here with 2 cases: single pulse of spaceborne (large-footprint) LiDAR with varying solar zenith angle, and multiple pulses of an airborne (small-footprint) LiDAR.

4.2 Solar noise in the waveform of a single pulse of a large-footprint LiDAR

Usually, actual pcLiDAR pulses have a much smaller energy than wLiDAR pulses. Thus, solar noise ratio for pcLiDAR is much larger than for wLiDAR. It can restrict the use of pcLiDAR devices to early or late in the day, as with the initial data of MABEL (McGill et al., 2013)). Solar zenith angle impact on solar noise is assessed for waveform from a fictive wLiDAR with pcLiDAR ATLAS parameters (Table 4). Platform altitude H = 496 km leads to footprint and FOV dimensions on the HIPlane equal to $r_{fp} = 4.22m$ and $r_{FOV} = 21.06m$, respectively. We consider the minimum pulse energy of 25μJ of all ATLAS beams (Yu et al., 2010), wavelength 532nm and $\delta t_{bin} = 1ns$.

Table 4: Instrumental configuration of a wLiDAR device similar to ATLAS.

Parameters	Symbols	Values
Sensor area	A_t	0.5024 m^2
Wavelength	λ	532 nm
Bandwitdth	Δλ	0.03 nm
Pulse energy		25 μJ
Pulse width		1.5ns
Time step per bin	δt_{bin}	1 ns
Distance step per bin	δd_{bin}	30 cm
Footprint divergence half angle	β_{fp}	8.5 μrad
FOV divergence half angle	β_{FOV}	41.65 μrad

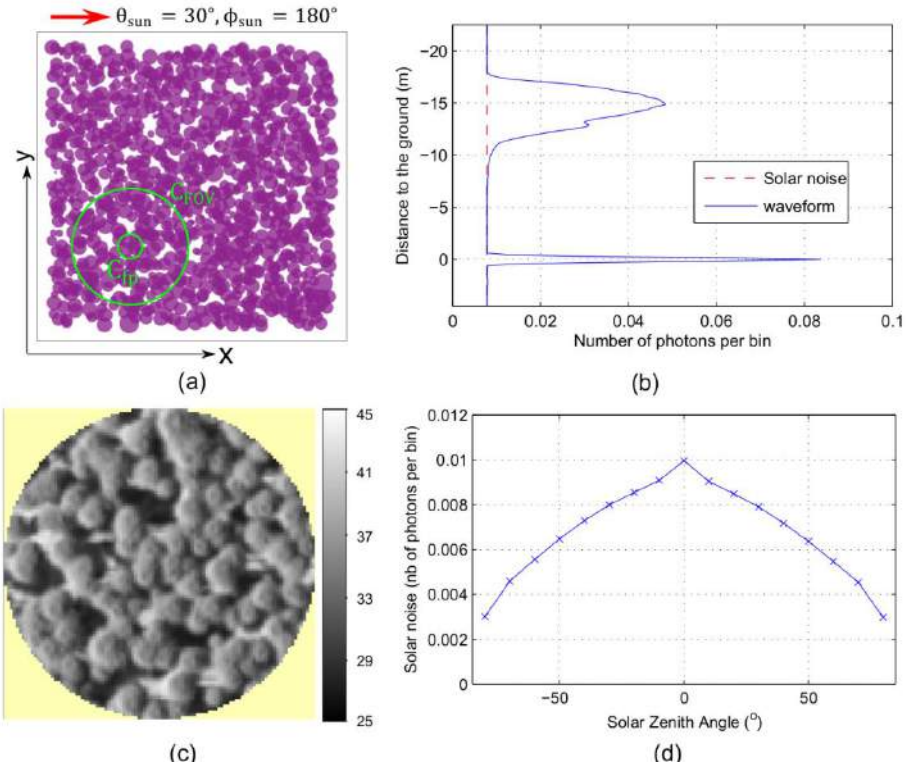

Figure 9: Impact of solar noise on the waveform of a fictive wLiDAR device with ATLAS parameters. (a) Jarvselja pine stand with LiDAR footprint and FOV projected regions ($\theta_{sun} = 45°$, $\phi_{sun} = 180°$). (b) Waveform with solar noise. (c) Radiance image (W/sr/m^2/nm) of a simulated pinhole camera which captures the LiDAR FOV region. (e) $N_{ph,SN,i,j,bin}$ with solar zenith angle from -80°to 80°

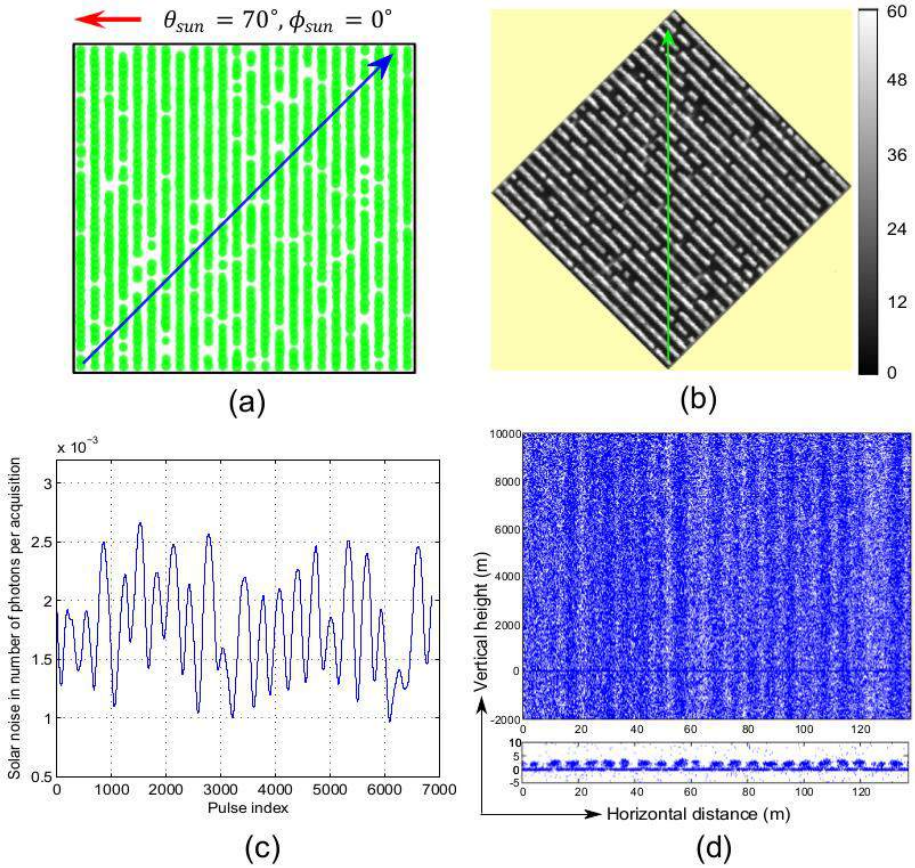

Figure 10 : Simulation of solar noise in MABEL data with $\lambda = 1064$nm. (a) Tree distribution in the Wellington Citrus Orchard test site. The blue arrow indicates the platform path. ($\theta_{sun} = 70°$, $\phi_{sun} = 0°$). (b) Pushbroom radiance image on the HIPlane. (c) Solar noise in number of photons per bin versus the pulse index. (d) Detected photons for 2 vertical ranges. Top: [-2000m, 10000m]). Bottom: [-5m, 10m])..

Solar noise simulation is conducted with Jarvselja pine stand of RAMI4. Figure 9(a) shows the pine distribution, together with LiDAR footprint and FOV projected regions on the ground (C_{fp} and C_{FOV}). Sun zenith and azimuth angles are $\theta_{sun} = 30°$ and $\phi_{sun} = 180°$, respectively. The atmosphere is clear sky with the same parameters as in section 2.3. Figure 9(b) shows the resultant waveform from -5m to 22m in altitude (blue curve) and solar noise contribution (red dashed line). Without solar noise, the maximum count per bin (in 15cm's distance) in the noiseless LiDAR signal is 0.0767 photons/bin (from the ground). Solar noise adds a constant number of photons $N_{ph,SN,bin} = 0.0078$ photons/bin (Equation (10)), and the maximum count per bin becomes 0.0845 photons/bin. $N_{ph,SN,bin}$ is computed through the simulation of the radiance image acquired by a pinhole camera that has the same LiDAR location, wavelength and bandwidth. For that, the radiance image on the HIPlane is segmented into LiDAR FOV C_{FOV} regions (Figure 9(c)) for computing the average radiance per pulse $L_{i,j}$. Crown and ground sunlit and shadowed areas appear

clearly in Figure 9(c). Their proportions affect $L_{i,j}$. As solar zenith angle varies during day time, these proportions change. Figure 9(d) shows how solar noise (number of photons per bin) changes during daytime with θ_{sun} from $-80°$ to $80°$ ($\theta_{sun} < 0°$ if $\phi_{sun} = 0°$). As θ_{sun} approaches $0°$ (nadir), shadows decrease, and $L_{i,j}$ increases. Solar noise variation with θ_{sun} is nearly symmetric, with a maximum for $\theta_{sun} = 0°$, partly due to the hot spot effect (Kuusk, 1991), when sun and LiDAR directions are identical (nadir). Actually, this change of θ_{sun} is unrealistic for Jarvselja site, because its latitude is larger than that of tropic of cancer.

4.3 Solar noise in multiple pulses of small-footprint photon counting LiDAR

Simulating N LiDAR pulses with solar noise for a moving platform, with the "single pulse" method (section 4.2) implies to simulate radiance images of N passive sensors. This solution is not optimal for computation time and memory usage. Thus, the adopted approach is to simulate the radiance image of a single passive linear pushbroom sensor. Indeed, a pushbroom imager measures fluxes entering the sensor over the swath through parallel-perspective projection. The along-track angular acquisition divergence of each individual pulse is neglected, because β_{FOV} is small. Similarly to the single pulse method, solar noise is computed for each segmented region on the HIPlane pushbroom image. Here, the test site is the Wellington citrus orchard (Figure 10(a)) of RAMI4. It comprises 1115 citruses (10 types) along 24 parallel rows (with some gaps) along the x axis. Their average height is 3.2m. Tree crowns are spherical with 1.53m maximum radius. Distance between tree rows along the x axis is ≈ 4.6m. Sun angles are $\theta_{sun} = 70°$ and $\phi_{sun} = 0°$. Thus, tree shadows occupy most gaps between the rows. The atmosphere is clear sky with the same parameters as in section 2.3.

MABEL pcLiDAR nadir-view beam is simulated with $\lambda = 1064$nm. Platform altitude being 20km, we have $r_{fp} = 1$m and $r_{FOV} = 2.16$m. A blue arrow ($\phi_p = 45°$) shows the 138.56m platform path. In all, 6929 pulses are launched with 0.02m step. The pushbroom radiance image (Figure 10(b)) on the HIPlane is simulated with pcLiDAR wavelength, bandwidth and platform path. Parallel-perspective projection is applied, and the image orientation is rotated to show the swath along the path. The effect of perspective projection is small because the simulated area is very small ($-0.2°$ on the left corner to $0.2°$ on the right corner), compared to platform altitude. In the image, citrus shadows cover the area between the parallel tree rows. All pulse reception regions are segmented in the radiance image (Figure 10(b)) to calculate their average radiance values $L_{i,j}$, which are transformed in a second stage into solar noise per pulse (Equation (11)). In theory, a pulse with a reception region in a shaded area has a small solar noise. Figure 10(c) plots the solar noise in number of photons per bin versus the pulse index. As expected, solar noise fluctuates as the platform overflies the citrus rows. In all, 23 peaks occur, which is consistent with the number of citrus rows that the platform overflies. Solar noise is maximal over vegetation and minimal over the shadows between rows. Figure 10(d) shows the detected photons by using the algorithms presented in Section 3, in both large ([-2000, 10000]) and small ([-5, 10]) vertical ranges. Similarly, noiseless pcLiDAR returns are more important over vegetation than over shadows. Thus, the along track heterogeneity of actual pcLiDAR returns is coherent with surface reflectance heterogeneity. Points scattered by citrus can still be recognized. In actual pcLiDAR data, solar noise can be reduced by special filters (e.g. etalon filter), and post-processing can also help. DART can provide information on solar noise and its spatial distribution for specific filtering per pulse.

5. CONCLUDING REMARKS

This paper is the second part of a paper that details the DART theory of single pulse LiDAR waveform simulation (Gastellu-Etchegorry et al., 2015b). It presents newly designed methods that

extend DART simulation functionalities to the simulation of actual multi-pulse waveform and photon counting wLiDAR and pcLiDAR systems in presence of solar noise. Multiple pulse simulations are illustrated with the cases of terrestrial and airborne LiDARs. Photon counting LiDAR data is simulated with a specifically designed statistical method that transforms DART simulated LiDAR waveforms. This method can also be applied to actual wLiDAR. LiDAR signals with solar noise are simulated with a method that combines the classical DART ray-tracking mode and the new LiDAR quasi MCRT mode. For that, the radiance image of a passive sensor is simulated with the ray tracking method, and the segmentation of this radiance image informs on the average radiance per pulse. In a following step, this average radiance is transformed into a number of solar photons per bin of waveform. The passive sensor is a pinhole camera for single pulse simulation and a linear pushbroom system or multiple beam system for multiple pulse acquisition. It constitutes a solution for the "2 sources - 1 sensor" configuration. These methodological improvements are applied to case studies with the aim to illustrate the potential of DART, while investigating common scientific questions. As expected, solar noise increases with the increase of the reflectance of Earth surfaces.

A major objective of our work is to make both pulse-by-pulse and comprehensive comparisons with actual data. All the examples of ALS multi-pulse simulation presented in this paper are based on regular scan pattern from rotating polygon (Figure 2(a)). Other regular scan patterns (Figure 2(c) and (d)) as well as other irregular patterns are not by default implemented in DART. Actually, in real-world LiDAR systems, all patterns are irregular. Non-straight platform path, platform fluctuation, error in positioning and look angle, and optical fibers used in pcLiDAR, etc… can be potential sources of any irregular pattern. In order to take these effects into account, we recently implemented a method to import and process information on the actual position (P_L) and orientation (Ω_L) of each pulse to simulate (Yin et al., 2015). For example, this information can be retrieved from the global navigation satellite system (GNSS) positioning for P_L and inertial measurement unit (IMU) for Ω_L in the CAO (Asner et al., 2012). Therefore, any scan pattern can be imported into DART, which serves as a preparation for pulse-by-pulse comparison with actual data. In future, other importations will be available, including temporal and spatial profile of each transmitted pulse, in order to better account the diversity between single pulses (none of them is exactly the same).

The new general-purpose LiDAR simulation tool that is implemented in DART can help to evaluate the influences of instrumental and experimental configurations on retrieved signals, and further help to develop inversion algorithms for specific current and future systems. For example, it can help in quantifying the sources of inaccuracy for retrieving biomass from LiDARs on board airborne (Popescu et al., 2011) and satellite (Montesano et al., 2015) systems.

DART is provided as free licenses for scientific research and education by Paul Sabatier University (http://www.cesbio.ups-tlse.fr/dart/license/en/index.php).

6. ACKNOWLEDGEMENT

This work was supported by the ANR in the frame of the FOLI3-D project and by the Centre National d'Etudes Spatiales (CNES) in the frame of the TOSCA projects 'Stem-Leaf' and 'Hypertropik'. Part of the work was conducted in the frame of the NASA project "DART-LiDAR". The authors are especially grateful to Bruce D. Cook, Douglas C. Morton, and Guoqing Sun from NASA's Goddard Space Flight Center for their suggestions in LiDAR configurations. The authors are thankful to all scientists who contributed to DART development since its first steps in 1992. The authors appreciate Pete Bunting and other scientists who contribute to the developments of SPDlib.

Appendix A: Nomenclature

Acronyms

ALS	Airborne Laser Scan.
ATLAS	Advanced Topographic Laser Altimeter System.
AtoMS	Airborne taxonomic Mapping System.
BRF	Bidirectional Reflectance Factor.
CAO	Carnegie Airborne Observatory.
DART	Discrete Anisotropic Radiative Transfer.
DEM	Digital Elevation Model.
FOV	Field Of View.
HDF	Hierarchy Data Format.
HIPlane	Horizontal Image Plane.
LiDAR	Light Detection and Ranging.
wLiDAR	waveform LiDAR.
pcLiDAR	photon-counting LiDAR.
MCRT	Monte Carlo Ray Tracing.
MABEL	Multiple Altimeter Beam Experimental LiDAR.
PRF	Pulse Repetition Frequency.
RTM	Radiative Transfer Model.
SIMPL	Swath Imaging Multi-polarization Photon-counting LiDAR.
SPD	Sorted Pulse Data.
SRMA	Scene Reference Minimum Altitude.
TLS	Terrestrial Laser Scan.

Symbols

$(\Omega, \Delta\Omega)$	Direction with unit vector Ω and solid angle $\Delta\Omega$.
A_t	LiDAR telescope area.
A_{swath}	Total covered area of swath on the SRMA plane.
$A_{E,rcp}$	Area of E_{rcp}.
C_{fp}, C_{FOV}	Circular footprint and FOV projected regions onto the SRMA plane, for nadir LiDAR (ALS).
c	Speed of light.
E_{ilm}, E_{rcp}	Elliptical footprint and FOV projected regions onto the SRMA plane, for oblique LiDAR (ALS).
f_s	Scan frequency within a recorded swath.
f_{dark}	Dark count rate.
g	Gain that converts waveform intensity unit from number of photons per bin $N_{ph,bin}$ into volts.
h	Plank's constant $6.62606957\ 10^{-34} m^2 kg/s$.
i, j	Indices of a LiDAR pulse.
$L_{i,j}$	Mean radiance of segmented FOV projected region (i,j) in the simulated passive sensor radiance image, for solar noise estimation.
N_p	Total number of pulses in a multi-pulse simulation.
N_{th}	Number of threads used in a multi-pulse simulation.

N_{bin}	Total number of recorded bins for a LiDAR pulse.
$N_{ph,bin}$	Number of received photons per bin.
$N_{ph,rcp,i,j}$	Total number of photons received for a pulse with indices {i,j}.
$N_{ph,SN,i,j,bin}$	Number of "solar noise" photons per waveform bin for LiDAR pulse with indices {i,j}.
n_s	Number of pulses per scan.
O_C, O_E	Center of C_{fp}, C_{FOV} and E_{ilm}, E_{rcp} (ALS).
p	Random generated number ($0 < p < 1$).
$P_L(x, y, H)$	LiDAR position with altitude H.
P_{conv}	LiDAR reception convergent point.
P_Q	LiDARQuantum efficiency (probability to detect a photon in a single-photon detector).
$P(\Delta t)$	LiDARProbability to detect a photon in a time period Δt for a single-photon detector.
$R_{i,j}$	LiDAR associated reflectance for pulse with indices {i,j}.
r_t	LiDAR telescope radius.
r_{fp}, r_{FOV}	Radii of C_{fp} and C_{FOV} (ALS).
$r_{\perp,ilm}$, $r_{\parallel,ilm}$	Short (perpendicular) and long (parallel) radii of E_{ilm} (ALS).
$r_{\perp,rcp}$, $r_{\parallel,rcp}$	Short (perpendicular) and long (parallel) radii of E_{rcp} (ALS).
t_{min}, t_{max}	Start and end record time of waveform.
t_{dead}	LiDARDead time of a single-photon detection.
t_{pc}	Modeling of time flow during functioning of a pcLiDAR.
V_{bin}	Recorded digital number per bin in wLiDAR data.
$V_{off,bin}$	Recorded electric offset per bin in actual wLiDAR data.
$V_{max,bin}$	Maximum voltage per bin.
v_p	Platform speed.
β_{fp}, β_{FOV}	Half divergence angle of LiDAR footprint and FOV.
$\lambda, \Delta\lambda$	Central wavelength and bandwidth of a band in a simulated system.
Δd	Total distance of recorded swath along platform track (ALS).
δd_s	Distance step between scans along platform track (ALS).
δd_{bin}	Photon path distance per stored wLiDAR bin or pcLiDAR acquisition.
Δt	Time period.
δt_{bin}	Time step per stored wLiDAR bin or pcLiDAR acquisition.
ρ_p	Density of pulses (ALS).
θ	Zenith angle.
θ_L	LiDAR look angle (ALS).
$\theta_{L,max,scan}$	Maximum look angle on a scan side (system-based; not swath-based).
$\Delta\theta_{L,swath}$	Look angle range difference within a recorded swath (ALS).
θ_{tls}	Zenith angle for terrestrial LiDAR orientation (TLS).
θ_{sun}	Solar zenith angle.
$\Delta\theta_{tls}$	Zenith angle range (TLS).
$\delta\theta_{tls}$	Zenith angle scan step (TLS).
$\delta\theta_L$	Look angle step between pulses in a scan (ALS).

ϕ	Azimuth angle.
ϕ_p	Platform track azimuth angle (ALS).
$\overrightarrow{\phi_p}$	Horizontal axis along ϕ_p (ALS).
ϕ_s	Cross-track scan azimuth angle (ALS).
$\overrightarrow{\phi_s}$	Horizontal axis along ϕ_s (ALS).
ϕ_{off}	Offset between angle perpendicular to ϕ_p and ϕ_s (ALS).
ϕ_{tls}	Azimuth angle for terrestrial LiDAR orientation (TLS).
ϕ_{sun}	Solar azimuth angle.
$\Delta\phi_{tls}$	Azimuth angle range (TLS).
$\delta\phi_{tls}$	Azimuth angle scan step (TLS).
$\Delta\omega$	Solid angle through which O_E sees the LiDAR telescope.
$\overrightarrow{\Omega_L}$	LiDAR orientation. It depends on (θ_L, ϕ_s) for ALS.

Appendix B: DART multi-pulse output data format

There are 4 records in the multi-pulse output data format:

1. Text Version Record. It stores the text header (e.g., version number).
2. Format Description Record. It stores DART input parameters: flag for wLiDAR or pcLiDAR product, precision format (4-byte float or 8-byte double), scanning pattern, and flags that indicate the optional presence of first-order scattering waveform, not convolved waveform and file that stores radiation statistics (scattered, absorbed, lost energy) per atmosphere-Earth segment.
3. Global Parameters Record. It stores global parameters to all pulses: time step (δt_{bin}) and distance step (δd_{bin}) represented by each bin, total number of recorded bins per pulse (N_{bin}), total number of simulated pulses (N_p), etc.
4. Data Record. It stores the data for all pulses. Thus, data recording of each single pulse is iterated N_p times. For each pulse, there are 5 sub-records:
   4.1. Parameter Sub-Record: configuration{P_L, $\overrightarrow{\Omega_L}$, i, j} per pulse. Begin time of each waveform (t_{min}) is also recorded to locate the starting position of each waveform. The associated waveform end time (t_{max}=$t_{min} + \delta t_{bin} \times N_{bin}$) can be calculated because N_{bin} is known.
   4.2. Waveform Sub-Record: number of photons per LiDAR bin. Thus, the sub-record length depends on N_{bin} and on the above defined precision format.
   4.3. - 4.6. Other Sub-Records: first-order waveform, waveform before Gaussian convolution and radiation statistics. These optional records are specified in the Format Description Record. The format of radiation statistics is omitted in Table B1. It is given in the DART user manual (Gastellu-Etchegorry, 2015).

Table B1. Data format of multi-pulse output binary file. Words in bold letters are variables which are used in the specification of stored data formats. Records marked with * are optional parameters defined by the user.

Record / Byte	Format	Description
1. Text Version Record		
1---50	char	Product type specifier = "DART_SIMULATED_LIDAR_WAVEFORM_VERSION_N.NN"
39---42	char	Version number = “N.NN” (i.e. 1.00, 1.01, ..., 1.10, ..., 2.00)

2. Format Description Record		
1---4	unsigned int	Lidar data type: (default: 0) 0: laser scanning data; 1: photon counting data
5---8	unsigned int	Scanning type: (default: 1) 0: not applicable; 1: spinning polygon; 2: sawtooth pattern; 3: sinusoidal pattern; 4: ellipsoid pattern.

9	bool	If the waveform record format is float (true) or double (false).
		true: **nbyte**=4; **wformat**=float;
		false: **nbyte**=8; **wformat**=double;

10	bool	If the unconvolved waveform is written (**ifNonconv**)
11	bool	If the first-order-scattering waveform is written (**lf1order**)
12	bool	If the statistical information is written (**ifStatinfo**)
3. Global Parameters Record		
1---8	double	Time step of each bin
9---16	double	Distance step of each bin
17---20	unsigned int	Number of bins for each convolved waveform (**nConv**)
21---24	unsigned int	Number of bins for each non-convolved waveform (**nNonconv**)
25---28	unsigned int	Total number of pulses (**N**)
4. Data Record (Totally ***N*** repetitive records)		
4.1. Prameter Record		
1—8	double	look angle (in rad) (from -pi/2 (left) to pi/2 (right))
9---24	double * 2	Incident angles: theta, phi (in rad)
25—48	double * 3	Incident unit distance: x, y, z (in meter)
49---72	double * 3	Platform position: x, y, z (in meter)
73---80	double	Beginning time of the convolved waveform
81---88	double	Beginning time of the non-convolved waveform
89---92	unsigned int	Number of bins from sensor to center of FOV
93---96	unsigned int	Pulse index i
97---100	unsigned int	Pulse index j
4.2. Convolved Waveform Record		
1 --- (***nConv**nbyte***)	***wformat* * *nConv***	Lidar convolved waveform
*4.3. First-Order Convolved Waveform Record (exist ***if1order*** == *true*)		
1 --- (***nConv**nbyte***)	***wformat* * *nConv***	Lidar first-order convolved waveform (it does not exist if ***if1order*** *is false*)
*4.4. Non-Convolved Waveform Record (***ifNonconv*** == *true*)		
1 --- (***nNonconv**nbyte***)	***wformat* * *nNonconv***	Lidar non-convolved waveform (it does not exist if ***ifNonconv*** *is false*)
*4.5. First-Order Non-Convolved Waveform Record (***ifNonconv*** == *true and* ***if1order*** == *true*)		
1 --- (*nNonconv*nbyte*)	***wformat* * *nNonconv***	Lidar first-order non-convolved waveform (it does not exist if ***ifNonconv*** *or* ***if1order*** *is false*)
*4.6. Statistics Record (**ifStatinfo** == true)		
1 --- (9+41***nbyte**)	……	Statistics Record (it does not exist if ***ifNonconv*** *or* ***ifStatinfo*** *is false*)

Chapter 5

In-flight fusion of imaging spectroscopy and LiDAR multi-sensor system

This chapter presents the a novel functionality through combination of Chapter 3 and Chapter 4.

Multi-sensor systems are increasingly demanding in recent airborne RS applications. They usually provide data which are combined by measurements of several active or passive devices, which reflect the properties of the Earth's landscape through various perspectives. These devices share the same sensor acquisition geometry which facilitate the fusion of their data.

Combination of waveform LiDAR and imaging spectrometers is an emerging technique used by several recent airborne systems, including CAO (Asner et al., 2012, 2007), G-LIHT (Cook et al., 2013), and NEON AOP (Kampe et al., 2010), etc... The combined data provide both functional and structural information, which makes this technique a unique tool for understanding and management of the Earth's ecosystems.

The rapid development of this technique urgently demands the simulation and validation of these combined data. Nowadays, several radiative transfer models can partially simulate spectrometer data or laser ranging and detection (LiDAR) data with limitations. The fusion of their simulated data has not been completely addressed due to theoretical and experimental bottlenecks of these models. In this chapter, we introduce a new combined method to simulate realistically large-scale data fusion which combined waveform LiDAR and imaging spectrometer, with any experimental, instrumental, and geometrical configurations of systems. This method benefits from the fact that DART is currently an unique model that can simulate data of both imaging spectrometry with multi-view configuration (Chapter 3) and waveform LiDAR with multiple pulses (Chapter 4). The fusion process acts on the data simulated by these two modes under the condition that geometrical configuration of the sensors are the same. Actually this method is an extension from the solar noise estimation algorithm presented in Section 3.1. Simulated data examples are presented with configurations of currently existing airborne devices based on both urban and forest landscapes. The dimensionality of principal components are analyzed on the fusion data. The results in this chapter verify that high-quality realistic data can be simulated and combined by DART for potential application and preparation of current and new multi-sensor systems.

5.1 Article: In-flight fusion for simulated data of airborne imaging spectrometer and waveform LiDAR multi-sensor system through DART model

In-flight fusion for simulated data of airborne imaging spectrometer and waveform LiDAR multi-sensor system through DART model

Tiangang Yin, Jean-Baptiste Feret, Jean-Philippe Gastellu-Etchegorry*, Nicolas Lauret

Centre d'Etudes Spatiales de la BIOsphere - CNES, CNRS, IRD, UNIVERSITE DE TOULOUSE
18 avenue. Edouard Belin, bpi 2801, 31401 Toulouse cedex 9, France
**jean-philippe.gastellu-etchegorry@cesbio.cnes.fr*

Abstract

Multi-sensor remote sensing system is capable to integrate several passive and/or active devices which share the same acquisition geometry to facilitate the combined use of their data. Fusion of light ranging and detection (LiDAR) and imaging spectroscopy is an emerging technique that combines both functional and structural information for understanding and management of the Earth's ecosystems. Nowadays, several radiative transfer models (RTMs) can partially simulate imaging spectroscopy and/or LiDAR data. The simulation of their combined data has not been completely addressed due to the constraints caused by both theoretical and experimental bottlenecks of these models. The discrete anisotropic radiative transfer (DART) model is capable to simulate both satellite and airborne spectrometer images and LiDAR waveforms with multiple pulses for any instrumental, geometrical and experimental configurations. A novel approach of using DART to simulate and combine multi-sensor airborne data with realistic configurations is presented here. The fusion process is based on a technique in which the LiDAR points are back-projected to the image plane of spectrometer through same sensor geometrical configurations. Examples of similar configurations as the Carnegie Airborne Observatory (CAO) for both urban and forest landscapes are presented. A selection of principal components is then analyzed for each sensor to evaluate the in-flight fusion technique on the simulated data. The results in this paper shows that DART becomes a powerful tool which simulates realistic data for validation of current and future multi-sensor systems.

Keywords: radiative transfer, DART, fusion, imaging spectroscopy, LiDAR, multi-sensor system, principal component analysis

1. Introduction

Remote sensing is an increasingly used source of data for the study of forest ecosystems. Spatial and temporal estimations of key biophysical and biochemical variables help understand local and global interactions between phenology, photosynthetic activity, ecological processes, climate changes and various other dynamic processes (Asner and Vitousek, 2005; Asner et al., 2006). Multi-sensor fusion becomes an emerging trend in the progression of current RS technologies due to the complementarity of information derived from each type of devices. Indeed, instead of processing information retrieved through different sensors

separately, data fusion techniques consist in the combination of multiple sources to obtain improved information. The data fusion framework is rich of a variety of techniques, the success of which relying at the first place on the accuracy of the registration/data alignment.

Imaging spectrometer and LiDAR data are essentially complementary to each other, which helps estimating both constitution and structure of the Earth's ecosystem. Imaging spectroscopy is a passive remote sensing (RS) technique which measures upwelling spectral radiance value per pixel, combining both emitted and reflected components. In the spectral domain from visible (VIS) to short wave infrared (SWIR), the reflection from solar and atmospheric radiations is predominant. When acquired under appropriate conditions, the recorded reflected radiometric signals from an imaging spectrometer provide information about the biophysical and biochemical properties of the Earth's ecosystems (Asner, 1998; Ustin et al., 2004). LiDAR is an active RS device using the time of flight technique, which records reflected laser pulse signals to retrieve the positions of scatterers. LiDAR data can be used to infer 3-D structure of vast landscapes through measurements of multiple pulses (Lefsky et al., 2002). The fusion of imaging spectrometer and LiDAR is a particularly active field of research (Asner et al., 2008; Dalponte et al., 2008, 2012; Féret and Asner, 2012). Previous works show that the fusion of hyperspectral and airborne laser scan (ALS) data can significantly improve the dimensionality of information obtained from Principal Components Analysis (PCA) (Asner et al., 2012) and accuracy of tree species classification (Dalponte et al., 2008; Mundt et al., 2006).

In order to facilitate data registration and fusion, multi-sensor systems are recently preferred. Hence all the sensors share the same acquisition geometry over comparable swath region. The so-called in-flight fusion method is adapted during data acquisitions on multi-sensor systems Asner et al. (2007). Airborne platforms are commonly accepted for their flexibility, relative low cost and high spatial and temporal resolution, so they are the primary choice for the calibration and validation of in-flight data fusion. Several Imaging Spectrometer and LiDAR Multi-sensor Systems (ISLMS) have been employed in airborne RS, including Carnegie Airborne Observatory (CAO, Asner et al. (2007, 2012)), National Ecological Observatory's Airborne Observation Platform (NEON AOP, Kampe et al. (2010)), and NASA Goddard's LiDAR, Hyperspectral and Thermal Airborne Imager (G-LIHT, Cook et al. (2013)). The sensors that are integrated in these systems include small-footprint scanning full-waveform LiDAR (wLiDAR), hyperspectral pushbroom sensor with spectral bands ranging from 400nm to 2500nm, as well as thermal infrared sensors for measuring temperature (only with G-LIHT). The rapid development of the ISLMS requires accurate and efficient simulation tool of a variety of data acquisitions, in order to validate data of current systems, identify limitations, and evaluate possible future systems.

Radiative transfer models (RTMs) are appropriate tools to simulate radiation propagation and interaction within the Earth's landscape based on physical processes. They are intensively used to simulate radiance for any given sun and observer geometry, thus radiometric properties such as bidirectional reflectance factor (BRF), albedo, as well as waveform of single LiDAR pulse, over simulated media of various complexity. The inversion of RTMs also is applied to measured RS data to retrieve biophysical and biochemical characteristics of observation area. The fusion of imaging spectrometer and LiDAR through RTM has not been completely addressed before. It was evaluated by Koetz et al. (2007) through combination of 2 different RTMs: 2-D GeoSAIL model (Koetz et al., 2007) for imaging spectrometer

simulation and a 3-D LiDAR waveform model developed by Sun and Ranson (2000). This method demonstrates the synergistic parameters retrieval, but the data simulation was limited to unrealistic conditions, including constrained description of simulated scene, large footprint wLiDAR with only first-order scattering signal, and single pulse per simulation. Furthermore, the combination of two independent models (in 2-D and 3-D, respectively, and developed by 2 institutes) induces extra difficulties for unification. Other than synergistic parameter retrieval per acquisition, another application of fusion is the systematic analysis of combined large-scale data to study the biodiversity of the Earth's ecosystem. To date, no single RTM that is open to the scientific community can efficiently simulate large-scale RS image and points retrieval from thousands or millions of wLiDAR pulses with consideration of realistic sensor geometry.

In order to simulate such data for ISLMS, several prerequisites have to be satisfied :

1. The model must work with 3-D heterogeneous scenes for both for imaging spectrometer and LiDAR configurations. Especially for wLiDAR simulation, photon tracking in 3-D space is essential for accurate waveform retrieval including multiple scatterings and the preliminary products are 3-D profiles.
2. The model must simulate reflectance images of the scene. Some of the existing RTMs can only calculate the reflectance of the whole simulated scene, which in many cases limits the pixel-wise validation with RS acquisitions, especially with high spatial resolution RS data. The reflectance must be accurately calculated per pixel based on each local content in the simulated landscape.
3. The model must consider varying view direction per pixel in a sensor image acquired by an imaging spectrometer, i.e., the sensor geometrical projection model. It is typically the case for RS systems such as pushbroom sensors with wide field of view (FOV). Parallel-perspective projection must be considered for linear pushbroom sensors (Gupta and Hartley, 1997; Chai and Shum, 2000; Zhu et al., 2004).
4. The model must simulate LiDAR waveforms of multiple pulses efficiently with various footprint size and consider the multiple scatterings especially in near infrared: Points (usually less than 10) can be extracted from each recorded waveform in ALS. Decomposed point cloud from multiple pulses is one of the primary products of ALS. Generally speaking, the density on the ground for ALS is about 1-20 pulses per m^2, and a scenes size that exceeds $100m \times 100m$ is common for certain types of application. The simulated ALS data should be capable to be processed into point cloud, by using state-of-art LiDAR data processing techniques.
5. The model must be capable to project locations of all LiDAR pulses at the image of pushbroom sensor, thus the registered data can be combined for fusion.

Most of theses prerequisites are quite challenging for many existing RTMs. Simulation tools which can fully satisfy all these prerequisites do not exist in previous works.

The Discrete Anisotropic Radiative Transfer (DART) model (Gastellu-Etchegorry et al., 1996, 2004, 2012) has satisfied most of theses requirements. DART has been developed since 1992, and becomes one of the most functional, comprehensive and accurate 3-D RTMs ((Pinty et al., 2004; Widlowski et al., 2007)) for simulating RS data from VIS to thermal infrared band and radiative budget of the Earth's landscape. It can simulate images of heterogeneous scenes (radiance value/reflectance/brightness temperature) with atmosphere

coupling (Grau and Gastellu-Etchegorry, 2013) through orthographic projection. Recently, a new approach, the so-called convergent tracking and perspective projection (CTPP) is introduced into DART, in order to simulate passive sensor images with a finite FOV through perspective projections (Yin et al., 2015b). DART simulates LiDAR waveform by using an approach called Ray Carlo method (Gastellu-Etchegorry et al., 2015a). This method also is extended into efficient multi-pulse simulation for both airborne and terrestrial laser scan systems (Yin et al., 2015a).

This paper presents a novel approach which combines the recent implementations in DART to simulate both data and in-flight fusion of ISLMS systems. The hyperspectral sensor images and wLiDAR data which are separately simulated in DART are linked in this approach. The ultimate objective of this approach is to simulate ISLMS data of any configuration, with the same quality as actual-acquired data. Two types of fusion process are illustrated:

1. The output of multi-pulse LiDAR simulation is converted into an industrial LiDAR data format for storage of waveform data, the sorted pulse data format (SPD, Bunting et al. (2013b)). The associated open-source library SPDlib (Bunting et al., 2013a) is used to process the data into point cloud. The retrieved point cloud is registered with simulated hyperspectral pushbroom sensor images. Examples of the combined points are demonstrated for both urban and vegetation landscapes.
2. In the case of vegetation landscape, processings aiming at extracting spectral features (PCA), identifying tree species (classification) and estimating biophysical properties (regression models for biophysical parameters) are applied to the simulated data cube (stacking of hyperspectral images and retrieved time-gated images from LiDAR waveforms). Classification and regression results are discussed to validate the improvements by the fusion process.

2. Review on DART simulation of passive sensor image and multi-pulse LiDAR

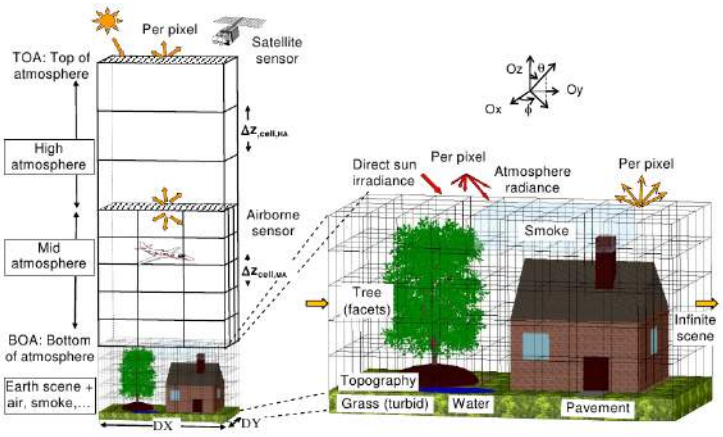

Figure 1: DART scene system

DART is a 3-D RTM which simulates ray propagation and interaction within Earth-atmosphere system, in spectral domain ranging from VIS to SWIR band. The implemen-

tations of DART which are used in simulating imaging spectrometers are briefly presented in this section, including the construction and parametrization of the simulated scene, ray tracking within the scene, and algorithm for image generation and projection. Readers are invited to refer to Gastellu-Etchegorry et al. (2004, 2012, 2015b) for more details.

2.1. Scene system and ray tracking method

The construction of a 3-D heterogeneous scene in DART is based on the division of the Earth-atmosphere system into cells (volume elements) of varying sizes and properties. Figure 1 shows an illustration of a simulated scene system made up of different types of cells. The 3 domains (the high atmosphere, the mid atmosphere, and the Earth's scene) are discretized into cells with different specific sizes for the sake of computational efficiency and contribution of each domain. Triangles and turbid media are the basic elements in each cell that constitutes the Earth's scene. They give rise to surface and volume interactions with rays, respectively. Atmosphere, vegetation, and any other type of fluid can be described as a turbid medium with specific properties such as aerosol density, vegetation leaf area index (LAI), leaf angle distribution (LAD), chlorophyll content, etc..., The attenuation of a ray in turbid mediums follows Beer's law. On the other hand, surfaces such as roofs, and walls of houses, trunks and branches of trees, foliar elements or part of them, as well as defined topography, can be represented using triangle formalism, with each triangle being defined by its precise location in 3-D space. They give rise to surface interactions. Their properties are specified with specular/isotropic/anisotropic reflectance, direct/isotropic transmittance, absorption, etc.... They are used to for calculating ray interactions at the boundaries of surfaces.

DART uses the so-called Ray Tracking method to simulate propagation of rays. In a steady state, for a ray $\vec{I}(r, \Omega_n)$ propagating along direction $\vec{\Omega}_n$ with radiant flux $I(\Omega_n)$, the 3-D discrete radiative transfer equation is repetitively solved:

$$\bigtriangledown \cdot \vec{I}(\Omega_n) = -\alpha(\Omega_n) I(\Omega_n) + J_e(\Omega_n) + \sum_{m=1}^{N} \alpha_d(\Omega_m) \frac{P(\Omega_m \rightarrow \Omega_n)}{4\pi} I(\Omega_m) \Delta\Omega_m \qquad (1)$$

where α is the total extinction coefficients of absorption and scattering ($\alpha = \alpha_a + \alpha_d$); $J_e(r, \Omega_n)$ is the emitted radiant flux along $\vec{\Omega}_n$; the summation term is the numerical integration of each incoming flux $\vec{I}(\Omega_m)$ along direction Ω_m which are scattered towards $\vec{I}(\Omega_n)$; $\frac{P(\Omega_m \rightarrow \Omega_n)}{4\pi}$ is the scattering phase function from Ω_m to Ω_n of the participating medium. In DART, any number N of discretized directions over the 4π space are pre-computed (Yin et al., 2013). $\frac{P(\Omega_m \rightarrow \Omega_n)}{4\pi}$ of all permuted directions combinations are as well pre-computed for each participating medium.

Ray tracking method in the Earth scene is divided into illumination step and scattering step. During the illumination step, both the solar radiation (through solar direction) and atmosphere radiations (through downward discrete directions) are calculated. They are tracked from the top faces of the cells at the top of the Earth scene (bottom of the atmosphere). Radiations are tracked along their associated directions until they are intercepted or absorbed. The scattering step is an iterative process running until convergence is reached. In each iteration, previously intercepted rays are scattered and tracked towards all the N discrete directions over the 4π space, according to the pre-calculated phase functions. These

rays are either absorbed, or intercepted to be scattered in the next iteration. For each iteration, the directional radiance images and the exitance of the simulated scene are recorded. Convergence is reached when the total exitance of an iteration is less than a given threshold. DART products are calculated by extrapolation of the last 3 iterations before convergence.

2.2. Simulation of passive sensor images

For each iteration during ray tracking, if a scattered ray reaches the top of a simulated scene, its power and its source scattering element area are projected along its associated direction onto a horizontal image plane (HIPlane). The HIPlane is a mesh grid with defined size, where areas of grids represent pixels comprising images for each direction on the HIPlane. The altitude of HIPlane is chosen to be at the scene reference minimum altitude (SRMA), which is either 0 for the scene without digital elevation model (DEM), or the lowest altitude of an imported DEM. At the SRMA, the HIPlane is co-registered with the georeferenced coordinate system of the simulated scene in DART. The radiance value generated by the ray are distributed to each occupied pixel with the proportion of the projected area within each pixel. The number of images on the HIPlane equals the total number of defined upwards directions in a simulation. Since projected images on the HIPlane are created for each direction, a direction-image bijection map is used in DART to store the images associated to their directions. In addition to the discrete directions that sample the 4π space, DART allows another kind of pre-defined direction, the so-called virtual direction. Virtual directions can be arbitrary defined with their zenith and azimuth angles. Rays scattered along a virtual direction (virtual rays) undergo interceptions as those along the other discrete directions, except that the intercepted virtual ray can not be scattered, thus the total energy is conserved. Therefore, virtual direction is purely used for calculation of reflectance and generation of images along an arbitrary direction.

For simulation of images, there are 3 types of projection simulated in DART: orthographic projection, perspective projection, and parallel-perspective projection. Orthographic projection is applied for images which are bijected to pre-defined directions. It is based on an assumption that the directions of all rays which generates a radiance image are parallel. The average pixel values of the HIPlane gives the reflectance of the scene along that direction. This corresponds to the BRF product, which in reality, is calculated by a region of RS images where divergence of the view angles within sensor FOV can be neglected. The orthographic projection is classically used in the previous DART releases. The convergent tracking and perspective projections (CTPP) method has been recently introduced (Yin et al., 2015b). It combines 3-D RTM with 3-D perspective projections, to simulate images specifically to imaging spectrometers with finite FOV. This method makes DART adapted with acquisition geometry configurations of general sensors, including classical perspective projection for cameras, and parallel-perspective projection for pushbroom sensors. For pushbroom sensor configuration, there are 2 key horizontal axes to consider: the platform direction, and the cross-track direction. They are usually perpendicular. The convergent point of radiations depends on the position of the scattering object. With known horizontal trajectory, the convergent point coordinates are determined from the intersection of the cross-track plane passing through the object and the trajectory path. Along the trajectory, parallel (orthographic) projection is adapted. Otherwise, along cross-track plane, perspective projection is

adapted. The projection orientation of a pushbroom sensor is usually selected to be horizontal, so the image on the HIPlane can be directly considered as the realistic raw image. With the CTPP approach, DART can simulate original pushbroom sensor images with any number of bands. Usually, these original images have to be orthorectified for RS applications. However, for purpose of fusion, original images are directly used, since orthorectification can induce loss of geometrical projection information for each pixel.

2.3. Single- and multi- pulse data simulation of waveform LiDAR

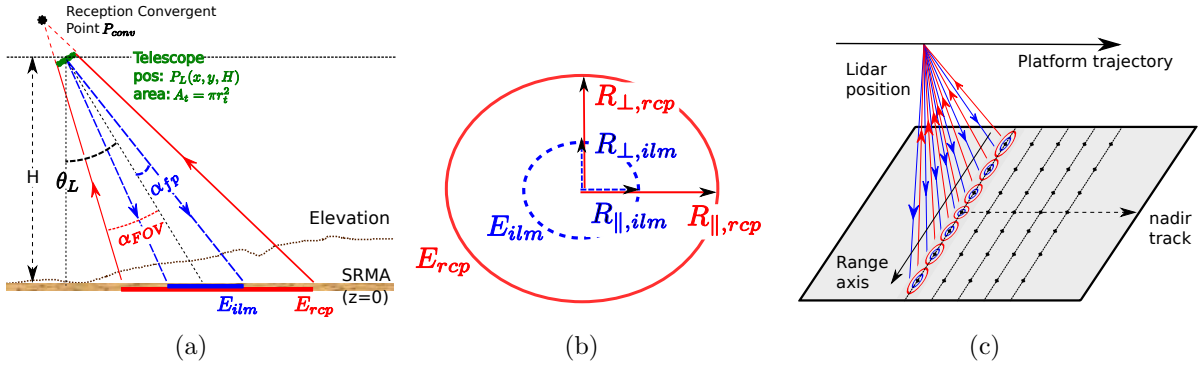

Figure 2: Geometries for single- and multi- pulse ALS simulation in DART. (a) LiDAR geometrical configuration and variables for a single pulse simulated in an ALS simulation (oblique view). (b) Projected region on the SRMA plane by footprint (blue dashed ellipse) and FOV (red solid ellipse). (c) Geometrical configuration and distribution of the scan pattern on the SRMA plane for an optical polygon rotation mirror in ALS. Black dots indicates the pulse center on the SRMA plane.

The approaches which are used to simulate wLiDAR data in DART are generally reviewed in this section. For details of single- and multi- pulse simulation and validation of LiDAR in DART, one is advices to refer to Gastellu-Etchegorry et al. (2015a); Yin et al. (2015a). DART is capable to simulate LiDAR pulse at any altitude with any LiDAR orientation and any footprint/FOV configurations (Figure 2). Figure 2(a) illustrates geometrical configuration of a LiDAR pulse in a DART simulation. For a scanning ALS device, the generated laser pulses are reflected by rotating/oscillating mirrors to direct pulses through various directions. The source of transmitted photons is considered to be located at $P_L(x, y, H)$ (width of beam is neglected at the exit of laser generator), which is also considered to be the LiDAR position. It also represents the location of the reception telescope, with radius r_t and area $A_t = \pi r_t^2$. Footprint and FOV are constant parameters for each LiDAR device which are represented by half dispersion angle α_{fp} and α_{FOV} respectively. All parameters above are the fixed instrumental parameters of a LiDAR device defined in DART. α_{fp} and α_{FOV} give rise to elliptical projected regions on the SRMA plane when the LiDAR has an oblique viewing angle θ_L. The elliptical projected regions of illumination and reception on the SRMA are represented by E_{ilm} and E_{rcp} respective in the scene's coordinate frame (Figure 2(b)). The details for calculating the short (perpendicular) radii ($R_{\perp,ilm}$ and $R_{\perp,rcp}$) and the long (parallel) radii ($R_{\parallel,ilm}$ and $R_{\parallel,rcp}$) are elaborated in Gastellu-Etchegorry et al. (2015a).

To simulate a LiDAR waveform, DART uses a quasi- Monte Carlo Ray Tracing (quasi-MCRT) method to simulate photon transportation within simulated scene. Actual number

of photons carried by a LiDAR pulse is unmanageable in terms of computational load. The concept of simulated photon is introduced in DART to represent every discrete energy that is launched from a laser generator. The simulated photons are launched from P_L towards E_{ilm} on the SRMA plane. They are continuously tracked until they are absorbed or their experienced order of scattering is larger than a defined number. Random number generation is frequently applied during photon interactions (i.e. transmission, interception, absorption, and scattering) with scene elements. When a simulated photon is scattered from an element, if the scattering position is inside the FOV of the LiDAR, a ray along a virtual direction (virtual ray) is created at the scattering position towards the sensor. The virtual ray is considered to reach the sensor by multiplying its energy by the direct transmittance of the path from the element to the sensor. The distance of this path is added to the photon propagation distance. With this method, almost every scattering event within the FOV cone volume gives rise to a measured signal propagation time. This method significantly reduces total number of launched simulated photons. The speed of simulation can be reduced to less than 0.001 seconds in certain cases which is far beyond current performance of any traditional Monte Carlo method. In DART, all photons are assumed to be launched at the same time, and the simulated signal is convolved with temporal profile of launched LiDAR pulse. The LiDAR signal from atmosphere is also simulated in the current version of DART.

In reality, wLiDAR devices for RS applications have pulse repetition frequencies up to 100's KHz. Rotation polygon mirror system (Shan and Toth, 2008) is implemented in multi-pulse simulation of DART. As illustrated in Figure 2(c), such system has a scan pattern which consists of a series of parallel lines of footprint and FOV on the ground plane. ALS system has geometrical configuration which is similar to the pushbroom sensor acquisitions (Section 2.2). Two axes are considered: the azimuth axis (platform trajectory direction), and the range axis (direction of parallel lines pointing to the right side of platform). The rotation velocity of the mirror and the speed of platform are both assumed to be constants, then geometric configuration of each pulse (Figure 2(a)) can be derived (P_L and θ_L). α_{fp} and α_{FOV} are both constant for the configuration of each pulse. According to the scan pattern of the parallel lines, each pulse is specified by 2-D indices (i, j). i is the scan index along the azimuth axis, and j is the pulse index of each scan along the range axis. Waveforms are simulated for each pulse, and they are stored in a binary file with their corresponding geometrical parameters and pulse indices. Since processing for each pulse are independent, multi-threading technique is introduced to accelerate the speed of multi-pulse simulation. With N_p parallel threads, the processing time is reduced by N_p times.

In order to process the simulated data into point cloud, the output binary file of multiple pulses is converted into an industrial LiDAR data format, the SPD format (Bunting et al., 2013b). SPD is specially designed store large set of the waveforms using hierarchy data format (HDF5) compound data type. The number of photons per bin N_b in industrial LiDAR format by setting a proper ratio (gain) g, where $C_b = N_b \times g$. The associated processing tool, SPDlib (Bunting et al., 2013a), supports Gaussian decomposition to generate point cloud from waveform data. For each pulse, multiple points can be generated, depending on detected number of Gaussian profiles. Theses points are ordered from nearest distance to farthest distance, where the first return usually represents the canopy position and the last return usually represents the ground position. The pulse indices (i,j) are preserved during the whole process, so the retrieved points are surjectively mapped to each pulse index.

3. In-flight fusion of simulated ISLMS data

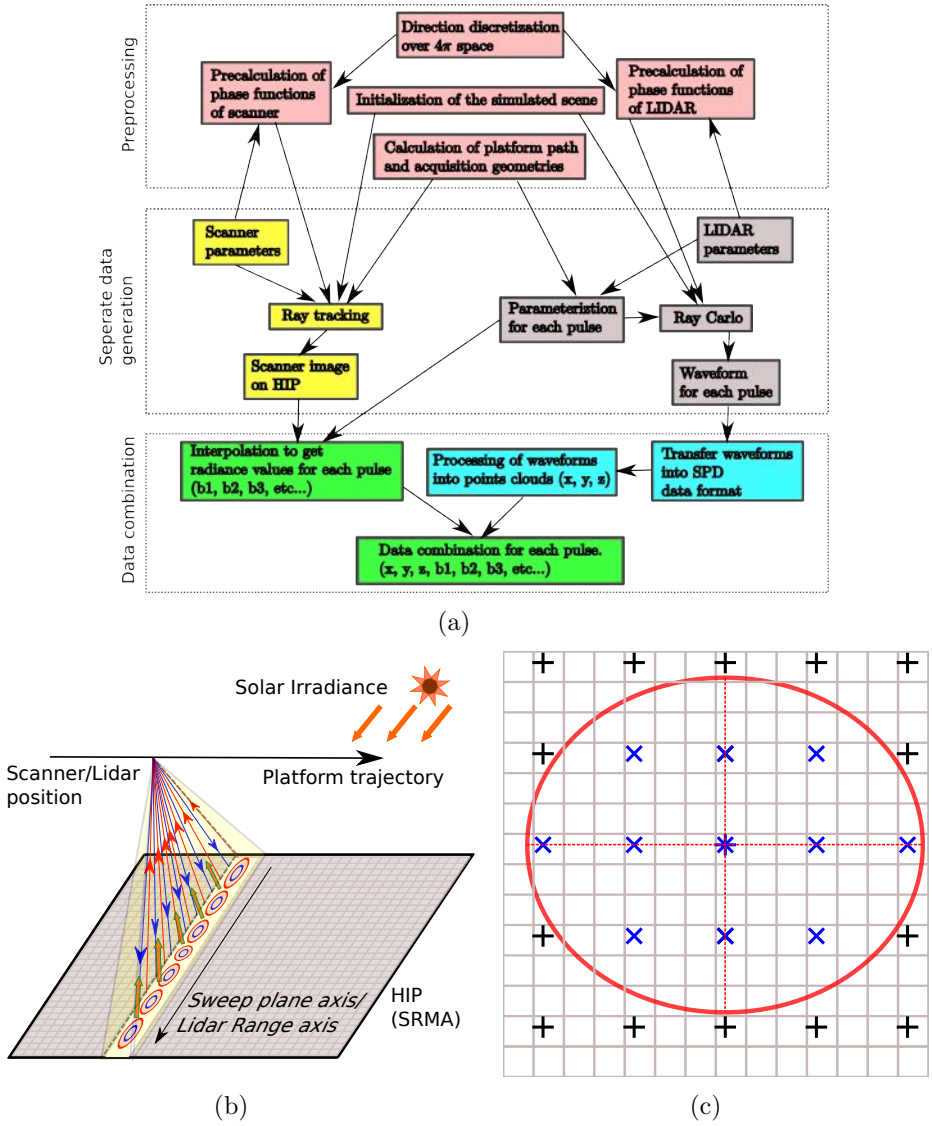

Figure 3: Data combination of imaging spectrometer and wLiDAR multi-sensor system. (a) The flow chart of the whole process. (b) Acquisition geometry diagram. (c) Interpolation diagram to retrieve the corresponding radiance value within wLiDAR FOV. The grid represents radiance image pixels on the HIPlane; the red ellipse is the FOV region on the HIPlane; '*' is the center of the FOV; ×s are points inside the FOV that can be selected for interpolation; +s are the points outside the FOV which are excluded in calculation.

The two streams of DART to simulate pushbroom sensor image and multi-pulse LiDAR data are linked for fusion of ISLMS.

3.1. Process chain

The acquisition geometry for ISLMS is illustrated in Figure 3(b). It can be summarized as 2 illumination sources (sun and wLiDAR) and 2 reception sensors (pushbroom imaging

spectrometer and scanning wLiDAR). The same platform path and acquisition geometry is shared by the 2 sensors. The cross-track plane of the pushbroom sensor and the range axis of the wLiDAR (rotating polygon system) are aligned. Figure 3(a) shows the workflow of ISLMS data fusion process in DART, which contains 3 stages:

1. Preprocessing. In this stage, pre-defined discrete and virtual directions are generated; simulated scene is initialized; platform path and cross-track plane/range axis are parameterized. These inputs are shared by both pushbroom sensor and wLiDAR simulation. The scattering phase functions according to the illumination source incident direction are separately calculated for pushbroom sensor and wLiDAR.
2. Separate data simulation. The preprocessed inputs are separately passed to simulations of pushbroom sensor and wLiDAR. The pushbroom sensor simulation gives multi-angle original images on the HIPlane, while the wLiDAR simulation gives a binary file which stores multi-pulse waveforms. During the wLiDAR simulation, the parametrization and acquisition geometry (Figure 2(a)) is calculated for each pulse. E_{rcp} are retrieved from the stored acquisition geometries for each pulse. They are temporarily stored.
3. Data combination. The HIPlane which stores the unorthoredtified image is also located at the SRMA, and thus is registered with DART coordinate system, a connection can be build between each pulse to the radiance images on HIPlane. Therefore, HIPlane is the rendezvous node for the outputs from the 2 streams. Figure 3(c) illustrates this connection, where the background grids are the pixels of a simulated image on the HIPlane. The position of the blue $\star$ represents the center of E_{rcp} from the stored output in Stage 2, which is not necessarily located at the center of a pixel on the HIPlane. Thus, radiance values are calculated by cubic spline interpolation of the HIPlane radiance images on the blue $\star$. These values are assigned to the pulse indices of the LiDAR simulation. To be more accurate, several points ($\times$ in Figure 3(c)) can be derived from the blue $\star$ along short and long axes of the ellipse in equal separation, where blue $\times$s are inside the ellipse and red $\times$s are outside the ellipse. So the radiance value assigned to the pulse is the average interpolated radiance values at the blue $\times$s. The radiance images of pulse indices are then added to the data cube generated by pure wLiDAR. The output wLiDAR file can also be converted into SPD format and processed by SPDlib into point cloud, with surjective map from 3-D points to 2-D indices of each pulse still being preserved. Until this step, the data are combined.

3.2. Registration of digital images with LiDAR point cloud

Figure 4 illustrates an example of multi-pulse wLiDAR simulation over the city center of Toulouse, France. The scene is a subregion of the urban database from CAPITOUL experiment (Masson et al., 2008). Table 1 provides the instrumental parameters setting of simulated small-footprint wLiDAR, and Table 2 provides the platform and acquisition configuration. Figure 4(a) illustrates the geometry of acquisition. The wLiDAR platform passes through the center of the scene at an altitude of $300m$ and the LiDAR orientation range is from $-39.8°$ (left view) to $39.8°$ (right view) over the whole scene. The density of points that are retrieved by SPDlib ($3.924/m^2$) is not much larger than the density of pulses ($3.711/m^2$), because majority components of the scene are buildings and topography, which mostly give rise to a unique single return per pulse. Multiple returns are retrieved only

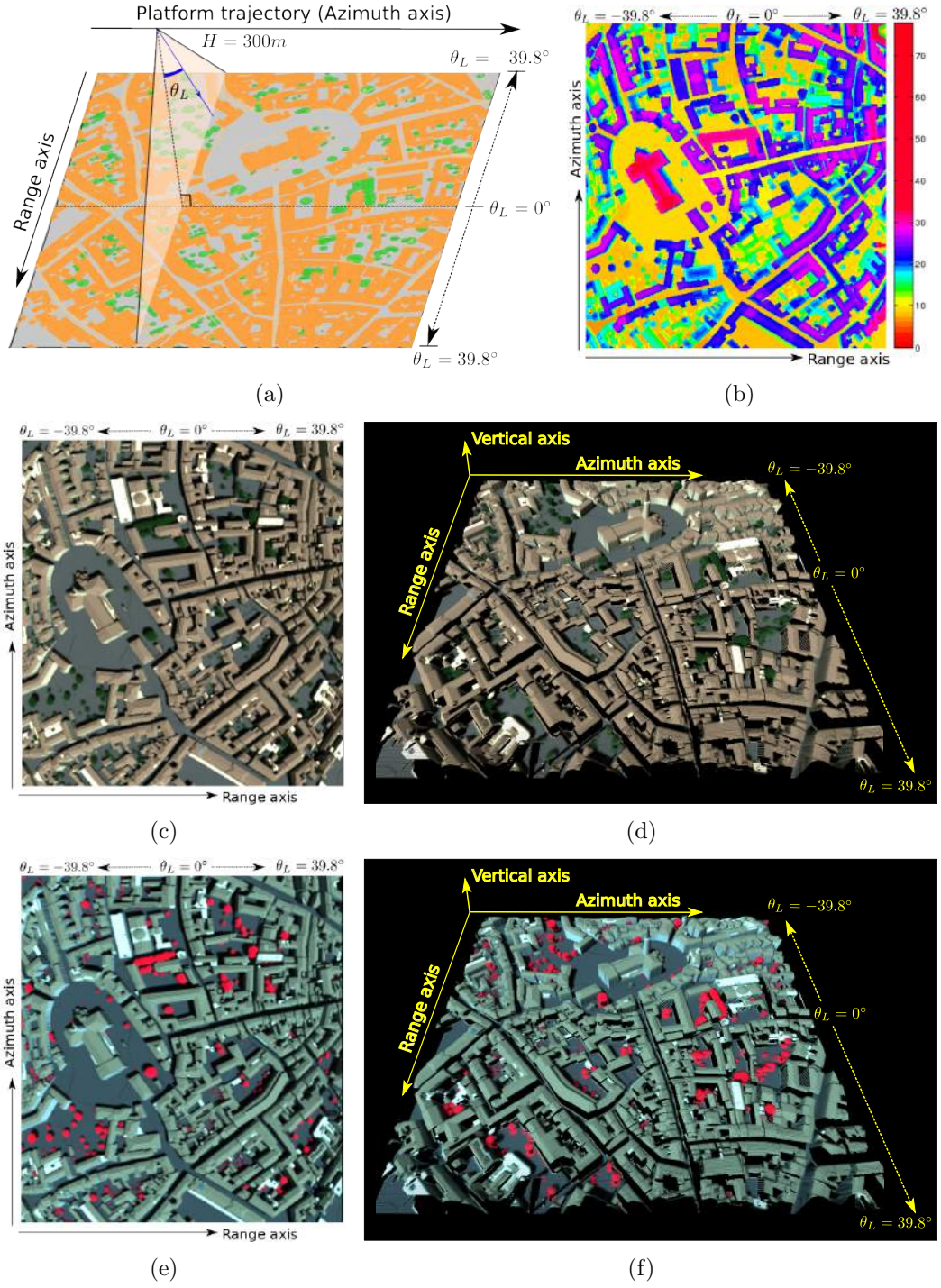

Figure 4: ISLMS data combination of the simulated scene of Toulouse city center (France). (a) Geometrical configuration of the ALS simulation over the scene. (b) Image of elevation of retrieved first returned point for each pulse, with range index as horizontal axis, and azimuth index as vertical axis. (c) and (e): Layers of true and false color composites of interpolated radiance value on the HIPlane for each pulse. (d) and (f): 3-D visualization of LiDAR point cloud with true and false color composite on each point.

Table 1: LiDAR instrumental configuration for multi-pulse simulation

Parameters	Value
Wavelength	$1064nm$
Bandwidth	$10nm$
Energy of each pulse	$1mJ$
Acquisition rate	$1ns$
Pulse duration at FWHM	$2ns$
Telescope area (A_t)	$0.1m^2$
Dispersion footprint (α_{fp})	$0.00025°$
Dispersion FOV (α_{fp})	$0.0004°$

Table 2: LiDAR platform and acquisition configuration for multi-pulse simulation over city center of Toulouse

Parameters	Value
Platform altitude (H)	$300m$
Viewing angle range	$(-39.8°, 39.8°)$
Separation of lines	$0.5m$
Separation of viewing angle	$0.0015rad$
Number of scanned lines	1001
Number of pulses per line	927
Total number of pulses	927927
Density of pulses	$3.711/m^2$
Total number of points	981065
Density of points	$3.924/m^2$

when a footprint is partially intercepted by the edge of the a roof and a surface underneath, or by tree crowns. Figure 4(b) presents an image with pulse indices (1001×927 pixels), in which pixel values give the height of the first return (highest return) for each pulse. It generally present the urban canopy structure from processed LiDAR points. The horizontal and vertical axes of the image indicate the range and azimuth indices. The pixels actually are not equally spaced in the horizontal direction. Some walls of buildings are observed from both sides of the platform path, including the walls on the left side facing right, and the walls of the right side facing left, where left-view and right-view LiDAR orientations are applied, respectively.

The wLiDAR simulation of Toulouse city center is combined with pushbroom sensor simulation. Four bands of pushbroom sensor original images on the HIPlane are simulated: 450nm 550nm 650nm and 850nm, with bandwidth of 10nm. Interpolations on the HIPlane are applied on the centers of reception ellipses for each LiDAR pulse. The true-color and false-color images associated to the corresponding pulse indices are generated from the data combination stages above (Figure 4(c) and 4(e)). The horizontal and the vertical axes of the layers represent the azimuth index and the range index, respectively. These layers are exactly registered to the first return height layer (Figure 4(b)) product of LiDAR simulation. Majority of rays which enter the sensor came from the canopy of the scene, so the patterns of these layers are also registered with the first return height layer. Walls are also seen on both side of the platform path. The walls facing right are presented on the side with negative θ_L, but missing on the side with positive θ_L, because they are not viewed by the sensors (same as in Figure 4(b)).

In addition to the data cube of the 4 bands of pushbroom sensor, the wLiDAR products

based on each pulse can be added as superimposed layers. The possible LiDAR products may include the first return height (proved to be the most useful attribute in classification in Dalponte et al. (2008)), the number of returns, apparent reflectance, count per bin of waveform (used in Asner et al. (2012)), etc.... All of them can potentially increase the data dimensionality comparing to purely pushbroom sensor data. The radiance values can be further assigned to the retrieved points of each pulse through the point-to-indices surjective map. 3-D visualizations of the LiDAR point cloud with true/false color composition assigned to each point are displayed in Figure 4(d) and 4(f). which is similar to the actual CAO data presented in (Asner et al., 2007) by the CAO.

3.3. Analysis of data cube generated with hyperspectral images and time-gated waveform images: application to forested areas

The airborne acquisition of LiDAR and imaging spectrometer data with metric spatial resolution allows improved performances of tasks such as species identification and linkages between biological diversity and environmental factors such as microtopography (Féret and Asner, 2014b). Understanding the interactions between incoming light and these complex ecosystems is the key for a correct interpretation of remotely sensed data (Morton et al., 2014). In this perspective, physically-based radiative transfer models are increasingly being used, allowing detailed 3-D description of vegetation and realistic simulation of remotely sensed data. Some research focus on the absolute accuracy of simulations when compared to experimental acquisitions, which involves an extremely detailed scene to identify the relative contribution of each element to the simulated radiometric signal at fine spectral and spatial scale (Schneider et al., 2014a,b). On the other hand, the maturity and computational efficiency of radiative transfer codes allow building sensitivity studies to estimate how viewing conditions, vegetation properties and instrumental characteristics globally influence the radiometric signal (Morton et al., 2014). Here our goal is to illustrate the possibilities offered by DART simulations for ecological and environmental applications. Therefore we focus on two applications: species classification of emerging trees and biophysical variable estimation, which in our case is the LAI.

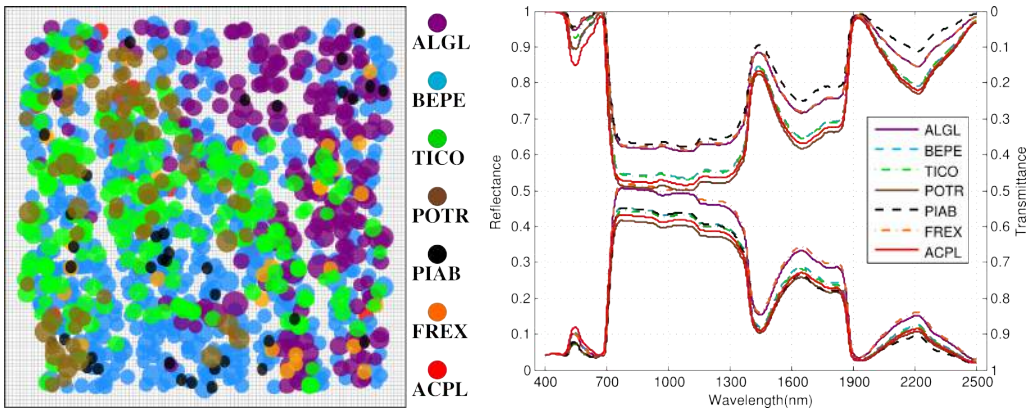

(a) (b)

Figure 5: Simulation of Jarvselja birch stand test site. (a) Location distribution of the tree species. (b) The optical property of leaf facets for each tree species.

We use DART to simulate both hyperspectral and full waveform LiDAR data based on a 3-D representation of a plot proposed by the RAMI-4 canopy experiment. This plot corresponds to the test site of Jarvselja birch stand (Estonia) in summer. The simulated scene ($110m \times 110m$) consists in a total of 18 importable tree objects, distributed between seven tree species summarized in Table 3. These imported objects are made of facets representing leaves, branches and trunks generated from actual measurements. For each tree species, between one and five 3-D objects are derived from actual measurements and used to build the scene. Species represented by more than one object correspond to dominant species emerging from the canopy. The spatial distribution of species in the scene is illustrated in Figure 5(a). Three species are particularly dominant in the upper canopy and represent a large majority of the emerging species : ALGL, BEPE and POTR. Each species is defined by a unique set of leaf optical properties (reflectance and transmittance), and each leaf is considered as a Lambertian scattering element. These leaf optical properties are initially provided by RAMI for 19 bands ranging from visible to near infrared. Our hyperspectral simulations require a finer spectral sampling over a broader spectral domain, so we estimated leaf structural and chemical properties for each species using PROSPECT inversion Feret et al. (2008) (Table 3), and further provide full-spectrum leaf-level optical properties, from $400nm$ to $2500nm$ with $1nm$ spectral sampling (Figure 5(b)). The absence of SWIR data provided for the initial leaf optical properties does not allow reliable estimation for EWT and LMA. However the main purpose of this scene is to illustrate DART simulations, and the exactness of the leaf optical properties corresponding to each species is not critical. To conclude about the tree representation, within-species variability of leaf optical properties is not taken into account, whereas within-species variability of structure and other physical parameters, such as crown dimensions, LAI and LAD, is partly taken into account for dominant and emerging species (Table 3, NBIO$>$ 1).

Once the simulated scene is prepared, all the leave facets are converted into turbid cell with dimension of $0.25m \times 0.25m \times 0.5m$. The LAI and LAD are calculated separately within each cell. The branches and trunks are embedded within the turbid cells. The parameter settings for the ISLMS are based on the configuration described for the CAO. For hyperspectral configuration, a total of 210 spectral bands are simulated from $405nm$ to $2495nm$, with spectral resolution of $10nm$ and bandwidth of $10nm$. The instrumental configuration of wLiDAR is the same as shown in Table 1. Table 4 gives the platform and acquisition configuration.

In this case, sensor altitude is set to $1000m$, so the viewing angle range is relatively small with the center at NADIR Figure 6 illustrates the elevation and number of returns derived from the point cloud extracted from SPDlib. Unlike the previous example of Toulouse city center, the density of extracted points ($20.598/m^2$) is significantly larger than the density of pulses ($7.891/m^2$), since multiple pulse returns corresponding to tree crown, branches, trunk and eventually ground can be recorded during the penetration of each laser through the canopy. The wLiDAR data is converted to time-gated data cube of digital numbers (209 overlapping images of digital numbers for the corresponding bins over various pulses). The distance represented by each bin is 15cm, so totally a vertical distance of approximately 31.35m is recorded. Prior to classification and regression tasks, we reduced the dimensionality of the data with a feature extraction method. We expect our scene to contain most of the information necessary for our tasks in a limited amount of latent features, due to

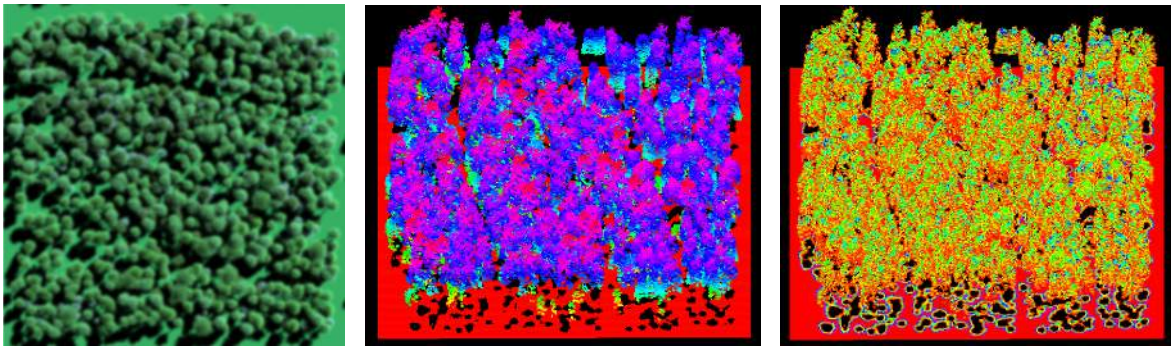

(a) (b) (c)

Figure 6: Primary simulated results of of Jarvselja birch stand test site before fusion. (a) Pushbroom sensor image of RGB band combination (b,c) Simulated LiDAR point cloud. (b) Elevation. (c) Counts number.

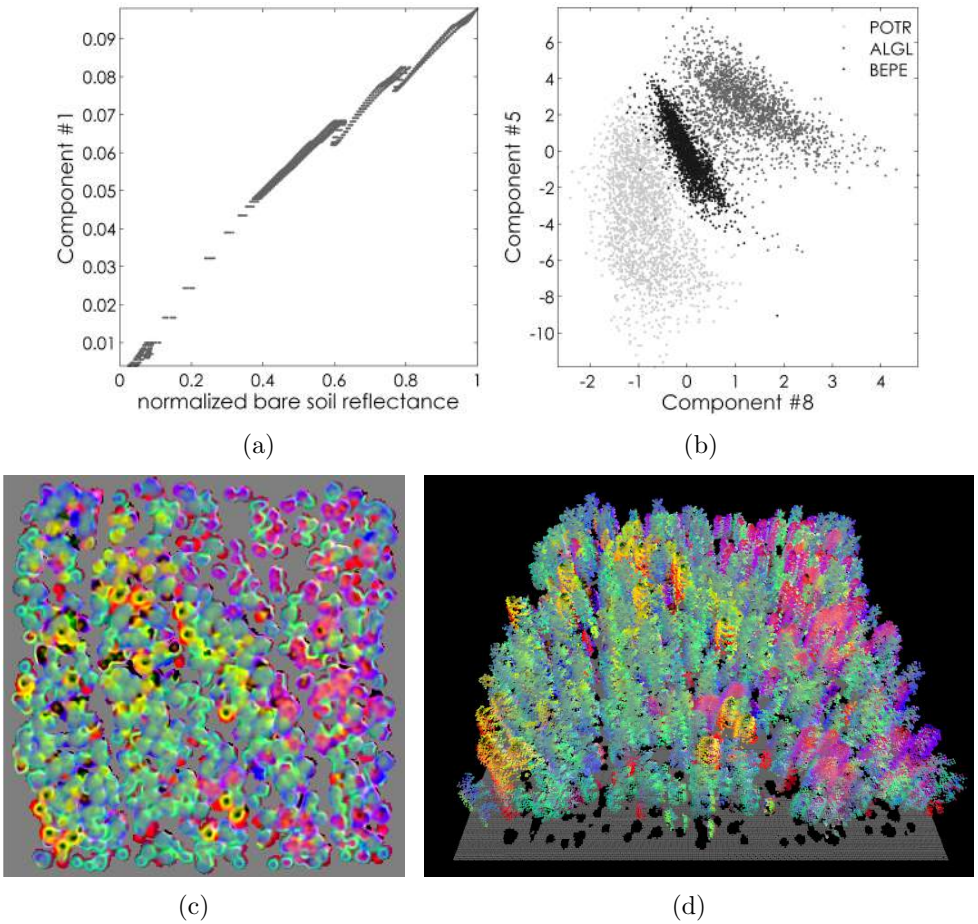

(a) (b)

(c) (d)

Figure 7: (a) Relationship between the normalized bare soil reflectance and the first principal component. (b) RGB Color composition of components 8, 5 and 4. (c) 3-D mapping of subfigure (d) by combination with LiDAR point cloud.

Table 3: Species in the test site of Jarvselja birch stand and corresponding biochemical parameters used for leave facets. (NBIO=number of importable objects, THPO=tree height per object, LSP=leaf structure parameter, CHL=chlorophyll concentration, CAR=carotenoid concentration, EMT=equivalent water thickness, LMA=leaf mass per area)

Species	Acronym	NBIO	THPO (m)	LSP	CHL (g/cm^2)	CAR (g/cm^2)	EWT (cm)	LMA (g/cm^2)
Alnus Glutinosa	ALGL	4	19.35 22.58 25.76 27.09	1.971	60.402	12.531	0.015	0.01235
Betula Pendula	BEPE	4	19.86 25.49 27.99 30.51	1.518	45.294	9.975	0.015	0.01
Tilia Cordata	TICO	5	5.91 11.27 14.41 18.34 20.70	1.486	62.998	13.538	0.015	0.01040
Populus Tremuloides	POTR	2	25.27, 30.49	1.324	52.848	11.627	0.015	0.01
Picea Abies	PIAB	1	10.90	1.818	72.791	13.152	0.01833	0.02150
Fraxinus Excelsior	FREX	1	13.72	2.038	65.489	10.601	0.015	0.01145
Acer Platanoides	ACPL	1	15.37	1.407	34.937	8.386	0.015	0.01

Table 4: LiDAR platform and acquisition configuration for multi-pulse simulation over test site of Jarvselja birch stand

Parameters	Value
Platform altitude (H)	$1000m$
viewing angle range	$(-2.862°, 2.862°)$
Separation of lines	$0.35m$
Separation of viewing angle	$0.0035rad$
Number of scanned lines	309
Number of pulses per line	309
Total number of pulses	95481
Density of pulses	$7.891/m^2$
Total number of points	249241
Density of points	$20.598/m^2$

the low biophysical and biochemical variability in the scene. Principal Component Analysis is a widespread unsupervised feature extraction method, following the postulate that the greater the variance, the greater the contribution to the representation. The selection of the components derived from PCA and the interpretation of the information they contain is not trivial: higher contribution of a component to the global variance of the scene does not allow to conclude that this component contains appropriate information for any given information. Although PCA is not the most appropriate method to study phenomena that cause subtle differences in target reflectance (Thenkabail et al., 2011; Wang and Chang, 2006), it has been used to reduce dimensionality of hyperspectral data and proved its ability to extract relevant information for vegetation studies such as biodiversity mapping (Féret and Asner, 2014a). In our study, we mask the pixels corresponding to bare soil and performed a PCA on both LiDAR and hyperspectral data. A quick analysis of the results of the PCA shows that only two components contribute to more than 99.9 percents of the total variance of the radiometric signal measured in the scene. Although low dimensionality was expected after PCA, such value is important. After analysis of the score of the first

component, we noticed a very strong signal corresponding to the contribution of the soil. Figure 7(a) shows the relationship existing between the scores of the first component and the normalized reflectance of pixels corresponding to bare soil. The first component then allows detecting pixels with strong radiometric influence of the soil. Therefore the varying properties of vegetation only contribute to a very minor part of the radiometric variability. The results obtained for LiDAR data show that the contribution to signal variance is distributed among a more important number of components: 34 components are required to explain 99 percent of the variability. This can be explained by a more diverse vertical variability. This vertical variability, evidenced by the PCA applied to LiDAR data, has a moderate impact on the variability of the spectral information measured by the hyperspectral sensor. We then perform a backward feature selection for classification and regression problems in order to identify the most relevant spectral components for each analysis.

1. Classification. We select pixels corresponding to each of the three main emerging species (ALGL, BEPE and POTR), avoiding mixed pixels. Linear Discriminant Analysis is used for classification, with 20 samples of each species used to train the classifier, and 2,000 samples per species then used to test the classifier. The backward feature selection performed on the 30 first components obtained from hyperspectral data shows that only six components are required to identify the three main species with more than 99 percent accuracy. These components are ranked as followed by decreasing discriminant power: 8, 5, 4, 3, 6, 7. After visual inspection, the second component which has very low discriminant power, corresponds to changes in illumination of the scene. This result confirms experimental observations. Figure 7(b) shows the distribution of the three dominant species in a 2-dimensional space corresponding to component 8 and 5, and Figure 7(c) displays a colored composition of the three most discriminant components (3-D display of combination with LiDAR point cloud on Figure 7(d)). The comparison with Figure 5(a) shows strong similarities in the distribution of spatial patterns: trees with yellow color in Figure 7(c) and Figure 7(d) correspond to POTR, while trees in purple correspond to ALGL and trees in blue correspond to BEPE. In the case of LiDAR data, the classification accuracy is not as good as for hyperspectral data, reaching 90 percent correct identification with seven component, and a maximum accuracy of 91.3 percent with 13 components. This can be partly explained by the fact that the vertical profile corresponding to a pixel identified based on the corresponding emerging species is not specific to that species, because of the presence of vegetation understorey.
2. Regression. We build a Partial Least Square regression model for the estimation of LAI. We first selected pixels in order to obtain a subset with uniform LAI distribution, then randomly selected 50 samples for training and 2,000 samples to test the model. to avoid overfitting, we chose the number of latent vectors to include in the regression model with respect to the minimum root mean squared error in cross-validation. As for classification, we performed backward feature selection using the 30 first components obtained from hyperspectral data and LiDAR data. Unlike classification, regression performed with PCA results obtained from hyperspectral and LiDAR data showed similar performances: six components from hyperspectral data and ten components from LiDAR data were necessary to obtain a regression model with close to optimal perfor-

mances (RMSE=1.24 and R^2=0.66 for hyperspectral data, RMSE=1.20 and R^2=0.67 for LiDAR data). The model derived from hyperspectral data shows a well described saturation of the estimated LAI for high values (Zhang et al, 2000; Haboudane et al., 2004) (Figure 8(a)). Such saturation appears to be milder when using LiDAR data to build a regression model (8(b)). LiDAR and multispectral fusion have been used for the estimation of various variables from forested ecosystems such as tree height (Popescu and Wynne, 2004) or timber volume (Tonolli et al., 2011). In our case, we combined the two regression models by averaging the estimated LAI from each regression model, which resulted in improved estimation of LAI, as showed in figure (8(c)), with RMSE decreasing to 1.01 and R^2 increasing to 0.77.

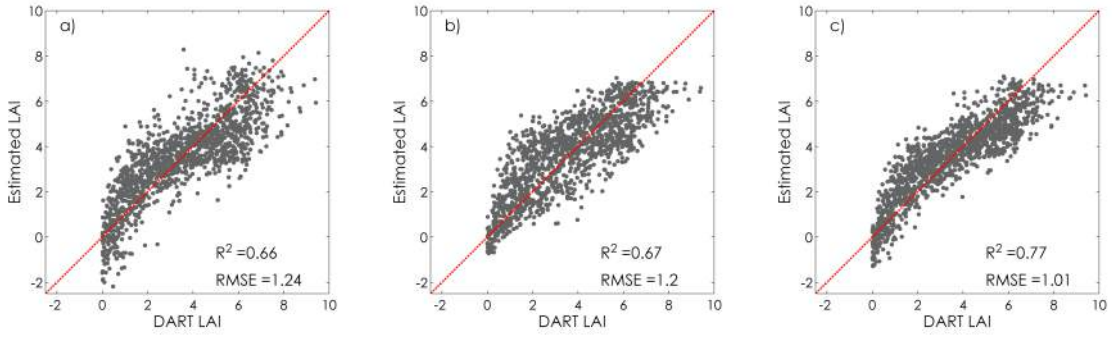

(a) (b) (c)

Figure 8: Estimation of LAI using a PLS regression model built with (a) 6 components of a PCA image derived from hyperspectral information, and (b) 10 components of a PCA image derived from LiDAR information; (c) LAI estimation averaged from the two regression models.

The relatively scattered results obtained for LAI estimation are explained by the relatively high LAI variability included in the 3-D scene, which is more realistic than the variability in leaf optical properties.

4. Conclusion, and prospect

The DART functionality of in-flight fusion for ISLMS through combination of multi-pulse LiDAR simulation and pushbroom sensor radiance image simulation, is presented in this paper. The workflow as illustrated in Figure 3(a) has been implemented in the latest release of DART (Version >= 5.5.0), with user-friendly interface. Two practical cases were studied in this paper, the first one focusing on urban environment, and the second one focusing on a forested ecosystem.

In the case of forested ecosystem, hyperspectral and LiDAR simulations were analyzed and PCA was applied to extract information and reduce dimensionality. These preliminary results showed that the radiometric signal corresponding to different components of the scene, such as soil properties, illumination effect and signal corresponding to tree species could be identified from the components derived from the hyperspectral image. We succeeded in applying methods routinely used to study vegetation such for applications such as species

identification and estimation of biophysical properties such as LAI, derived from both LiDAR and hyperspectral simulations. Although purely illustrative and simplistic compared to real situations (particularly for the definition of the optical properties of the scene), these results meet our expectations, providing a promising basis for further studies focusing on studying complex natural ecosystems. This new functionality of the DART model offers the possibility to explore the potential of sensor fusion for the monitoring of various vegetation variables, as well as the uncertainty they are associated with.

The ultimate objectives of our work are to create realistic system-based simulated data which can be pixel-wisely or pulse-wisely compared with actual acquisition, and to develop and assess new data processing algorithm which can be applied to actual data. The cases investigated in this paper are based on the default DART settings of parallel scan lines for both pushbroom sensor and wLiDAR, which is valid for whiskbroom pushbroom sensor, pushbroom sensor and LiDAR using rotating polygon to redirect laser pulses, etc... Actually, the scan pattern from actual data acquisition is irregular, which makes it difficult for data adaptation. For example, the oscillating mirror system in some LiDAR devices produces saw-toothed or sinusoidal scan patterns. Nonlinear platform path, fluctuation and oscillation can potentially produce any pattern of irregularity. In order to account for irregular patterns, DART support importation of a file which contains the platform position, and direction for each acquisition in both pushbroom sensor image and wLiDAR simulation. These information are usually available with actual data through devices like the global navigation satellite system (GNSS) and inertial measurement unit (IMU) (Asner et al., 2012). However, a more difficult part is the precise reconstruction of a simulated scene. If that can be achieved, combination of precise parameters in both instrument and experiment can possibly make realistic simulated data.

A similar approach is applied to simulate background solar noise of LiDAR device, which can play an important role especially for photon counting devices during day time acquisition (Yin et al., 2015a). It is achieved by setting the accompanied pushbroom sensor with the same band and bandwidth as the LiDAR, thus the radiance captured in the reception of pushbroom sensor for each pulse can be converted to number of photons per LiDAR acquisition bin. Therefore, temporal and localized solar noise can be assigned to each pulse in a multi-pulse LiDAR simulation. Case studies are presented in another work.

In addition, the ill-posed problem is one of the most common problems in RS data fusion. It can be easily implemented with defined or statistically random shift of reception ellipse center as illustrated in Figure 3(c). Actually, the fusion approach presented in this paper is not limited to in-flight fusion of multi-sensor systems. It can be expanded to a general fusion approach for sensors from different systems, by defining separate paths for each system. All these works are currently in progress.

5. Acknowledgement

Jean-Baptiste Féret was funded by the CNES/TOSCA program.

Conclusion and perspectives

This dissertation presents my contributions since 2011 for improving radiative transfer in the Earth surfaces and the atmosphere, with aim to improve the simulation of remote sensing signals from spectroradiometer and Lidar devices and also the radiative budget of natural and urban Earth surfaces. This improvement was conducted with the Discrete Anisotropic Radiative Transfer (DART) model. The four main chapters present separately the four research domains of my work. These domains are very much related to each other.

Each chapter ends with conclusive remarks that are directly related to the research domain of the Chapter. Here, the objective is to stress the relations between these domains and to give more general conclusion and remarks.

Chapter 2 introduces a new direction discretization and oversampling method, the so-called iterative uniform squared discretization (IUSD), for general radiative transfer modeling. The method focuses on the restriction of the squared shape and optimized selection of the centroid of each angular sector that sample the spherical surface of the 4π space. Algorithms for generating both uniform and cosine-weighted distribution of discrete directions are presented. Results shows that the discretization method provides more accurate and fast-convergent results compared with traditional methods, and the oversampling method gives precise results with high resolution for strongly anisotropic simulated scene (e.g. hot spot, specular surface, urban canyon radiative balance etc...). A major advantage of the IUSD is that it produces precise results with a rather small total number of directions. The application of the IUSD is not limited in RTMs for remote sensing field. For example, the heat transfer field could also benefit from this approach, which actually used to have more discussions in this domain. The concept of virtual direction is developed in order to generate reflectance/radiance result along a flexible pre-defined direction. A ray traveling along a virtual direction (a virtual ray) does not contribute to any further scattering event. The virtual direction concept is the prerequisite for both passive sensor simulation through a finite FOV (Chapter 3), and the Ray Carlo method (Chapter 4) in LIDAR waveform simulation.

Chapter 3 presents a method that combines perspective projection with 3D RTM, the so-called converging tracking and perspective projection (CTPP), to simulate sensor images with finite FOV. The pre-defined virtual direction concept presented in Chapter 2 is extended to the automated steering virtual direction (ASVD). The ASVDs are not pre-defined. Their directional vectors change during ray tracking, according to the vector from scattering/emission element position towards the sensor position. The simulated sensor image stores spectral radiance per pixel. These radiance values depend on

the position-to-sensor directional reflectance. Simulation of cameras (through perspective projections) and cross-track imager (through parallel-perspective projections) are both presented. Examples are illustrated including video captured by a drone, regional hot spot effect on a sensor image, as well as the variation of reflectance between airborne and spaceborne measurements (sub-pixel shadow effect), etc. The image generated by this method makes it possible to have pixel-wise comparison with other simulated images or actual data. An iterative technique is developed to import the platform track and view direction to derive the view direction for each element within a simulated scene. Thus, this technique makes DART output well adapted to comparisons with actual data. The DART simulated images are compared with the Airborne Prism Experiment (APEX) hyperspectral data. This comparison illustrates important improvements compared with past works, in which images were simulated through orthographic projection along the average view direction of the swath. The CTPP method proved to be very useful for estimating solar noise in LIDAR signals (Chapter 4), and also for LIDAR and imaging spectroscopy image fusion (Chapter 5).

Chapter 4 presents how DART simulates LIDAR data. A new mode of quasi Monte Carlo Ray Tracing (quasi-MCRT) is designed to simulate photon propagation in the Earth's scene. Based on that, 2 new approaches, the so-called Box method and Ray Carlo method, are implemented to provide robust simulation of LIDAR waveform with any geometrical configuration, any footprint size, any simulated landscape, and any atmosphere distribution. The box method discretized the probability of a scattering phase function into a large number of boxes through usage of computer memory, and each scattering event is simulated by random selection of box instead of a series of tedious calculations in the traditional MCRT models. It optimizes and enormously accelerates the selection of scattering direction of a photon during interaction with materials of anisotropic properties. The Ray Carlo method brings DART traditional ray tracking into Monte Carlo simulation. For each scattering event occurs within the LIDAR FOV, a virtual ray (Chapter 2) is directly sent back to LIDAR through a ASVD (Chapter 3), and contribute to the total waveform. The Ray Carlo method increases the significant signals received by a LIDAR with reduced number of initially launched simulated photons. Simulated waveforms are validated with reflectance value generated by traditional ray tracking mode of DART. An approach to simulate LIDAR signals in atmosphere is also presented to avoid the discontinuous signals at the boundaries of the layers. The quasi-MCRT method for simulation of single-pulse waveform is extended to multi-pulse simulation for both airborne laser scan (ALS) and terrestrial laser scan (TLS). The parameterization for ALS simulation is quite similar to the scanner as presented in Chapter 3. An advantage of this implementation is that the simulated waveforms for both ALS and TLS can be converted into industrial data format and processed by real-world data processing software. Furthermore, a method is designed to convert the simulated LIDAR waveforms into data of photon counting system by modeling the acquisitions of single photon detector. In addition, solar noise in LIDAR signal, in presence of atmosphere, is modeled through the combination of LIDAR waveform simulation and radiance image simulation from passive sensors with finite FOV (Chapter 3). It corresponds to a system with two sources (solar radiation and LIDAR pulses) and one sensor (LIDAR telescope). It is implemented in an user-friendly manner. The field of view

(FOV) projected regions on the ground image plane are segmented from the simulated radiance image of multi-view sensor. Through estimation of the average radiance within the FOV projected regions on the ground image plane, the number of photons per unit time that is recorded by the sensor is calculated. As expected, results show that solar noise plays a more important role in photon counting systems than in waveform LIDAR systems. As view direction importation presented in Chapter 3, LIDAR position and orientation for each pulse can also be imported with available data from actual measurement. This facilitates the comprehensive multi-pulse comparison with actual data, in future.

In Chapter 5, the 2 sources and 1 sensor system presented in Chapter 4 is extended to simulate the in-flight fusion technique which is used in many existing LIDAR and hyperspectral multi-sensor platforms (e.g. Carnegie Airborne Observatory, Goddard's LIDAR, Hyperspectral and Thermal Imager, etc...). The hyperspectral images and the LIDAR data are simulated with algorithms presented in Chapter 3 and Chapter 4, respectively. The FOV projected region of each pulse is exactly registered with the segmented average radiance. An image cube is created with superimposition of bands provided by both LIDAR and hyperspectral imaging spectrometer. The dimensionality of principal components are analyzed on the fusion data. This work validates the acquisition principals of several existing multi-sensor systems.

In addition to these new functionalities, multi-thread parallelization in also introduced in both ray tracking and LIDAR mode of DART. This helps DART to efficiently simulate large-scale data without waiting for several days of running the simulation.

DART model was surely the most complete radiative transfer model before my work. It is even more complete now, and work continues in DART team in order to bring new major improvements. A few prospective works are mentioned below. Some of these works already started in DART team at CESBIO, but also in other laboratories and centers such as NASA (GSFC, USA) and RSL (University of Zurich, Switzerland).

1. The IUSD of uniform and cosine-weighted distribution of directions can be compared with each other or other approaches to find the optimized direction discretization method in RTMs for remote sensing applications.

2. Image simulation of passive sensors with finite FOV, for further pixel-wise comparison on the at-sensor radiance over much larger scenes (e.g., 5 km x 5 km) with more varying view directions over the simulated scene, and with atmosphere coupling. This work is currently in progress through collaboration with Remote Sensing Laboratory of Zürich University, for the case of mountain forests.

3. An algorithm will be developed to simulate an ordinary camera or a hemispherical camera within the scene, viewing towards horizontal or upward direction. It will be very useful for simulating ground measurement devices (e.g. hemispherical camera for retrieval of vegetation chlorophyll content and LAI).

4. Simulation of images of RS sensors that are operated in geometric configurations such as the so called hot spot affects those images. This approach allows to "filter" the hot spot effect in

the images, and consequently to avoid erroneous interpretation of these images. For example, the analysis of satellite images of the Amazon forest without consideration of the hot spot effect explains that during many years, until very recently, that this forest was regreening (i.e., so-called green illusion) during the dry season (Morton et al., 2014).

5. Ground based atmosphere LIDAR viewing upward will be implemented to simulate downward signals received from atmosphere scattering.

6. Terrestrial LIDAR can be further extended for simultaneous localization and mapping (SLAM), i.e. a moving vehicle carrying a LIDAR with it to scan the 3D map of a city.

7. Comparison of simulated results with existing waveform or photon counting LIDAR data in various dimensions, for both single pulse and multiple pulses.

8. Generally speaking, DART has become a very powerful tool for the preparation of future spectro-radiometer and LIDAR systems onboard satellite, plane and UAV, and also for better processing data of existing RS devices.

9. The fusion algorithm in Chapter 5 has the potential to be extended to simulate general fusion data (e.g. LIDAR and hyperspectral data from different systems), and develop fusion algorithms with biases (e.g. accuracy of registration) taken into account.

Finally, it is interesting to note that many exchanges with scientists who use DART and / or wish to use it are an important source of inspiration. The very open policy of the University Paul Sabatier, CNES, CNRS and IRD in the distribution of DART (free licenses for scientists, annual training on DART, etc.) contributes to the emergence of innovative ideas.

Conclusion et perspectives

Cette thèse présente le travail que j'ai réalisé depuis 2011 pour améliorer la modélisation du transfert radiatif au sein des surfaces terrestres et de l'atmosphère, avec pour objectif de mieux simuler à la fois le bilan radiatif et les mesures de télédétection des surfaces terrestres naturelles et urbaines par des spectroradiomètres et Lidars embarqués sur satellite et avion. Cette amélioration a été réalisée dans le cadre du développement du modèle DART (Discrete Anisotropic Radiative Transfer). Les quatre domaines de recherche de mon travail sont préssentés dans les quatre principaux chapitres de ce manuscript.

Chaque chapitre se termine par des remarques concluantes qui sont directement liées au domaine de recherche du Chapitre. Ici, l'objectif est de souligner les relations entre ces domaines et de donner des remarques et conclusions plus générales.

Le chapitre 2 présente une nouvelle méthode de discrétisation des directions de l'espace 4π, appelée IUSD (iterative uniform squared discretization), pour la modélisation générale de transfert radiatif. La méthode met l'accent sur la restriction de la forme carrée et la sélection optimisée du centre de gravité de chaque secteur angulaire qui échantillonne l'espace 4π. Des algorithmes pour générer à la fois une distribution uniforme et une distribution pondérée par les cosinus des directions discrètes sont présentés. Les résultats montrent que la méthode de discrétisation fournit des résultats plus précis et qui convergent plus rapidement par rapport aux méthodes traditionnelles. De même, la méthode de suréchantillonnage s'avère être bien adaptée pour prendre en compte l'hétérogénéité angulaire du rayonnement, par exemple associés aux phénomènes du point chaud (hot spot) et de la réflexion spéculaire. De même l'approche permet de simuler avec beaucoup plus de précision le bilan radiatif qui sont spatialement très hétérogènes, comme les milieux urbains qui comportent des immeubles. Un avantage majeur de la IUSD est qu'il produit des résultats précis avec un assez petit nombre de directions. L'application de la IUSD n'est pas limitée à la modélisation du transfert radiatif. Ainsi, le domaine du transfert de chaleur peut également bénéficier de cette approche. Il s'agit d'un domaine où la distribution des direction de propagation des flux est un sujet couramment débattu. De plus, ce chapitre introduit la notion de direction virtuelle de manière à simuler la propagation du rayonnement lue long de directions flexibles pré-définies. Un rayon se déplaçant le long d'une direction virtuelle (i.e., rayon virtuel) ne peut donner de phénomène de diffusion supplémentaire. Le concept de direction virtuelle, ou plus exactement son extension, est très utile pour à la fois pour la simulation de capteur passif à champ de vue fini (chapitre 3), et pour la simulation des capteurs Lidars via le procédé Ray Carlo (chapitre 4).

Le Chapitre 3 présente une méthode qui combine la projection en perspective avec les modèles "clas-

siques" de transfert radiatif. Il s'agit de la méthode CTPP (converging tracking and perspective projection), conçue pour simuler les mesures de capteurs avec FOV fini. Le concept de direction virtuelle pré-défini présenté dans le chapitre 2 est étendu à la notion de ASVD (automated steering virtual direction). Contrairement aux autres directions, les ASVDs ne sont pas pré-définies. Leurs vecteurs directeurs ne sont pas constants. Ils dépendent du lieu du point de diffusion / émission du rayonnement et de la position du capteur. Toute image de capteur correspond à une distribution 2D de luminances dont les directions dépendent de la position relative du capteur et des points de diffusion / émission. Ce nombre de directions est plus ou moins égal au nombre de points diffusants / émetteurs dans une scène. Cette approche est mise en œuvre pour simuler différents capteurs satellites et avion : caméra, via la projection en perspective,) et capteur à visée transverse (scanner, pushbroom,...), via la combinaison de projections parallèle et perspective. Plusieurs exemples de simulations sont présentés : vidéo capturée par un drone, perception du hot spot selon l'altitude de la plateforme, évolution de la réflectance et luminance entre des mesures avion et satellite, etc. Les images simulées avec cette approche sont tout à fait adaptées aux comparaisons pixel à pixel avec des images acquises par des spectroradiomètres. La méthode de comparaison utilisée avec les modèles classiques de transfert radiatif est souvent imprécise, car ces modèles négligent la projection perspective. D'autre part, une technique itérative a été conçue pour importer la position et l'attitude de la plateforme et du capteur obtenues à partir d'instruments embarqués (GPS, IMU). Cette possibilité facilite la comparaison de simulations DART avec des mesures réelles. Cette comparaison a été réalisée avec les données hyperspectrales acquises dans le cadre de l'expérience Airborne Prism (APEX). Le résultat de la comparaison montre que la prise en compte de la projection perspective améliore la comparaison, par rapport aux travaux antérieurs, où les images étaient simulées avec la projection orthogonale le long de la direction moyenne du champ de vue. La méthode CTPP s'est avérée extrêmement utile pour simuler le bruit solaire dans les mesures Lidar (chapitre 4) et pour simuler la fusion "données Lidar - Images hyperspectrales" (chapitre 5).

Le chapitre 4 présente l'approche utilisée par DART pour simuler les mesures des LIDARs. Cette approche s'appuie sur une modélisation originale dite quasi-MCRT (Monte Carlo Ray Tracing), conçue pour simuler la propagation des photons dans les paysages terrestres et l'atmosphère. Elle comprend deux méthodes majeures, la méthode dite Box et la méthode Ray Carlo, pour simuler de manière précise et robuste les formes d'onde Lidars, pour configuration géométrique d'acquisition, tout paysage et toute atmosphère. La méthode dite de la boîte discrétise la probabilité d'une fonction de phase (i.e., fonction de diffusion) selon dans un grand nombre de boîtes, fonction de la mémoire ordinateur disponible, si bien que chaque événement de diffusion est simulé par sélection aléatoire d'une boîte, au lieu de recourir aux calculs fastidieux réalisés dans les modèles traditionnels MCRT. Cette méthode optimise et accélère considérablement la sélection de la direction de diffusion d'un photon lors de l'interaction du rayonnement avec des matériaux de propriétés optiques anisotropes. La méthode Ray Carlo apporte dans le suivi de rayons "classique" de DART l'approche Monte Carlo. Chaque événement de diffusion se traduit par l'envoi d'un rayon virtuel (Chapitre 2) dans le champ de vue du LIDAR. Il s'agit d'un rayon ASVD (chapitre 3), qui contribue à la formation de forme d'onde. Ainsi, la méthode Ray Carlo

permet de simuler avec précision des mesures Lidars avec un nombre de photons beaucoup plus réduit (exemple : facteur 10-10) que le nombre nécessaire avec une méthode Monte Carlo directe classique. Différentes approches, internes à DART, sont développées pour tester la validité des simulations. Ainsi, DART calcule la réflectance des surfaces terrestres associée à chaque impulsion. Une approche pour simuler des signaux LIDAR dans l'atmosphère est également présentée. Elle permet d'éviter les signaux discontinus aux limites des couches atmosphériques.

La méthode quasi-MCRT de simulation d'une impulsion unique forme d'onde a été étendue dans le but de simuler l'acquisition d'impulsions multiples, à la fois par des capteurs Lidars aéroportés (ALS) et terrestres (TLS). L'approche adoptée pour simuler les mesures aéroportées présente de fortes similitudes avec l'approche mise en œuvre pour simuler les images des spectroradiomètres du type scanner et pushbroom (chapitre 3). Au vu de la complexité des méthodes mlises en œuvre pour traiter les données Lidar, une méthode a été développée pour exporter les simulations DART dans un format "industriel", dans le but de pouvoir traiter les simulations DART avec des logiciels dédiés. Ce Chapitre présente deux autres développements importants. 1) La transformation des formes d'onde de données LIDAR en des acquisitions réalisées par des détecteurs dits à comptage de photon, à partir d'une approche statistique. 2) La modélisation du bruit solaire dans les mesures Lidars. L'approche s'appuie sur la modélisation des images à champ de vue fini (chapitre 3). Il s'agit d'un système à deux sources de rayonnement (soleil et Lidar) et à 1 système de capteur (télescope du Lidar). Les régions associées au champ de vue (FOV) du Lidar et projetées sur le plan de l'image du sol sont segmentées au sein de l'image du spectroradiomètre. Ainsi, l'estimation de la luminance moyenne dans les régions FOV projetées sur l'image de plan de plus basse altitude fournit un nombre de photons par unité de temps, qui est enregistré en tant que bruit solaire. Les simulations réalisées avec des caractéristiques réalistes d'instruments montrent que le bruit solaire joue un rôle plus important dans les systèmes de comptage de photons que dans les systèmes LIDAR de forme d'onde. De manière similaire à l'importation de la configuration géométrique d'acquisition de spectroradiomètres (chapitre 3), la position et l'orientation de chaque impulsion LIDAR peut être importée. Cela approche facilite la comparaison de simulations et de mesures.

Le chapitre 5 étend le concept de système à 2 sources et 1 capteur présenté dans le chapitre 4 dans le but de simuler la technique de fusion en vol qui est utilisée dans de nombreux systèmes multi-capteurs LIDARs et hyperspectraux tels que le système "Carnegie Airborne Observatory" et le système GLIGHT (LIDAR, hyperspectrale et thermique) de la NASA. Les images hyperspectrales et les données LIDAR sont simulées avec des algorithmes respectivement présentés dans les chapitres 3 et 4. La région associée au FOV de chaque impulsion est projetée dans le plan image correspondant au plan image du spectroradiomètre. Un cube image est ainsi créé avec les images hyperspectrales et Lidar superposées, ce qui permet l'analyse de ce produit de fusion à partir d'analyse en composantes principales. Cette approche permet de valider les principes d'acquisition de plusieurs systèmes multi-capteurs existants.

En plus des nouvelles fonctionnalités indiquées ci-dessus, mon travail a aussi porté sur l'amélioration des performances techniques de DART. La principale amélioration technique porte sur la parallélisation du code "Lidar" de DART, réalisé en collaboration avec Nicolas Lauret. Il est intéressant de noter que

ce travail de parallélisation se poursuit actuellement de manière à accélérer toutes les parties du code (e.g., simulation de paysages) qui se prêtent à cette amélioration). Cette parallélisation offre l'avantage de pouvoir travailler sur de grands paysages avec de faibles temps de calcul.

Avant le début de mon travail, DART était déjà le modèle le plus complet dans le domaine de la télédétection optique. Les nouvelles fonctionnalités que j'ai introduites ouvrent la porte à de nouveaux travaux de recherche et/ou facilitent des travaux déjà existants. Quelques exemples sont indiqués ci-dessous. Certains des travaux indiqués ont déjà démarré dans le cadre de l"équipe DART au CESBIO, mais aussi dans d'autres laboratoires et Centres comme la NASA (GSFC, USA) et RSL (Université de Zurich, Suisse).

1. La méthode dite IUSD, de distribution uniforme et pondérée par les cosinus des directions peut être utilisée pour déterminer la meilleure discrétisation des directions discrètes pour les modèles de transfert radiatif.

2. Simulation d'image de capteur passif à FOV fini, par modélisation du transfert radiatif dans les paysages terrestres et l'atmosphère, dans le but de comparaisons pixel à pixel des luminances simulées et mesurées par des capteurs embarqués sur satellite ou avion, pour de plus grands paysages (e.g., 5km x5km). Ce travail est actuellement en cours de réalisation, en collaboration avec le Laboratoire de télédétection de l'Université de Zürich, pour un paysage de forêt de montagne.

3. Développement de la modélisation de capteur, appareil photo ordinaire ou caméra hémisphérique, situé dans le paysage terrestre (e.g., forêt, culture, ville, etc.) et qui observe le milieu selon toute direction (e.g., verticale). Cette modélisation sera très utile pour simuler les mesures d'appareils de mesure de terrain, comme les caméras hémisphériques et l'instrument Licor 2000 utilisés pour estimer le LAI et la concentration en chlorophylle des cultures et forêts.

4. Simulation d'images de capteurs embarqués acquises dans des configurations géométriques telles que l'effet dit du hot spot affecte ces images. Cette approche permet de "filtrer" l'effet "hot spot" au sein de ces images et donc d'éviter des erreurs d'interprétation de ces images. Ainsi, l'analyse des images satellites de la forêt amazonienne sans prise en compte de cet effet a conduit les scientifiques à estimer pendant de nombreuses années, jusqu'à très récemment, que cette forêt "verdissait" durant la saison sèche (Morton et al., 2014).

5. Modélisation des mesures de capteurs Lidar dédiés à la mesure des rétrodiffusions atmosphériques. Il s'agit de capteurs Lidars au sein des paysages terrestres et qui émettent des photons selon des directions montantes.

6. Extension de la modélisation des Lidars terrestres pour des applications en lien avec la localisation et la cartographie simultanées (SLAM: Simultaneous Localization And Mapping), par exemple dans le cas de véhicule qui embarquent un Lidar terrestre pour établir des cartes 3D de ville.

7. Comparaison de simulations et mesures Lidar forme d'onde ou comptage de photons, à la fois pour les cas "simple impulsion" et "impulsions multiples".

8. D'une manière générale, DART est devenu un outil très puissant pour la préparation des futurs systèmes d'observation (spectroradiomètres et Lidars) embarqués sur satellite, avion et drone, et aussi pour mieux exploiter les mesures des systèmes actuels.

9. L'algorithme de fusion introduit dans le chapitre 5 est adapté à la fusion de tout type de mesures de spectroradiomètres et de Lidars, ce qui facilite le développement d'algorithmes de fusion et d'exploitation des données résultantes, avec prise en compte des conditions réelles d'acquisition, comme les incertitudes de recalage géométrique.

Finalement, il est intéressant que de noter que les nombreux échanges avec les scientifiques qui utilisent DART et/ou souhaitent l'utiliser constituent une source importante d'inspiration. La politique très ouverte de l'Université Paul Sabatier, du CNES, du CNRS et de l'IRD en matière de distribution de DART (licences gratuites pour les scientifiques, formations annuelles sur DART, etc.) participe cette émergence d'idées novatrices.

Bibliography

Abdalati, W., Zwally, H., Bindschadler, R., Csatho, B., Farrell, S., Fricker, H., Harding, D., Kwok, R., Lefsky, M., Markus, T., Marshak, A., Neumann, T., Palm, S., Schutz, B., Smith, B., Spinhirne, J., Webb, C., May 2010. The ICESat-2 Laser Altimetry Mission. Proceedings of the IEEE 98 (5), 735–751. 9, 17

Ackermann, F., 1999. Airborne laser scanning—present status and future expectations. ISPRS Journal of Photogrammetry and Remote Sensing 54 (2), 64–67. 92

Anthony, W. Y., Stephen, M. A., Li, S. X., Shaw, G. B., Seas, A., Dowdye, E., Troupaki, E., Liiva, P., Poulios, D., Mascetti, K., 2010. Space laser transmitter development for ICESat-2 mission. In: SPIE LASE. International Society for Optics and Photonics, pp. 757809–757809. 9, 17, 95

Asner, G. P., 1998. Biophysical and biochemical sources of variability in canopy reflectance. Remote Sensing of Environment 64 (3), 234–253. 1

Asner, G. P., Knapp, D. E., Boardman, J., Green, R. O., Kennedy-Bowdoin, T., Eastwood, M., Martin, R. E., Anderson, C., Field, C. B., 2012. Carnegie Airborne Observatory-2: Increasing science data dimensionality via high-fidelity multi-sensor fusion. Remote Sensing of Environment 124, 454–465. 2, 9, 17, 95, 153

Asner, G. P., Knapp, D. E., Kennedy-Bowdoin, T., Jones, M. O., Martin, R. E., Boardman, J., Field, C. B., 2007. Carnegie Airborne Observatory: in-flight fusion of hyperspectral imaging and waveform light detection and ranging for three-dimensional studies of ecosystems. Journal of Applied Remote Sensing 1 (1), 013536–013536–21. 2, 9, 17, 18, 95, 153

Asner, G. P., Knapp, D. E., Kennedy-Bowdoin, T., Jones, M. O., Martin, R. E., Boardman, J., Hughes, R. F., 2008. Invasive species detection in Hawaiian rainforests using airborne imaging spectroscopy and LiDAR. Remote Sensing of Environment 112 (5), 1942–1955.

Asner, G. P., Martin, R. E., Carlson, K. M., Rascher, U., Vitousek, P. M., 2006. Vegetation–climate interactions among native and invasive species in Hawaiian rainforest. Ecosystems 9 (7), 1106–1117.

Asner, G. P., Vitousek, P. M., 2005. Remote analysis of biological invasion and biogeochemical change. Proceedings of the National Academy of Sciences of the United States of America 102 (12), 4383–4386.

ASPRS, 2006. Asprs lidar data exchange format standard version 1.1. 91

Banskota, A., Wynne, R. H., Thomas, V. A., Serbin, S. P., Kayastha, N., Gastellu-Etchegorry, J. P., Townsend, P. A., 2013. Investigating the utility of wavelet transforms for inverting a 3-D radiative transfer model using hyperspectral data to retrieve forest LAI. Remote Sensing 5 (6), 2639–2659.

Barbier, N., Couteron, P., Gastelly-Etchegorry, J.-P., Proisy, C., 2012. Linking canopy images to forest structural parameters: potential of a modeling framework. Annals of forest science 69 (2), 305–311.

Barbier, N., Couteron, P., Proisy, C., Malhi, Y., Gastellu-Etchegorry, J.-P., 2010. The variation of apparent crown size and canopy heterogeneity across lowland Amazonian forests. Global Ecology and Biogeography 19 (1), 72–84.

Bater, C. W., Coops, N. C., 2009. Evaluating error associated with lidar-derived DEM interpolation. Computers & Geosciences 35 (2), 289–300. 92

Berk, A., 1996. MODTRAN band model transmittance. Rpt. No. SSI-SR 69, 1–11.

Berk, A., Anderson, G. P., Bernstein, L. S., Acharya, P. K., Dothe, H., Matthew, M. W., Adler-Golden, S. M., Chetwynd, Jr., J. H., Richtsmeier, S. C., Pukall, B., Allred, C. L., Jeong, L. S., Hoke, M. L., 1999. MODTRAN4 radiative transfer modeling for atmospheric correction. In: Proc. SPIE's International Symposium on Optical Science, Engineering, and Instrumentation. International Society for Optics and Photonics, pp. 348–353.

Berk, A., Bernstein, L. S., Robertson, D. C., 1987. MODTRAN: A moderate resolution model for LOWTRAN. Tech. rep., DTIC Document. 5

Berni, J., Zarco-Tejada, P. J., Suárez, L., Fereres, E., 2009. Thermal and narrowband multispectral remote sensing for vegetation monitoring from an unmanned aerial vehicle. Geoscience and Remote Sensing, IEEE Transactions on 47 (3), 722–738.

Blair, J., Rabine, D. L., Hofton, M. A., 1999. The Laser Vegetation Imaging Sensor: a medium-altitude, digitisation-only, airborne laser altimeter for mapping vegetation and topography . {ISPRS} Journal of Photogrammetry and Remote Sensing 54 (2–3), 115 – 122.

Blair, J. B., Hofton, M. A., 1999. Modeling laser altimeter return waveforms over complex vegetation using high-resolution elevation data. Geophysical Research Letters 26 (16), 2509–2512. 93

Borel, C. C., Gerstl, S. A., Powers, B. J., 1991. The radiosity method in optical remote sensing of structured 3-D surfaces. Remote Sensing of Environment 36 (1), 13–44. 5, 15

Bruniquel-Pinel, V., Gastellu-Etchegorry, J.-P., 1998. Sensitivity of texture of high resolution images of forest to biophysical and acquisition parameters. Remote Sensing of Environment 65 (1), 61–85.

Bunting, P., Armston, J., Clewley, D., Lucas, R. M., 2013a. Sorted pulse data (SPD) library—Part II: A processing framework for LiDAR data from pulsed laser systems in terrestrial environments. Computers & Geosciences 56, 207–215. 9, 17, 94

Bunting, P., Armston, J., Lucas, R. M., Clewley, D., 2013b. Sorted Pulse Data (SPD) Library. Part I: A generic file format for LiDAR data from pulsed laser systems in terrestrial environments. Computers & Geosciences 56, 197–206. 9, 17, 94

Campbell, J., HAAG, M. U., GRAAS, F., 2007. Terrain-Referenced Precision Approach Guidance: Proof-of-Concept Flight Test Results. Navigation 54 (1), 21–29. 91

Chai, J. C., Lee, H. S., Patankar, S. V., 1994a. Finite volume method for radiation heat transfer. Journal of Thermophysics and Heat Transfer 8 (3), 419–425.

Chai, J. C., Lee, H. S., Patankar, S. V., 1994b. Finite volume method for radiation heat transfer. Journal of Thermo-physics and Heat Transfer 8 (3), 419–425.

Chai, J.-X., Shum, H.-Y., 2000. Parallel projections for stereo reconstruction. In: Computer Vision and Pattern Recognition, 2000. Proceedings. IEEE Conference on. Vol. 2. IEEE, pp. 493–500. 1, 8, 16

Chandrasekhar, S., 1969. Radiative Transfer. Dover Publications. 2

Chauve, A., Mallet, C., Bretar, F., Durrieu, S., Deseilligny, M. P., Puech, W., 2007. Processing full-waveform lidar data: Modelling raw signals. In: International Archives of Photogrammetry, Remote Sensing and Spatial Information Sciences, 36 (Part 3/W52. pp. 102–107. 93

Chen, J. M., Leblanc, S. G., 1997. A four-scale bidirectional reflectance model based on canopy architecture. Geoscience and Remote Sensing, IEEE Transactions on 35 (5), 1316–1337. 4

Chen, J. M., Leblanc, S. G., 2001. Multiple-scattering scheme useful for geometric optical modeling. Geoscience and Remote Sensing, IEEE Transactions on 39 (5), 1061–1071. 5

Chen, Q., 2007. Airborne lidar data processing and information extraction. Photogrammetric engineering and remote sensing 73 (2), 109. 91

Chui, E. H., Raithby, G. D., 1993. Computation of radiant heat transfer on a nonorthogonal mesh using the finite-volume method. Numerical Heat Transfer Part B: Fundamentals 23, 269–288.

Cook, B. D., Corp, L. A., Nelson, R. F., Middleton, E. M., Morton, D. C., McCorkel, J. T., Masek, J. G., Ranson, K. J., Ly, V., Montesano, P. M., 2013. NASA Goddard's LiDAR, Hyperspectral and Thermal (G-LiHT) Airborne Imager. Remote Sensing 5 (8). 9, 18, 153

Côté, J.-F., Fournier, R. A., Egli, R., 2011. An architectural model of trees to estimate forest structural attributes using terrestrial LiDAR. Environmental Modelling & Software 26 (6), 761–777. 2

Côté, J.-F., Widlowski, J.-L., Fournier, R. A., Verstraete, M. M., 2009. The structural and radiative consistency of three-dimensional tree reconstructions from terrestrial lidar. Remote Sensing of Environment 113 (5), 1067–1081. 2

Dabney, P., Harding, D., Abshire, J., Huss, T., Jodor, G., Machan, R., Marzouk, J., Rush, K., Seas, A., Shuman, C., et al., 2010. The Slope Imaging Multi-polarization Photon-counting Lidar: development and performance results. In: Geoscience and Remote Sensing Symposium (IGARSS), 2010 IEEE International. IEEE, pp. 653–656.

Dalponte, M., Bruzzone, L., Gianelle, D., 2008. Fusion of hyperspectral and LIDAR remote sensing data for classification of complex forest areas. Geoscience and Remote Sensing, IEEE Transactions on 46 (5), 1416–1427.

Dalponte, M., Bruzzone, L., Gianelle, D., 2012. Tree species classification in the Southern Alps based on the fusion of very high geometrical resolution multispectral/hyperspectral images and LiDAR data. Remote sensing of environment 123, 258–270.

Dare, P. M., 2005. Shadow analysis in high-resolution satellite imagery of urban areas. Photogrammetric Engineering & Remote Sensing 71 (2), 169–177.

Dawson, T. P., Curran, P. J., Plummer, S. E., 1998. LIBERTY—Modeling the effects of leaf biochemical concentration on reflectance spectra. Remote Sensing of Environment 65 (1), 50–60. 5

Demming, R., Duffy, D. J., 2010. Introduction to the Boost C++ Libraries; Volume I-Foundations. Datasim Education BV.

Diner, D., Beckert, J., Reilly, T., Bruegge, C., Conel, J., Kahn, R., Martonchik, J., Ackerman, T., Davies, R., Gerstl, S., Gordon, H., Muller, J.-P., Myneni, R., Sellers, P., Pinty, B., Verstraete, M., Jul 1998. Multi-angle Imaging SpectroRadiometer (MISR) instrument description and experiment overview. Geoscience and Remote Sensing, IEEE Transactions on 36 (4), 1072–1087.

Disney, M., Lewis, P., North, P., 2000. Monte Carlo ray tracing in optical canopy reflectance modelling. Remote Sensing Reviews 18 (2-4), 163–196. 5, 15, 93

Duan, M., Min, Q., Lü, D., 2010. A polarized radiative transfer model based on successive order of scattering. Advances in Atmospheric Sciences 27 (4), 891–900. 5, 15

Durrieu, S., Cherchali, S., Costeraste, J., Mondin, L., Debise, H., Chazette, P., Dauzat, J., Gastellu-Etchegorry, J.-P., Baghdadi, N., Pélissier, R., 2013. Preliminary studies for a vegetation ladar/lidar space mission in france. In: Proc. Geoscience and Remote Sensing Symposium (IGARSS), 2013 IEEE International. pp. 4332–4335.

Engelsen, O., Pinty, B., Verstraete, M., Martonchik, J., 1996. Parametric bidirectional reflectance factor models: Evaluation, improvements and applications. EC Joint Research Centre. Tech. rep., Technical Report No. EUR 16426 EN. 3

Féret, J.-B., Asner, G. P., 2012. Semi-supervised methods to identify individual crowns of lowland tropical canopy species using imaging spectroscopy and LiDAR. Remote Sensing 4 (8), 2457–2476.

Féret, J.-B., Asner, G. P., 2014a. Mapping tropical forest canopy diversity using high-fidelity imaging spectroscopy. Ecological Applications 24 (6), 1289–1296.

Féret, J.-B., Asner, G. P., 2014b. Microtopographic controls on lowland Amazonian canopy diversity from imaging spectroscopy. Ecological Applications 24 (6), 1297–1310.

Feret, J.-B., François, C., Asner, G. P., Gitelson, A. A., Martin, R. E., Bidel, L. P., Ustin, S. L., le Maire, G., Jacquemoud, S., 2008. PROSPECT-4 and 5: Advances in the leaf optical properties model separating photosynthetic pigments. Remote Sensing of Environment 112 (6), 3030–3043. 5

Fiveland, W., 1988a. Three-dimensional radiative heat-transfer solutions by the discrete-ordinates method. Journal of Thermophysics and Heat Transfer 2 (4), 309–316.

Fiveland, W. A., 1984. Discrete ordinate methods for radiative transport equation for rectangular enclosures. Journal of Heat Tranfer 106, 699–706.

Fiveland, W. A., 1987. Discrete ordinate methods for radiative heat transfer in isotropically and anisotropically scattering media. Journal of Heat Tranfer 109, 809–812.

Fiveland, W. A., 1988b. Three-dimensional radiative heat-transfer solutions by the discrete-ordinates method. Journal of Heat Tranfer 2 (4), 309–316.

Fournier, R., St-Onge, B., Bégin, J., 2011. La technologie LiDAR pour mieux sonder notre environnement, Université de Sherbrooke.
URL http://www.frqnt.gouv.qc.ca/documentsPublications/pdf/2013/FRQNT-JdeR2013-Fournier.pdf

Gascon, F., Gastellu-Etchegorry, J.-P., Lefèvre, M.-J., 2001. Radiative transfer model for simulating high-resolution satellite images. Geoscience and Remote Sensing, IEEE Transactions on 39 (9), 1922–1926.

Gascon, F., Gastellu-Etchegorry, J.-P., Lefevre-Fonollosa, M.-J., Dufrene, E., 2004. Retrieval of forest biophysical variables by inverting a 3-D radiative transfer model and using high and very high resolution imagery. International Journal of Remote Sensing 25 (24), 5601–5616.

Gastellu-Etchegorry, J.-P., 2008. 3D modeling of satellite spectral images, radiation budget and energy budget of urban landscapes. Meteorology and atmospheric physics 102 (3-4), 187–207.

Gastellu-Etchegorry, J.-P., Demarez, V., Pinel, V., Zagolski, F., 1996. Modeling radiative transfer in heterogeneous 3-D vegetation canopies. Remote Sensing of Environment 58, 131–156. 5, 6, 7, 16

Gastellu-Etchegorry, J.-P., Grau, E., Lauret, N., 2012. Modeling and simulation in Engineering. Intech, Oxford, Ch. DART: a 3D model for remote sensing images and radiative budget of earth surfaces. 6

Gastellu-Etchegorry, J.-P., Guillevic, P., Zagolski, F., Demarez, V., Trichon, V., Deering, D., Leroy, M., 1999. Modeling BRF and radiation regime of boreal and tropical forests: I. BRF. Remote Sensing of Environment 68 (3), 281–316.

Gastellu-Etchegorry, J.-P., Martin, E., Gascon, F., 2004a. DART: a 3-D model for simulating satellite images and surface radiation budget. International Journal of Remote Sensing 25(1), 75–96. 6

Gastellu-Etchegorry, J.-P., Martin, E., Gascon, F., 2004b. DART: a 3D model for simulating satellite images and studying surface radiation budget. International Journal of Remote Sensing 25 (1), 73–96.

Gastellu-Etchegorry, J.-P., Yin, T., Grau, E., Lauret, N., Rubio, J., July 2013. Lidar radiative transfer modeling in the Atmosphere. In: Proc. Geoscience and Remote Sensing Symposium (IGARSS), 2013 IEEE International. pp. 4554–4557. 94

Gastellu-Etchegorry, J.-P., Yin, T., Lauret, N., 2015a. Simulation of satellite, airborne and terrestrial LiDAR with DART (I): waveform simulation with quasi-Monte Carlo ray tracing. Remote Sensing of Environment, submitted.

Gastellu-Etchegorry, J.-P., Yin, T., Lauret, N., Cajgfinger, T., Gregoire, T., Grau, E., Feret, J.-B., Lopes, M., Guilleux, J., Dedieu, G., Malenovský, Z., Cook, B. D., Morton, D., Rubio, J., Durrieu, S., Cazanave, G., Martin, E., Ristorcelli, T., 2015b. Discrete Anisotropic Radiative Transfer (DART 5) for modeling airborne and satellite spectroradiometer and LIDAR acquisitions of natural and urban landscapes. Remote Sensing 7 (2), 1667–1701.

Gatebe, C., Dubovik, O., King, M., Sinyuk, A., 2010. Simultaneous retrieval of aerosol and surface optical properties from combined airborne-and ground-based direct and diffuse radiometric measurements. Atmospheric Chemistry and Physics 10 (6), 2777–2794.

Gatebe, C. K., King, M. D., Platnick, S., Arnold, G. T., Vermote, E. F., Schmid, B., 2003. Airborne spectral measurements of surface–atmosphere anisotropy for several surfaces and ecosystems over southern Africa. Journal of Geophysical Research 108 (D13).

Govaerts, Y. M., 1996. A model of light scattering in three-dimensional plant canopies: a Monte Carlo ray tracing approach. Office for Official Publ. of the Europ. Communities. 91

Govaerts, Y. M., Verstraete, M. M., 1998. Raytran: A Monte Carlo ray-tracing model to compute light scattering in three-dimensional heterogeneous media. Geoscience and Remote Sensing, IEEE Transactions on 36 (2), 493–505. 6

Grau, E., 2012. Modélisation DART du transfert radiatif Terre-Atmosphère pour simuler les bilans radiatif, images de télédétection et mesures LIDAR des paysages terrestres. Ph.D. thesis, Université Paul Sabatier-Toulouse III. 94

Grau, E., Gastellu-Etchegorry, J.-P., 2013. Radiative transfer modeling in the Earth–Atmosphere system with DART model. Remote Sensing of Environment 139, 149–170. 5

Guillevic, P., Gastellu-Etchegorry, J.-P., 1999. Modeling BRF and radiation regime of boreal and tropical forest: II. PAR regime. Remote Sensing of Environment 68 (3), 317–340.

Gupta, R., Hartley, R. I., 1997. Linear pushbroom cameras. Pattern Analysis and Machine Intelligence, IEEE Transactions on 19 (9), 963–975. 1, 8, 16

Hancock, S., Disney, M., Muller, P. L. J.-P., 2008. Exploring the measurement of forests with full waveform lidar through Monte-Carlo Ray Tracing. The International Archives of Photogrammetry, Remote Sensing and Spatial Information Sciences 37.

Hapke, B., 1981. Bidirectional reflectance spectroscopy: 1. Theory. Journal of Geophysical Research: Solid Earth (1978–2012) 86 (B4), 3039–3054. 5

Hapke, B., DiMucci, D., Nelson, R., Smythe, W., 1996. The cause of the hot spot in vegetation canopies and soils: Shadow-hiding versus coherent backscatter. Remote Sensing of Environment 58 (1), 63–68.

Hapke, B. W., Nelson, R. M., Smythe, W. D., 1993. The Opposition Effect of the Moon: The Contribution of Coherent Backscatter. Science 260 (5107), 509–511. 2

Harding, D., Abshire, J., Dabney, P., Seas, A., Shuman, C., Sun, X., Valett, S., Vasilyev, A., Yu, T., Huss, T., et al., 2008. The swath imaging multi-polarization photon-counting lidar (SIMPL): A spaceflight prototype. In: Proceedings of the 2008 IEEE International Geoscience & Remote Sensing Symposium. pp. 06–11. 92

Hladik, C., Schalles, J., Alber, M., 2013a. Salt marsh elevation and habitat mapping using hyperspectral and LIDAR data. Remote Sensing of Environment 139, 318–330.

Hladik, C., Schalles, J., Alber, M., 2013b. Salt marsh elevation and habitat mapping using hyperspectral and LIDAR data . Remote Sensing of Environment 139 (0), 318 – 330.
URL http://www.sciencedirect.com/science/article/pii/S0034425713002617 2

Hodgson, M. E., Jensen, J., Raber, G., Tullis, J., Davis, B. A., Thompson, G., Schuckman, K., 2005. An evaluation of lidar-derived elevation and terrain slope in leaf-off conditions. Photogrammetric Engineering & Remote Sensing 71 (7), 817–823.

Huete, A. R., Didan, K., Shimabukuro, Y. E., Ratana, P., Saleska, S. R., Hutyra, L. R., Yang, W., Nemani, R. R., Myneni, R., 2006. Amazon rainforests green-up with sunlight in dry season. Geophysical Research Letters 33 (6).

Itten, K. I., Dell'Endice, F., Hueni, A., Kneubühler, M., Schläpfer, D., Odermatt, D., Seidel, F., Huber, S., Schopfer, J., Kellenberger, T., Bühler, Y., D'Odorico, P., Nieke, J., Alberti, E., Meuleman, K., 2008. APEX-the hyperspectral esa airborne prism experiment. Sensors 8 (10), 6235–6259.

Jacquemoud, S., Baret, F., 1990. Prospect: A model of leaf optical properties spectra. Remote Sensing of Environment 34 (2), 75 – 91.
URL http://www.sciencedirect.com/science/article/pii/0034425790901002 5

Jehle, M., Hueni, A., Damm, A., D'Odorico, P., Weyermann, J., Kneubiihler, M., Schlapfer, D., Schaepman, M., Meuleman, K., Nov 2010. APEX - current status, performance and validation concept. In: Proc. Sensors, 2010 IEEE. pp. 533–537.

Kampe, T. U., Johnson, B. R., Kuester, M., Keller, M., 2010. NEON: the first continental-scale ecological observatory with airborne remote sensing of vegetation canopy biochemistry and structure. Journal of Applied Remote Sensing 4 (1), 043510–043510. 9, 18, 153

Kim, S. H., Huh, K. Y., 2000. A new angular discretization scheme of the finite volume method for 3-D radiative heat transfer in absorbing, emitting and anisotropically scattering media. International Journal of Heat and Mass Transfer 43 (7), 1233–1242. 57

Kimes, D., Kirchner, J., 1982. Radiative transfer model for heterogeneous 3-D scenes. Appl. Opt. 21, 4119–4129. 4, 57

King, M. D., Strange, M. G., Leone, P., Blaine, L. R., 1986. Multiwavelength scanning radiometer for airborne measurements of scattered radiation within clouds. Journal of Atmospheric and Oceanic Technology 3 (3), 513–522.

Koetz, B., Sun, G., Morsdorf, F., Ranson, K., Kneubühler, M., Itten, K., Allgöwer, B., 2007. Fusion of imaging spectrometer and LIDAR data over combined radiative transfer models for forest canopy characterization. Remote Sensing of Environment 106 (4), 449–459.

Kotchenova, S. Y., Shabanov, N. V., Knyazikhin, Y., Davis, A. B., Dubayah, R., Myneni, R. B., 2003. Modeling lidar waveforms with time-dependent stochastic radiative transfer theory for remote estimations of forest structure. Journal of Geophysical Research: Atmospheres (1984–2012) 108 (D15).

Kuusk, A., 1991. The hot spot effect in plant canopy reflectance. In: Photon-Vegetation Interactions. Springer, pp. 139–159. 4

Kuusk, A., Kuusk, J., Lang, M., 2009. A dataset for the validation of reflectance models. Remote Sensing of Environment 113 (5), 889–892.

Lathrop, K. D., 1966. Use of discrete-ordinate methods for solution of photon transport problems. Nuclear Science and Engineering 24, 381–388.

Lathrop, K. D., Carlson, B. G., 1965. Discrete-ordinates angular quadrature of the newtron transport equation. Technical Information Series Report LASL-3186, Los Alamos Scientific Laboratory.

Lawrence, D., Zheng, Y., Upton, R., Tillard, J., Disque, S., Howell, S., 2013. Recent advances in photon-counting, 3d imaging lidars. In: 18th International Workshop on Laser Ranging.

Leblanc, S. G., Chen, J. M., 2000. A windows graphic user interface (GUI) for the five-scale model for fast BRDF simulations. Remote Sensing Reviews 19 (1-4), 293–305. 5

Lefsky, M. A., Cohen, W. B., Parker, G. G., Harding, D. J., 2002. Lidar Remote Sensing for Ecosystem Studies Lidar, an emerging remote sensing technology that directly measures the three-dimensional distribution of plant canopies, can accurately estimate vegetation structural attributes and should be of particular interest to forest, landscape, and global ecologists. BioScience 52 (1), 19–30. 2, 92

Lewis, P., 1999. Three-dimensional plant modelling for remote sensing simulation studies using the Botanical Plant Modelling System. Agronomie 19 (3-4), 185–210. 6

Li, X., Strahler, A. H., 1992. Geometric-optical bidirectional reflectance modeling of the discrete crown vegetation canopy: Effect of crown shape and mutual shadowing. Geoscience and Remote Sensing, IEEE Transactions on 30 (2), 276–292. 4

Liang, S., Strahler, A. H., Barnsley, M. J., Borel, C. C., Gerstl, S. A., Diner, D. J., Prata, A. J., Walthall, C. L., 2000. Multiangle remote sensing: Past, present and future. Remote Sensing Reviews 18 (2-4), 83–102.

Liu, S., Liu, Q., Liu, Q., Wen, J., Li, X., 2010. The angular and spectral kernel model for BRDF and albedo retrieval. Selected Topics in Applied Earth Observations and Remote Sensing, IEEE Journal of 3 (3), 241–256. 3

Liu, X., 2008. Airborne LiDAR for DEM generation: some critical issues. Progress in Physical Geography 32 (1), 31–49. 91

Malenovskỳ, Z., Homolová, L., Zurita-Milla, R., Lukeš, P., Kaplan, V., Hanuš, J., Gastellu-Etchegorry, J.-P., Schaepman, M. E., 2013. Retrieval of spruce leaf chlorophyll content from airborne image data using continuum removal and radiative transfer. Remote Sensing of Environment 131, 85–102.

Malenovskỳ, Z., Martin, E., Homolová, L., Gastellu-Etchegorry, J.-P., Zurita-Milla, R., Schaepman, M. E., Pokornỳ, R., Clevers, J. G., Cudlín, P., 2008. Influence of woody elements of a Norway spruce canopy on nadir reflectance simulated by the DART model at very high spatial resolution. Remote Sensing of Environment 112 (1), 1–18.

Mallet, C., Bretar, F., 2009. Full-waveform topographic lidar: State-of-the-art. ISPRS Journal of photogrammetry and remote sensing 64 (1), 1–16. 9, 17

Martin, E., 2006. DART: MODÈLE 3D MULTISPECTRAL ET INVERSION D'IMAGES OPTIQUE DE SATELLITE-APPLICATION AUX COUVERTS FORESTIERS. Ph.D. thesis, Université Paul Sabatier-Toulouse III.

Martonchik, J. V., 1997. Determination of aerosol optical depth and land surface directional reflectances using multiangle imagery. Journal of Geophysical Research: Atmospheres (1984–2012) 102 (D14), 17015–17022. 3

Masson, V., Gomes, L., Pigeon, G., Liousse, C., Pont, V., Lagouarde, J.-P., Voogt, J., Salmond, J., Oke, T. R., Hidalgo, J., Legain, D., Garrouste, O., Lac, C., Connan, O., Briottet, X., Lachérade, S., Tulet, P., 2008. The Canopy and Aerosol Particles Interactions in TOulouse Urban Layer (CAPITOUL) experiment. Meteorology and Atmospheric Physics 102 (3-4), 135–157.

McGill, M., Hlavka, D., Hart, W., Scott, V. S., Spinhirne, J., Schmid, B., 2002. Cloud physics lidar: Instrument description and initial measurement results. Applied Optics 41 (18), 3725–3734.

McGill, M., Markus, T., Scott, V. S., Neumann, T., 2013. The multiple altimeter beam experimental lidar (MABEL): An airborne simulator for the ICESat-2 mission. Journal of Atmospheric and Oceanic Technology 30 (2), 345–352. 9, 17, 95

Mishra, S. C., Chugh, P., Kumar, P., Mitra, K., 2006. Development and comparison of the DTM, the DOM, and the FVM formulations for the short-pulse laser transport through a participating medium. International Journal of Heat and Mass Transfer 49, 1820–1832. 57

Modest, M. F., 2003. Radiative Heat Transfer, 2nd Edition. 57

Modest, M. F., 2013. Radiative heat transfer. Academic press.

Montesano, P., Rosette, J., Sun, G., North, P., Nelson, R., Dubayah, R., Ranson, K., Kharuk, V., 2015. The uncertainty of biomass estimates from modeled ICESat-2 returns across a boreal forest gradient . Remote Sensing of Environment 158 (0), 95 – 109. 2, 9, 17

Morsdorf, F., Kötz, B., Meier, E., Itten, K., Allgöwer, B., 2006. Estimation of LAI and fractional cover from small footprint airborne laser scanning data based on gap fraction. Remote Sensing of Environment 104 (1), 50–61.

Morsdorf, F., Meier, E., Kötz, B., Itten, K. I., Dobbertin, M., Allgöwer, B., 2004. LIDAR-based geometric reconstruction of boreal type forest stands at single tree level for forest and wildland fire management. Remote Sensing of Environment 92 (3), 353–362.

Morsdorf, F., Nichol, C., Malthus, T., Woodhouse, I. H., 2009. Assessing forest structural and physiological information content of multi-spectral LiDAR waveforms by radiative transfer modelling. Remote Sensing of Environment 113 (10), 2152–2163.

Morton, D. C., Nagol, J., Carabajal, C. C., Rosette, J., Palace, M., Cook, B. D., Vermote, E. F., Harding, D. J., North, P. R., 2014. Amazon forests maintain consistent canopy structure and greenness during the dry season. Nature 506 (7487), 221–224. 178, 182

Mundt, J. T., Streutker, D. R., Glenn, N. F., 2006. Mapping sagebrush distribution using fusion of hyperspectral and lidar classifications. Photogrammetric Engineering & Remote Sensing 72 (1), 47–54.

Myneni, R., Asrar, G., Hall, F., 1992. A three-dimensional radiative transfer method for optical remote sensing of vegetated land surfaces. Remote Sensing of Environment 41 (2), 105–121.

Myneni, R., Marshak, A., Knyazikhin, Y., G., A., Aug 1991. Discrete ordinate method for photon transport in leaf canopies, Photon-vegetation Interactions. Photon-vegetation Interactions: Applications in Optical Remote Sensing and Plant Ecology, 45–109. 4, 57

Ni-Meister, W., Jupp, D. L., Dubayah, R., 2001. Modeling lidar waveforms in heterogeneous and discrete canopies. Geoscience and Remote Sensing, IEEE Transactions on 39 (9), 1943–1958. 93

Nickalls, R., 1993. A new approach to solving the cubic: Cardan's solution revealed. The Mathematical Gazette, 354–359.

Nilson, T., Kuusk, A., 1989. A reflectance model for the homogeneous plant canopy and its inversion. Remote Sensing of Environment 27 (2), 157–167.

North, P., 1996. Three-dimensional forest light interaction model using a Monte Carlo method. Geoscience and Remote Sensing, IEEE Transactions on 34 (4), 946–956. 6, 93

North, P., Rosette, J., Suárez, J., Los, S., 2010. A Monte Carlo radiative transfer model of satellite waveform LiDAR. International Journal of Remote Sensing 31 (5), 1343–1358.

Peddle, D., Franklin, S., Johnson, R., Lavigne, M., Wulder, M., 2003. Structural change detection in a disturbed conifer forest using a geometric optical reflectance model in multiple-forward mode. IEEE Transactions on Geoscience and Remote Sensing 41 (1), 163–166. 4

Pinty, B., Gobron, N., Widlowski, J., Gerstl, S., Vertraete, M., Antunes, M., Bacour, C., Gascon, F., Gastellu-Etchegorry, J.-P., Jacquemoud, S., North, P., Qin, W., Thompson, R., 2001a. Sensitivity of Texture of High Resolution Images of Forest to Biophysical and Acquisition Parameters. Remote Sensing of Environment 65, 61–85.

Pinty, B., Gobron, N., Widlowski, J.-L., Gerstl, S. A. W., Verstraete, M. M., Antunes, M., Bacour, C., Gascon, F., Gastellu, J.-P., Goel, N., Jacquemoud, S., North, P., Qin, W., , Thompson, R., 2001b. Radiation transfer model intercomparison (RAMI) exercise. Journal of Geophysical Research 106(D11), 11937–11956. 6

Pinty, B., Widlowski, J.-L., Taberner, M., Gobron, N., Verstraete, M. M., Disney, M., Gascon, F., Gastellu, J.-P., Jiang, L., Kuusk, A., Lewis, P., Li, X., Ni-Meister, W., Nilson, T., North, P., Qin, W., Su, L., Tang, S., Thompson, R., Verhoef, W., Wang, H., Wang, J., Yan, G., Zang, H., 2004. Radiation Transfer Model Intercomparison (RAMI) exercise: Results from the second phase. Journal of Geophysical Research 109, D06210. 6

Popescu, S. C., Zhao, K., Neuenschwander, A., Lin, C., 2011. Satellite lidar vs. small footprint airborne lidar: Comparing the accuracy of aboveground biomass estimates and forest structure metrics at footprint level . Remote Sensing of Environment 115 (11), 2786 – 2797, {DESDynI} VEG-3D Special Issue. 2

Press, W. H., 2007. Numerical recipes 3rd edition: The art of scientific computing. Cambridge university press.

Proisy, C., Barbier, N., Guéroult, M., Pélissier, R., Gastellu-Etchegorry, J.-P., Grau, E., Couteron, P., 2011. Biomass prediction in tropical forests: the canopy grain approach. Remote sensing of biomass: principles and applications, 1–18.

Quadros, N., Collier, P., Fraser, C., 2008. Integration of bathymetric and topographic LiDAR: a preliminary investigation. The International Archives of the Photogrammetry, Remote Sensing and Spatial Information Sciences 36, 1299–1304. 2

Rahman, H., Pinty, B., Verstraete, M. M., 1993. Coupled surface-atmosphere reflectance (CSAR) model: 2. Semiempirical surface model usable with NOAA advanced very high resolution radiometer data. Journal of Geophysical Research: Atmospheres (1984–2012) 98 (D11), 20791–20801. 3

Raithby, G. D., 1999. Discussion of the finite-volume method for radiation, and its application using 3D unstructured meshes. Numerical Heat Transfer, Part B: Fundamentals 35 (4), 389–405. 57

Raithby, G. D., Chui, E. H., 1990. A finite-volume method for predicting a radiant heat transfer enclosures with participating media. Journal of Heat Transfer 112 (2), 415–423.

Ristorcelli, T., 2013. Evaluation de l'apport des visées multi-angulaires en imagerie laser pour la reconstruction 3d des couverts végétaux. Ph.D. thesis, Institut Supérieur de l'Aéronautique et de l'Espace-ISAE. 6, 93

Ristorcelli, T., Hamoir, D., Briottet, X., 2014. Simulating space lidar waveforms from smaller-footprint airborne laser scanner data for vegetation observation. Geoscience and Remote Sensing Letters, IEEE 11 (2), 534–538. 6, 93

Román, M. O., Gatebe, C. K., Schaaf, C. B., Poudyal, R., Wang, Z., King, M. D., 2011. Variability in surface BRDF at different spatial scales (30m–500m) over a mixed agricultural landscape as retrieved from airborne and satellite spectral measurements. Remote Sensing of Environment 115 (9), 2184–2203.

Román, M. O., Gatebe, C. K., Shuai, Y., Wang, Z., Gao, F., Masek, J. G., He, T., Liang, S., Schaaf, C. B., 2013. Use of in situ and airborne multiangle data to assess MODIS-and Landsat-based estimates of directional reflectance and albedo. Geoscience and Remote Sensing, IEEE Transactions on 51 (3), 1393–1404.

Rosell, J. R., Llorens, J., Sanz, R., Arno, J., Ribes-Dasi, M., Masip, J., Escolà, A., Camp, F., Solanelles, F., Gràcia, F., et al., 2009. Obtaining the three-dimensional structure of tree orchards from remote 2D terrestrial LIDAR scanning. Agricultural and Forest Meteorology 149 (9), 1505–1515. 2, 9, 17

Rosette, J., Field, C., Nelson, R., DeCola, P., Cook, B., et al., 2011. A new photon-counting lidar system for vegetation analysis. Proceedings of SilviLaser, 16–19. 92

Ross, I., 1981. The radiation regime and architecture of plant stands. No. 3. Springer Science & Business Media. 2, 4

Roujean, J.-L., Leroy, M., Deschamps, P.-Y., 1992. A bidirectional reflectance model of the Earth's surface for the correction of remote sensing data. Journal of Geophysical Research: Atmospheres (1984–2012) 97 (D18), 20455–20468. 3

Rouse Jr, J., Haas, R., Schell, J., Deering, D., 1974. Monitoring vegetation systems in the Great Plains with ERTS. NASA special publication 351, 309.

Schaepman, M. E., de Vos, L., Itten, K. I., 1998. APEX-Airborne PRISM Experiment: hyperspectral radiometric performance analysis for the simulation of the future ESA land surface processes earth explorer mission. In: Proc. SPIE's International Symposium on Optical Science, Engineering, and Instrumentation. International Society for Optics and Photonics, pp. 253–262.

Schaepman, M. E., Jehle, M., Hueni, A., D'Odorico, P., Damm, A., Weyermann, J., Schneider, F. D., Laurent, V., Popp, C., Seidel, F. C., Lenhard, K., Gege, P., Küchler, C., Brazile, J., Kohler, P., Vos, L. D., Meuleman, K., Meynart, R., Schläpfer, D., Kneubühler, M., Itten, K. I., 2015. Advanced radiometry measurements and Earth science applications with the Airborne Prism Experiment (APEX). Remote Sensing of Environment 158, 207–219.

Schaepman-Strub, G., Schaepman, M., Painter, T., Dangel, S., Martonchik, J., 2006. Reflectance quantities in optical remote sensing—definitions and case studies. Remote Sensing of Environment 103 (1), 27 – 42. 6

Schneider, F. D., Leiterer, R., Morsdorf, F., Gastellu-Etchegorry, J.-P., Lauret, N., Pfeifer, N., Schaepman, M. E., 2014a. Simulating imaging spectrometer data: 3D forest modeling based on LiDAR and in situ data. Remote Sensing of Environment 152, 235–250. 2, 8, 16

Schneider, F. D., Yin, T., Gastellu-Etchegorry, J.-P., Morsdorf, F., Schaepman, M. E., 2014b. At-sensor radiance simulation for airborne imaging spectroscopy. IEEE WHISPERS 2014, in press.

Schutz, B., Zwally, H., Shuman, C., Hancock, D., DiMarzio, J., 2005. Overview of the ICESat mission. Geophysical Research Letters 32 (21).

Shan, J., Toth, C. K., 2008. Topographic laser ranging and scanning: principles and processing. CRC Press. 8, 17

Smolander, S., et al., 2006. Radiative transfer, interception and scattering in coniferous forests: models and applications for production ecology and remote sensing. Dissertationes Forestales. 4

Sobrino, J., Mattar, C., Gastellu-Etchegorry, J.-P., Jimenez-Munoz, J., Grau, E., 2011. Evaluation of the DART 3D model in the thermal domain using satellite/airborne imagery and ground-based measurements. International Journal of Remote Sensing 32 (22), 7453–7477.

Sonka, M., Hlavac, V., Boyle, R., 2008. Image processing, analysis, and machine vision. Vol. 3. Thomson Toronto. 1, 8, 16

Soudani, K., François, C., 2014. Remote sensing: A green illusion. Nature 506 (7487), 165–166.

Spinhirne, J. D., 1993. Micro pulse lidar. Geoscience and Remote Sensing, IEEE Transactions on 31 (1), 48–55.

Sun, G., Ranson, K. J., 2000. Modeling lidar returns from forest canopies. Geoscience and Remote Sensing, IEEE Transactions on 38 (6), 2617–2626. 93

Suykens, F., 2002. On robust Monte Carlo algorithms for multi-pass global illumination. status: published.

Thenkabail, P. S., Lyon, J. G., Huete, A., 2011. Hyperspectral remote sensing of vegetation. CRC Press.

Thompson, R., Goel, N. S., 1998. Two models for rapidly calculating bidirectional reflectance: Photon spread (ps) model and statistical photon spread (sps) model. Remote Sensing Reviews 16 (3), 157–207.

Truelove, J. S., 1987. Discrete-ordinate solutions of the radiation transport Equation. Journal of Heat Tranfer 109 (4), 1048–1051.

Truelove, J. S., 1988. Three-dimensional radiation in absorbing-emitting-scattering media using the discrete-ordinates approximation. Journal of Quantitative Spectroscopy and Radiative Transfer 39 (1), 27–31.

UEBERSCHLAG, A., 2010. Etude des couverts forestiers par inversion de formes d'onde Lidar à l'aide du modèle de transfert radiatif DART développé par le CESBIO. Ph.D. thesis, INSA de Strasbourg.

Ustin, S. L., Roberts, D. A., Gamon, J. A., Asner, G. P., Green, R. O., 2004. Using imaging spectroscopy to study ecosystem processes and properties. BioScience 54 (6), 523–534. 1

Verhoef, W., 1984. Light scattering by leaf layers with application to canopy reflectance modeling : The SAIL model. Remote Sensing of Environment 16, 125–141. 5, 14

Vermote, E. F., Tanré, D., Deuze, J.-L., Herman, M., Morcette, J.-J., 1997. Second simulation of the satellite signal in the solar spectrum, 6S: An overview. Geoscience and Remote Sensing, IEEE Transactions on 35 (3), 675–686. 5

Vierling, K. T., Vierling, L. A., Gould, W. A., Martinuzzi, S., Clawges, R. M., 2008. Lidar: shedding new light on habitat characterization and modeling. Frontiers in Ecology and the Environment 6 (2), 90–98. 91

Wagner, W., Ullrich, A., Ducic, V., Melzer, T., Studnicka, N., 2006. Gaussian decomposition and calibration of a novel small-footprint full-waveform digitising airborne laser scanner. ISPRS Journal of Photogrammetry and Remote Sensing 60 (2), 100–112.

Wang, J., Chang, C.-I., 2006. Independent component analysis-based dimensionality reduction with applications in hyperspectral image analysis. Geoscience and Remote Sensing, IEEE Transactions on 44 (6), 1586–1600.

Wanner, W., Li, X., Strahler, A., 1995. On the derivation of kernels for kernel-driven models of bidirectional reflectance. Journal of Geophysical Research: Atmospheres (1984–2012) 100 (D10), 21077–21089. 3

Wehr, A., Lohr, U., 1999. Airborne laser scanning—an introduction and overview . {ISPRS} Journal of Photogrammetry and Remote Sensing 54 (2–3), 68 – 82.

Widlowski, J.-L., Pinty, B., Clerici, M., Dai, Y., Kauwe, M. D., de Ridder, K., Kallel, A., Kobayashi, H., Lavergne, T., Ni-Meister, W., Olchev, A., Quaife, T., Wang, S., Yang, W., Yang, Y., Yuan, H., 2011a. RAMI4PILPS: An intercomparison of formulations for the partitioning of solar radiation in land surface models. Journal of Geophysical Research 116, G02019. 6

Widlowski, J.-L., Pinty, B., Lopatka, M., Atzberger, C., Buzica, D., Chelle, M., Disney, M., Gastellu-Etchegorry, J.-P., Gerboles, M., Gobron, N., Grau, E., Huang, H., Kallel, A., Kobayashi, H., Lewis, P. E., Qin, W., Schlerf, M., Stuckens, J., Xie, D., 2011b. The fourth radiation transfer model intercomparison (RAMI-IV): Proficiency testing of canopy reflectance models with ISO-13528. Journal of Geophysical Research 118, 6869–6890. 6

Widlowski, J.-L., Robustelli, M., Disney, M., Gastellu-Etchegorry, J.-P., Lavergne, T., Lewis, P., North, P., Pinty, B., Thompson, R., Verstraete, M., 2008. The RAMI On-line Model Checker (ROMC): A web-based benchmarking facility for canopy reflectance models. Remote Sensing of Environment 112 (3), 1144–1150. 6

Widlowski, J.-L., Taberner, M., Pinty, B., Bruniquel-Pinel, V., Disney, M., Fernandes, R., Gastellu-Etchegorry, J.-P., Gobron, N., Kuusk, A., Lavergne, T., Leblanc, S., Lewis, P. E., Martin, E., Mõttus, M., North, P. R. J., Qin, W., Robustelli, M., Rochdi, N., Ruiloba, R., Soler, C., Thompson, R., Verhoef, W., Verstraete, M. M., Xie, D., 2007. Third Radiation Transfer Model Intercomparison (RAMI) exercise: Documenting progress in canopy reflectance models. Journal of Geophysical Research 112, D09111. 6

Yan, W. Y., Shaker, A., El-Ashmawy, N., 2015. Urban land cover classification using airborne LiDAR data: A review . Remote Sensing of Environment 158 (0), 295 – 310. 2

Yang, X., Strahler, A. H., Schaaf, C. B., Jupp, D. L., Yao, T., Zhao, F., Wang, Z., Culvenor, D. S., Newnham, G. J., Lovell, J. L., Dubayah, R. O., Woodcock, C. E., Ni-Meister, W., 2013. Three-dimensional forest reconstruction and structural parameter retrievals using a terrestrial full-waveform lidar instrument (Echidna®) . Remote Sensing of Environment 135 (0), 36 – 51. 2

Yin, T., Gastellu-Etchegorry, J., Grau, E., Lauret, N., Rubio, J., July 2013a. Simulating satellite waveform Lidar with DART model. In: Proc. Geoscience and Remote Sensing Symposium (IGARSS), 2013 IEEE International. pp. 3029–3032. 94

Yin, T., Gastellu-Etchegorry, J.-P., Lauret, N., 2015a. Simulation of satellite, airborne and terrestrial LiDAR with DART (II): ALS and TLS multi-pulse acquisitions, photon counting, and solar noise. Remote Sensing of Environment, submitted. 93

Yin, T., Gastellu-Etchegorry, J.-P., Lauret, N., Grau, E., Rubio, J., 2013b. A new approach of direction discretization and oversampling for 3D anisotropic radiative transfer modeling. Remote Sensing of Environment 135, 213–223. 5, 15

Yin, T., Lauret, N., Gastellu-Etchegorry, J.-P., 2015b. Simulating images of passive sensors with finite field of view by coupling 3-d radiative transfer model and sensor perspective projection. Remote Sensing of Environment 162 (0), 169 – 185.
URL http://www.sciencedirect.com/science/article/pii/S0034425715000796

You, D., Wen, J., Liu, Q., Tang, Y., 2014. The Angular and Spectral Kernel-Driven Model: Assessment and Application. 3

Zhang, J., Tong, Y., Yang, X., Gong, J., Gong, W., 2011. Detection of atmospheric composition based on Lidar. In: Journal of Physics: Conference Series. Vol. 276. IOP Publishing, p. 012036. 2

Zhang, K., Chen, S.-C., Whitman, D., Shyu, M.-L., Yan, J., Zhang, C., 2003. A progressive morphological filter for removing nonground measurements from airborne LIDAR data. Geoscience and Remote Sensing, IEEE Transactions on 41 (4), 872–882. 9, 17

Zhu, Z., Hanson, A. R., Riseman, E. M., 2004. Generalized parallel-perspective stereo mosaics from airborne video. Pattern Analysis and Machine Intelligence, IEEE Transactions on 26 (2), 226–237. 8, 16

Zwally, H., Schutz, B., Abdalati, W., Abshire, J., Bentley, C., Brenner, A., Bufton, J., Dezio, J., Hancock, D., Harding, D., et al., 2002. ICESat's laser measurements of polar ice, atmosphere, ocean, and land. Journal of Geodynamics 34 (3), 405–445. 2

Appendix I: Generation of cosine-weighted direction set

Cosine-Weighted hemispherical sampling is a well-known technique for Monte-Carlo ray tracing (MCRT), in order to avoid the cosine distributed scattered energy sampling towards uniformly distributed solid angles, to have uniformly distributed scattered energy sampling towards cosine-weighted solid angles. This technique was usually applied to reduce the sampling noise. In contrast, for the equally celebrated discrete-ordinate ray tracking technique, a uniformly distribution of the sampling is usually preferred. The objective of this appendix is to find a way to adapt the cosine weighted distribution to discrete ordinates.

Probability density of uniformly distributed direction set

DART combine exact kernel and discrete ordinate techniques for solving the radiative transfer equation. The IUSD method presented in Chapter 2 generates a set of uniformly distributed directions with equal solid angles and well-defined shapes. Table 1 of Chapter 2 gives the attributes of any direction (Ω, $\Delta\Omega$). The center of the solid angle is selected to be the center of mass, which divides the solid angle (Ω, $\Delta\Omega$) into 2 equal solid angles ($\Delta\Omega/2$). The center of (Ω, $\Delta\Omega$) is defined as:

$$\theta_c = \arccos(\cos\theta_0 - \Delta\cos\theta/2) = \arccos(\frac{\cos\theta_0 + \cos\theta_1}{2}) \tag{1}$$

$$\phi_c = \frac{\phi_0 + \phi_1}{2} \tag{2}$$

and the solid angle is calculated as:

$$\Delta\Omega = \Delta\cos\theta \times \Delta\phi \tag{3}$$

The zenith angles of the directions are equally spaced. It leads to several layers, with different number of directions within each layer. Another condition is used in order to ensure the shape of solid angles is more or less a square: the within solid angle vertical and horizontal arc that pass through the direction center (θ_c, ϕ_c) have equal lengths. It is:

$$\Delta\theta = \sin\theta_c \Delta\phi \tag{4}$$

By substitution of Equation (4) into Equation (3), we get:

$$\Delta\Omega = (\cos\theta_0 - \cos\theta_1)\frac{\Delta\theta}{\sin\theta_c}$$

If $\Delta\theta$ is determined, the corresponding layer can be generated. Assume the superscript l to be the layer index, the total solid angle of a layer is:

$$\Delta\Omega^l = (\cos(\theta_0^l) - \cos(\theta_1^l)) \times 2\pi$$

Therefore, the number of directions n in layer l is:

$$n^l = \frac{2\pi \times \sin\theta_c}{\Delta\theta^l}$$

Let N be the total number of directions, the probability of a direction located in layer l is:

$$P^l = \frac{2\pi \times \sin\theta_c}{\Delta\theta^l \times N}$$

This expression can be converted to an average probability density ($p(\theta_c)$) of layer l in terms of θ, it gives:

$$p(\theta_c)^l = \frac{2\pi \times \sin\theta_c}{\Delta\theta^l \times \Delta\theta^l \times N} \tag{5}$$

We have:

$$p(\theta) \propto \sin\theta \tag{6}$$

Within each layer, the solid angle of each direction is equal, so the ϕ is uniformly distributed. The resultant DART direction is shown in Figure 2 of Chapter 2. As $N \to 10^6$, the histogram of direction distribution of upper hemisphere over θ is shown in Figure 1, which is corresponding to Eqa.(6).

Cosine-weighted direction set

The cosine-weighted hemisphere sampling method provides a 3D distribution of rays. The angle density of which on the sphere is proportional to that of a Lambertian surface. The energy that a Lambertian surface has in a solid angle $d\Omega = sin\theta d\theta d\phi$ is $\frac{1}{2}Lsin(2\theta)d\theta d\phi$, where L is the surface radiance. The classical random method for obtaining the rays (i.e., directions) is shown below:

1. Choose 2 random number $r1$, $r2$ in the range (0, 1).
2. $\phi(r1) = 2\pi \times r1$

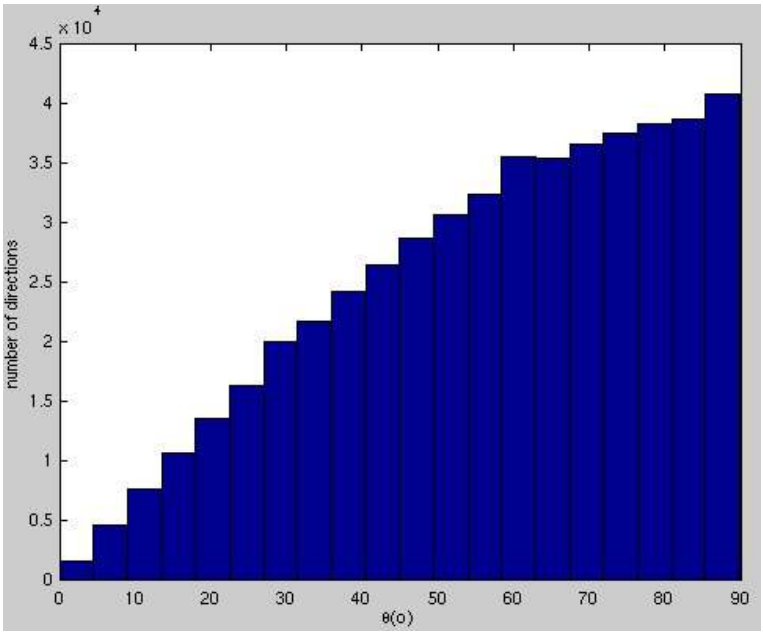

Fig. 1*: The histogram of* 5×10^5 *DART directions over upper hemisphere*

3. $\theta(r2) = arccos(\sqrt{r2})$

It implies that ϕ is uniformly distributed in the 2π space. θ is not uniformly distributed. The probability density function (pdf) of $r2$ is a constant equals 1 ($f_X(r2) = 1$). According to the "change of variable" rule of pdf:

$$\begin{aligned} f_Y(\theta) &= |\frac{d}{d\theta} r2(\theta)| \times f_X(r2(\theta)) \\ &= |\frac{d}{d\theta}(cos^2(\theta))| \\ &= |-2cos(\theta)sin(\theta)| \\ &= sin(2\theta) \end{aligned} \tag{7}$$

Figure 2 shows a histogram of 5×10^5 cosine-weighted sampling, which corresponds to Eqa. (7).

Cosine-weighted discrete ordinates can be difined through Eqa.(5) and Eqa.(7). The only parameter that is flexible is $\Delta\theta$. It means that $\Delta\theta$ must be such that the density of DART directions equals the probability density of cosine-weighted sampling. We must have:

$$(\Delta\theta^l)^2 \propto \frac{1}{cos(\theta_c^l)} \tag{8}$$

which means for every layer of the sphere of directions, the term $(\theta_1 - \theta_0)^2 \times \frac{cos(\theta_0)+cos(\theta_1)}{2}$ must be considered. We can reduce the computation complexity with the approximation $(\theta_1 - \theta_0) \times \frac{cos(\theta_0)+cos(\theta_1)}{2} = sin(\theta_1) - sin(\theta_0)$. If the total number of layers is L, we have $L-1$ equations with $L-1$ unknowns

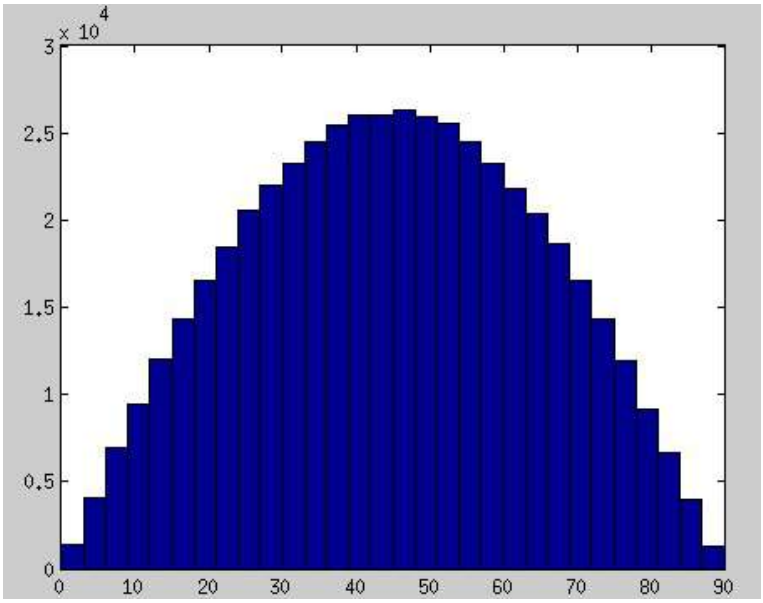

Fig. 2*: The histogram of* 5×10^5 *cosine-weighted sampling of upper hemisphere*

(subscript as the index):

$$\begin{cases} sin(\theta_1) \times \theta_1 = (sin(\theta_2) - sin(\theta_1)) * (\theta_2 - \theta_1) \\ (sin(\theta_2) - sin(\theta_1)) * (\theta_2 - \theta_1) = (sin(\theta_3) - sin(\theta_2)) * (\theta_3 - \theta_2) \\ \quad . \\ \quad . \\ (sin(\theta_{L-2}) - sin(\theta_{L-3})) * (\theta_{L-2} - \theta_{L-3}) = (sin(\theta_{L-1}) - sin(\theta_{L-2})) * (\theta_{L-1} - \theta_{L-2}) \\ (sin(\theta_{L-1}) - sin(\theta_{L-2})) * (\theta_{L-1} - \theta_{L-2}) = (1 - sin(\theta_{L-1})) * (\pi/2 - \theta_{L-1}) \end{cases} \tag{9}$$

There is no simple analytical solution to the above equation set. However, the Newton-Raphson Method for Nonlinear Systems of Equations gives fairly good and fast estimation of the roots. Details can be found from Numerical Recipes (C++) 3rd Edition (2007). Figure 3 shows the resultant cosine-weighted discrete ordinate directions. . Figure 4 is the histogram of 431464 cosine-weighted discrete ordinates in the upper sphere. It samples very well to the histogram of the cosine-weighted directions that are obtained by the random pulling method (Figure 4).

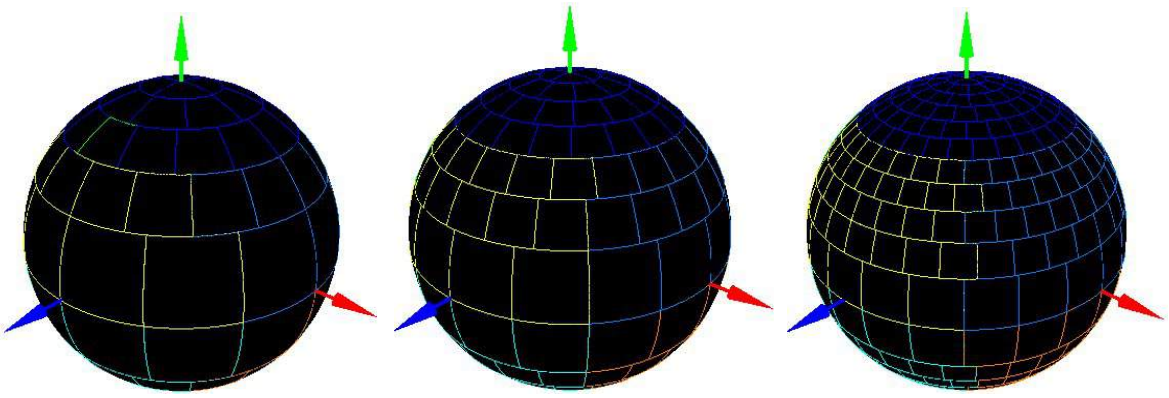

(a) 110 directions with region oversampling

(b) 216 directions

(c) 528 directions

Fig. 3*: The 3D spherical distribution of directions for cosine-weighted 110, 216 and 528 ordinates*

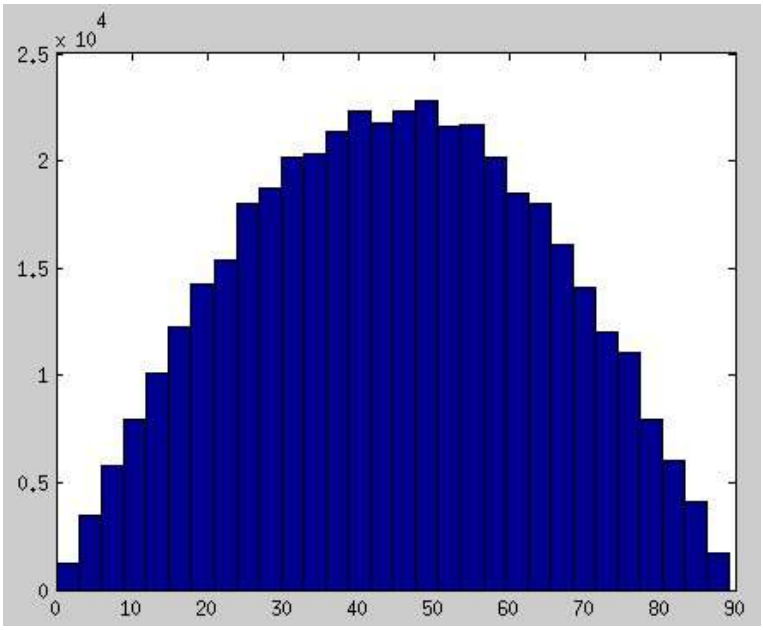

Fig. 4*: The histogram of 431464 cosine-weighted directions in the upper sphere*

Appendix II: Conference proceeding: At-Sensor Radiance Simulation for Airborne Imaging Spectroscopy

AT-SENSOR RADIANCE SIMULATION FOR AIRBORNE IMAGING SPECTROSCOPY

F.D. Schneider[1], T. Yin[2], J.-P. Gastellu-Etchegorry[2], F. Morsdorf[1], M.E. Schaepman[1]

[1] Remote Sensing Laboratories, University of Zurich, Winterthurerstrasse 190, 8057 Zurich, Switzerland, Email: fabian-daniel.schneider, felix.morsdorf, michael.schaepman@geo.uzh.ch
[2] Centre d'Études Spatiales de la Biosphère, Paul Sabatier University - CNES - CNRS - IRD, 18 Avenue Edouard Belin, BPI 2801, 31401 Toulouse, Cedex 9, France, Email: yint, jean-philippe.gastellu-etchegorry@cesbio.cnes.fr

ABSTRACT

Physically-based radiative transfer modeling is the key to remote sensing of forest ecosystems. To scale spectral information from the leaf to the sensor level, the canopy architecture of a forest, illumination conditions and the viewing geometry have to be taken into account. Therefore, a new airborne image simulation approach is being developed for the 3D radiative transfer model DART to model individual viewing angles for each pixel of a scene. A first comparison to actual imaging spectrometer data showed promising results, mainly because the atmosphere simulation could be improved compared to previous versions of the DART model.

Index Terms— Radiative transfer modeling, Airborne image simulation, Airborne imaging spectroscopy

1. INTRODUCTION

Scaling spectral information from the leaf to the sensor level is one of the main challenges in the remote sensing of forest ecosystems. The estimation of biochemical constituents of leaves or needles from remotely sensed data is of high interest, but not trivial due to atmospheric influences and the structural complexity of natural forests [1, 2]. The reflectance of a forest canopy is not only determined by the leaf optical properties but also by factors like canopy structure, illumination conditions and viewing geometry [3, 4, 5]. Their influence is especially large for natural forests growing on steep slopes. Thus, a sophisticated radiative transfer model is needed to scale leaf or needle optical properties to at-sensor radiance.

The DART model (Discrete Anisotropic Radiative Transfer [6]) is one of the most complete coupled canopy-atmosphere 3D radiative transfer models. It was initially designed to simulate spaceborne remote sensing images of natural landscapes [7]. The physically based 3D model allows to simulate virtually any illumination or viewing angle, but was limited to parallel incoming and outgoing rays. This simplification was acceptable for simulating spaceborne sensors, but not made for airborne sun-earth-sensor constellations having a much larger angular variation within a scene. Since DART is predestined to simulate high-dimensional airborne imaging spectrometer data, a new module is being implemented to simulate airborne pushbroom scanners and frame cameras. We present here first results of the new airborne imaging simulation in comparison to previous modeling results and real measurements of the state-of-the-art airborne imaging spectrometer APEX (Airborne Prism EXperiment [8]).

2. STUDY AREA AND DATA

The study area covers 300 m x 300 m and is located at the Laegern, a temperate mixed forest in Switzerland. It is a highly diverse forest dominated by beech and Norway spruce trees, which is characterized by steep, rugged terrain, a heterogeneous spectral background and a complex canopy architecture. Airborne and terrestrial laser scanning as well as leaf optical properties measurements were combined with in situ data of plant area index and leaf angle distribution to fully describe the test site (see [9] for more details).

Imaging spectrometer data was acquired on June 16th, 2012 at 10:26 UTC at a solar illumination angle of 27.1° in zenith and 147.4° in azimuth (defined from north clockwise). The study area was measured under clear sky conditions and covered by a single flight line. The average flight altitude was 4526 m above sea level resulting in a ground pixel size of 2 m. The airborne imaging spectrometer APEX was used being a state-of-the-art pushbroom scanner system with a spectral sampling interval varying between 2.5 nm and 13.9 nm and a full width at half maximum between 3.4 nm and 14.3 nm, depending on wavelength. The viewing angle at scene center was 6.76° in zenith and 331.8° in azimuth. The exact viewing angles of each pixel are shown in Figure 1.

Traceable radiometric calibration of the APEX data included compensation for spatial coregistration effects of the VNIR and SWIR detector, dark current and keystone correction. The uncertainty of calibrated radiance values was lying within 0.5% and 3% in the range of 400 to 1900 nm, as estimated by a calibration model. APEX data was georefer-

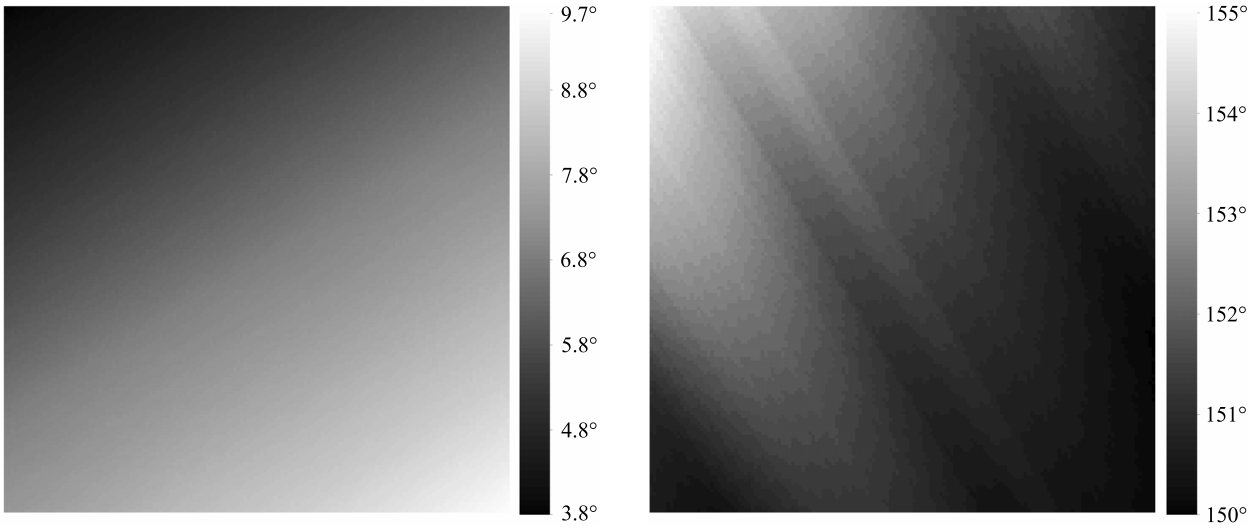

(a) Zenith angle (b) Azimuth angle

Fig. 1. Specific viewing angle of each pixel, as derived from the APEX acquisition of the scene.

enced to the Swiss national grid CH1903+ and orthorectified using nearest neighbor resampling in PARGE [10]. The geocorrection was based on the digital terrain model DHM25 of the Swiss Federal Office of Topography (Swisstopo, Switzerland).

3. METHODS

A forest scene of 300 m x 300 m was parameterized in DART following a voxel-based forest reconstruction approach described in [9]. In the DART model, a vegetation volume is modeled as a turbid medium parameterized by leaf optical properties, leaf angle distribution, and a plant area index. The final DART scene, which was used for the radiative transfer simulations, consisted of the canopy background (terrain model, background optical properties) and a 3D voxel grid, which was filled by turbid media according to airborne laser scanning and in situ measurements. The voxel size was 2 m x 2 m x 2 m, matching the resolution of the APEX data.

The DART atmosphere was parameterized based on standard gas and aerosol models of MODTRAN and in situ measurements of AERONET [11, 12]. The main principle of atmosphere radiative transfer modeling in DART is described in [13]. It is based on voxels of the bottom, mid, and high atmosphere, being filled by gases and aerosols. To model the interactions of radiation (scattering, absorption) with the gases and aerosols, specific phase functions are modeled in DART. Recently, the vertical distribution of gases and aerosols as well as the Henyey-Greenstein coefficients that define the aerosol phase function were improved according to the MODTRAN atmosphere model, which can be seen as a standard for radiative transfer modeling within the atmosphere. Compared to results simulated with previous DART versions (v5.4.3 and earlier), an improved accuracy of the atmosphere simulation is expected.

Furthermore, a new module is under development to simulate radiance and reflectance values as measured by passive optical airborne imaging systems. However, the so called airborne image simulation is not limited to sensors mounted on an airplane. It refers to any situation, where the distance between the sensor and the measured target is not large enough to neglect angular variations in viewing geometry by assuming parallel outgoing rays along a single viewing direction.

Instead of one universal viewing direction, a specific azimuth and zenith angle can be defined for each pixel (x,y) of the scene. The ray tracing is then calculated along specific virtual directions, whose vector can change according to the position of the scattering element and the sensor. The concept of virtual directions as additional outputs to discretized directions over the 2-π upper hemisphere was introduced in [14]. It is an efficient way to track rays along arbitrary directions without further contributing to the ray tracing along the fixed, discretized paths.

For a first evaluation of the newly implemented DART functionalities, airborne image simulations were carried out at four selected bands (533, 570, 680, 780 nm) and compared to APEX data and simulations of DART version 5.4.3 along a single view direction. The images were simulated according to the APEX acquisition of the scene and orthorectified for best comparability. The viewing angles were defined according to the azimuth and zenith angles shown in Figure 1.

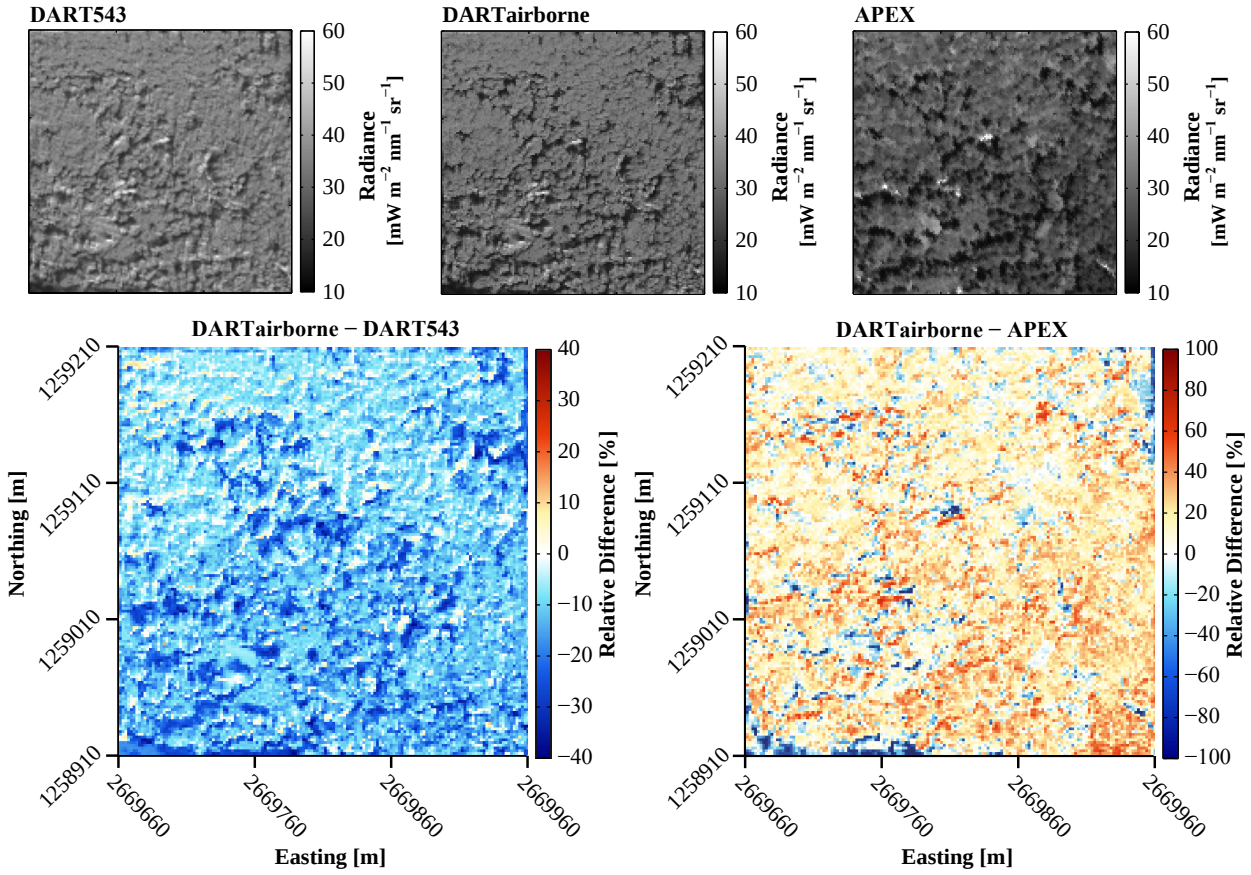

Fig. 2. Images of at-sensor radiance and corresponding relative differences at 570 nm, as simulated by DART version 5.4.3 (DART543), the new airborne image simulation (DARTairborne), and measured by APEX (APEX).

4. RESULTS AND DISCUSSION

We present here the first results of the new airborne image simulation. The simulated and measured at-sensor radiance images at 570 nm and the relative difference images are shown in Figure 2. The new simulation leads to lower radiance values over the whole scene, but especially in shadowed areas. The values can be up to 40% lower and are therefore closer to the values measured by APEX. Generally, the dynamic range is slightly lower in the newly simulated image, because a simplified orthorectification algorithm was used. To calculate an orthorectified image for the airborne image simulation is much more difficult than for a simple directional image, which is why a more sophisticated algorithm is still under development.

Lower radiance values can be observed in all bands of the visible, whereas higher values can be observed in the near infrared. This can be explained by an improved atmosphere modeling using the new airborne image simulation. On one hand, the aerosol phase functions and vertical distribution of gases and aerosols were improved. On the other hand, the atmosphere flux tracking is more accurate if the correct viewing angles are simulated. This effect is especially strong, when at-sensor radiance is simulated.

Since vegetation is absorbing most of the radiation in the visible range, a lower atmospheric path radiance leads to lower at-sensor radiance. The opposite can be observed in the near infrared, because vegetation is strongly scattering. Even though the atmosphere simulation was improved, atmospheric effects are still slightly smaller in the APEX data. The average difference to the APEX image is 4.27, 4.37, 2.08, -25.73 mW m^{-2} nm^{-1} sr^{-1} at 533, 570, 680, 780 nm respectively, whereas it was 9.26, 8.59, 9.14, -37.12 mW m^{-2} nm^{-1} sr^{-1} with DART version 5.4.3.

A pixel-wise comparison with the APEX data shows that there are still major differences at all simulated bands. In the visible, some of the larger differences occur due to local shifts between the images. This is because the projection of modeled (DART) and measured (APEX) data is not exactly the same. More distinct patterns of under- and overestimation

can be observed in the near infrared, which are mainly due to small-scale structural effects. These effects were discussed in detail in [9].

5. CONCLUSION AND OUTLOOK

We presented here first results of a new airborne image simulation within the 3D radiative transfer model DART. The new module allows to define specific viewing angles for each pixel (x,y), instead of assuming parallel outgoing rays along a single viewing direction. A temperate mixed forest scene was simulated according to the measurement of the airborne imaging spectrometer APEX. Compared to the APEX data and simulations of the previous DART release, modeling results could be improved by introducing the airborne image simulation as well as new phase functions and vertical distributions of aerosols and gases. Both, the DART as well as the APEX orthorectification should be improved for future comparisons. Finally, a larger scene has to be modeled to further study the influence of angular variations from near to far range.

6. ACKNOWLEDGEMENTS

This study has been supported by European Space Agency (ESA) Support to Science Element (STSE) ESRIN contract No. AO/1-6529/10/I-NB, '3D Vegetation Laboratory'. Contributions of FS, FM and MS were funded by the University of Zurich Research Priority Program on 'Global Change and Biodiversity'. We thank Paul Sabatier University and French Space Center (CNES) for supporting DART development (TOSCA project STEM-LEAF).

7. REFERENCES

[1] Z. Malenovský, H.M. Bartholomeus, F.W. Acerbi-Junior, J.T. Schopfer, T.H. Painter, G.F. Epema, and A.K. Bregt, "Scaling dimensions in spectroscopy of soil and vegetation," *International Journal of Applied Earth Observation and Geoinformation*, vol. 9, no. 2, pp. 137 – 164, 2007.

[2] M.E. Schaepman, S.L. Ustin, A.J. Plaza, T.H. Painter, J. Verrelst, and S. Liang, "Earth system science related imaging spectroscopy - an assessment," *Remote Sensing of Environment*, vol. 113, Supplement 1, no. 0, pp. S123 – S137, 2009.

[3] N.S. Goel, "Models of vegetation canopy reflectance and their use in estimation of biophysical parameters from reflectance data," *Remote Sensing Reviews*, vol. 4, no. 1, pp. 1–212, 1988.

[4] G.P. Asner, "Biophysical and biochemical sources of variability in canopy reflectance," *Remote Sensing of Environment*, vol. 64, no. 3, pp. 234 – 253, 1998.

[5] J. Verrelst, M.E. Schaepman, Z. Malenovský, and J.G.P.W. Clevers, "Effects of woody elements on simulated canopy reflectance: Implications for forest chlorophyll content retrieval," *Remote Sensing of Environment*, vol. 114, no. 3, pp. 647 – 656, 2010.

[6] J.P. Gastellu-Etchegorry, E. Grau, and N. Lauret, "DART: A 3D model for remote sensing images and radiative budget of earth surfaces," in *Modeling and Simulation in Engineering*, Catalin Alexandru, Ed., chapter 2. 2012.

[7] J.P. Gastellu-Etchegorry, V. Demarez, V. Pinel, and F. Zagolski, "Modeling radiative transfer in heterogeneous 3-D vegetation canopies," *Remote Sensing of Environment*, vol. 58, no. 2, pp. 131 – 156, 1996.

[8] M. Jehle, A. Hueni, A. Damm, P. D'Odorico, J. Weyermann, M. Kneubühler, D. Schläpfer, M.E. Schaepman, and K. Meuleman, "APEX - current status, performance and validation concept," in *Sensors, 2010 IEEE*, 2010, pp. 533–537.

[9] F.D. Schneider, R. Leiterer, F. Morsdorf, J.-P. Gastellu-Etchegorry, N. Lauret, N. Pfeifer, and M.E. Schaepman, "Simulating imaging spectrometer data: 3D forest modeling based on LiDAR and in situ data," *Remote Sensing of the Environment*, 2014, in revision.

[10] D. Schläpfer, M.E. Schaepman, and K.I. Itten, "PARGE: parametric geocoding based on gcp-calibrated auxiliary data," in *Imaging Spectrometry IV*. The International Society for Optical Engineering, 1998, vol. 3438, pp. 334–344.

[11] L.S. Berstein and D.C. Roberston, "MODTRAN: a moderate resolution model for LOWTRAN 7," Tech. Rep. GL-TR-89-0122, Geophys. Lab, Bedford, MA, 1989.

[12] B.N. Holben, T.F. Eck, I. Slutsker, D. Tanré, J.P. Buis, A. Setzer, E. Vermote, J.A. Reagan, Y.J. Kaufman, T. Nakajima, F. Lavenu, I. Jankowiak, and A. Smirnov, "AERONET - a federated instrument network and data archive for aerosol characterization," *Remote Sensing of Environment*, vol. 66, no. 1, pp. 1–16, 1998.

[13] E. Grau and J.-P. Gastellu-Etchegorry, "Radiative transfer modeling in the earth-atmosphere system with DART model," *Remote Sensing of Environment*, vol. 139, no. 0, pp. 149 – 170, 2013.

[14] T. Yin, J.-P. Gastellu-Etchegorry, N. Lauret, E. Grau, and J. Rubio, "A new approach of direction discretization and oversampling for 3d anisotropic radiative transfer modeling," *Remote Sensing of Environment*, vol. 135, no. 0, pp. 213 – 223, 2013.